ornl

OAK RIDGE NATIONAL LABORATORY

MARTIN MARIETTA

NUREG/CR-4219
Vol. 5, No. 1
ORNL/TM-9593/V5&N1

Heavy-Section Steel Technology Program Semiannual Progress Report for October 1987–March 1988

W. R. Corwin

Prepared for the U.S. Nuclear Regulatory Commission
Office of Nuclear Regulatory Research
Under Interagency Agreements DOE 0551-0551-A1 and 0552-0552-A1

OPERATED BY
MARTIN MARIETTA ENERGY SYSTEMS, INC.
FOR THE UNITED STATES
DEPARTMENT OF ENERGY

Available from

Superintendent of Documents
U.S. Government Printing Office
Post Office Box 37082
Washington, D.C. 20013-7982

and

National Technical Information Service
Springfield, VA 22161

NUREG/CR-4219
Vol. 5, No. 1
ORNL/TM-9593/V5&N1
Dist. Category RF

Engineering Technology Division

HEAVY-SECTION STEEL TECHNOLOGY PROGRAM SEMIANNUAL PROGRESS REPORT FOR OCTOBER 1987—MARCH 1988

W. R. Corwin

Manuscript Completed — July 13, 1988
Date Published — August 1988

NOTICE: This document contains information of a preliminary nature. It is subject to revision or correction and therefore does not represent a final report.

Prepared for the
U.S. Nuclear Regulatory Commission
Office of Nuclear Regulatory Research
under Interagency Agreements DOE 0551-0551-A1 and 0552-0552-A1

NRC FIN No. B0119

Prepared by the
OAK RIDGE NATIONAL LABORATORY
Oak Ridge, Tennessee 37831
operated by
MARTIN MARIETTA ENERGY SYSTEMS, INC.
for the
U.S. DEPARTMENT OF ENERGY
under Contract No. DE-AC05-84OR21400

CONTENTS

LIST OF FIGURES

LIST OF TABLES

PREFACE

The Heavy-Section Steel Technology (HSST) Program, which is sponsored by the Nuclear Regulatory Commission, is an engineering research activity devoted to extending and developing the technology for assessing the margin of safety against fracture of the thick-walled steel pressure vessels used in light-water-cooled nuclear power reactors. The program is being carried out in close cooperation with the nuclear power industry. This report covers HSST work performed in October 1987—March 1988. The work performed by Oak Ridge National Laboratory (ORNL) and by subcontractors is managed by the Engineering Technology Division (ETD) of ORNL. Major tasks at ORNL are carried out by the ETD and the Metals and Ceramics Division. Prior progress reports on this program are ORNL-4176, ORNL-4315, ORNL-4377, ORNL-4463, ORNL-4512, ORNL-4590, ORNL-4653, ORNL-4681, ORNL-4764, ORNL-4816, ORNL-4855, ORNL-4918, ORNL-4971, ORNL/TM-4655 (Vol. II), ORNL/TM-4729 (Vol. II), ORNL/TM-4805 (Vol. II), ORNL/TM-4914 (Vol. II), ORNL/TM-5021 (Vol. II), ORNL/TM-5170, ORNL/NUREG/TM-3, ORNL/NUREG/TM-28, ORNL/NUREG/TM-49, ORNL/NUREG/TM-64, ORNL/NUREG/TM-94, ORNL/NUREG/TM-120, ORNL/NUREG/TM-147, ORNL/NUREG/TM-166, ORNL/NUREG/TM-194, ORNL/NUREG/TM-209, ORNL/NUREG/TM-239, NUREG/CR-0476 (ORNL/NUREG/TM-275), NUREG/CR-0656 (ORNL/NUREG/TM-298), NUREG/CR-0818 (ORNL/NUREG/TM-324), NUREG/CR-0980 (ORNL/NUREG/TM-347), NUREG/CR-1197 (ORNL/NUREG/TM-370), NUREG/CR-1305 (ORNL/NUREG/TM-380), NUREG/CR-1477 (ORNL/NUREG/TM-393), NUREG/CR-1627 (ORNL/NUREG/TM-401), NUREG/CR-1806 (ORNL/NUREG/TM-419), NUREG/CR-1941 (ORNL/NUREG/TM-437), NUREG/CR-2141, Vol. 1 (ORNL/TM-7822), NUREG/CR-2141, Vol. 2 (ORNL/TM-7955), NUREG/CR-2141, Vol. 3 (ORNL/TM-8145), NUREG/CR-2141, Vol. 4 (ORNL/TM-8252), NUREG/CR-2751, Vol. 1 (ORNL/TM-8369/V1), NUREG/CR-2751, Vol. 2 (ORNL/TM-8369/V2), NUREG/CR-2751, Vol. 3 (ORNL/TM-8369/V3), NUREG/CR-2751, Vol. 4 (ORNL/TM-8369/V4), NUREG/CR-3334, Vol. 1 (ORNL/TM-8787/V1), NUREG/CR-3334, Vol. 2 (ORNL/TM-8787/V2), NUREG/CR-3334, Vol. 3 (ORNL/TM-8787/V3), NUREG/CR-3744, Vol. 1 (ORNL/TM-9154/V1), NUREG/CR-3744, Vol. 2 (ORNL/TM-9154/V2), NUREG/CR-4219, Vol. 1 (ORNL/TM-9593/V1), NUREG/CR-4219, Vol. 2 (ORNL/TM-9593/V2), NUREG/CR-4219, Vol. 3, No. 1 (ORNL/TM-9593/V3&N1), NUREG/CR-4219, Vol. 3, No. 2 (ORNL/TM-9593/V3&N2), NUREG/CR-4219, Vol. 4, No. 1 (ORNL/TM-9593/V4&N1), and NUREG/CR-4219, Vol. 4, No. 2 (ORNL/TM-9593/V4&N2).

SUMMARY

1. PROGRAM MANAGEMENT

The Heavy-Section Steel Technology (HSST) Program is arranged into 12 tasks: (1) program management, (2) fracture methodology and analysis, (3) material characterization and properties, (4) special technical assistance, (5) crack-arrest technology, (6) irradiation effects studies, (7) stainless steel cladding evaluations, (8) intermediate vessel tests and analyses, (9) thermal-shock technology, (10) pressurized-thermal-shock (PTS) technology, (11) Pressure-Vessel-Research Users' Facility (PVRUF), and (12) shipping cask material evaluations. Progress reports are issued on a semiannual basis, and the report chapters correspond to the tasks.

The work is performed by the Oak Ridge National Laboratory (ORNL) and through a number of research and development (R&D) subcontracts. During the report period, 32 program briefings, reviews, or presentations were made; 23 technical documents were published.

2. FRACTURE METHODOLOGY AND ANALYSIS

Analytical and experimental studies were performed to provide an improved basis for establishing fracture criteria governing inelastic crack propagation-arrest behavior in reactor pressure vessel (RPV) steels. Viscoplastic-dynamic fracture computer programs were modified for improved efficiency and applied to analyses of large-scale (wide-plate) and small-scale specimens to assess the impact of including viscoplastic effects in computational models. Experimental efforts focused on small-specimen testing techniques, including refinement of crack propagation time-length measurements, development of new stress wave loading procedures for crack-arrest toughness determination, and establishment of explosive and impact loading methods of measuring crack initiation toughness in RPV steels. Cleavage-fibrous transition studies were carried out on 72W weld metal specimens, and optical topography was used to study regions of two wide-plate fractures where cleavage arrest was followed by a fibrous-tear reinitiation. Additional high strain-rate tests of A 533 grade B class 1 steel were performed for purposes of characterizing viscoplastic constitutive models used in inelastic crack-arrest studies.

3. MATERIAL CHARACTERIZATION AND PROPERTIES

Compact crack-arrest tests were conducted with the A 533 grade B chemistry base metal used for the clad-plate studies. Specimens of three different sizes were tested in the L-T orientation at temperatures from −25 to 75°C; the nil ductility temperature (NDT) of the material is 36°C. The results showed K_{Ia}/K_{IR} values ranging from 1.23 to 2.49.

Development of fabrication and testing procedures for 50-mm-thick duplex crack-arrest specimens continued. Metallographic and microhardness studies were conducted to assist in an understanding of the importance of the electron-beam (EB) welding, microstructural, and welding parameters on crack arrest. Successful tests have been conducted with 2 1/4 Cr-1 Mo specimens, but very limited success has been achieved with A 533 grade B class 1 steel and submerged-arc welds. The studies are continuing with EB weld procedures as well as potential changes in specimen geometry, specifically, the side-grooving practice.

4. SPECIAL TECHNICAL ASSISTANCE

In recognition of the virtual completion of the environmental crack-growth studies within the HSST Program in conjunction with the numerous relatively short-term topics of interest to the Nuclear Regulatory Commission (NRC) that arise on a continuing basis, Task 4 has been redefined to provide coverage of these topics. During this reporting period, the specific topics that were active included (1) the evaluation of the possible enhanced low-temperature, low-flux irradiation embrittlement of RPV supports; (2) an assessment of boiling-water-reactor (BWR) vessel integrity; and (3) a reevaluation of the applicability of various formulations of the J-integral in assessing relatively large amounts of crack extension.

5. CRACK-ARREST TECHNOLOGY

Thirteen wide-plate, crack-arrest tests have been completed to date (one during this reporting period). When combined with other large-specimen test results, the wide-plate crack-arrest toughness values form a consistent trend, showing that arrest can and does occur at temperatures up to and above that which corresponds to the onset of Charpy upper-shelf behavior. Also, the measured K_{Ia} values extend above the limit in Sect. XI of the *ASME Code*.

Preparations were continued for testing of the stub panel, intermediate-size, crack-arrest specimens with emphasis on experimental definition of data acquisition requirements.

6. IRRADIATION EFFECTS STUDIES

All planned testing for the Fifth Irradiation Series on K_{Ic} curve shift has now been completed. Final analyses of test results are under way as are various statistical analyses of the data obtained. A tentative procedure for analysis of small cleavage instabilities (pop-ins) has also been selected.

In the Sixth Irradiation Series on the K_{Ia} curve shift, the first of two crack-arrest irradiation capsules has been disassembled, and the dosimeters are being analyzed. The second capsules should be completed by the end of June. The remote hot cell fixture for crack-arrest testing has been used to test unirradiated specimens in the laboratory. Several enhancements to the fixture are under way, based on the results of those tests before its installation in the hot cell.

In the Seventh Irradiation Series on cladding, Charpy and tensile tests were completed for the three-wire, series-arc, stainless steel cladding specimens irradiated to 2 and 5×10^{19} neutrons/cm^2 (>1 MeV). At those fluences, the room temperature yield strength increased 20 and 16%, respectively; the Charpy 41-J transition temperature increased 13 and 28°C, respectively.

7. CLADDING EVALUATIONS

The work within the cladding evaluation task during this reporting period included the completion of the second experimental study of the effect of cladding on the propagation of small surface flaws using clad plates. In addition, nondestructive examination of both the BWR and pressurized-water-reactor (PWR) clad vessel segments was completed.

8. INTERMEDIATE VESSEL TESTS AND ANALYSIS

There was no activity in the intermediate vessel tests and analysis task for this period.

9. THERMAL-SHOCK TECHNOLOGY

There was no activity in the thermal-shock technology task for this period.

10. PRESSURIZED-THERMAL-SHOCK TECHNOLOGY

The feasibility and utility of additional PTS experiments are being investigated. Potential experiments with a clad vessel and with a low-upper-shelf weld are being considered. Effects of cladding are pertinent because it has not been demonstrated whether cladding is always a benefit with respect to fracture. An experiment with a flaw in a low-upper-shelf weld would clarify questions raised by experiments PTSE-1 and -2 about the analysis of stable and unstable ductile tearing.

11. FLAW DENSITY STUDIES FOR PRESSURE-VESSEL-RESEARCH USERS' FACILITY

ORNL undertook an initiative in concert with the NRC and Department of Energy (DOE) to establish a Pressure-Vessel-Research Users' Facility. The facility is to be centered around a complete PWR pressure vessel and is to provide unique R&D opportunities for a number of organizations.

The overall research plan and conceptual design of the facility to house the vessel will begin when appropriate funding is arranged. Initial R&D activities, however, will proceed with the vessel in its temporary location at the K-25 Plant in Oak Ridge. One early HSST-funded task will characterize the density, size, location, and orientation of flaws in this vessel for use in probabilistic integrity assessment methods.

Detailed plans for the flaw detection were prepared and initiated during this report period. The first activities included modification of the facility to allow for nondestructive examination of the vessel in its current location and horizontal position.

12. SHIPPING CASK MATERIAL EVALUATIONS

There was no reportable activity in the shipping cask material evaluations task for this period.

HEAVY-SECTION STEEL TECHNOLOGY PROGRAM SEMIANNUAL PROGRESS REPORT FOR OCTOBER 1987—MARCH 1988*

W. R. Corwin

ABSTRACT

The Heavy-Section Steel Technology (HSST) Program is conducted for the Nuclear Regulatory Commission (NRC). The studies relate to all areas of the technology of materials fabricated into thick-section primary-coolant containment systems of light-water-cooled nuclear power reactors. The focus is on the behavior and structural integrity of steel pressure vessels containing cracklike flaws. The program is organized into 12 tasks: (1) program management, (2) fracture methodology and analysis, (3) material characterization and properties, (4) special technical assistance, (5) crack-arrest technology, (6) irradiation effects studies, (7) cladding evaluations, (8) intermediate vessel tests and analysis, (9) thermal-shock technology, (10) pressurized-thermal-shock (PTS) technology, (11) Pressure-Vessel-Research Users' Facility (PVRUF), and (12) shipping cask material evaluations. During this period, improvements were made in the computational efficiencies of fracture-analysis codes, and enhancements were made in the constitutive models and inelastic fracture criteria in the dynamic-viscoplastic fracture version of the ADINA-ORMGEN-ORVIRT analysis codes at Oak Ridge National Laboratory (ORNL). Elastodynamic analyses and development work on viscoplastic fracture-analysis techniques were performed by ORNL and the Southwest Research Institute (SwRI) in support of both small specimen testing and the wide-plate, crack-arrest tests that are being performed by the National Bureau of Standards (NBS) for the HSST Program. Three new areas of NRC topical support were begun: (1) the evaluation of possible enhanced low-temperature, low-flux irradiation embrittlement of reactor pressure vessel supports; (2) an assessment of boiling-water-reactor vessel integrity; and (3) a reevaluation of the applicability of various formulations of the J-integral in assessing relatively large amounts of crack extension. One additional wide-plate, crack-arrest test was performed by NBS, bringing to 13 the total of such tests. Crack-arrest and other fracture characterization data were obtained for clad-plate test materials. Testing of all specimens was completed in the Fifth HSST Irradiation Series for the study of K_{Ic} shifts for

---

*This report is written in terms of metric units. Conversions from SI to English units for all SI quantities are listed on a foldout page at the end of this report.

welds with different copper contents. All irradiated Charpy V-notch and tensile testing was completed for the second phase of the Seventh HSST Irradiation Series on cladding. Nondestructive examinations were completed on a segment of a clad pressurized-water reactor (PWR) vessel. The remainder of the second series of the clad-plate fracture tests of reactor vessel steels were performed. The report on the second PTS test (PTSE-2) was published. The detailed planning of the nondestructive flaw assessment of the PWR pressure vessel to be used in the ORNL PVRUF was completed and a modification of the temporary facility begun.

---

1. PROGRAM MANAGEMENT

W. R. Corwin

The Heavy-Section Steel Technology (HSST) Program, a major safety program sponsored by the Nuclear Regulatory Commission (NRC) at Oak Ridge National Laboratory (ORNL), is concerned with the structural integrity of the primary systems [particularly, the reactor pressure vessels (RPVs)] of light-water-cooled nuclear power reactors. The structural integrity of these vessels is ensured by (1) designing and fabricating RPVs according to standards set by the code for nuclear pressure vessels, (2) detecting flaws of significant size that occur during fabrication and while in service, and (3) developing methods of producing quantitative estimates of conditions under which fracture could occur. The program is concerned mainly with developing pertinent fracture technology, including knowledge of (1) the material used in these thick-walled vessels, (2) the flaw-growth rate, and (3) the combination of flaw size and load that would cause fracture and, thus, limit the life and/or operating conditions of this type of reactor plant.

The program is coordinated with other government agencies and with the manufacturing and utility sectors of the nuclear power industry in the United States and abroad. The overall objective is a quantification of safety assessments for regulatory agencies, professional code-writing bodies, and the nuclear power industry. Several activities are conducted under subcontract by research facilities in the United States and through an informal cooperative effort on an international basis. Seven research and development subcontracts are currently in force.

The program tasks are arranged according to the work breakdown structure shown in Fig. 1.1. Accordingly, the chapters of this progress report correspond to these 12 tasks.

During this period, nine program briefings, reviews, or presentations were made by the HSST staff during program reviews and visits with NRC staff or others. Five topical reports,[1-5] two foreign trip reports,[6-7] and fourteen technical papers[8-21] were published. In addition twenty-three technical presentations were made: ten[22-31] at the Fifteenth Water

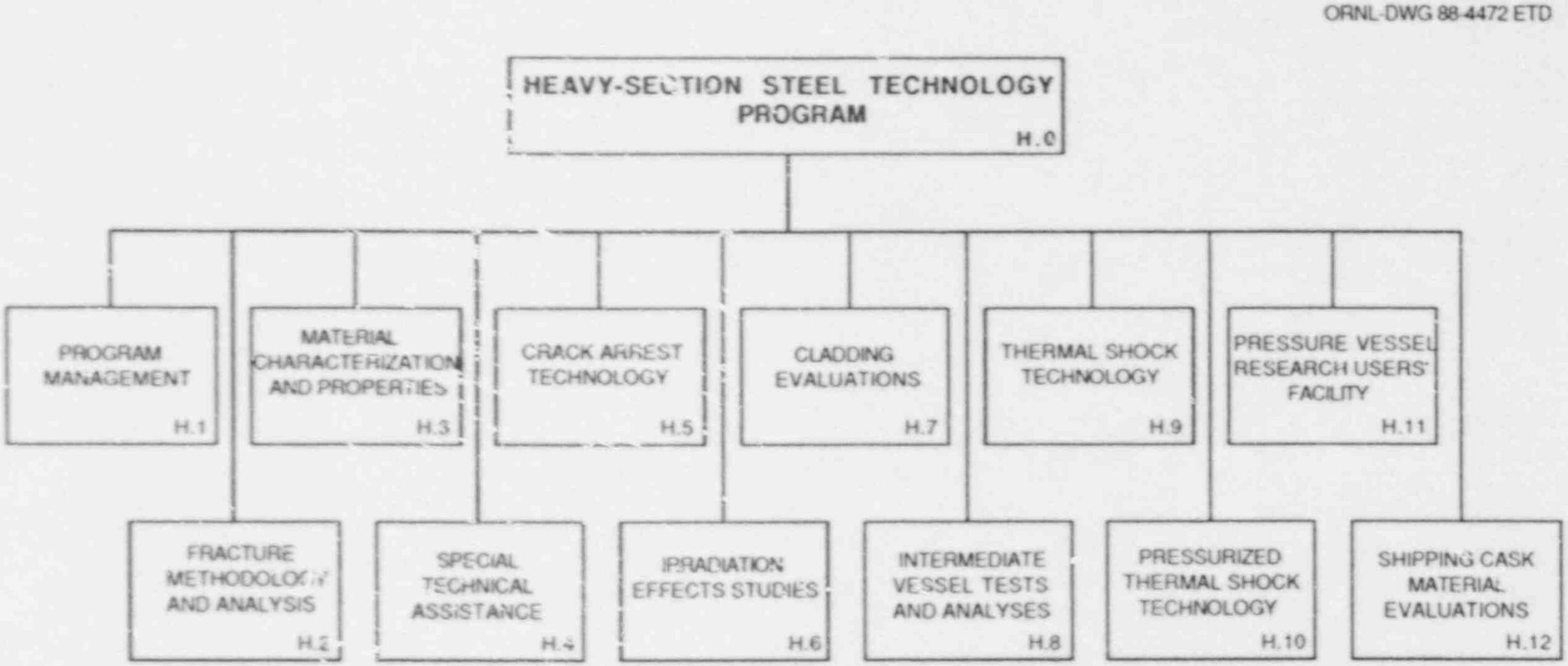

Fig. 1.1. Level-2 work breakdown structure for HSST Program.

Reactor Safety Information Meeting held at the National Bureau of Standards (NBS) in Gaithersburg, Maryland, on October 26–29, 1987; three[32-34] at the ASME Pressure Vessel and Piping Division Fall Conference held in Knoxville, Tennessee, on October 23, 1987; three[35-37] at the Society for Experimental Mechanics Fall Conference held in Savannah, Georgia, on October 26–28, 1987; one[38] at the Conference of Materials for Nuclear Applications held at the University of Missouri-Rolla on October 26, 1987; one[39] at the Nordic Materials Research Seminar held in Copenhagen, November 25–26, 1987; one[40] at the ASTM Mini-Symposium on Fracture Toughness Shift held in Albuquerque, New Mexico, on January 28, 1988; one[41] at the First UTAM Symposium on Recent Advances in Nonlinear Fracture Mechanics held at California Institute of Technology on March 14–16, 1988; two[42-43] at the Engineering Technology Division Information Meeting held at ORNL, Oak Ridge, Tennessee, on March 17–19, 1988; and one[44] at the Engineering College, Arkansas State University on March 31, 1988.

References

1. R. H. Bryan et al., *Pressurized-Thermal-Shock Test of 6-in.-Thick Warm Prestressing*, NUREG/CR-4888 (ORNL-6377), Martin Marietta Energy Systems, Inc., Oak Ridge Natl. Lab., December 1987.

2. D. B. Barker, R. Chona, W. L. Fourney, and G. R. Irwin, *A Report on the Round Robin Program Conducted to Evaluate the Proposed ASTM Standard Test Method for Determining the Plane Strain Crack Arrest Fracture Toughness, K_{Ia}, of Ferritic Materials*, NUREG-CR-4996 (ORNL/Sub/79-7778/4), by the University of Maryland for Martin Marietta Energy Systems, Inc., Oak Ridge Natl. Lab., January 1988.

3. K. V. Cook and R. W. McClung, *Flaw Density Examinations of a Clad Boiling Water Reactor Pressure Vessel Segment*, NUREG/CR-4860, Rev. 1 (ORNL/TM-10364/R1), Martin Marietta Energy Systems, Inc., Oak Ridge Natl. Lab., February 1988.

4. R. deWit et al., *Wide-Plate Crack-Arrest Testing: A Description and Discussion of the First Two Wide-Plate Tests and the Results of Six, Full Thickness, Bend Bar Tests*, NBSIR 87-3627, National Bureau of Standards for Martin Marietta Energy Systems, Inc., Oak Ridge Natl. Lab., February 1988.

5. L. F. Miller, C. A. Baldwin, F. W. Stallman, and F. B. Kam, *Neutron Exposure Parameters for the Metallurgical Test Specimens in the Fifth Heavy-Section Steel Technology Irradiation Series Capsules*, NUREG/CR-5019 (ORNL/TM-10582), Martin Marietta Energy Systems, Inc., Oak Ridge Natl. Lab., March 1988.

6. S. K. Iskander, ORNL Foreign Trip Report, ORNL/FTR-2759, Martin Marietta Energy Systems, Inc., Oak Ridge Natl. Lab., November 1987.

7. B. R. Bass, ORNL Foreign Trip Report, ORNL/FTR-2780, Martin Marietta Energy Systems, Inc., Oak Ridge Natl. Lab., December 1987.

8. J. J. McGowan and R. K. Nanstad, "A Statistical Analysis of Fracture Toughness of Irradiated Low-Alloy Steel Plate and Welds," pp. 569–89 in *Influence of Radiation on Material Properties: 13th International Symposium (Part II), ASTM STP 956*, F. A. Garner, C. H. Henager, Jr., and N. Igata, eds., American Society for Testing and Materials, Philadelphia, Pa., 1987.

9. R. J. Sanford and J. W. Dally, "Strain Gage Methods for Measuring the Opening-Mode Stress Intensity Factor, K_I," *Exp. Mech.* 27(4), 381–87, 1987.

10. X. J. Zhang, R. W. Armstrong, and G. R. Irwin, "Cleavage Fracturing in the Upper Transition Temperature Range for Pressure Vessel Steels," p. 242 in *Materials Week '87*, Extended Abstract, ASM International, Metals Park, Ohio, 1987.

11. J. W. Dally and D. B. Barker, "A Method to Measure Crack Initiation Toughness in Steel at Very High Loading Rates," pp. 59–65 in *Proc. Fall 1987 Society for Experimental Mechanics Meeting, Savannah, Ga., October 25–28, 1987.*

12. C. W. Schwartz, H. C. Lee, and B. R. Bass, "Dynamic Fracture Propagation Relations Inferred from Wide Plate Crack Arrest Tests of A533B Steel," pp. 66–71 in *Proc. Fall 1987 Society for Experimental Mechanics Meeting, Savannah, Ga., October 25–28, 1987.*

13. B. R. Bass, C. E. Pugh, J. Keeney-Walker, R. J. Dexter, P. E. O'Donoghue, and C. W. Schwartz, "Evaluation of Viscoplastic Fracture Criteria and Analysis Methods," NUREG/CP-0091, Vol 2, pp. 59–92 in *Proc. Fifteenth Water Reactor Safety Information Meeting, Gaithersburg, Md., October 26–29, 1987*, U.S. Nuclear Regulatory Commission.

14. R. H. Bryan et al., "Performance of Low-Upper-Shelf Material Under Pressurized-Thermal-Shock Loading (PTSE-2)," NUREG/CP-0091, Vol 2, pp. 41–58 in *Proc. Fifteenth Water Reactor Safety Information Meeting, Gaithersburg, Md., October 26–29, 1987*, U.S. Nuclear Regulatory Commission.

15. K. V. Cook and R. M. McClung, "Detection and Characterization of Flaws in Segments of Light-Water Reactor Pressure Vessels," NUREG/CP-0091, Vol. 2, pp. 139–54 in *Proc. Fifteenth Water Reactor Safety Information Meeting, Gaithersburg, Md., October 26–29, 1987*, U.S. Nuclear Regulatory Commission.

16. J. G. Merkle, "Constraint and Strain Rate Effects in Fracture Toughness Testing," NUREG/CP-0091, Vol. 2, pp. 5–16 in *Proc. Fifteenth Water Reactor Safety Information Meeting, Gaithersburg, Md., October 26–29, 1987*, U.S. Nuclear Regulatory Commission.

17. F. M. Haggag, W. R. Corwin, D. J. Alexander, and R. K. Nanstad, "Effects of Irradiation on Strength and Toughness of Commercial LWR Vessel Cladding," NUREG/CP-0091, Vol. 2, pp. 177–94 in *Proc. Fifteenth Water Reactor Safety Information Meeting, Gaithersburg, Md., October 26–29, 1987.*, U.S. Nuclear Regulatory Commission.

18. S. K. Iskander et al., "Effects of Commercial Cladding on the Fracture Behavior of Pressure Vessel Steel Plates," NUREG/CP-0091, Vol. 2, pp. 123–38 in *Proc. Fifteenth Water Reactor Safety Information Meeting, Gaithersburg, Md., October 26–29, 1987*, U.S. Nuclear Regulatory Commission.

19. M. F. Kanninen et al., "Viscoplastic-Dynamic Analyses of Small-Scale Fracture Tests to Obtain Crack Arrest Toughness Values for PTS Conditions," NUREG/CP-0091, Vol. 2, pp. 93–112 in *Proc. Fifteenth Water Reactor Safety Information Meeting, Gaithersburg, Md., October 26–29, 1987*, U.S. Nuclear Regulatory Commission.

20. D. J. Naus, B. R. Bass, J. Keeney-Walker, R. J. Fields, R. deWit, and S. R. Low III, "Summary of HSST Wide-Plate Crack-Arrest Tests and Analyses," NUREG/CP-0091, Vol. 2, pp. 17–40 in *Proc. Fifteenth Water Reactor Safety Information Meeting, Gaithersburg, Md., October 26–29, 1987*, U.S. Nuclear Regulatory Commission.

21. C. W. Schwartz and B. R. Bass, "Evaluation of the Presence of Constraint in Crack Run/Arrest Events," NUREG/CP-0091, Vol. 2, pp. 113–22 in *Proc. Fifteenth Water Reactor Safety Information Meeting, Gaithersburg, Md., October 26–29, 1987*, U.S. Nuclear Regulatory Commission.

22. B. R. Bass, C. E. Pugh, J. Keeney-Walker, R. J. Dexter, P. E. O'Donoghue, and C. W. Schwartz, "Evaluation of Viscoplastic Fracture Criteria and Analysis Methods," presented at the Fifteenth Water Reactor Safety Information Meeting, Gaithersburg, Md., October 26–29, 1987.

23. R. H. Bryan et al., "Performance of Low-Upper-Shelf Material Under Pressurized-Thermal-Shock Loading (PTSE-2)," presented at the the Fifteenth Water Reactor Safety Information Meeting, Gaithersburg, Md., October 26–29, 1987.

24. K. V. Cook and R. M. McClung, "Detection and Characterization of Flaws in Segments of Light-Water Reactor Pressure Vessels," presented at Fifteenth Water Reactor Safety Information Meeting, Gaithersburg, Md., October 26–29, 1987.

25. J. W. Dally and G. R. Irwin, "Dynamic Fracture Initiation Studies," presented at the Fifteenth Water Reactor Safety Information Meeting, Gaithersburg, Md., October 26–29, 1987.

26. F. M. Haggag, W. R. Corwin, D. J. Alexander, and R. K. Nanstad, "Effects of Irradiation on Strength and Toughness of Commercial LWR Vessel Cladding," presented at the Fifteenth Water Reactor Safety Information Meeting, Gaithersburg, Md., October 26–29, 1987.

27. S. K. Iskander et al., "Effects of Commercial Cladding on the Fracture Behavior of Pressure Vessel Steel Plates," presented at the Fifteenth Water Reactor Safety Information Meeting, Gaithersburg, Md., October 26–29, 1987.

28. M. F. Kanninen et al., "Viscoplastic-Dynamic Analyses of Small-Scale Fracture Tests to Obtain Crack Arrest Toughness Values for PTS Conditions," presented at the Fifteenth Water Reactor Safety Information Meeting, Gaithersburg, Md., October 26–29, 1987.

29. R. K. Nanstad, "Effects of Irradiation on K_{Ic} Curves for High-Copper Welds," presented at the Fifteenth Water Reactor Safety Information Meeting, Gaithersburg, Md., October 26–29, 1987.

30. D. J. Naus, B. R. Bass, and R. J. Fields, "Summary of HSST Wide-Plate Crack-Arrest Tests and Analyses," presented at the Fifteenth Water Reactor Safety Information Meeting, Gaithersburg, Md., October 26–29, 1987.

31. C. W. Schwartz and B. R. Bass, "An Evaluation of the Presence of Constraint in Crack/Run Arrest Events," presented at the Fifteenth Water Reactor Safety Information Meeting, Gaithersburg, Md., October 26–29, 1987.

32. J. W. Bryson, "Finite Element Fracture Analysis on a Microcomputer," presented at the ASME Pressure Vessels and Piping Division Fall Conference, October 23, 1987, Knoxville, Tenn.

33. C. E. Pugh, "An Overview of the Pressure Vessel Research Users' Facility," presented at the ASME Pressure Vessels and Piping Division Fall Conference, October 23, 1987, Knoxville, Tenn.

34. D. A. Steinett, "Dynamic Fracture and Graphic Analysis," presented at the ASME Pressure Vessels and Piping Division Fall Conference, October 23, 1987, Knoxville, Tenn.

35. B. R. Bass, "A Comparison of Dynamic Viscoplastic Fracture Criteria," presented at the Fall 1987 Society for Experimental Mechanics Meeting, Savannah, Ga., October 25–28, 1987.

36. J. W. Dally and D. B. Barker, "A Method to Measure Crack Initiation Toughness in Steel at Very High Loading Rates," presented at the Fall 1987 Society for Experimental Mechanics Meeting, Savannah, Ga., October 25–28, 1987.

37. C. W. Schwartz, H. C. Lee, and B. R. Bass, "Dynamic Fracture Propagation Relations Inferred from Wide-Plate Crack-Arrest Tests of A533B Steel," presented at the Fall 1987 Society for Experimental Mechanics Meeting, Savannah, Ga., October 25–28, 1987.

38. R. K. Nanstad, "Reactor Pressure Vessel Materials," presented as an invited talk at the Conference on Materials for Nuclear Applications, University of Missouri-Rolla on October 26, 1987.

39. B. R. Bass, "An Overview of Ongoing Large-Scale Crack-Arrest Tests of Pressure Vessel Steels in the U.S.A.," presented at the Nordic Materials Research Seminar, Copenhagen, Denmark, November 25–26, 1987; on December 1, 1987, at the Royal Institute of Technology, Stockholm, Sweden.

40. R. K. Nanstad, "Comparison of Charpy Impact and Fracture Toughness Transition Temperature Shifts Due to Irradiation (HSST Irradiation Series 4 and 5)," presented at a Mini-Symposium, "Is the Charpy Shift Representative of the Fracture-Toughness Shift?" sponsored by the E10.02 Task Group on Fracture Toughness, Albuquerque, N.M., January 1988.

41. R. J. Fields, "Plastic Zone Formation Around An Arresting Crack," presented at the First UTAM Symposium on Recent Advances in Nonlinear Fracture Mechanics, California Institute of Technology, March 14–16, 1988.

42. B. R. Bass, "Development of Dynamic Inelastic Fracture Analysis Methods for Light-Water Reactor Applications," presented at the Engineering Technology Division Information Meeting, Oak Ridge Natl. Lab., March 17, 1988.

43. W. R. Corwin, "Behavior of Low-Upper-Shelf Toughness Steels in Light-Water Reactor Pressure Vessels," presented at the Engineering Technology Division Information Meeting, Oak Ridge Natl. Lab., March 17, 1988.

44. G. C. Robinson, "Nuclear Reactor Pressure Vessel Integrity," presented at the Engineering College, Arkansas State University, March 31, 1988.

2. FRACTURE METHODOLOGY AND ANALYSIS

2.1 Summary of Viscoplastic-Dynamic Fracture Analyses of the WP-1 Series of Wide-Plate Tests

B. R. Bass* J. Keeney-Walker*
C. W. Schwartz†

2.1.1 Introduction

The role of nonlinear rate-dependent effects in the interpretation of crack run-arrest events in ductile materials is being investigated by the Heavy-Section Steel Technology (HSST) Program through the development and application of viscoplastic-dynamic finite-element analysis techniques. During this report period, a draft version of a topical report[1] was prepared to describe the studies in which various viscoplastic constitutive models and several proposed nonlinear fracture criteria have been installed in general purpose (ADINA)[2] and special purpose (VISCRK)[3] finite-element computer programs. The constitutive models implemented in these computer programs include the Bodner-Partom[4] and the Perzyna[5] viscoplastic formulations; the proposed fracture criteria include three parameters based on energy principles. The predictive capabilities of the nonlinear techniques are being evaluated partly through applications to a series of HSST wide-plate crack-arrest tests. In the topical report,[1] values of fracture parameters calculated in elastodynamic and viscoplastic dynamic analyses of the wide-plate tests are compared with one another to assess the effect of including viscoplastic effects in the computational models. A summary of the results from these analyses follows.

2.1.2 Summary of viscoplastic-dynamic fracture analyses of the WP-1 series

Viscoplastic-dynamic fracture analyses of wide-plate tests WP-1.2 to WP-1.7 (WP-1 series)[6] were conducted with the ADINA/VPF[7] program at ORNL. Finite-element models having improved mesh refinement near the plane of crack propagation were generated for these analyses. The finite-element model used to analyze tests WP-1.2 to 1.6 is shown in Fig. 2.1(*a*); the model used for test WP-1.7 is shown in Fig. 2.1(*b*). Both models consist of 2258 nodes and 715 eight-noded isoparametric elements. For the two models, Fig. 2.2 depicts the viscoplastic element group (consisting of 429 elements) adjacent to the plane of crack propagation. The dimensions of the elements along the crack path in Fig. 2.2 are 20 by 20 mm.

---

*Computing and Telecommunications Division, Martin Marietta Energy Systems, Inc., Oak Ridge National Laboratory, Oak Ridge, Tennessee.

†Department of Civil Engineering, University of Maryland, College Park.

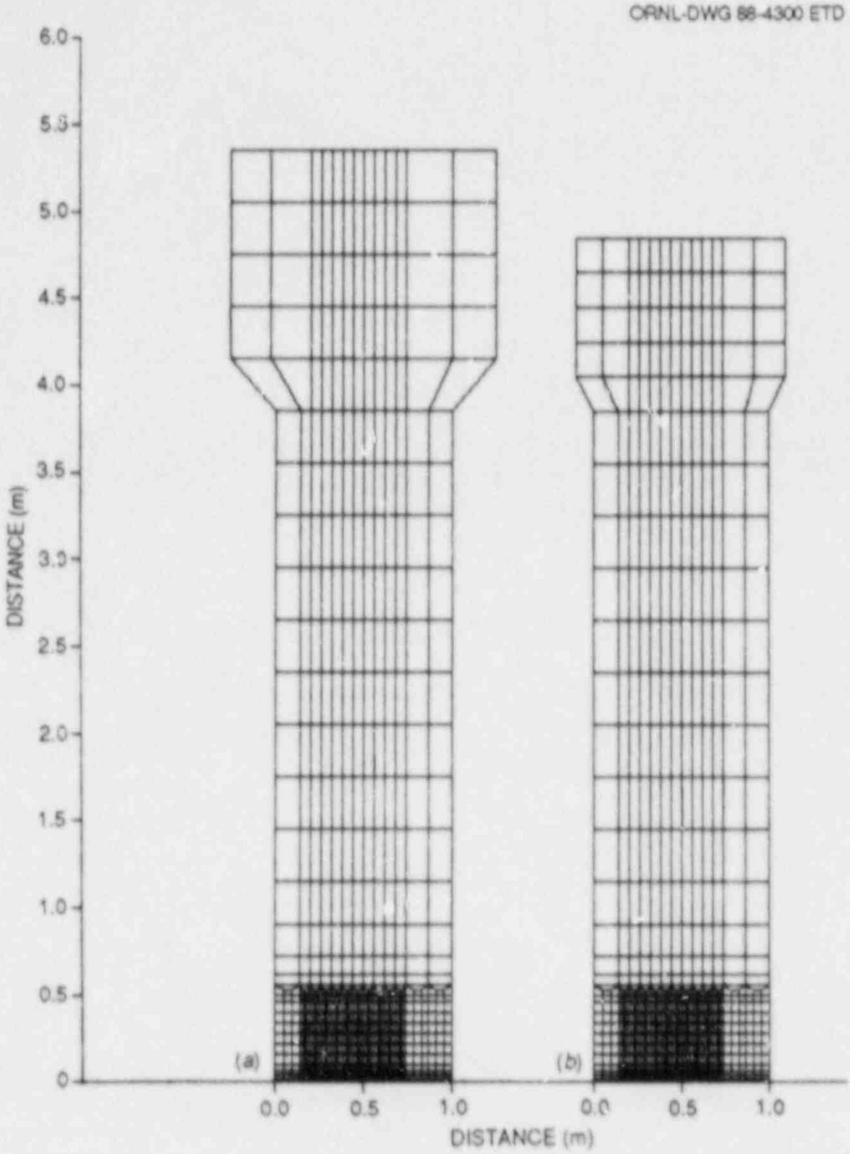

Fig. 2.1. Finite-element models used in dynamic analyses of tests WP-1.2 through WP-1.7. (*a*) Model of WP-1.2 through WP-1.6, (*b*) model of WP-1.7.

For each analysis, the measured fracture load (from Table 2.1) was applied at the approximate location of the load-pin hole to determine the initial conditions for the crack run-arrest event. For the dynamic analyses, the applied load was fixed at the value that prevailed at initiation. The in-plane thermal bending of the plate caused by the imposed linear temperature gradient in each test was ignored in these analyses. The Gauss point rule selected for the integration of the finite-element model was 2 × 2 for the stiffness matrix and 3 × 3 for the consistent mass matrix. The time step was set at $\Delta t = 2$ μs for the elastodynamic

ORNL-DWG 88-4301 ETD

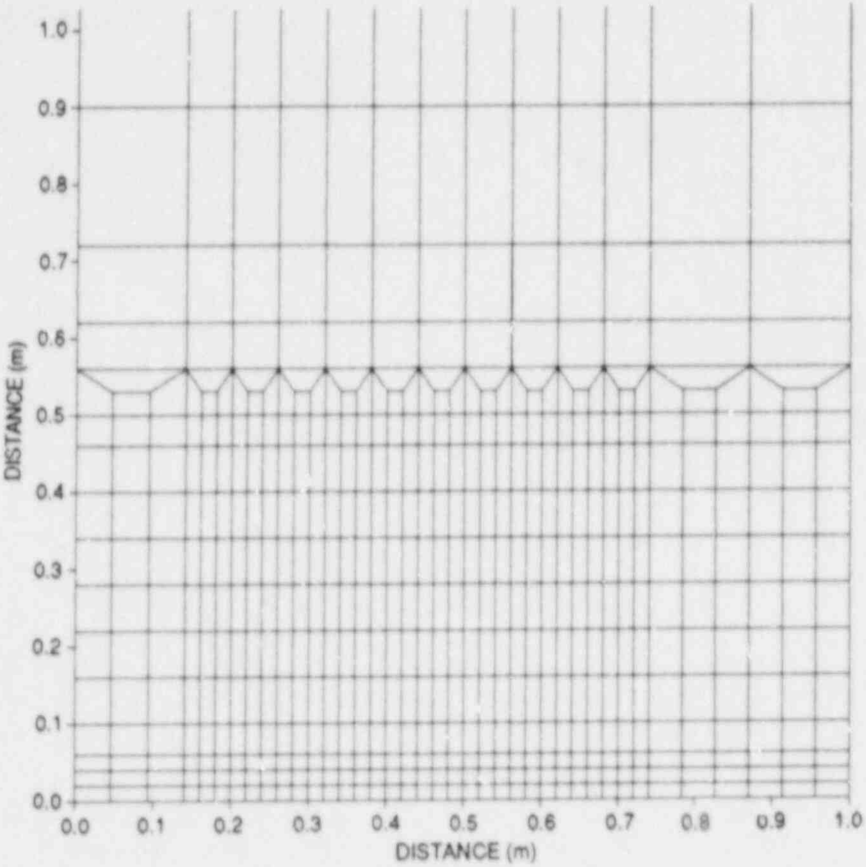

Fig. 2.2. Crack-plane viscoplastic-element group of finite-element models used in dynamic analyses of tests WP-1.2 through WP-1.7.

analyses and at $\Delta t = 1$ μs for the viscoplastic-dynamic analyses. The Bodner-Partom constitutive model defined in Ref. 8 was used exclusively for the viscoplastic analyses.

Generation-mode dynamic analyses of wide-plate tests WP-1.2 to 1.7 were performed using the estimates of crack position vs time given in Ref. 6. A summary of the six test results is presented in Figs. 2.3–2.9 and in Table 2.2. For each viscoplastic-dynamic analysis, the following results are given as a function of time: crack-tip position; maximum effective viscoplastic strain rate; and the fracture parameters T^* (from Ref. 9), $\hat{J}$ (from Ref. 10), and γ (from Ref. 11) expressed as pseudo-stress-intensity factors ($K_I = \sqrt{EJ}$). Values of the fracture parameters computed in elastodynamic analyses are also given for comparison with the viscoplastic analyses.

Results from the analysis of wide-plate test WP-1.2 for the first 3 ms of the dynamic event are presented in Fig. 2.3. The interval of crack arrest beginning at time $t = 1$ ms [Fig. 2.3(*a*)] coincides with a sharp drop in the maximum effective viscoplastic strain rate [Fig. 2.3(*b*)]. (For the analyses presented in this section, the maximum effective viscoplastic strain rate is plotted as a function of time from the

Table 2.1. Summary of HSST wide-plate crack-arrest test conditions for A 533 grade B class 1 steel: WP-1 series

Test No.	Crack location (cm)	Crack-tip temperature (°C)	Initiation load (MN)	Arrest location (cm)	Arrest temperature (°C)	Arrest $T - RT_{NDT}$ (°C)
WP-1.1[a]	20	−60	20.1	50.2	51	74
WP-1.2A	20	−33	18.9	55.5	62	85
WP-1.2B	55.5	62	18.9	64.5	92	115
WP-1.3	20[b]	−51	11.25	48.5	54	77
WP-1.4A	20.7[b,c]	−63	7.95	44.1	29	52
WP-1.4B	44.1	29	9.72	52.7	60	83
WP-1.5A	20[b]	−30	11.03	52.1	56	79
WP-1.5B	52.1	56	11.03	58.0	72	95
WP-1.6A	20[b]	−19	14.50	49.3	54	77
WP-1.6B	49.3	54	14.50	59.3	80	103
WP-1.7A	20.2[b]	−24	26.2	52.8	61	84
WP-1.7B	52.8	61	26.2	63.5	88	111

[a] Specimen was warm prestressed by loading to 10 MN at 70°C; specimen was also preloaded to 19 MN.

[b] Crack front was cut to chevron configuration.

[c] Pillow jack was used to apply pressure load to specimen's machined notch.

Table 2.2. Summary of dynamic analyses of the WP-1 series of wide-plate crack-arrest tests

Test	Material[a] model	Initiation load (MN)	a_o (m)	T_o (°C)	K_{Io} (MPa·$\sqrt{m}$)	a_f (m)	T_f (°C)	K_{If} (MPa·$\sqrt{m}$)
WP-1.2	EL	18.9	0.20	−33	227.35	0.56	62	394.9
	EL	18.9	0.56	62	522.9	0.64	92	659.4
	VP	18.9	0.20	−33	211.17	0.56	62	204.4
	VP	18.9	0.56	62	405.9	0.64	92	301.3
WP-1.3	EL	11.25	0.20	−51	135.33	0.49	54	217.0
	VP	11.25	0.20	−51	136.56	0.49	54	168.5
WP-1.4	El	7.952	0.20	−63	95.65	0.44	29	142.6
	VP	7.952	0.20	−63	95.65	0.44	29	137.7
WP-1.5	EL	11.03	0.20	−30	132.68	0.52	56	213.8
	VP	11.03	0.20	−30	127.95	0.52	56	169.6
WP-1.6	EL	14.50	0.20	−19	174.42	0.50	54	260.0
	VP	14.50	0.20	−19	160.70	0.50	54	181.6
WP-1.7	EL	26.20	0.20	−24	213.53	0.53	61	326.2
	VP	26.20	0.20	−24	204.8	0.53	61	201.5

[a] EL = elastodynamic; VP = viscoplastic dynamic.

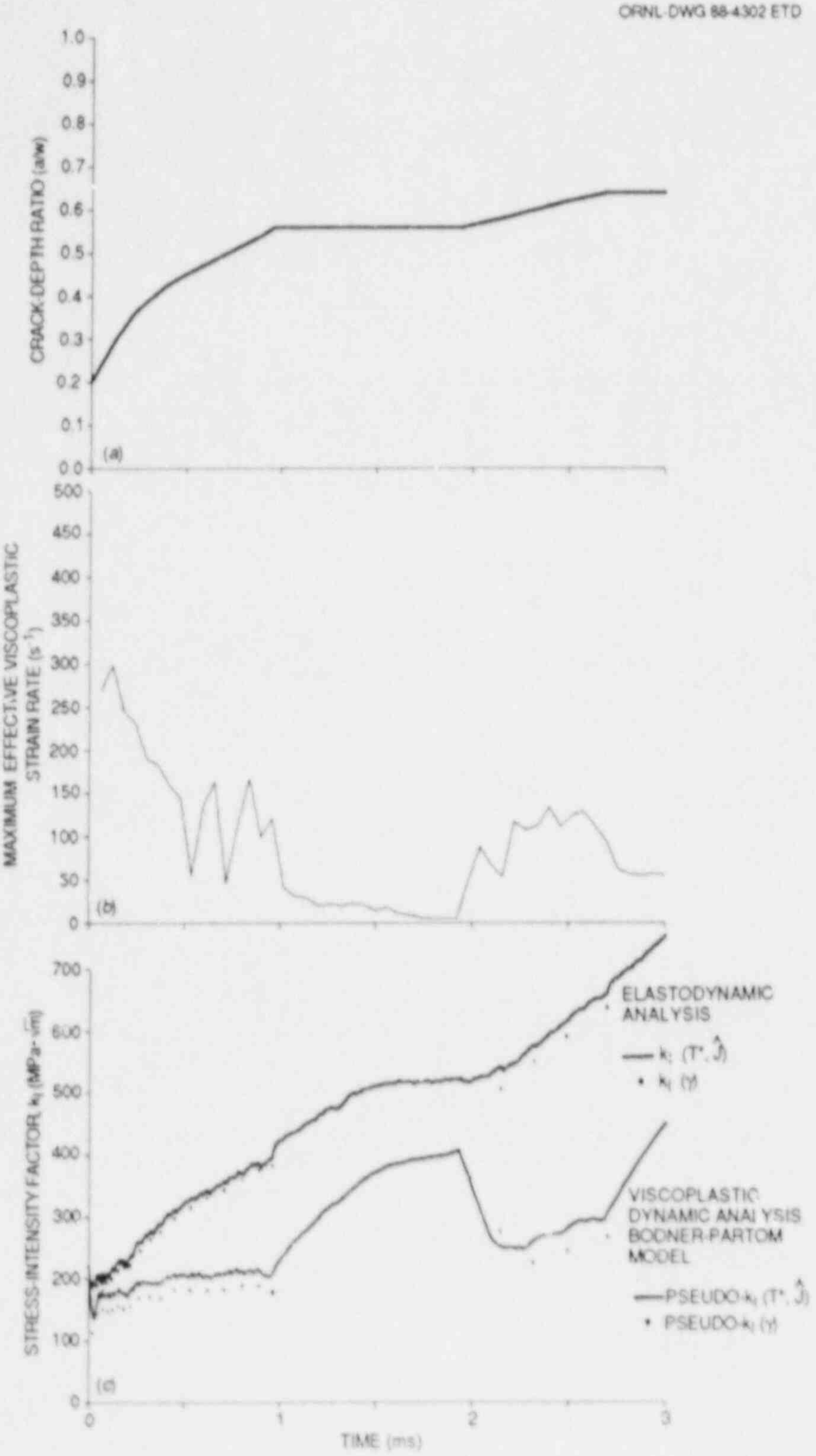

Fig. 2.3. Time histories of crack-depth ratio, maximum effective viscoplastic strain rate, and fracture parameters from analysis of wide-plate test WP-1.2. (*a*) Crack-depth ratio, (*b*) maximum effective viscoplastic strain rate, (*c*) fracture parameters.

ORNL-DWG 88-4303 ETD

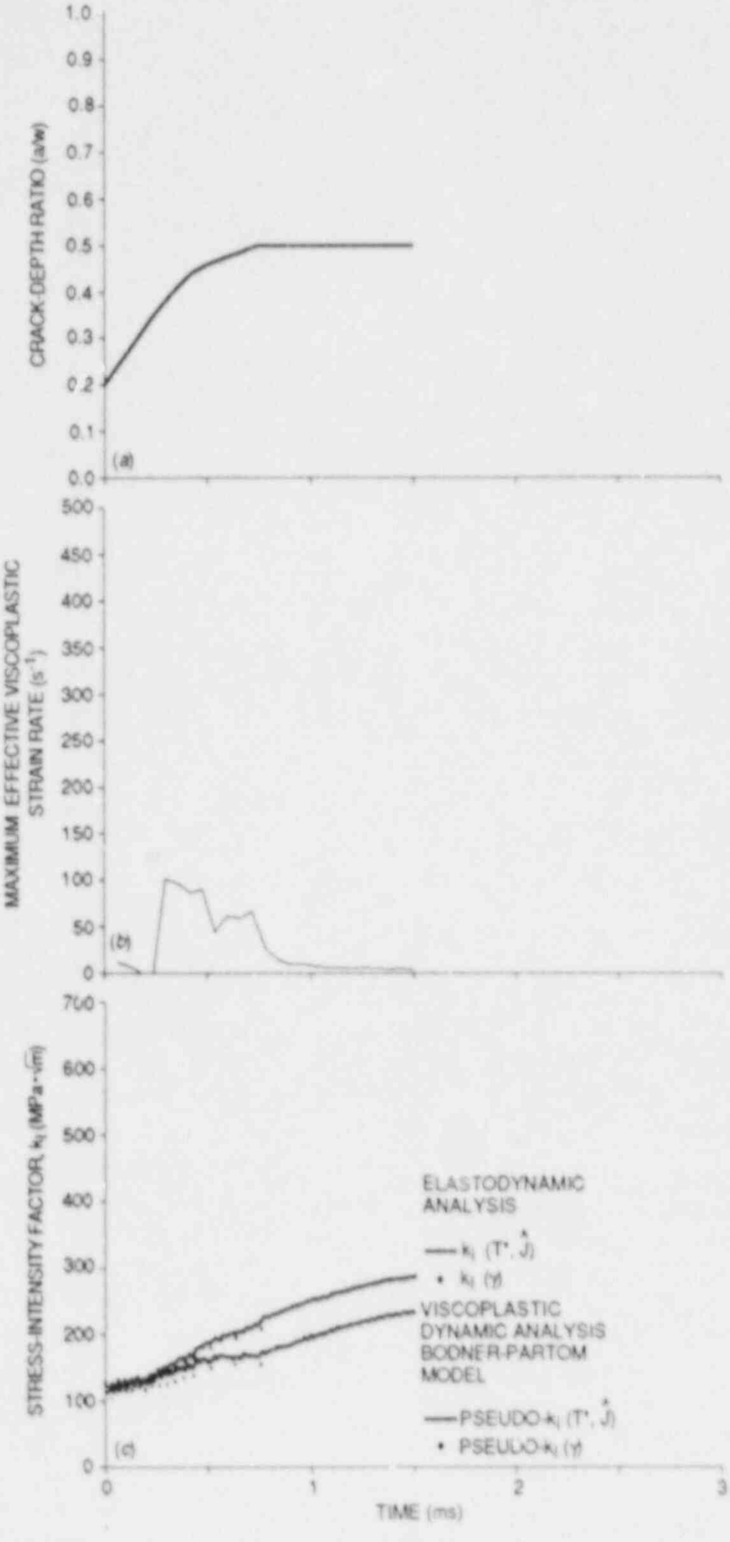

Fig. 2.4. Time histories of crack-depth ratio, maximum effective viscoplastic strain rate, and fracture parameters from analysis of wide-plate test WP-1.3. (*a*) Crack-depth ratio, (*b*) maximum effective viscoplastic strain rate, (*c*) fracture parameters.

ORNL-DWG 88-4304 ETD

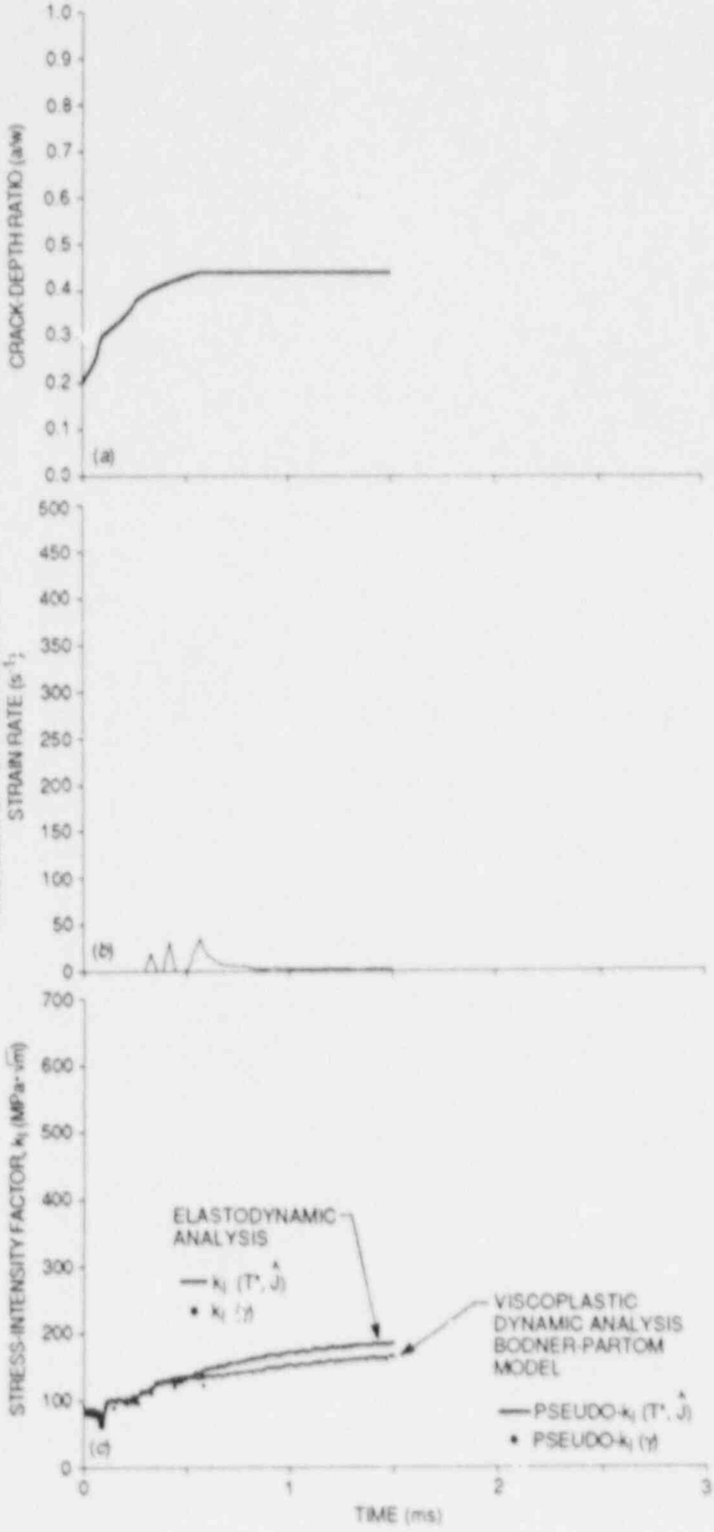

Fig. 2.5. Time histories of crack-depth ratio, maximum effective viscoplastic strain rate, and fracture parameters from analysis of wide-plate test WP-1.4. (*a*) Crack-depth ratio, (*b*) maximum effective viscoplastic strain rate, (*c*) fracture parameters.

ORNL-DWG 88-4305 ETD

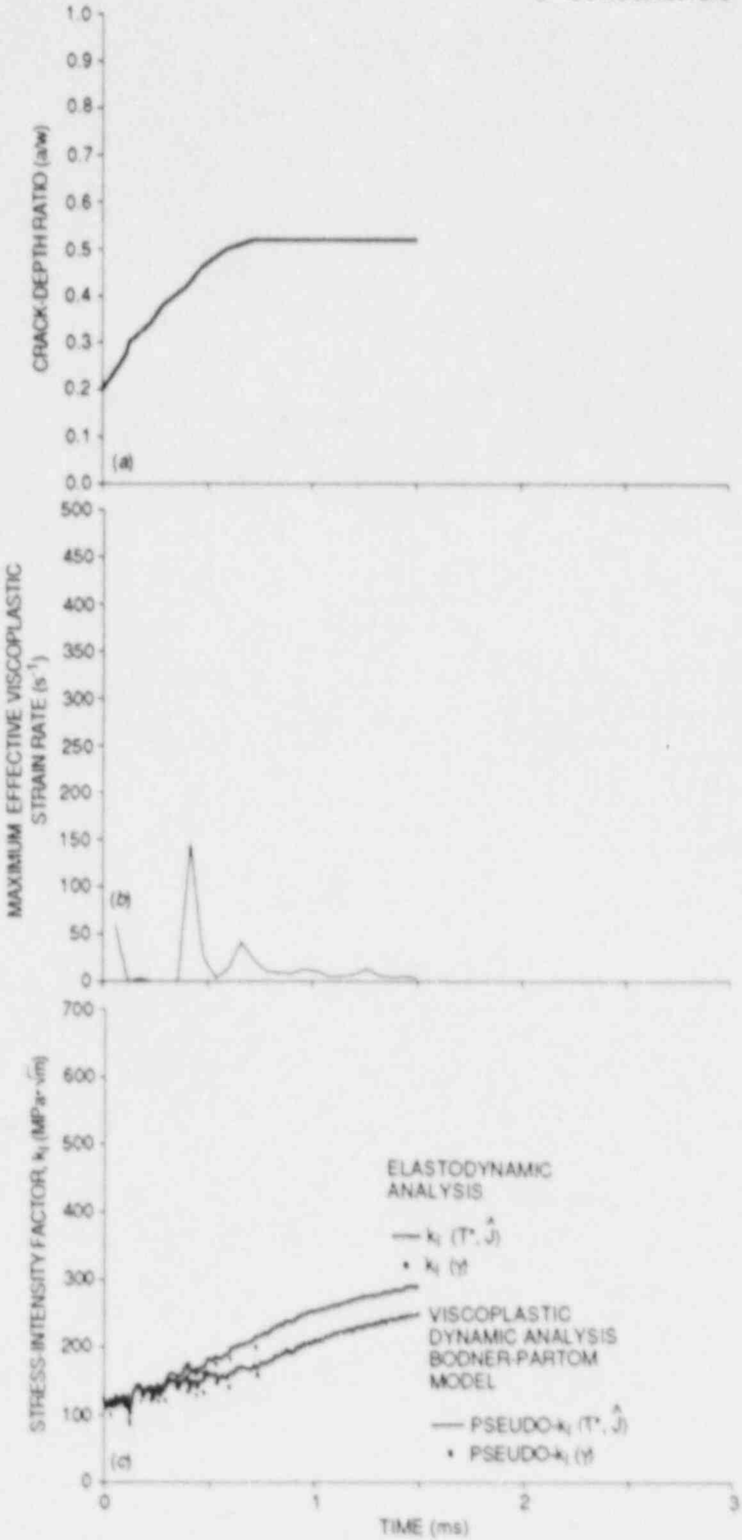

Fig. 2.6. Time histories of crack-depth ratio, maximum effective viscoplastic strain rate, and fracture parameters from analysis of wide-plate test WP-1.5. (*a*) Crack-depth ratio, (*b*) maximum effective viscoplastic strain rate, (*c*) fracture parameters.

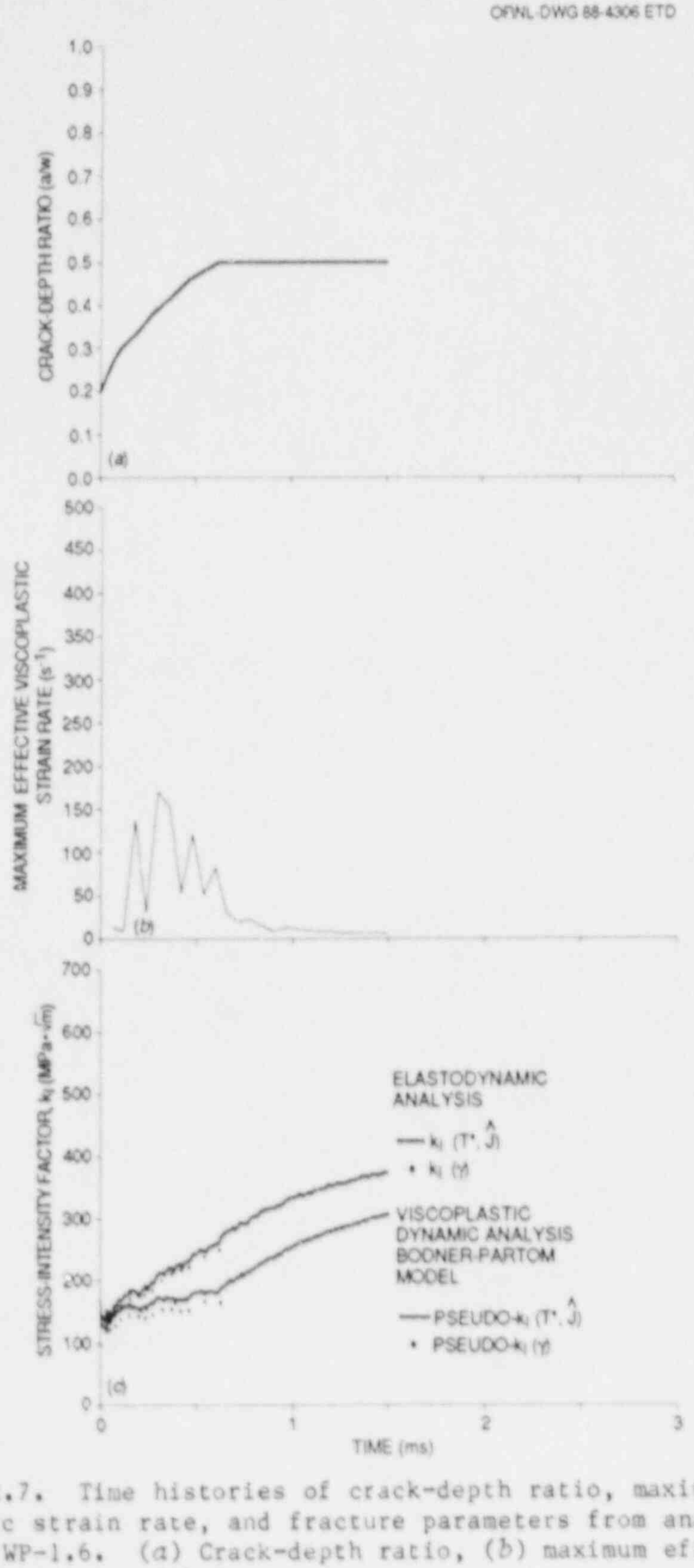

Fig. 2.7. Time histories of crack-depth ratio, maximum effective viscoplastic strain rate, and fracture parameters from analysis of wide-plate test WP-1.6. (*a*) Crack-depth ratio, (*b*) maximum effective viscoplastic strain rate, (*c*) fracture parameters.

ORNL-DWG 88-4307 ETD

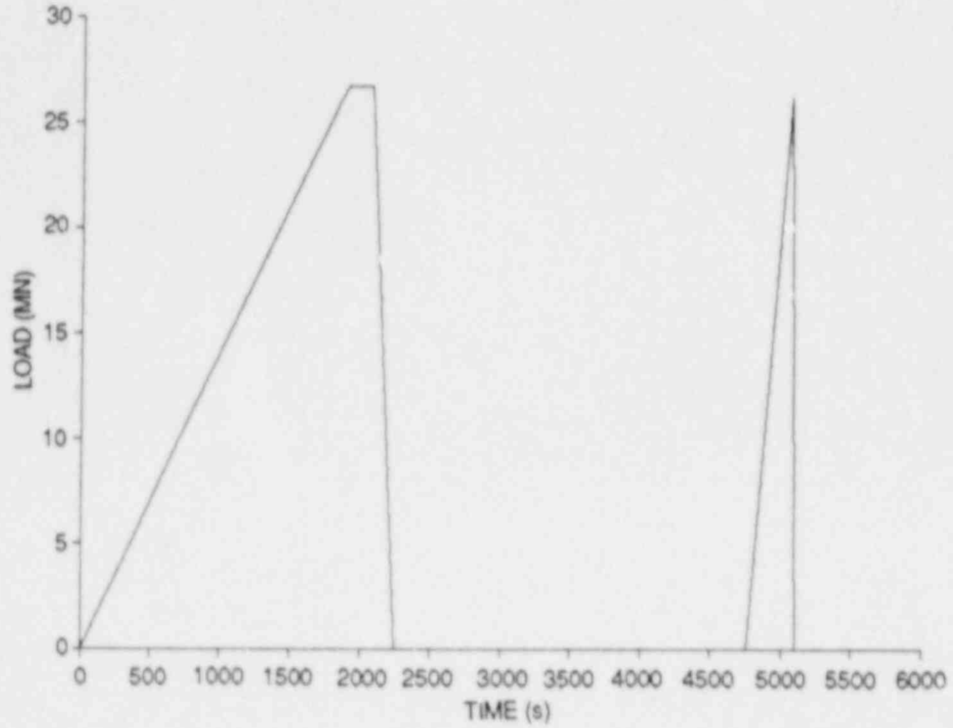

Fig. 2.8. Tensile load vs time curve used in generation-mode dynamic analyses of wide-plate test WP-1.7.

computed results sampled at the element Gauss points at 60 μs time intervals.) Generally, the maximum strain rate values in Fig. 2.3(*b*) occur at a Gauss point immediately ahead of the crack tip and closest to the plane of crack propagation. These maximum values depend partly on the finite-element mesh refinement and on the Gauss point rule selected for the analysis. The K_I-values computed in elastodynamic and viscoplastic-dynamic analyses of WP-1.2 using the finite-element model of Fig. 2.1(*a*) are compared in Fig. 2.3(*c*). The inelastic values of K_I at crack arrest given in Fig. 2.3(*c*) and in Table 2.2 are lower than those reported in Ref. 7 for less refined models, indicating that convergence of the solution has not been established.

Results from analyses of the single crack run-arrest event recorded in test WP-1.3 are depicted in Fig. 2.4. As indicated in Fig. 2.4(*a*), crack arrest occurred at $t = 0.75$ ms and at a crack depth ratio of $a/w = 0.5$. Beginning with test WP-1.3, the crack front was cut into a truncated chevron to initiate the crack at a lower load than was achieved in the previous tests. The lower initiation load recorded in test WP-1.3 ($F_{IN} = 11.25$ MN from Table 2.1) leads to less pronounced plasticity effects in the dynamic analysis as compared with results from test WP 1.2.

Results for the first of two cleavage run-arrest events observed in test WP-1.4 are presented in Fig. 2.5. In that test, the tensile load on the specimen was maintained constant at 7.95 MN while a pillow jack[6]

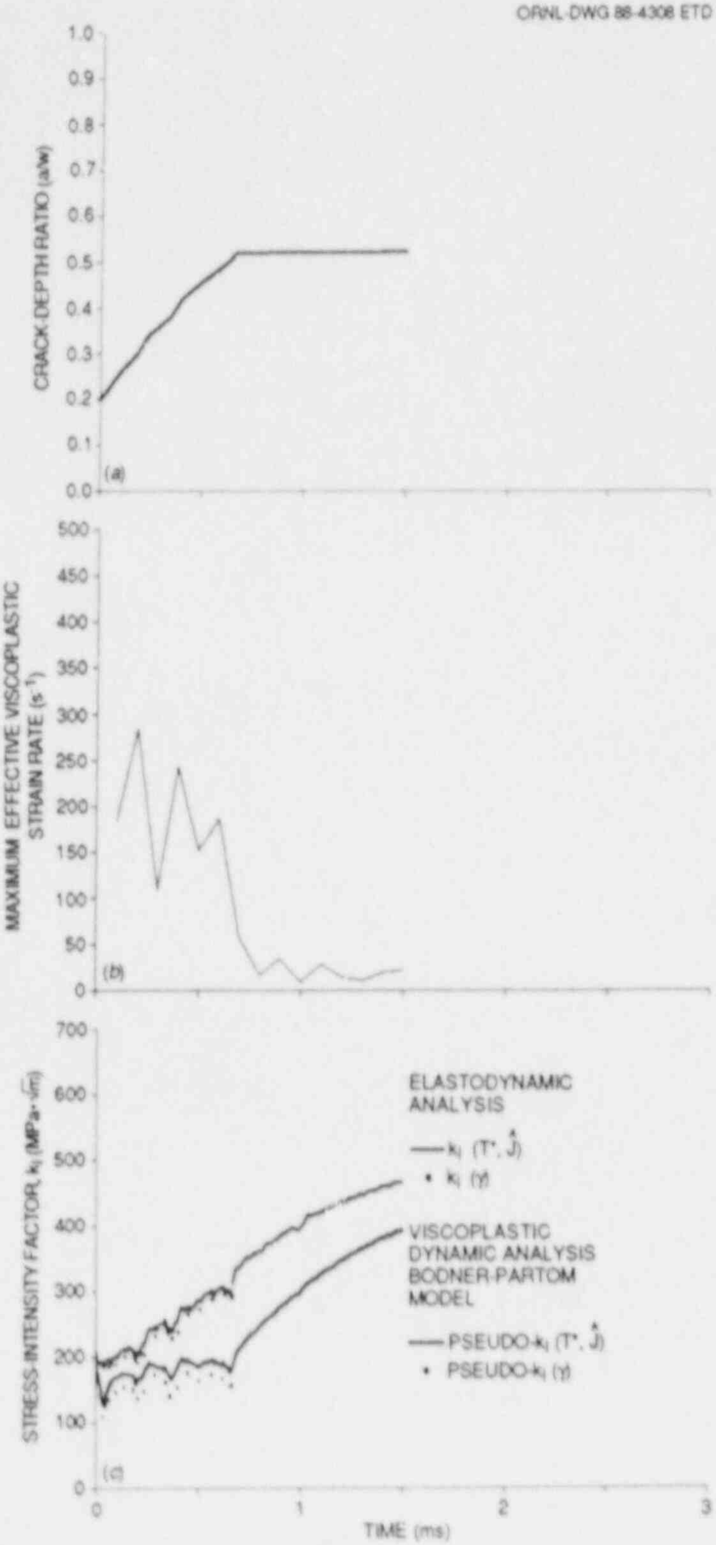

Fig. 2.9. Time histories of crack-depth ratio, maximum effective viscoplastic strain rate, and fracture parameters from analysis of wide-plate test WP-1.7. (*a*) Crack-depth ratio, (*b*) maximum effective viscoplastic strain rate, (*c*) fracture parameters.

placed in the specimen notch was pressurized to produce crack initiation. The tensile load was low enough to achieve a completely stable arrest at t = 0.57 ms and at a crack depth ratio of a/w = 0.44 [see Fig. 2.5(*a*)]. The relatively low crack-driving force in the first run-arrest event leads to very limited viscoplastic effects for the results from analyses presented in Fig. 2.5(*b*) and (*c*).

Tests WP-1.5 and WP-1.6 both exhibited multiple cleavage run-arrest events before the onset of unstable ductile tearing. Results from analyses of the first event are presented in Fig. 2.6 for test WP-1.5 and in Fig. 2.7 for test WP-1.6. The first crack arrest occurred in test WP-1.5 at t = 0.72 ms and a/w = 0.52 [Fig. 2.6(*a*)] and in test WP-1.6 at t = 0.62 ms and a/w = 0.49 [Fig. 2.7(*a*)]. A higher initiation load was achieved in test WP-1.6 (F_{IN} = 14.5 MN) as compared with test WP-1.5 (F_{IN} = 11.03 MN) by increasing the initial crack-tip temperature of WP-1.6 (T_{CT} = −19°C) above that of WP-1.5 (T_{CT} = −30°C). The higher tensile loads led to increased viscoplastic effects in the analysis of test WP-1.6 as compared with that of test WP-1.5. For both tests, subsequent cleavage events began ~8 ms after the first crack arrest.[6] Viscoplastic dynamic analyses of these late cleavage events will be performed in future crack-arrest studies.

Results from analyses of test WP-1.7 (Ref. 12) are given in Figs. 2.8 and 2.9. Test WP-1.7 used a 152-mm-thick specimen and an alternate set of pull plates; one-half of the assembly is represented in the finite-element model given in Fig. 2.1(*b*). During test WP-1.7, the wide-plate assembly was subjected to two loading cycles that are represented (approximately) by Fig. 2.8. The second loading cycle became necessary when the crack failed to initiate before reaching the tensile load capacity of the testing machine, 26.7 MN. The fracture initiated in the second loading cycle at a tensile load of 26.2 MN, causing two cleavage crack run-arrest events (see Table 2.1). In the finite-element analysis of the test, the model was loaded according to the two cycles of Fig. 2.8 to determine the initial conditions of the dynamic event. Results from analyzing the first cleavage-fracture event are presented in Fig. 2.9. Figure 2.9(*a*) indicates that crack arrest occurred at t = 0.68 ms and at a crack depth ratio of a/w = 0.53. As indicated in Fig. 2.9(*b*) and (*c*), the relatively high tensile load on the specimen produced significant viscoplastic effects in the dynamic analysis of the first event.

Additional generation-mode analyses of test WP-1.7 were performed using data from the first 8 ms of the dynamic event described in Ref. 12. Included in this time interval is a cleavage-reinitiation event at t = 7.4 ms, followed by crack arrest at t = 7.7 ms and a/w = 0.64. A viscoplastic-dynamic analysis (not shown here) produced effective plastic strain values >10% in the region near the crack plane during the second cleavage arrest (t = 7.7 ms). Since these strain values violate the small-strain assumption upon which the analysis was based, results for the latter portion of the time interval are not valid. The above results indicate that a viscoplastic-dynamic fracture formulation incorporating a large strain option is required to perform a valid inelastic analysis of the late cleavage event in WP-1.7; such a formulation is not now available in ADINA/VPF.

These fracture analyses of portions of the dynamic events recorded in the six wide-plate tests WP-1.2 to -1.7 indicate that the effects of including viscoplasticity in the fracture-parameter calculations are significant. Dissipative processes that occur in the developing plastic zone lead to reduced energy flow to the crack-tip region and, hence, to lower values for the fracture parameters (compared with elastodynamic values). However, a more definitive evaluation of the utility of these fracture parameters in predicting crack run-arrest behavior in wide plates must await results from other numerical studies. As described in Ref. 13, a comparison of results from wide-plate analyses performed by Oak Ridge National Laboratory (ORNL), Swedish Plant Inspectorate, and Southwest Research Institute (SwRI) revealed that values of the inelastic fracture parameters (such as T^*) decrease as the mesh is refined along the crack plane (for ratios of element width-to-plate width as low as 1/80). Not yet established is the degree of mesh refinement necessary to get convergence of the fracture parameters or whether the parameters will converge to nonzero values. Development plans include mesh-refinement studies to determine whether the proposed fracture parameters (such as T^*) converge to nonzero values in viscoplastic-dynamic analyses or whether they are controlled by the element length used along the path of crack propagation.

2.2 Elastodynamic and Viscoplastic-Dynamic Fracture Mechanics

M. F. Kanninen*
S. J. Hudak, Jr.*
R. J. Dexter*
H. Couque*
E. Z. Polch†
P. E. O'Donoghue*
J. D. Achenbach‡
C. H. Popelar§

2.2.1 Introduction and summary

The HSST program is directed toward the development of fundamentally based procedures needed for the prediction of crack arrest at the high upper-shelf toughness conditions involved in postulated pressurized thermal-shock (PTS) events. The objective of the SwRI contribution to the overall HSST effort is to provide analysis methods for pressure-vessel integrity assessments that are derived from small-scale test specimens. These methods include the dynamic effects and large-scale inelastic and time-dependent material deformation that could arise in both of these tests and in PTS conditions. The objective is therefore

---

*Engineering and Materials Sciences Division, Southwest Research Institute, San Antonio, Texas.

†Formerly Southwest Research Institute; presently at Digital Equipment Corporation, Colorado Springs, Colorado.

‡Department of Civil Engineering, Northwestern University, Evanston, Illinois.

§Engineering Mechanics Department, Ohio State University, Columbus, Ohio.

being accomplished by combining dynamic fracture mechanics finite-element analyses, viscoplastic-material characterization testing, small-scale fracture experimentation, near-tip mathematical analyses, and elastic-plastic tearing instability computations. Figure 2.10 shows the resulting internal interactions and the interactions between the SwRI effort and related elements in the HSST Program.

A specific goal of this project is to develop crack-arrest toughness data applicable to PTS conditions through small-scale test specimens. As shown in Fig. 2.10, this research goal uses compact duplex (A 533 grade B class 1/4340 steel) laboratory fracture specimens provided by ORNL. The fracture propagation-arrest data drawn from the analyses of these experiments will be applied to the National Bureau of Standards (NBS) wide-plate tests in the proof-of-principle mode. Satisfactory agreement will validate a crack-arrest assessment procedure that should then be valid for the entire range of PTS conditions.

Analysis done during this reporting period has centered on SwRI's viscoplastic-dynamic fracture-mechanics finite-element code VISCRK. Efficiency improvements have been implemented and complete documentation has been prepared as a necessary precursor to the detailed analyses of crack-propagation-arrest events in duplex specimens, analyses that previous work has shown necessary.[14,15] The experimental work has focused

ORNL-DWG 88-4309 ETD

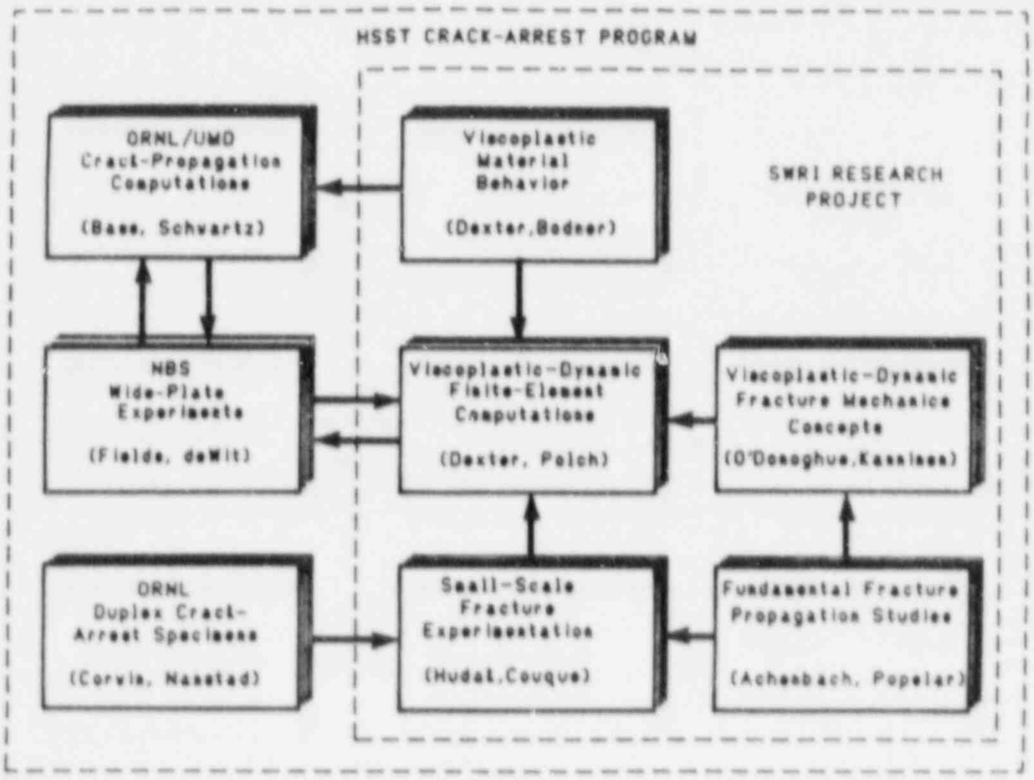

Fig. 2.10. Relation of SwRI interactive research with HSST Program.

on developing and verifying crack propagation time-length measurement techniques suitable for A 533 grade B class 1 steel in the appropriate temperature regime. For this purpose, several small duplex experiments have been completed and strain records analyzed. In addition, a new stress-wave loading procedure developed at SwRI has been pursued and found to have considerable promise for extending the measurement capability range.

2.2.2 Viscoplastic-dynamic fracture-mechanics finite-element analyses

During the previous year of work on this project, the viscoplastic-dynamic fracture-analysis program VISCRK was tested and used to perform benchmark demonstration problems.[14] Work in this period has focused on the documentation of VISCRK and on the implementation of improvements to increase the utility and efficiency of the analyses. In particular, timing of the subroutines in preliminary VISCRK runs revealed that over 60% of the time was being spent within subroutines that integrated the constitutive equations. Efficiency improvements have therefore focused on these subroutines.

The integration scheme involves some iterations for the solution of a highly nonlinear equation. The tolerance level of the iterations, previously set to an absolute value of the plastic Lagrange parameter, has a varying effect on the resulting level of error in the stress. Therefore, a scheme was derived to calculate the level of error in the stress, with a stress-based tolerance level being defined.

Several nonlinear interpolation schemes were investigated for inclusion in the iteration algorithm to find the root. Pade, cubic polynomial, and biquadratic schemes were tested. The best results were obtained with the Pade scheme. However, the cost of this scheme (i.e., 2.43 μs per call) was considerably higher than that of the existing linear scheme (i.e., 1.44 μs per call). It was therefore decided to implement a scheme whereby the Pade interpolation would only be used for high changes in slope on either side of the root. Prior interpolations more remote from the root will be performed with the linear interpolation. This scheme will be implemented in VISCRK. At ORNL, preparations have been made for a new set of analyses done on the CRAY with this new procedure.

Documentation of the development, use, and applications of VISCRK is now complete. This documentation is contained in three reports that have been prepared as chapters for a forthcoming SwRI topical report. The titles and brief descriptions are

1. Viscoplastic Characterization of A 533 Grade B Steel: This chapter describes the Bodner-Partom constitutive model and the method of determining the material parameters.
2. Development of Dynamic Viscoplastic Finite-Element Fracture Mechanics Computer Program: This chapter explains the underlying theory for the development of VISCRK.
3. Fracture Mechanics Analyses of Wide-Plate and Duplex Tests: This chapter gives a summary of the applications and findings that have been made with VISCRK to date.

An appendix containing complete instructions on how to use the program has also been prepared and is included in the topical report. This topical report will be submitted soon.

Analyses of NBS wide-plate tests and SwRI small duplex experiments have continued. Typical results obtained from an analysis of the small-duplex (SD) experiment SD6 (13AKB03) are shown in Fig. 2.11. As shown in Fig. 2.12, the mesh for these analyses was composed of elements having linear dimensions of about 12 mm.

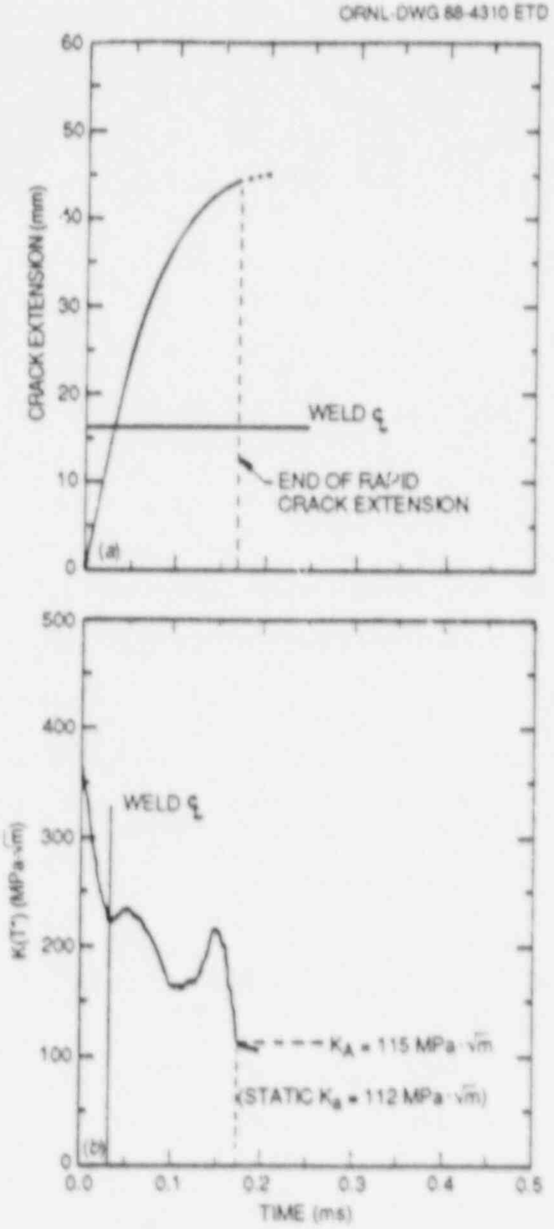

Fig. 2.11. Results from duplex specimen SD6 showing estimation of K_A. (*a*) Polynomial-least-squares fit to crack extension history, (*b*) pseudo-stress-intensity factor history (w = 127 mm, 33 mm thick).

ORNL-DWG 88-4311 ETD

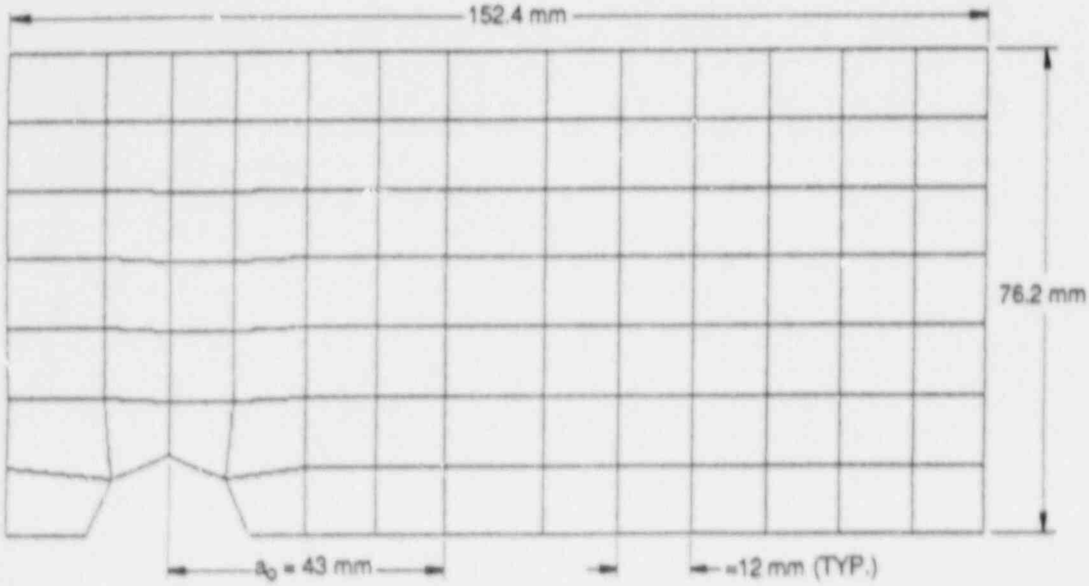

Fig. 2.12. Coarse finite-element mesh for analysis of duplex specimen.

Figure 2.11(*a*) shows the polynomial fit to the crack-extension history. The crack-extension histories in the 4340 steel and the A 533 grade B class 1 steel have been fitted separately over their individual ranges of crack extension. This procedure clearly reflects the change in velocity evident in the experimental records as the crack traverses the electron-beam (EB) weld. At the same time, this procedure retains the desirable averaging effects of the polynomial fit.

Earlier analyses have shown that the computed K values are not significantly affected by changes in the fit to the experimental crack-extension history, provided that the average velocity remains the same.[16] Thus, the computed pseudo-stress-intensity factor history shown in Fig. 2.11(*b*) should be reliable.

In Fig. 2.11(*a*), a sharp increase occurs in K at the same time that the crack traverses the EB weld. This finding corresponds to the time of the observed crack acceleration, an increase that can be correlated with the arrival time of the reflection (tensile) of the unloading wave from the crack-initiation event.

Although the crack-extension history shown in Fig. 2.11(*a*) continues out to several hundred microseconds, the latter portion is apparently very slow crack extension. The choice has been made to determine the dynamic K_A value at the end of rapid crack propagation but before the complete arrest. This point is indicated in [illegible] 2.11(*a*). The latter stages of crack extension may not be continuous rapid crack extension, but rather may consist of a series of small reinitiation, propagation, and arrest events. Note that, with the large gradient of the K history at the arrest point, the K_A value is very sensitive to the location of the point that ends rapid crack extension.

Because these analyses were carried out with relatively coarse meshes, it is not expected that the computed strain histories would correlate well with the experimentally measured strain histories described below. Finer mesh analyses are to be performed and the comparisons made in future work on this project.

Results similar to those of Fig. 2.11 were published previously[14,15] for the duplex experiment SD2 (13AK22E). The values of K as a function of crack-velocity resulting from these analyses are shown in Fig. 2.13. Figure 2.14 shows the K_A values plotted with the ORNL equation for K_{Ia}

ORNL-DWG 88-4312 ETD

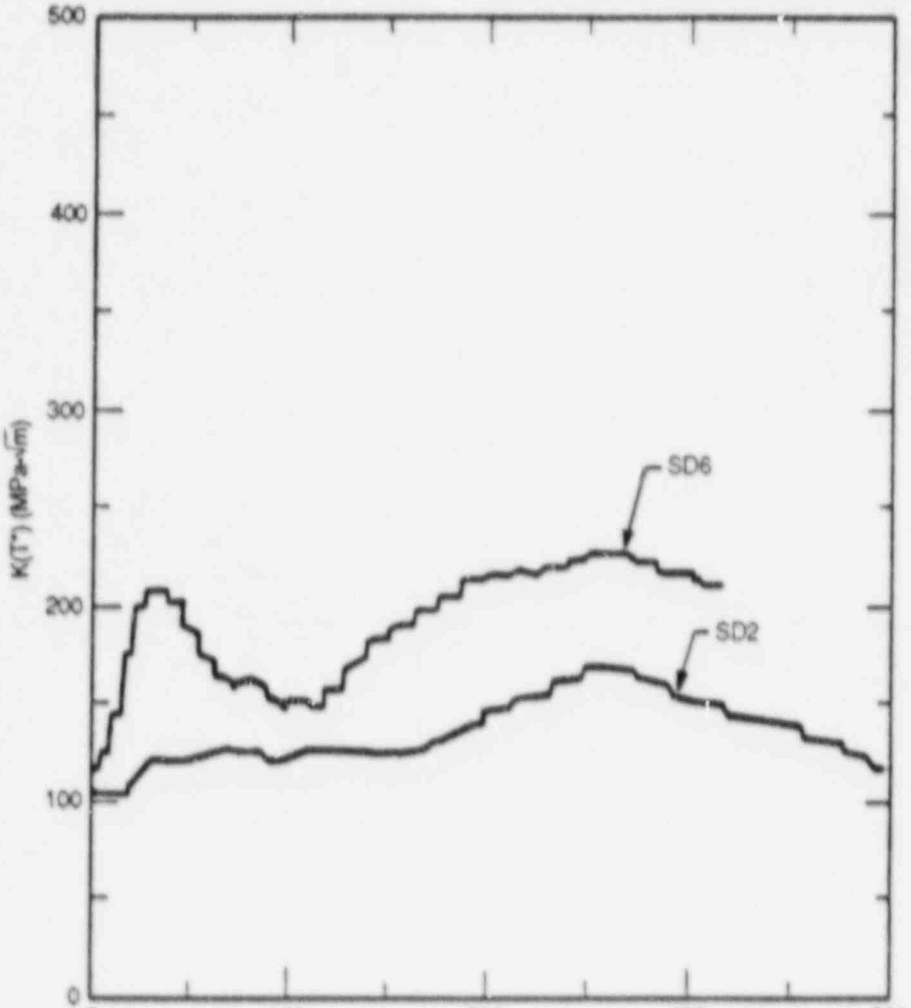

Fig. 2.13. Pseudo-stress-intensity factor vs crack velocity for A 533 grade B class 1 steel test piece (excluding 4340 starter section) for two duplex specimens SD2 and SD6 (w = 127 mm, 33 mm thick).

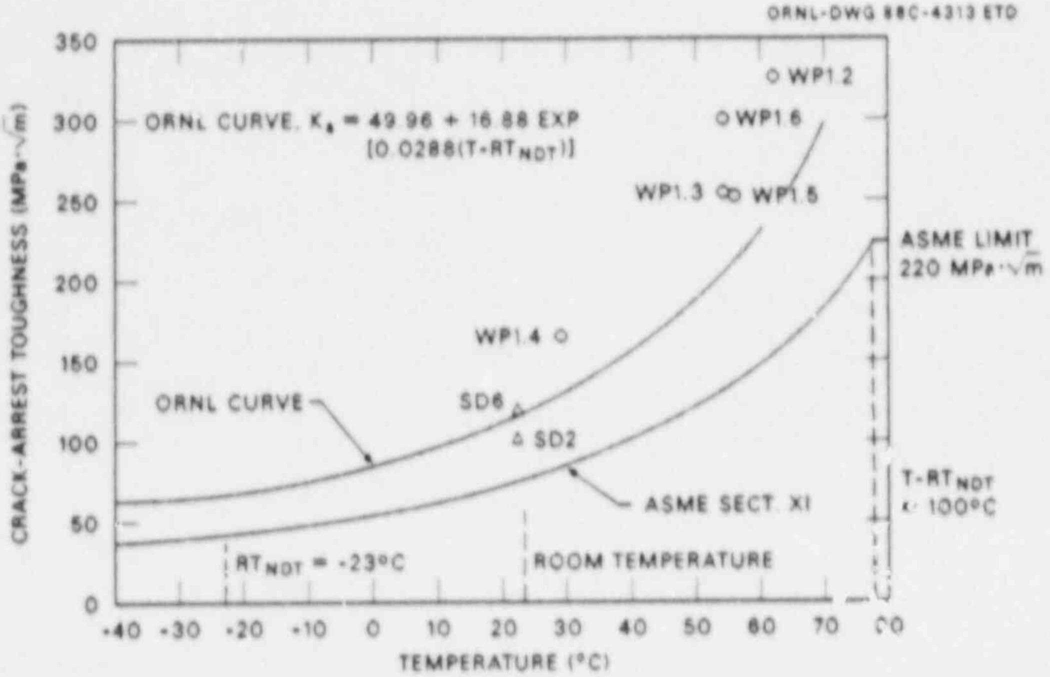

Fig. 2.14. Pseudo-stress intensity factor at the instant of crack arrest determined from SwRI viscoplastic-dynamic finite-element analyses [results include sidegroove correction of $(4/3)^{1/2}$].

and the ASME K_{IR} curve. Similarly, the K_A values for all SwRI analyses of the first crack-extension event in the NBS wide-plate experiments are shown in Fig. 2.14. The latter figure, which constitutes a key result of this work, shows that results equivalent to those obtained with wide-plate specimens can be obtained with specimens that are several orders of magnitude smaller.

2.2.3 Dynamic crack propagation experimentation

The experimental research is directed toward obtaining dynamic crack-propagation data in A 533 grade B class 1 steel using small-scale specimens. For this purpose, a series of duplex A 533 grade B class 1/4340 steel specimens of effective width, w = 127 mm, were instrumented and tested at 23°C. As noted in Fig. 2.10, these specimens were supplied by ORNL. Crack growth was monitored on both surfaces of each specimen using crack gages, whereas a crack-line displacement was measured using an eddy-current transducer. Dynamic-strain measurements were also obtained and used to examine the detailed interaction between stress-wave propagation and crack-growth response.

The crack-gage response on one side of the specimen was recorded with the Nicolet digital recorder. The high-speed counter developed at SwRI was used to record the response on the other side. Both recorders were calibrated simultaneously by using a printed circuit to simulate the response of the crack gage. Fast switches having 10 ns response were used to represent the breaking of the crack gage. A delay of 5 µs between switches was monitored using resistance capacitors. The responses of both recorders were in agreement at 0.1 µs. Such excellent resolution implies that crack-velocity measurements in duplex specimens can be performed with either the high-speed counter or the Nicolet digital recorder.

The correspondence between the crack-gage response and the actual crack position has been investigated with duplex specimens SD6 and SD7. The duplex specimen SD7 was instrumented with three strain gages located above crack gages 6, 7, and 8 at a distance of 6.5 mm from the side groove, as shown in Fig. 2.15. The time difference between the successive strain peaks and between the failure times of the crack gages are similar.

The peak strain occurs at an earlier time than does the failure of the crack gage. As indicated from the results of the experiments SD6 and

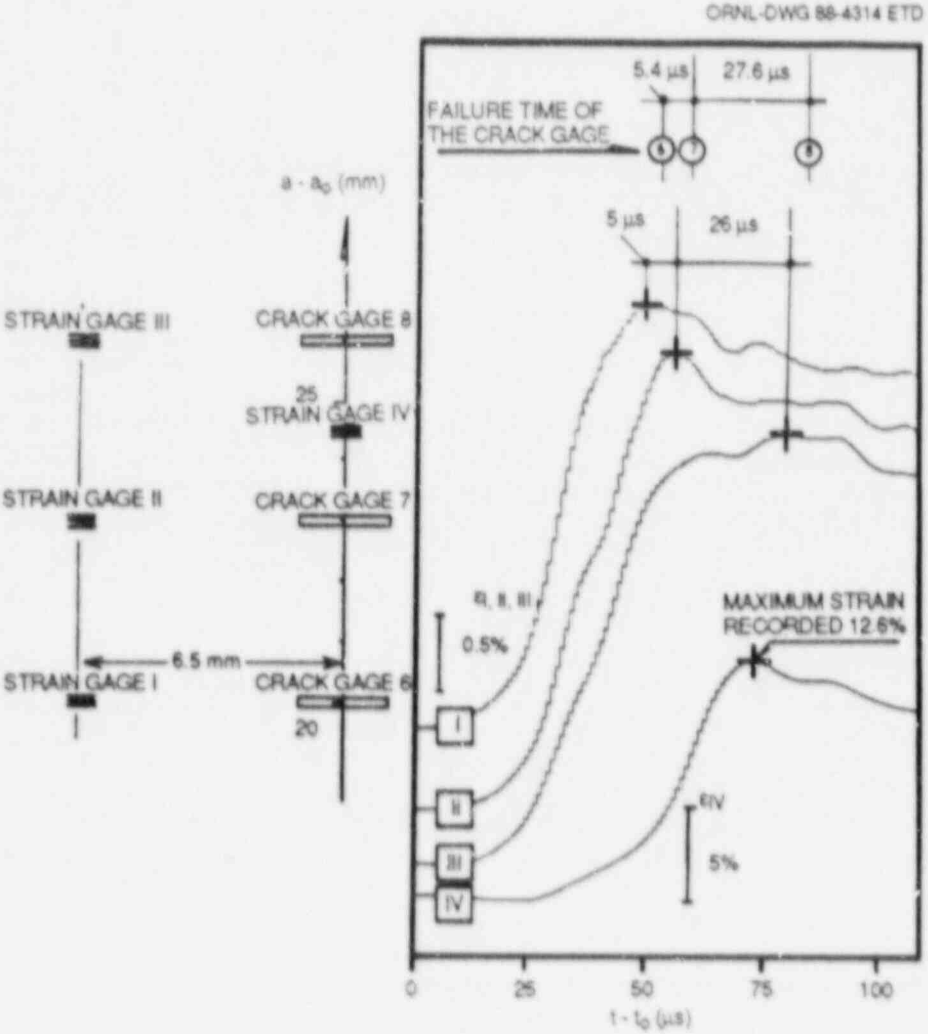

Fig. 2.15. Dynamic strain record of the axial strain gages located at the level of crack gages 6, 7, and 8.

SD7 in Table 2.3, this delay corresponds with a strain peak ahead of the crack tip with an angle of ~73°. This angle is similar to the peak-strain angle of 70° for the elastostatic-plane stress field. Based on this estimate, the failure of the crack gage occurs 2 μs before the crack reaches the crack-gage location.

Table 2.3. Comparison of strain gage and crack-gage data

$a - a_o$ (mm)	Strain gage strain peak time t_1 (μs)	Crack-gage failure time t_2 (μs)	$t_2 - t_1$ (μs)	ϕ
		Duplex SD-6		
20	18.8	25.0	6.2	73.5
23	36.8	43.5	6.7	72.8
		Duplex SD-7		
20	48.8	52.5	3.7	71.4
23	53.8	57.3	3.5	72.5
26	79.8	83.8	4.0	79.0 +6.0

Such an angle cannot be measured with precision when large crack-velocity variations occur, such as for the specimen SD7 at crack gage 8 (see Fig. 2.15). However, this measurement can be improved by using crack gages with smaller spacings. Strains up to 12% were recorded with a strain gage located on the crack path between crack gages 7 and 8, a finding that is shown in Fig. 2.15. This strain level, reached at 10.9 μs before the failure of crack gage 8, corresponds with the strain limit of the adhesive of the strain gage. Using VISCRK, this measurement will be compared with the strain measurement from the analysis when results obtained with suitably refined meshes become available (see Sect. 2.2.2).

A new technique developed at SwRI enables two relatively small specimens to be tested simultaneously using stress-wave loading from Hopkinson-type pressure bars. Trial experiments were conducted by pre-loading the pressure bars, connected through a starter specimen, to about 100 kips. The test specimens were then inserted into slots in the bars and secured with wedges. Next, fracture of the starter specimen was initiated by introducing a sharp cut into the circumferential notch, which then released in the bars an unloading wave that imparted a rapid crack-opening-displacement rate to the test specimens. The test configuration is shown in Fig. 2.16.

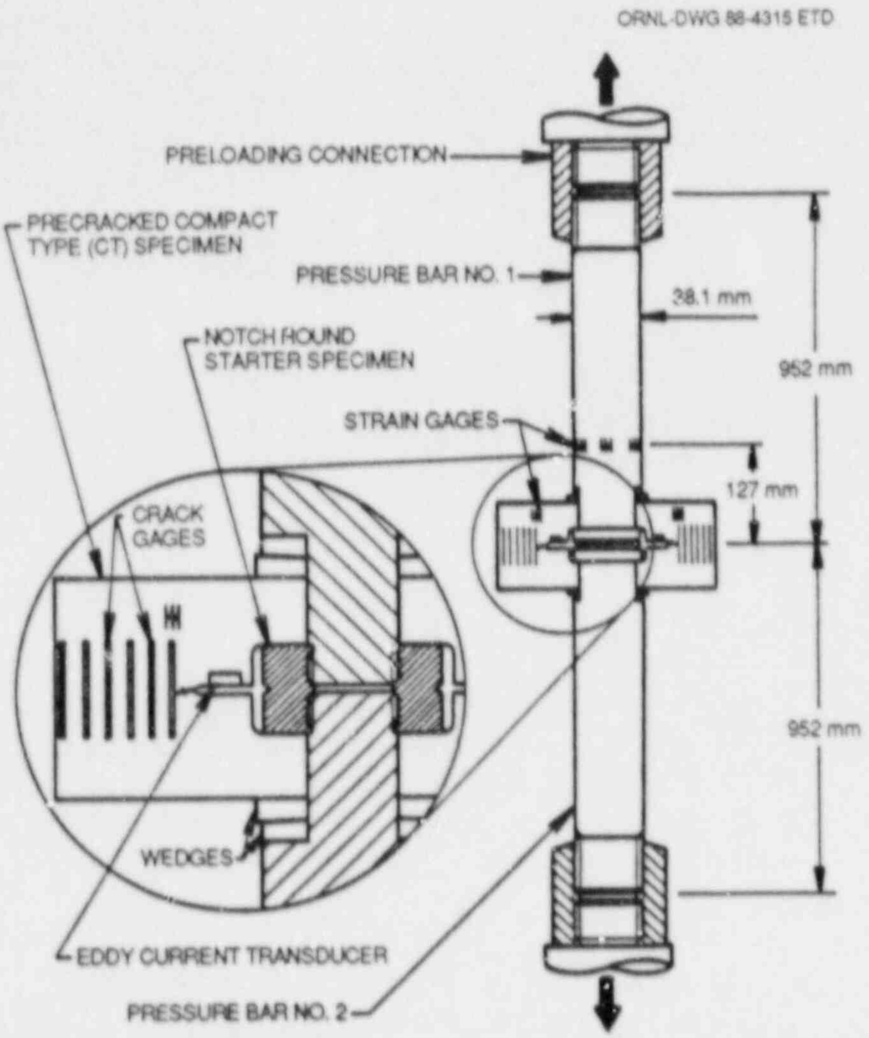

Fig. 2.16. Schematic diagram of the coupled pressure bar experiment.

Precracked compact-type A 533 grade B class 1 steel specimens, without side-grooves and having an effective width w = 44 mm, have been tested at 23 and 37°C. Crack growth of ~15 mm was achieved. Two A 533 grade B class 1 specimens with side-grooves and a modified fastening mechanism to the pressure bars are being prepared for testing at temperatures ranging from 37 to 50°C. Under such conditions, complete failure of the specimens is expected.

Figure 2.17 compares the A 533 grade B class 1 steel specimens from the coupled pressure bar experiment with larger specimens that were tested previously at SwRI of the same heat of material. The accomplishment is a significant one. Note that previous tests using the large

ORNL PHOTO 3000-88

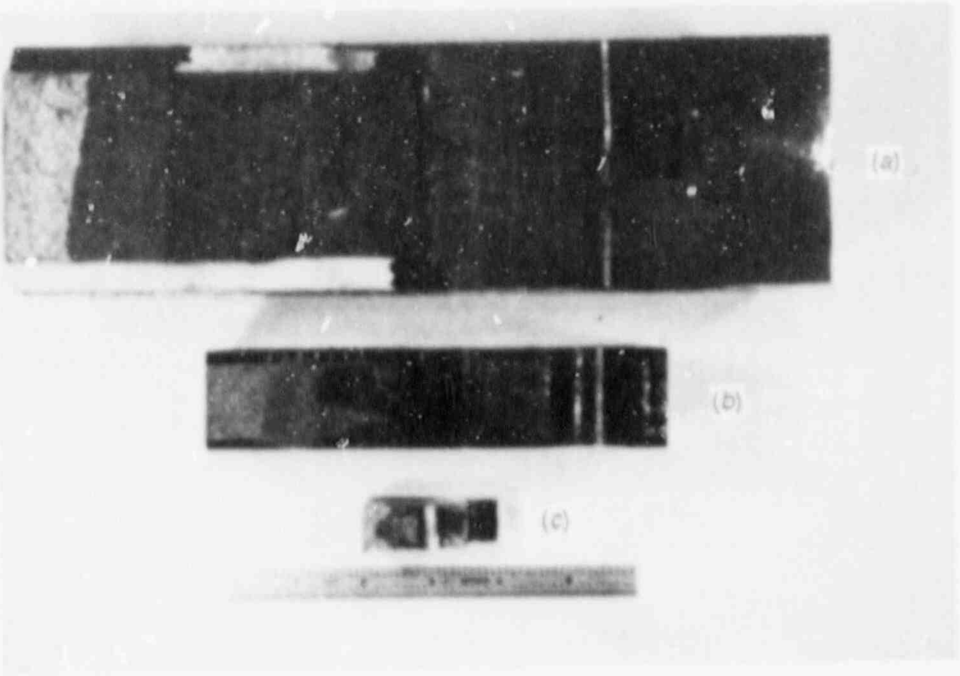

Fig. 2.17. Comparison of the measurement capacity of various A 533 grade B class 1 specimens. (*a*) Monolithic specimen (w = 203 mm) tested at −50°C, (*b*) 4340/A 533 grade B class 1 duplex specimens (w = 127 mm) tested at 25°C, (*c*) pressure-bar loaded specimen (w = 44 mm) tested at 37°C.

monolithic specimens (w = 203 mm) were successful only at inducing rapid fracture to −50°C, whereas the next smaller-sized duplex 4340/A 533 grade B class 1 steel specimens (w = 127 mm) have only been successful to 25°C.

The fact that dynamic initiation, propagation, and arrest data can be measured on the same relatively small specimen is also an attractive feature of the newly developed test technique. Moreover, the successful demonstration of dynamic crack propagation in A 533 grade B class 1 steel at 64°C above NDT is a very promising result, particularly with the specimen size used. These small specimens will also be particularly helpful in determining the influence of stress state on dynamic propagation and crack arrest. This research issue will be a focal point of the work planned for this year.

2.3 Investigation of Damping and Cleavage-Fibrous Transition in Reactor-Grade Steel at the University of Maryland*

W. L. Fourney[†] G. R. Irwin[†]
D. B. Barker[†] J. W. Dally[†]
C. W. Schwartz[‡] X.-J. Zhang[†]

Work at the University of Maryland (UM) over the past 6 months includes (1) cleavage-fibrous transition studies, (2) optical examinations of selected wide-plate tests, (3) dynamic crack-initiation testing, and (4) dynamic computational support of crack-arrest testing.

2.3.1 Cleavage-fibrous transition model studies

At the October 1987 ASM International meeting in Cincinnati, a paper by X.-J. Zhang, R. W. Armstrong, and G. R. Irwin was presented on "Cleavage Behavior in the Upper Transition Temperature Range for Pressure Vessel Steels." (The paper was not published.) In it, the main cleavage behavior characteristics reported in Refs. 17 and 18 were reviewed. Also, measurements of the change in cleavage orientation, with the passage of cleavage through ferrite grain boundaries, were reported and discussed.

The change of cleavage orientation can be represented by three angles (total, twist, and tilt), as shown in Fig. 2.18. For nuclear vessel steels, even at low testing temperature, the surface orientation changes in "smooth curve" fashion across the grain boundary. A sharp indication of the grain boundary, as depicted in Fig. 2.18, is not visible. In the UM work, twist and tilt angles were calculated as though the grain boundary line were normal to the apparent direction of cleavage advancement before grain boundary passage. For this reason, the UM-calculated angles of twist and tilt are less significant than the orientation changes in terms of the total angle.

The measurement results shown in Table 2.4 and Fig. 2.19 were obtained using specimens of 72W weld metal. Typical isolated cleavage regions (ICRs) of substantial size were used for the higher temperature results. The low-temperature fracture surface was all cleavage. Measurements pertaining to the low temperature were done using selected regions of similar size, within which directions of fracturing and the transit of cleavage through grain boundaries were most clearly indicated. Although this measurement-region selection process might be thought to reduce the observed changes of cleavage orientation, the actual results for total angle change, shown in Fig. 2.19, indicate

---

*Work sponsored by the HSST Program under Subcontract No. 7778 between Martin Marietta Energy Systems, Inc., and the University of Maryland.

[†] Department of Mechanical Engineering, University of Maryland, College Park.

[‡] Department of Civil Engineering, University of Maryland, College Park.

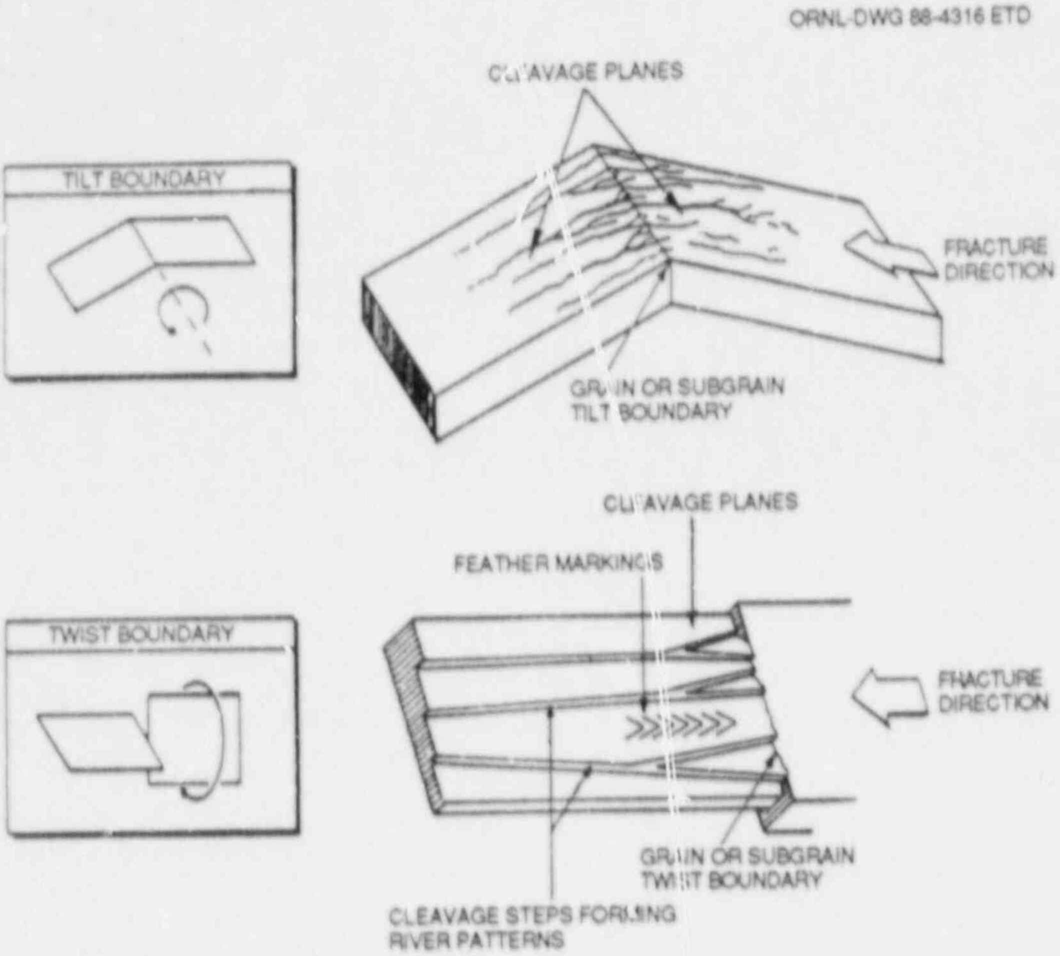

Fig. 2.18. Change of cleavage orientation represented by three angles (total, twist, and tilt). The river markings shown here are not typical of those seen in the transition temperature range. *Source:* H. L. Ewalds and R. J. H. Wanhill, *Fracture Mechanics*, p. 239.

nearly random changes of total angle between zero and 75°. In contrast, at the higher temperature, all of the total angle changes were <30°.

These results indicate a pronounced change in the resistance to the passage of cleavage through grain boundaries with a temperature increase such that the spread of cleavage across grain boundaries is further limited to a smaller degree of crystallographic mismatch. The expected result is a decreasing ability of a spreading unit of cleavage to adjust to changes in tensile stress direction, leading to larger late-breaking connections. As noted in Ref. 19, the increasing density and size of late-breaking connections between regions of cleavage with increasing temperature contribute importantly to the elevation of fracture toughness in the transition temperature range.

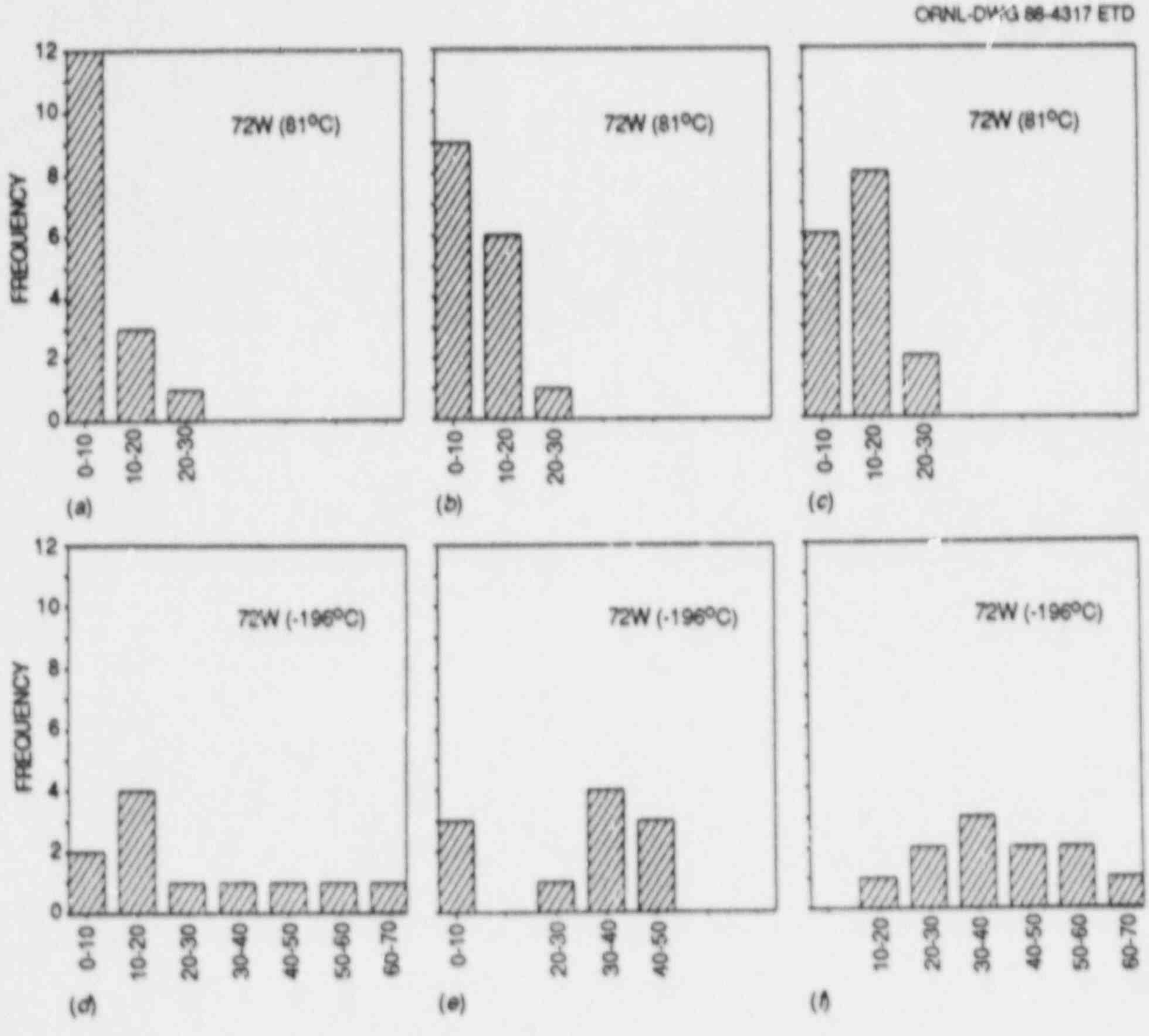

Fig. 2.19. Frequency graphs of various tilt, twist, and total angles across grain boundary passages of M-CVN specimens of 72W weld metal at temperatures of 81 and −196°C. (*a*) Tilt angle (81°C), (*b*) twist angle (81°C), (*c*) total angle (81°C), (*d*) tilt angle (−196°C), (*e*) twist angle (−196°C), (*f*) total angle (−196°C).

Table 2.4. Tilt, twist, and total angle measurements for two M-CVN specimens of 72W weld metal tested at −196°C and 81°C, respectively

Measurement No.	Specimen A (−196°C) (deg)			Specimen B (81°C) (deg)		
	Tilt angle	Twist angle	Total angle	Tilt angle	Twist angle	Total angle
1	36	39	47	5	18	19
2	67	42	68	4	12	13
3	17	52	52	5	6	8
4	12	28	29	14	2	15
5	50	9	50	8	1	8
6	1	37	37	16	7	18
7	28	1	28	2	19	19
8	48	48	58	22	14	26
9	8	33	33	9	13	16
10	13	33	34	4	12	13
11	11	6	13	2	22	22
12				3	2	3
13				4	6	7
14				1	4	4
15				5	1	5
16				13	8	15
Average	26	30	41	7	9	13

Improved scanning electron microscopy (SEM) equipment is now available at the University of Maryland and has been used to obtain photographs of cleavage-initiation regions at higher magnification. Figure 2.20 shows a cleavage-origin region in 72W weld metal that is adjacent to a broken silicate particle. Figure 2.21 shows a cleavage origin in A 508 steel that is near a particle clump. Very small (~0.1-μm) particles are present within the region where the development of a cleavage embryo of adequate size must have occurred. Requiring further study is the issue of whether or not the indicated density of such particles is unusually high in cleavage-initiation regions.

2.3.2 Optical topography results from wide-plate crack-arrest tests WP-CE-1 and WP-1.7

During recent years, topographic analysis of fracture surfaces using stereo-SEM and relative height measurements has received increasing attention. An optical stereographic technique has been used successfully

ORNL PHOTO 3001-88

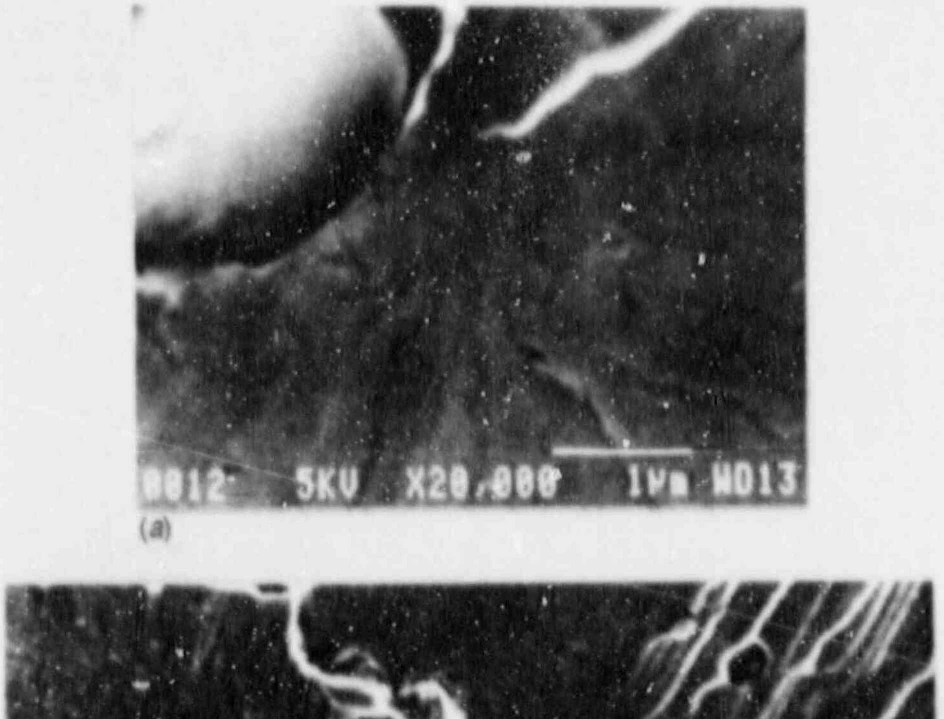

Fig. 2.20. Low-voltage SEM fractographs showing details in a region of cleavage initiation adjacent to a fractured silicate particle in 72W weld metal at two magnifications.

ORNL PHOTO 3002-88

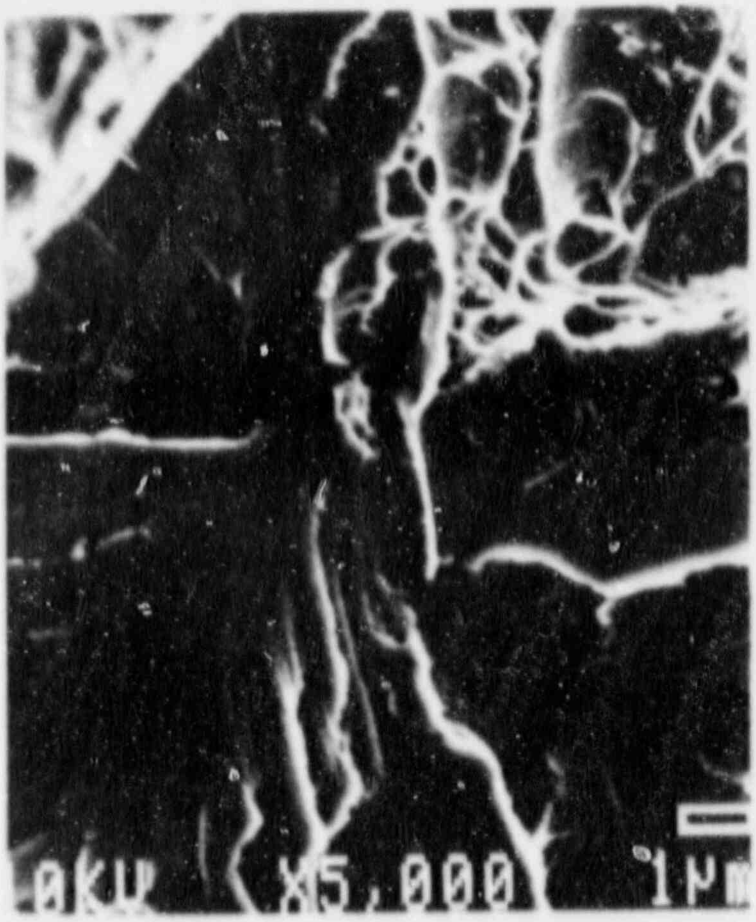

Fig. 2.21. Low-voltage SEM fractograph showing details in a region of cleavage initiation adjacent to a particle clump in A 508 steel.

(Ref. 20) to determine the local sequences of separation for the initiation region of a wide-plate fracture, test WP-2.4. This method does not require sectioning the broken halves of the test plate. Optical topography was used in this study to examine regions of two wide-plate fractures in which cleavage arrest was followed by a fibrous-tear reinitiation. Results for specimen WP-CE-1 (100 mm thick) and specimen WP-1.7 (152 mm thick) are presented. The method of relative height measurements is discussed in Ref. 21.

2.3.2.1 Specimen WP-CE-1. A 102-mm-thick specimen of A 533 grade B class 1 steel, provided to ORNL by Combustion Engineering, Inc., was used for this test. The initial loading provided a single cleavage run-arrest event. After several minutes, loading was continued and produced a long segment of fibrous tearing. The plate temperature pertaining to crack arrest and reinitiation was 30°C.

Figure 2.22 shows the area of the fracture surface used for topographic analysis and the location of the lines along which height measurements were made. Relative heights were determined along seven lines.

ORNL PHOTO 3003-88

Fig. 2.22. Area of the fracture surface of WP-CE-1 specimen selected for optical topographic analysis.

Lines A1, A2, and A3 were estimated crack-front contours in the cleavage region. Lines B1, B2, and B3 were estimated forward-crack-extension lines crossing the crack arrest. Line C1 was an estimated crack-front contour line in the region of fibrous tearing. For each of the mating fracture surfaces, one surface point was selected for reference. All height measurements were made relative to the surface height at that point.

Figure 2.23 shows measurement results on lines A1, A2, and A3. The results are arranged as if the upper and lower fracture surfaces were held a small distance apart. The ordinate scale measures the separation of measurement points from a flat surface (the middle line) held above it

ORNL-DWG 88-4318 ETD

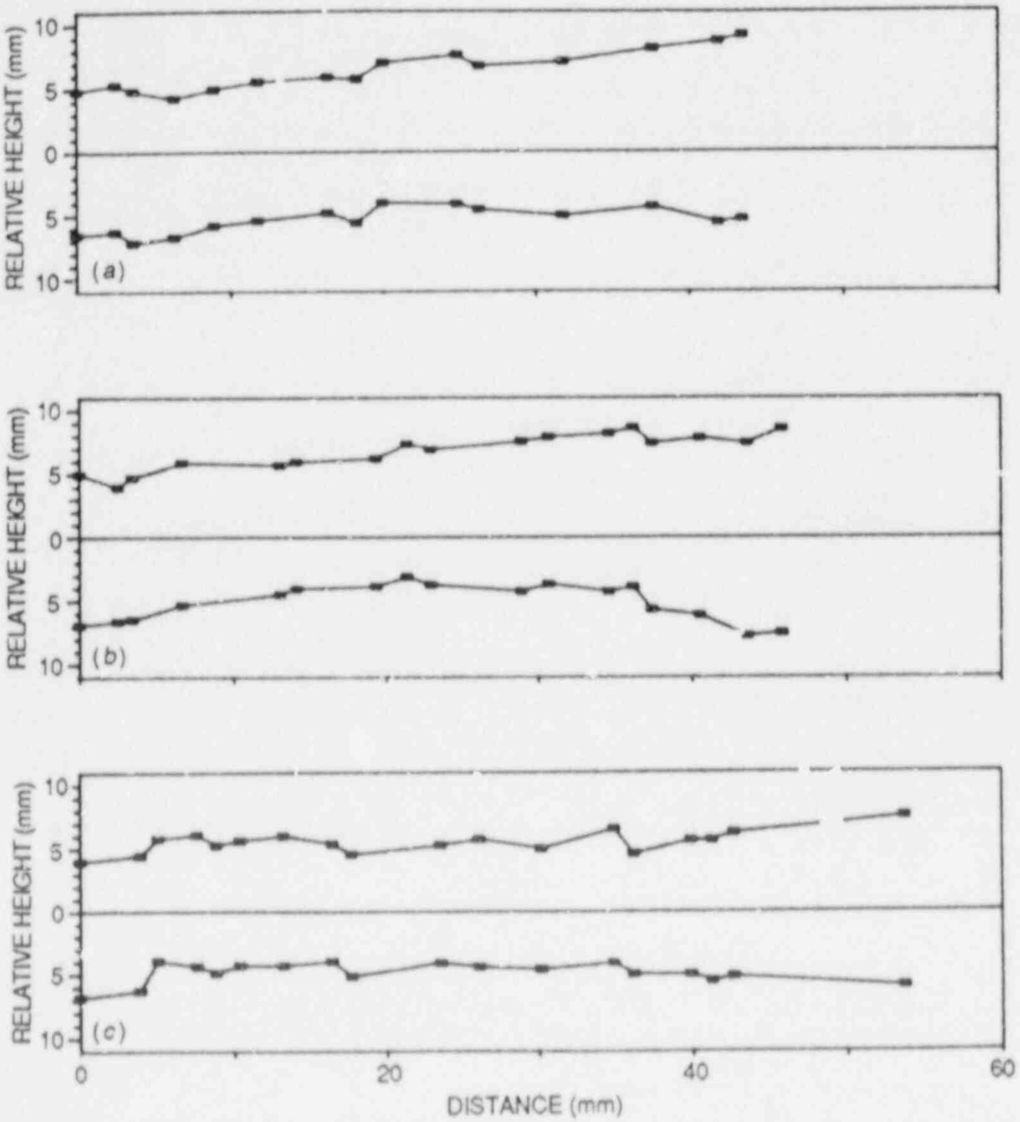

Fig. 2.23. Relative height measurements along lines A1, A2, and A3 within cleavage region in Fig. 2.22. (The abscissa zero is on the left in Fig. 2.22.) (*a*) Line A1-A1, (*b*) line A2-A2, (*c*) line A3-A3.

(for the lower surface) and below it (for the upper surface). If fracturing were nearly simultaneous at all points on the measurement lines, the average local separation between the two fracture surfaces would be nearly constant. A significant deviation from this behavior would suggest that regions of larger separation broke earlier than other regions. The results indicate that a small portion at the right extremities of lines A1, A2, and A3 may have been drawn too far from the crack-arrest position. Otherwise, the separations are uniform, as expected if the lines represented previous locations of the crack front. The abscissa scale has its zero at the left end of each line. To provide the abscissa points, distances between measurement points were measured parallel to the line and summed.

Similarly, Fig. 2.24 shows separations between the fracture surfaces along lines B1, B2, and B3. The abscissa increases in the direction of crack extension. Figure 2.25 shows results for line C1 in the region of fibrous tearing. For line C1, the increase of separation away from the

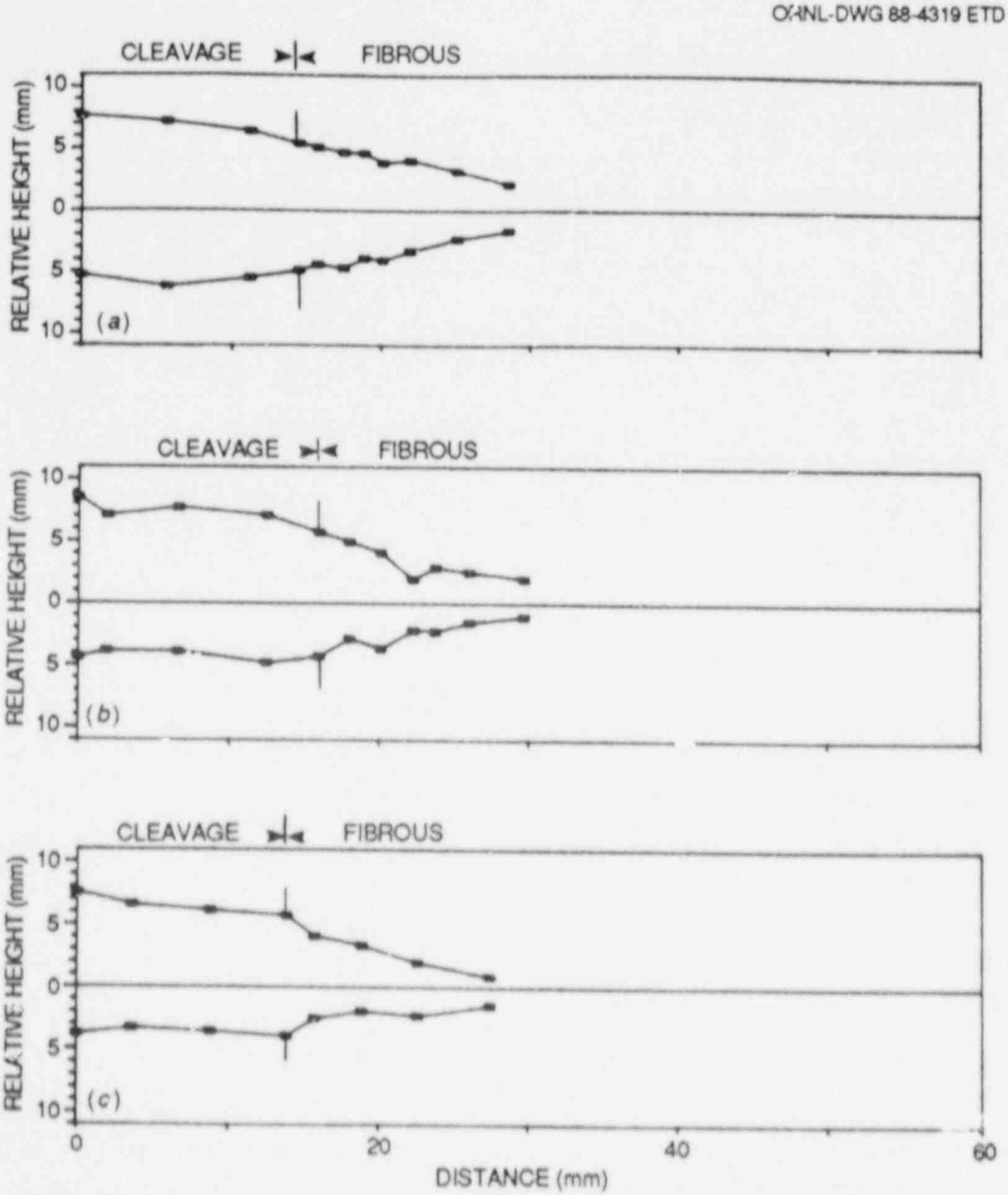

Fig. 2.24. Relative height measurements along lines B1, B2, and B3 showing separations between surfaces (the abscissa increases in the direction of crack extension). (*a*) Line B1-B1, (*b*) line B2-B2, (*c*) line B3-B3.

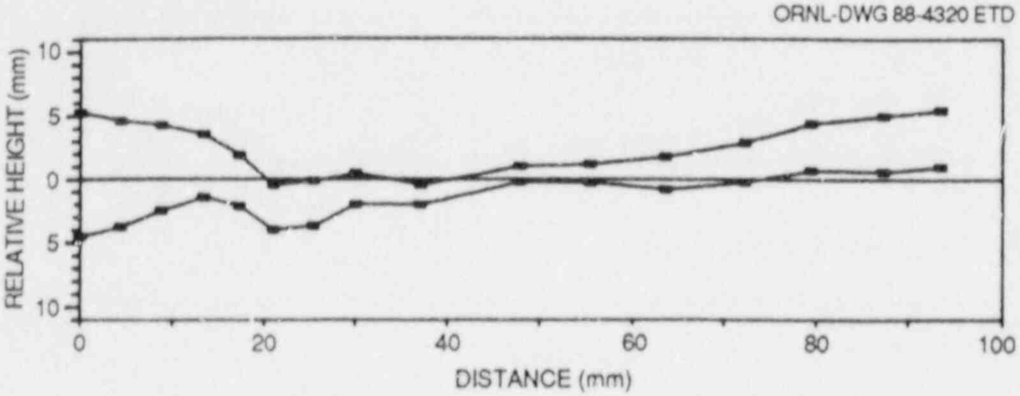

Fig. 2.25. Relative height measurement along line C1 within the fibrous region.

midregion of the plate suggests that the crack front was leading in these regions by an amount larger than that indicated by the curvature of the assumed crack-front line.

Large fracture-surface irregularities, introduced by midplane impurities, assisted the development of a pronounced inverse curvature of the crack front. In the cleavage portion of the fracture, where plastic strain is too small to produce lamination-type midplane separations, the crack-front and -surface irregularities are much less affected by midplane effects.

For lines B1, B2, and B3, a method somewhat like that used for J_{IC} determinations seemed reasonable and was used. For each measurement line, Fig. 2.26 shows estimates of residual crack-opening displacement (RCOD) for positions of the crack front within the fibrous region. These estimates were obtained by subtracting each measured opening separation in the fibrous region from the opening measured in the cleavage region very close to the crack-arrest position. The result was a graph of RCOD (at the cleavage edge position) as a function of apparent forward motion of the fibrous tear. Assuming that RCOD was proportional to J, the graph is similar to those of J vs Δa used in both J_{IC} and J-R testing. Use of a blunting line, from the equation RCOD equals twice Δa, in place of the zero abscissa line had little influence on the results. Large fracture-surface irregularities introduced substantial irregularities into the measurement results. Lacking evidence for curving trends in RCOD increase with crack extension, it was assumed that a uniform rate of RCOD increase was a reasonable choice for on-average behavior. "Least squares" straight lines through the fibrous region data points resulted in estimates of crack-tip-opening displacement (CTOD) for the three lines — B1, B2, and B3 — of 0.00, 2.03, and 1.78 mm, respectively, for an average of 1.19 mm.

In future trials of this nature, a larger number of height measurements should be used to compensate for the influence of fracture-surface irregularities. However, the above-average value of CTOD can be shown in

ORNL-DWG 88-4321 ETD

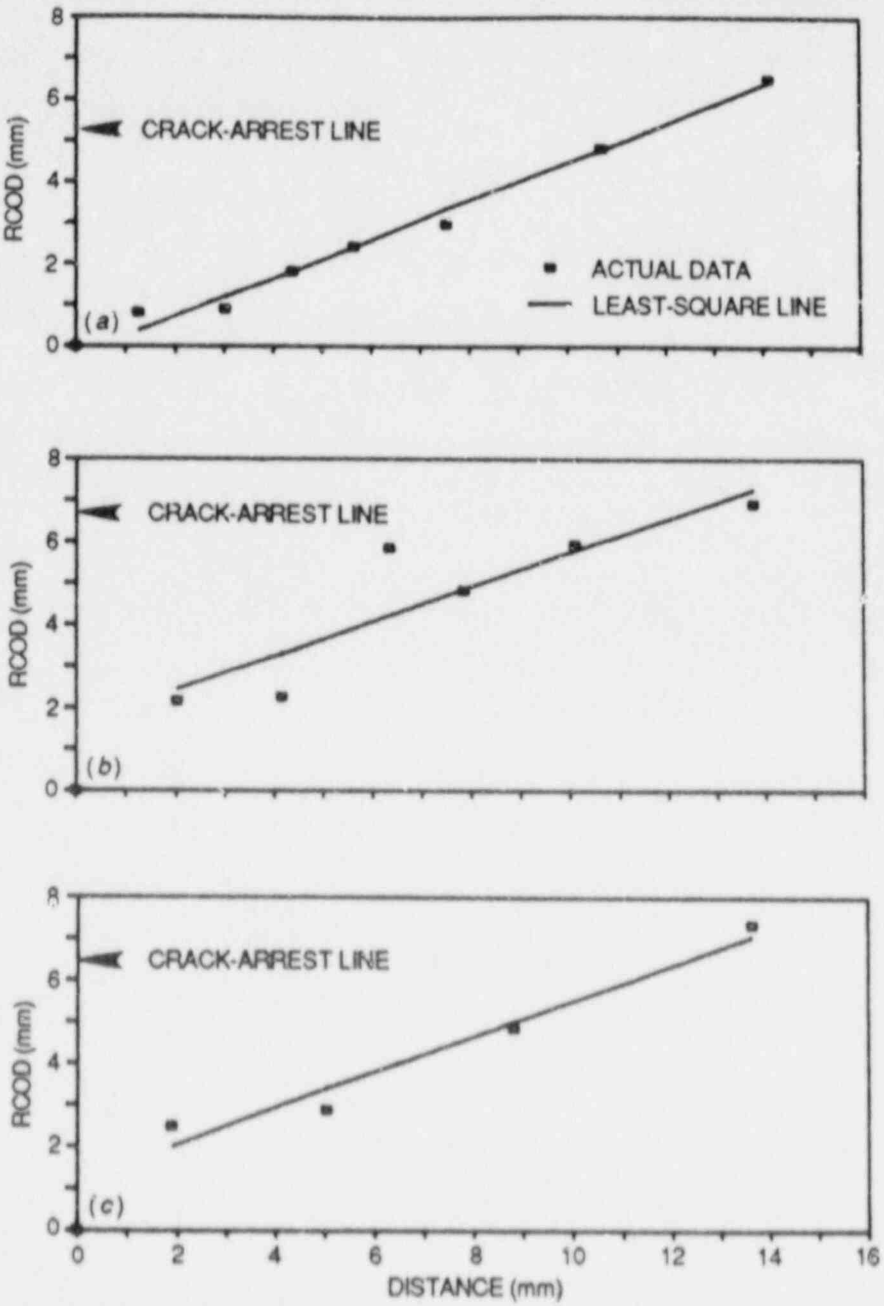

Fig. 2.26. RCOD vs distance from crack-arrest line for specimen WP-CE-1. (*a*) Line B1, (*b*) line B2, (*c*) line B3.

several ways to be a plausible rough approximation. The equation relating CTOD to K is

$$K^2 = E\,\sigma_Y \cdot \mathrm{CTOD}, \tag{2.1}$$

where

$\mathrm{CTOD} = 1.19 \times 10^{-3}$ m,

$E = 206 \times 10^3$ MPa,

$\sigma_Y = 517$ MPa (75 ksi).

Tensile test results for this wide plate are not yet currently available. From other A 533 grade B class 1 plate data, 517 MPa was selected as an intermediate value between the slow-load values for yield and ultimate strength. The resulting estimate of K is 356 MPa•$\sqrt{\text{m}}$. Reference 22 provides two dynamic-calculation estimates of K at crack arrest: 170 and 159 MPa•$\sqrt{\text{m}}$. No dynamic-program calculations of the reinitiation K are now available for this test. The large elevation of the reinitiation K above the K at crack arrest corresponds well to the elevation of the reinitiation K obtained in other tests by means of dynamic calculations that have provided both results.

A second comparison feature is provided by measurements after the test of plate-thickness reduction, as shown in Fig. 2.27. Here again, some averaging is necessary. The arrested crack-front curves across the plate thickness from a position (at 38 cm) where thickness reduction was ~0.5% to a position at 42 cm where thickness reduction was 2%. The average thickness reduction was assumed to be 1.5 mm. Unpublished experiments* in the 1960s at the Welding Institute in England (Ref. 23) and at Frankfurt Arsenal in Philadelphia indicated a direct proportionality between thickness reduction at the tip of a stationary crack and either measured values of CTOD or values of CTOD derived from the equation for K^2. The proportionality factor indicated that the thickness reduction and CTOD were of similar magnitude. Using the thickness reduction of 1.5 mm in place of CTOD in the K^2 equation gives a K-value for reinitiation of 400 MPa•$\sqrt{\text{m}}$. Although the uncertainties of both the topographic estimate of CTOD and the thickness-reduction estimates are large, the two estimates of reinitiation K have some value. They support other indications that a high K-value is necessary for the start of fibrous tearing from an arrested cleavage crack in the upper transition temperature range.

2.3.2.2 Specimen WP-1.7. A 152-mm-thick plate of A 533 grade B class 1 steel from ORNL was used for this test. The initial run-arrest event ended near the middle of the plate, where the plate temperature was 61°C. This event was followed immediately (7-ms pause) by a short

---

*Unpublished data on CTOD measurements in comparison with thickness reduction at the crack tip were obtained by F. M. Burdekin in 1963. These results suggest that CTOD would nearly equal thickness reduction.

ORNL PHOTO 3004-88

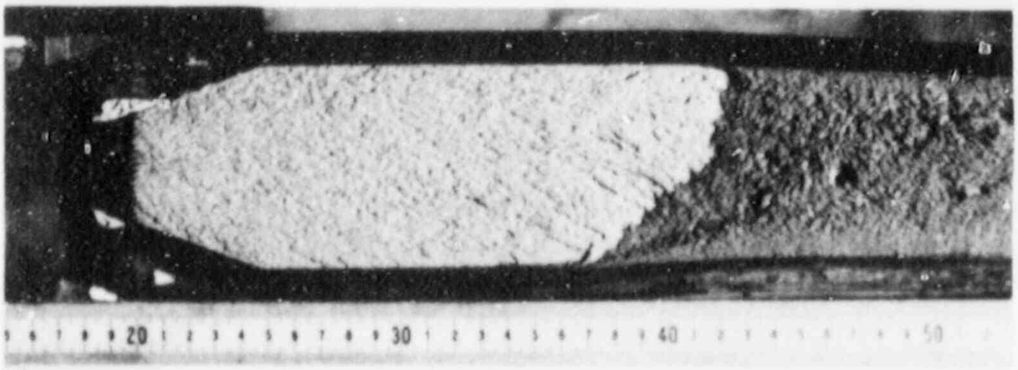

(*a*)

Fig. 2.27. Fracture surface and posttest reduction-in-thickness contours of WP-CE-1 specimen. (*a*) Fracture surface (scale on plate front surface), (*b*) posttest reduction-in-thickness contours.

segment of fibrous tearing that converted to cleavage. The second cleavage event was divided at midthickness because of the development of lamination-type tearing in that region. The optical topography study centered attention on the position where the first cleavage event arrested. Figure 2.28 shows this region of the test plate. Dashed lines show the measurement paths selected for height determinations. Three lines on

ORNL PHOTO 3005-88

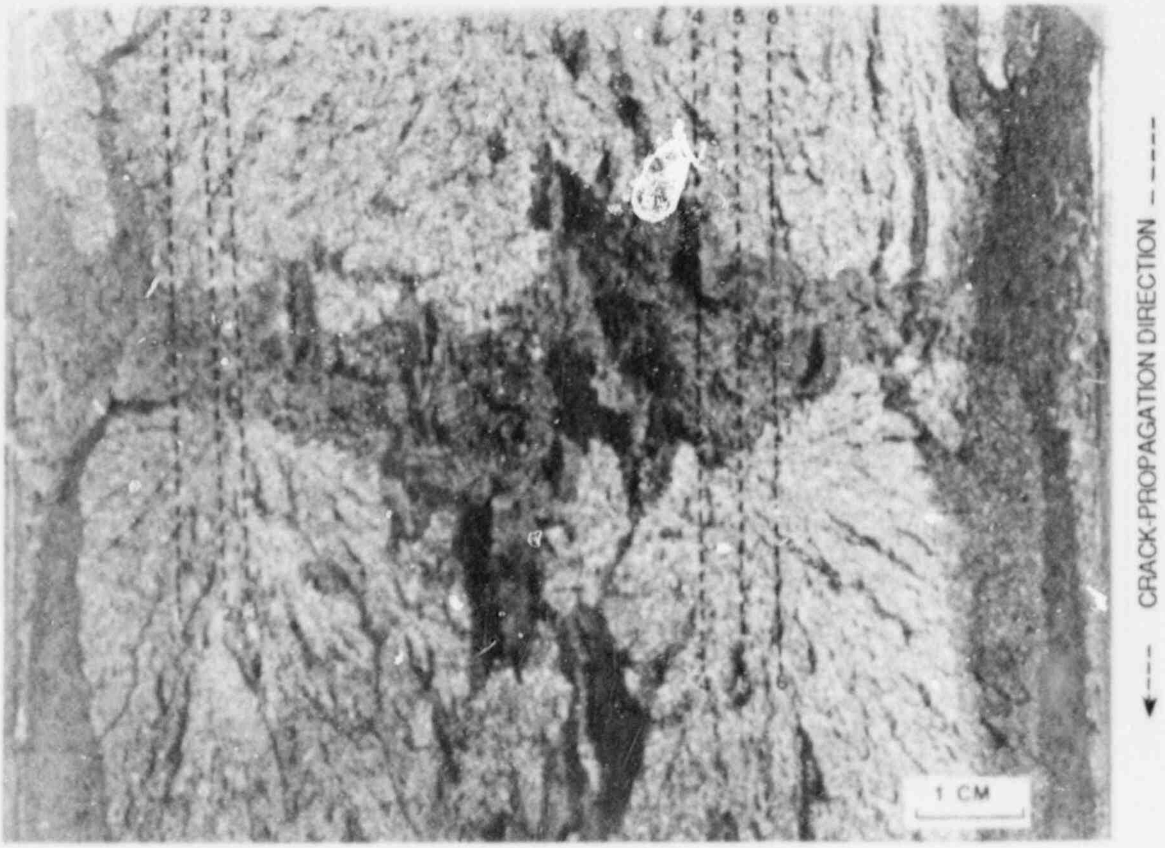

Fig. 2.28. Fracture surface of WP-1.7 specimen. Lines 1–6 show the location where relative height measurements were performed.

each side of midthickness were positioned to avoid the most pronounced midthickness surface irregularities.

Figure 2.29 shows the change of separation of the fracture surfaces in the same manner as shown for plate WP-CE-1. Determinations of RCOD values at cleavage positions very close to the start of fibrous tearing are shown in Fig. 2.30. Using the method of "least squares," straight lines through the fibrous separation positions gave CTOD values of 2.30, 0.81, 0.27, 0.66, 0.27, and 2.30 mm for lines 1 through 6, respectively. The average CTOD was 1.10 mm. Using Eq. (2.1), with $\sigma_Y = 517$ MPa + 138 MPa = 655 MPa and $E = 206 \times 10^3$ MPa, the CTOD for fibrous tear reinitiation corresponds to a K-value of 385 $\text{MPa}\cdot\sqrt{\text{m}}$. Values of 592 and 456 $\text{MPa}\cdot\sqrt{\text{m}}$ were the dynamic-analysis estimates for this reinitiation provided in Ref. 24.

Comparing the thickness-reduction measurements, as shown in Fig. 2.31, reveals that they differed considerably on the top and bottom halves of the plate at this crack-arrest location, ranging from slightly >2% to <1%. Using a rough average value of 1.25%, the thickness reduction was 1.91 mm. Setting CTOD equal to 1.91 mm in Eq. (2.1) results in a K-value of 508 $\text{MPa}\cdot\sqrt{\text{m}}$. (Note that 138 MPa was added to the slow-load value of σ_Y as an adjustment for rapid loading.)

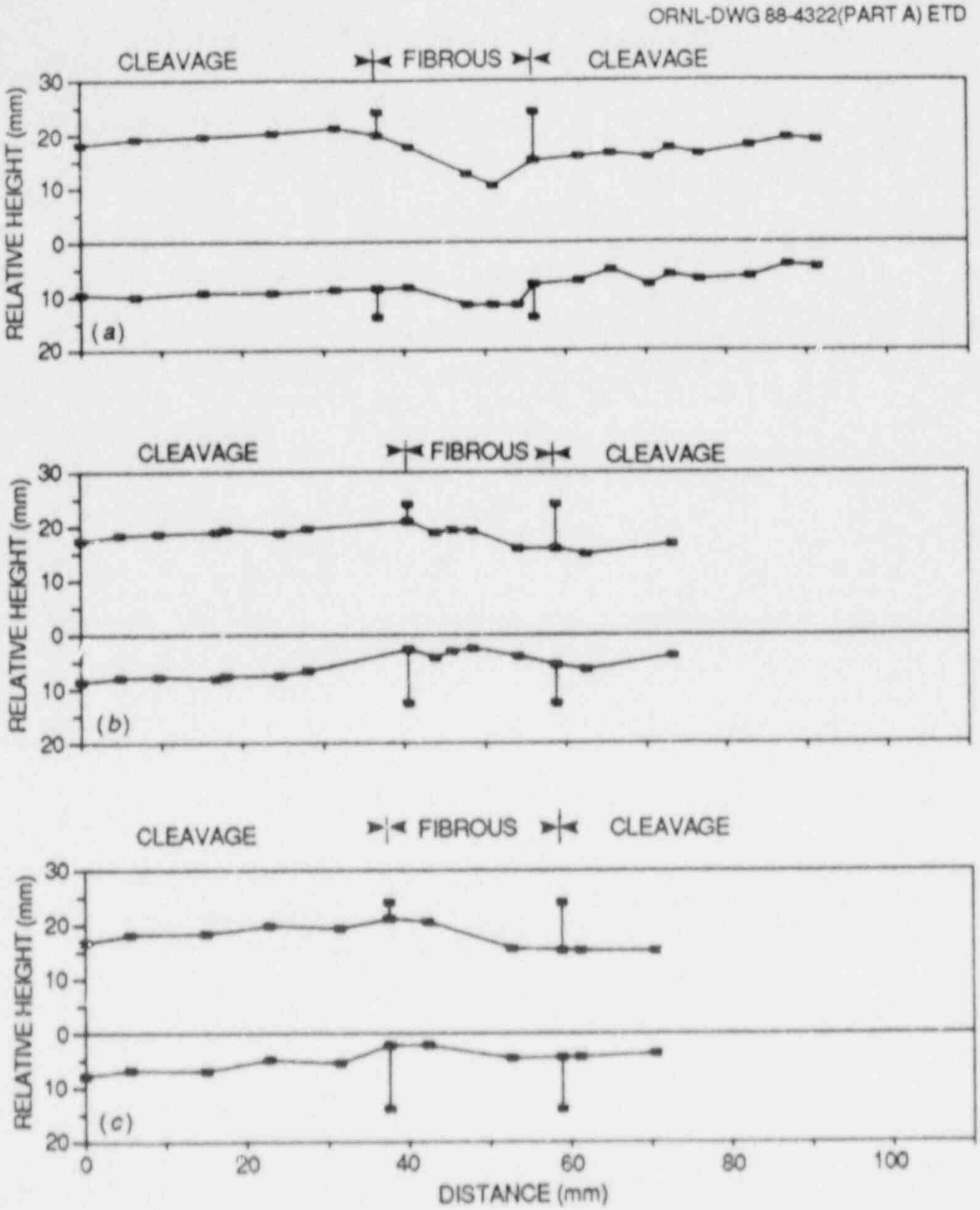

Fig. 2.29. Fracture surface contours along lines 1–6 in Fig. 2.28 for specimen WP-1.7. (*a*) Line 1-1, (*b*) line 2-2, (*c*) line 3-3, (*d*) line 4-4, (*e*) line 5-5, (*f*) line 6-6.

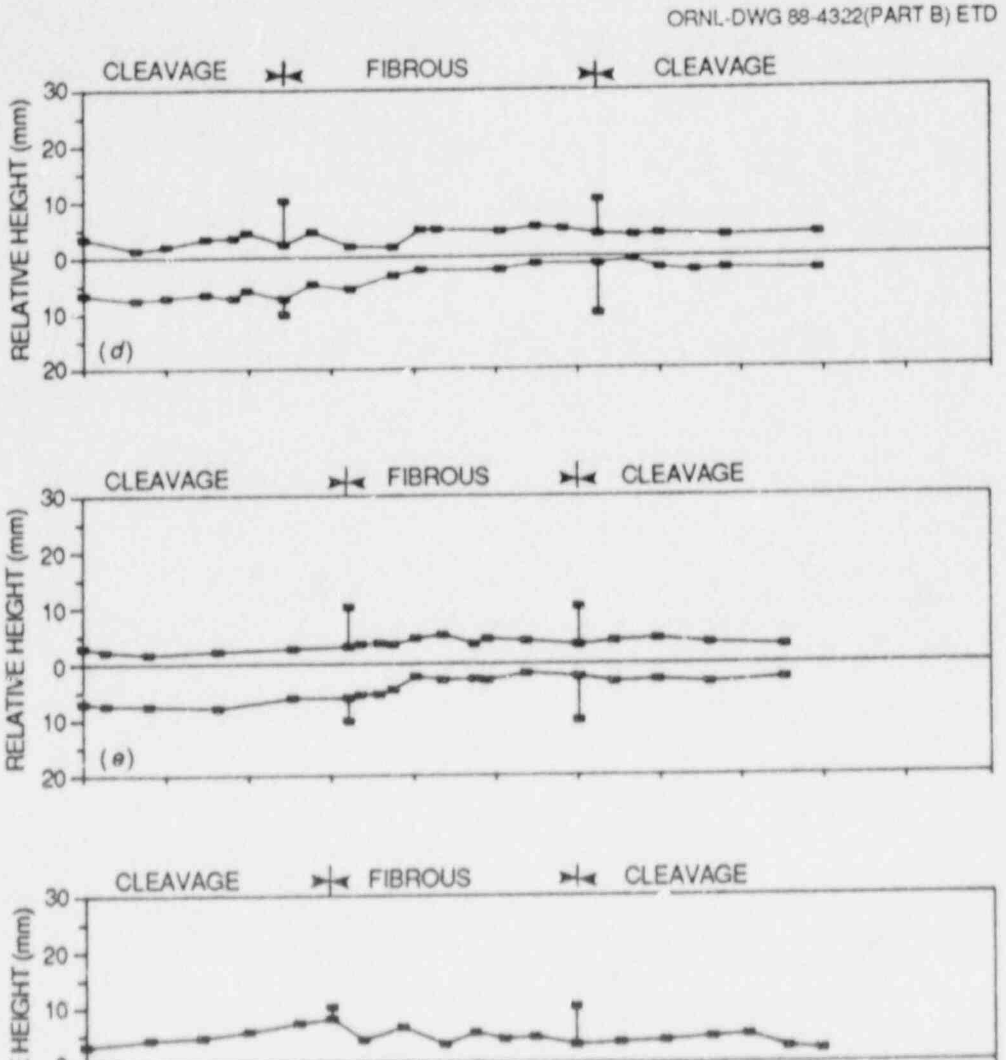

Fig. 2.29 (continued)

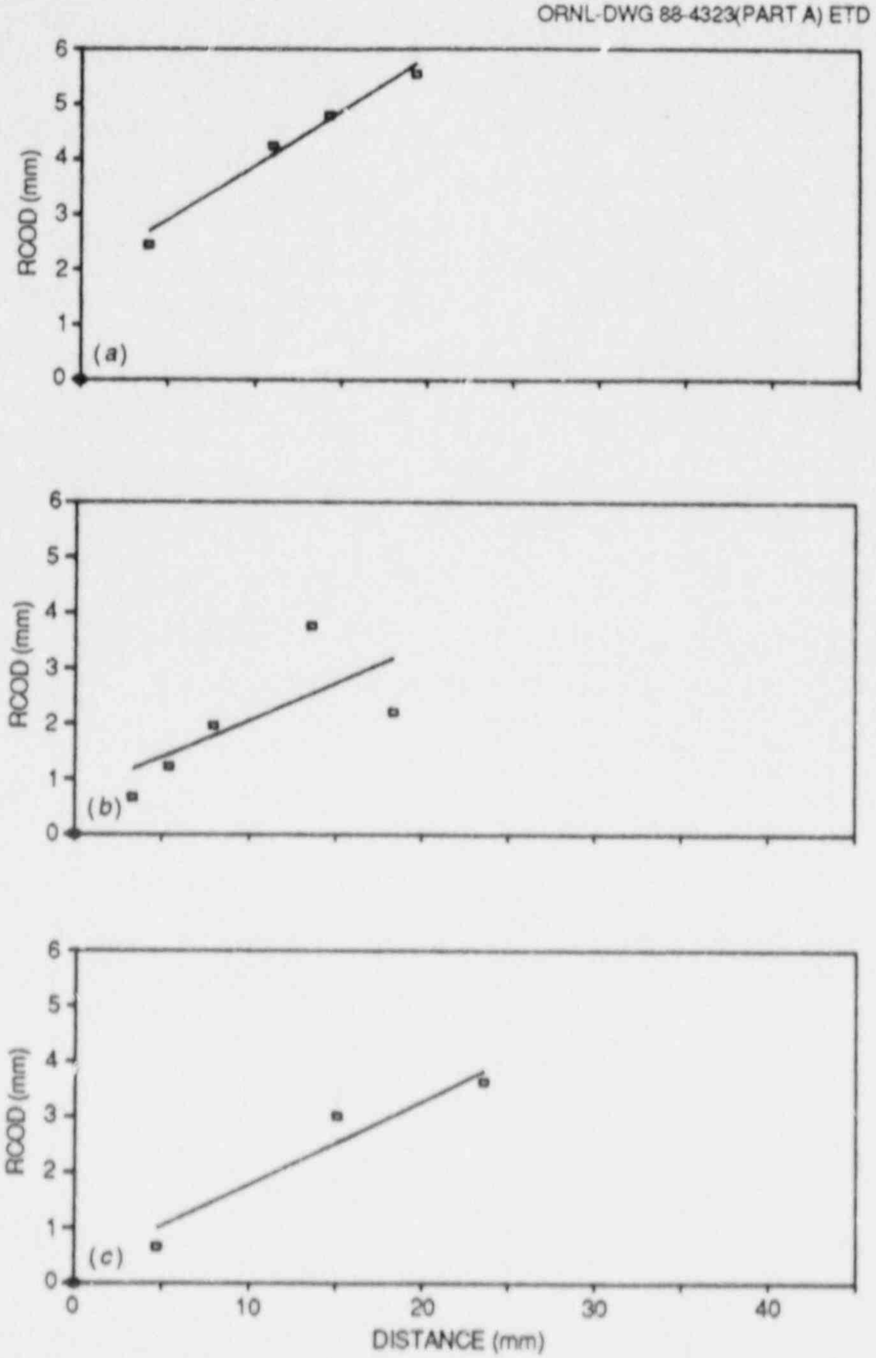

Fig. 2.30. RCOD vs distance from crack-arrest line within the fibrous region for specimen WP-1.7. (*a*) Line 1, (*b*) line 2, (*c*) line 3, (*d*) line 4, (*e*) line 5, (*f*) line 6.

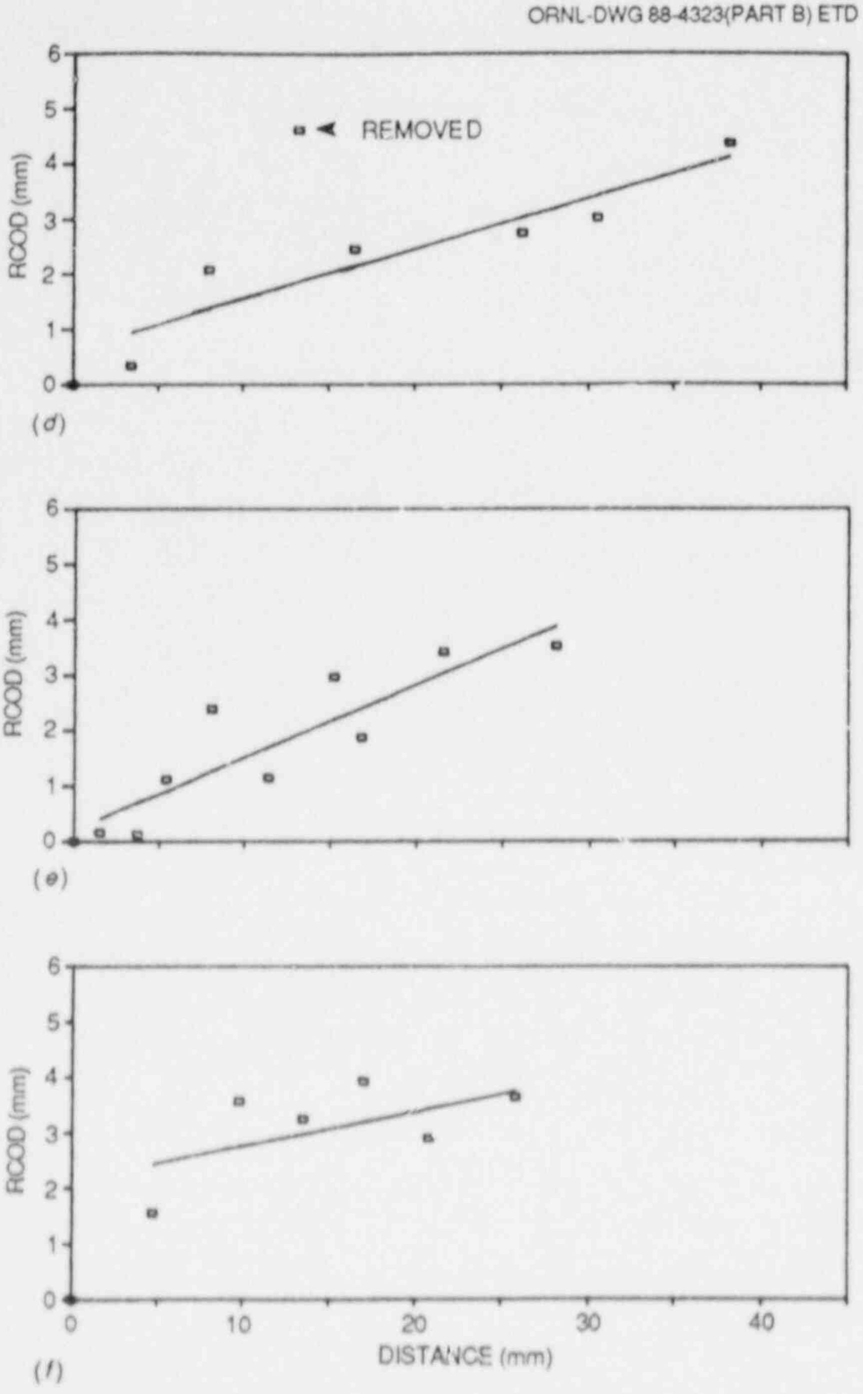

Fig. 2.30 (continued)

ORNL-DWG 88-4324 ETD

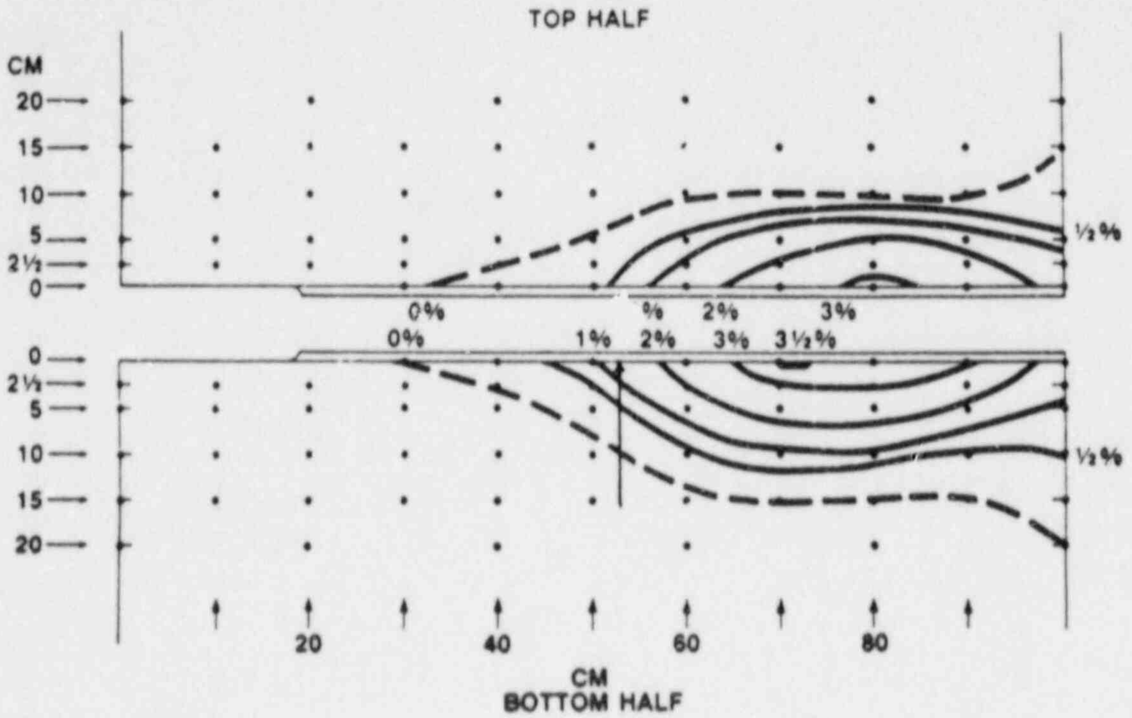

Fig. 2.31. Thickness reduction measurements for WP-1.7 specimen. (Measurements provided by R. Fields, NBS.)

Obviously, large uncertainties exist in the topographic estimates of K for cleavage reinitiation in this test plate, as they did for plate WP-CE-1. However, the uncertainty can be reduced substantially by improving the topographic mapping of the regions of interest. In addition, eliminating out-of-plane bending of specimens through electroslag welding can be expected to result in improved uniformity of the crack front. The possibility of obtaining useful estimates of K from plate-thickness reduction is also of special interest and deserves continued attention.

2.3.3 Dynamic crack initiation

Efforts to establish new methods of measuring crack-initiation toughness in reactor steels have followed two different lines of study, including explosively loaded notched short bars and impact-loaded notched round bars. A description of the status of both series of experiments follows.

2.3.3.1 Explosively loaded notched short-bar experiments. After using dynamic photoelasticity to establish the feasibility of explosively loading a short bar dog-bone specimen with four symmetric charges detonated simultaneously, the method was applied to steel specimens. The first specimens were made from 4340 steel that was heat treated to Rc of 51. In the first test, the amount of explosive used was excessive, and fracture occurred at the ends of the specimen as well as at the center. In the second test, the amount of explosive was reduced to about 8 g (2 g on each corner of the specimen). Strain-gage records were obtained, as indicated in Fig. 2.32. These records indicated that K_{Id} was 53.0 MPa•$\sqrt{m}$ and that failure began within 2 μs after the arrival of the strain wave. This value of dynamic-initiation toughness is about the same as that measured by Zehnder and Rosaskis[25] for 4340 steel with about the same hardness.

With progress made in developing the testing parameters for 4340 steel, attention was directed to specimens made from A 533 grade B class 1 steel. The material available was in blocks ~50 × 200 × 200 mm. The dog-bone specimen was redesigned to be made from three pieces cut from those blocks and included two identical end pieces and a center piece. These pieces were metal inert gas (MIG) welded together with series 70 wire to produce an extended bar, as shown in Fig. 2.33. The bar was extended to a length of 400 mm in the straight bar region to move the strain gages away from the explosive charges and to allow more time for the wave to propagate to the center notch. The additional time and distance is also beneficial in shielding the instrumentation from electrical noise at detonation and from the blast wave.

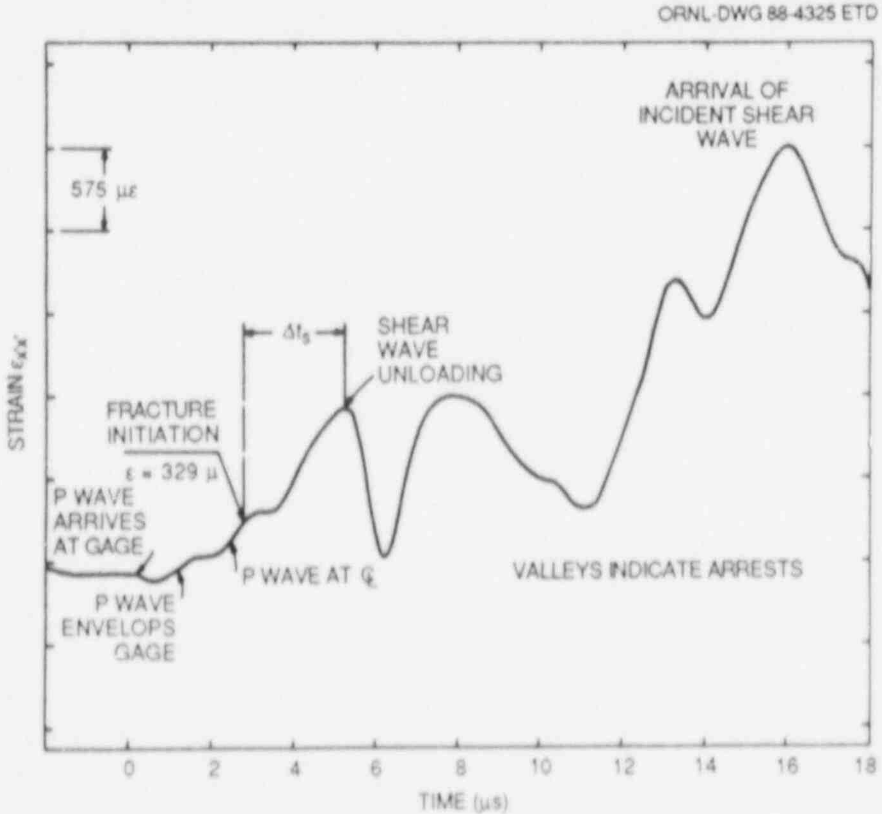

Fig. 2.32. Strain-time trace for the explosively loaded dog-bone specimen.

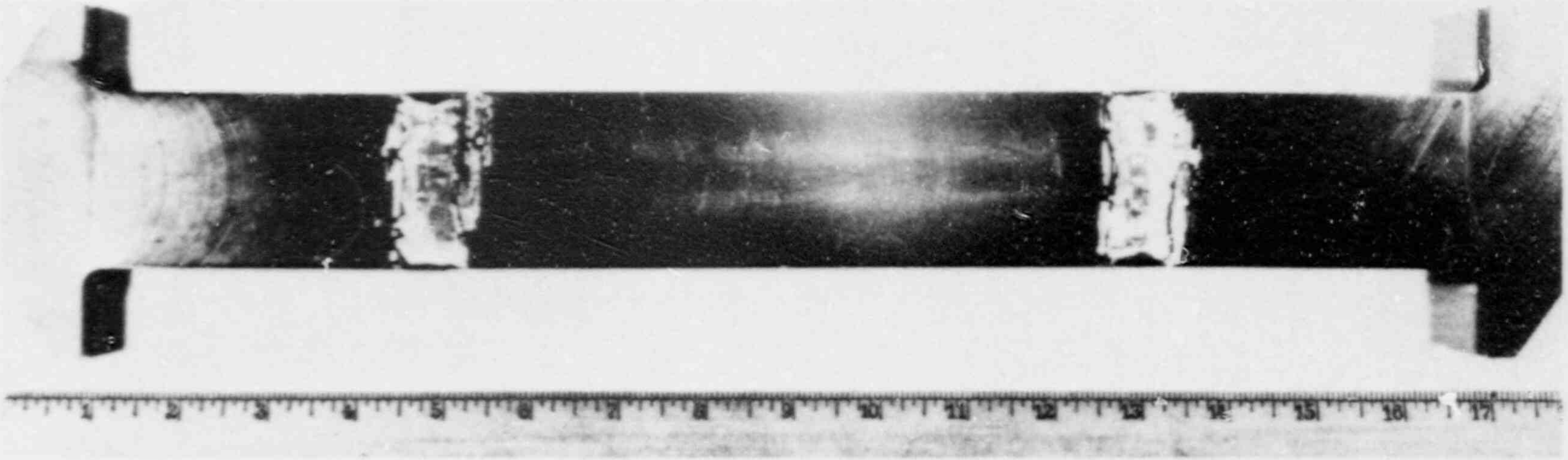
ORNL PHOTO 3006-88

Fig. 2.33. Extended dog-bone specimen fabricated from three pieces of A 533 grade B class 1 steel.

The center notch will be fatigue sharpened, and testing of the A 533 grade B class 1 steel under very high rates of loading will begin during the next report period.

2.3.3.2 Impact-loaded notched round-bar experiments. The impact-loading device used with the notched round-bar specimens can introduce nominal strains of 0.0014 into the large-diameter region of the bar. The nominal strain rate approaches 20/s. The actual strains and strain rates at the notch are much higher because of the 4/1 area ratio and because of the large strain concentration that occurs at the tip of the root radius. Initial tests indicated that the notched bar would not fail with a full height drop of 1.78 m when the root radius was 0.13 mm. No attempt was made to machine a sharper radius; instead, the notch was sharpened by loading the bar in axial compression. Loads of 55×10^3 kg were imposed on the A 508 specimens, causing the center region of the bar to yield and the walls of the notch in the local region of the root radius to close together. The localized yielding action produced a pseudocrack about 0.3 mm deep, as indicated in Fig. 2.34.

Five specimens made from the A 508 steel with compression-formed pseudocracks were tested in axial impact. In all of the tests, loading was accomplished by dropping the 58.6 kg weight a distance of 1.78 m. All five specimens failed, and data were obtained that permitted the determination of K_{Id}. The results obtained are shown in Table 2.5. The values of K_{Id} show remarkable consistency when compared with more conventional forms of fracture-initiation testing. This finding was surprising because data from the six strain gages mounted on the notched round bar showed considerable deviation. However, when four to six gage readings were averaged and this average strain at fracture initiation was used to determine K, the results were repeatable. The largest deviation was with Test No. 4, which had a dynamic-initiation toughness of 66 $\text{MPa}\cdot\sqrt{\text{m}}$. The strain-gage records in this test were atypical and indicated that initiation was followed by arrest rather than by a complete rupture of the reduced section. The fracture surface of this specimen will be analyzed in

ORNL PHOTO 3007-88

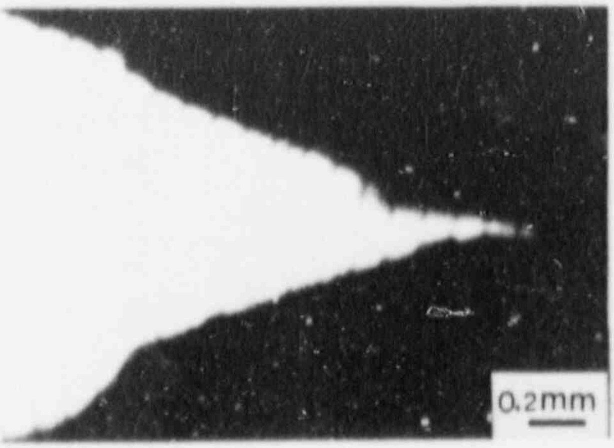

Fig. 2.34. Profile image of notch tip showing the development of a pseudocrack by axial compression.

Table 2.5. Dynamic initiation toughness in A 508 steel at 20°C

Test No.	K_{Id} (MPa·$\sqrt{m}$)
1	51.2
2	49.6
3	50.9
4	66.0
5	52.0
Average	53.9

more detail. Initial fracture examination at UM showed excessive notch closure and transverse, rather than concentric, crack extension.

As these five specimens were tested over an extended period, improvements were made in the instrumentation system used to record the strain-gage signals. These improvements included installing better grounding to reduce noise, providing a single gate to trigger all six channels of data at the same instant, and reducing the time resolution to 100 ns. As these improvements were incorporated, some unusual dynamic behavior in the strain-time traces was observed. Several of these records are being examined to better understand the dynamics of the specimen just before and immediately after crack initiation. Apparently, it is possible to observe premature pop-ins and arrest before the main fracture initiation. It is also possible to observe some effects of stress-wave propagation in the specimen caused both by the loading wave and the unloading waves produced by initiation.

2.3.3.3 Fractographic analysis. An extensive analysis of the fracture surface of specimen DWIT-4 (Test No. 3) was performed to characterize the crack tip, the initiation site, and the degree of cleavage before and after initiation. A typical strain-time record for this specimen, shown in Fig. 2.35, indicates two premature pop-ins (at B and C) before the major initiation leading to failure at D.

An optical fractograph of the fracture surfaces of the specimen is presented in Fig. 2.36. The fracture surface is planer and was contained and controlled by the notch. A ridge near the center of the surface is caused by intersecting cracks that have propagated along different planes. Much better detail of the fracture-surface features can be observed in the SEM fractograph presented in Fig. 2.37. A large number of cleavage-initiation regions, ~50, are identified by the small white dots located about the periphery of the bar along the pseudocrack tip. Only a few of these many initiation sites were of importance in developing the running crack. The two main cleavage-initiation regions, indicated by the letters A and B, are located 120° apart. The cracks formed at these two sites propagated in the directions shown by the small white arrows.

ORNL-DWG 88-4326 ETD

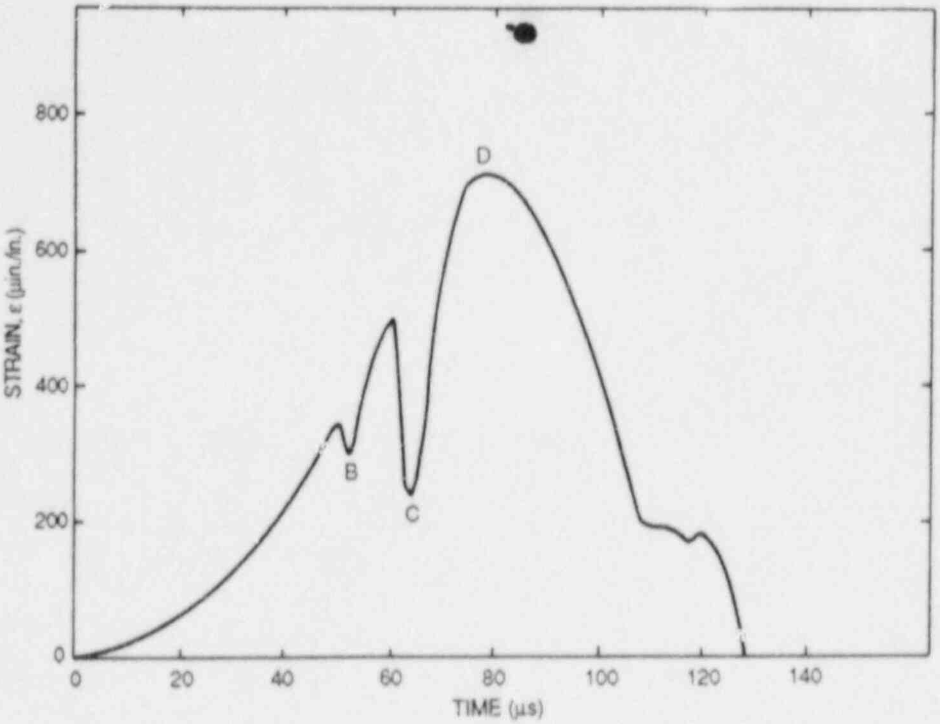

Fig. 2.35. Strain-time record for gage T-2 from specimen DWIT-4.

ORNL PHOTO 3008-88

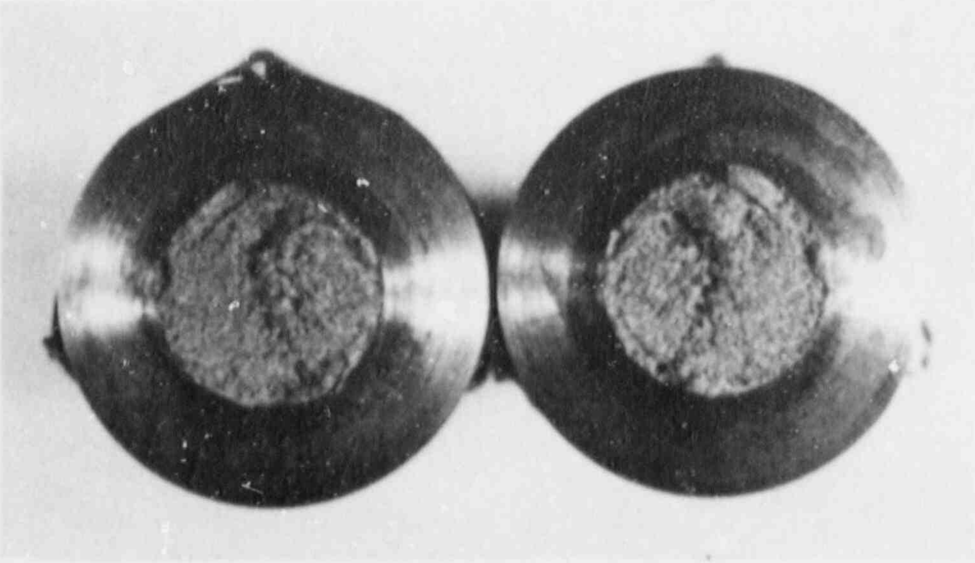

Fig. 2.36. Optical fractograph of fracture surface of specimen DWIT-4.

ORNL PHOTO 3009-88

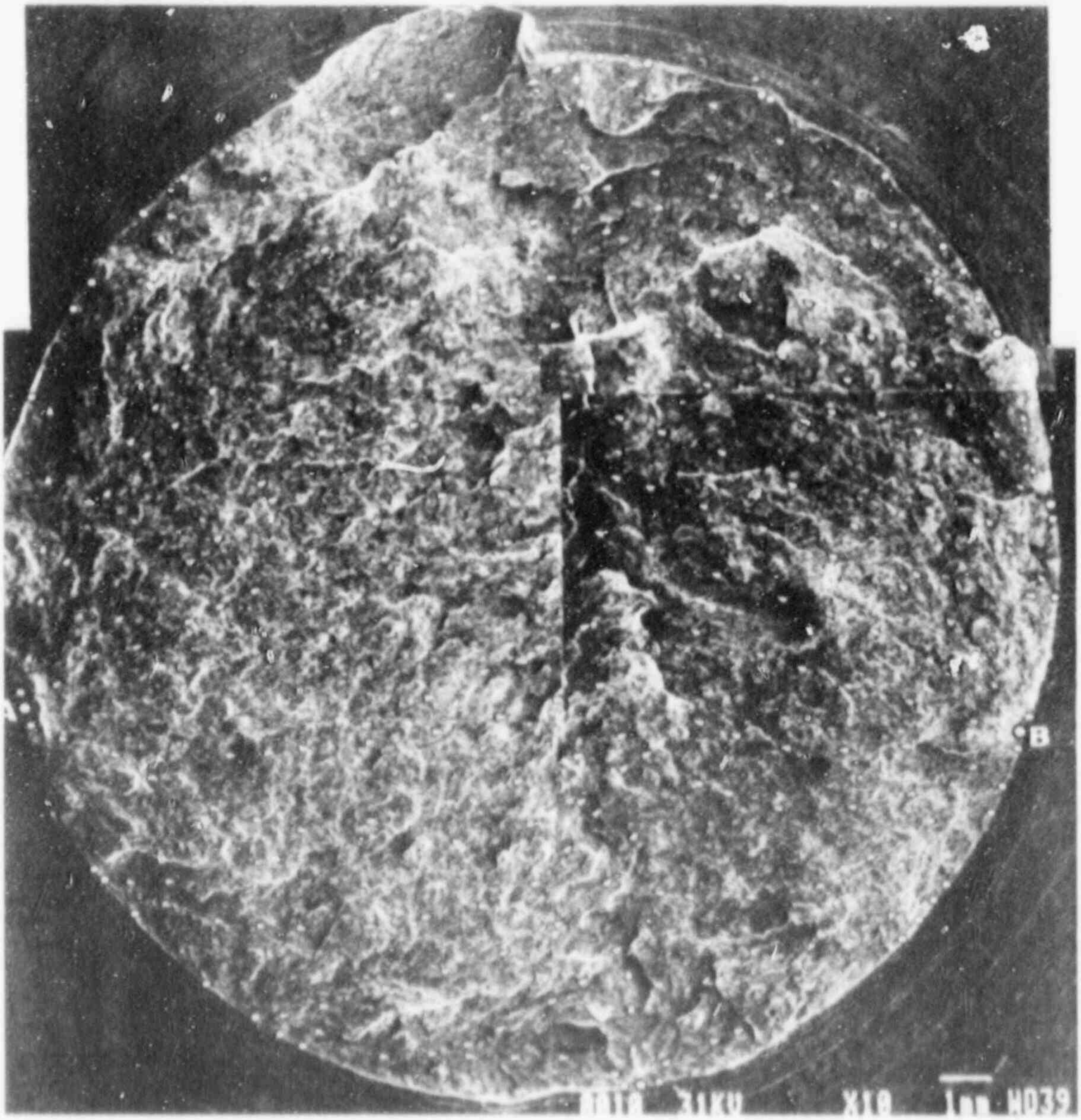

Fig. 2.37. SEM fractograph of fracture surface of specimen DWIT-4. Numerous cleavage initiation regions along the precompression crack tip are indicated by dots, among which A and B are main initiation regions. Crack propagation directions are indicated by arrows.

These two major cracks joined near the center of the specimen, forming the ridge most easily observed in Fig. 2.36. The pseudocrack is clearly evident in Fig. 2.37. It is the dark annular band about the circumference of the specimen. It is of uniform depth (0.5 mm) about the entire circle, indicating good control of the specimen deformation in the axial compression loading.

Detail features of initiation region B are presented in Fig. 2.38 with two SEM fractographs. In Fig. 2.38(*a*), three dominant characteristics are evident. The first of these is the precompressed zone that formed the pseudocrack. The second is a stretched and ductile fracture zone ~50 μm deep. The third is a cleavage zone that extends over the remainder of the fracture surface. Where the stretched and ductile zone meets the cleavage zone, initiation region B is identified within the square. Figure 2.38(*b*) presents an enlargement of this square and clearly locates the initiation site with its adjacent cleavage planes. The surface features of the stretched and ductile fracture zone show evidence of plastic deformations in this localized region.

A similar set of SEM enlargements corresponding to fracture initiation region A is presented in Fig. 2.39. The stretched and ductile fracture zone is larger and more irregular for this region, as shown in Fig. 2.39(*a*). The ductility is achieved by void formation and hole coalescence. The initiation region, again located within the square, occurs where the ductile fracture zone meets the cleavage zone. The cleavage-initiation origin located at position x in Fig. 2.39(*b*) indicates that the micromechanics of the initiation process is associated with particle clump rupture.

2.3.3.4 Future plans. Twenty notched round-bar specimens are now being machined from A 533 grade B class 1 steel and will be tested under impact loading. The temperature will be varied in these tests to determine the change in the initiation toughness from the lower to the upper shelf.

Further work will characterize the dynamic behavior of the specimen and develop a systematic method to interpret the strain-time traces. A formal paper describing the loading system, instrumentation method, data analysis, specimen dynamics, and fractographic analysis will be prepared.

Experiments will be conducted with the explosively loaded dog-bone specimens of A 533 grade B class 1 steel with the objective of achieving failure in <10 μs.

2.3.4 Numerical studies at UM

Numerical studies performed at UM during this reporting period have continued to focus on two areas: (1) determining and validating appropriate crack-tip velocity vs dynamic stress-intensity factor vs temperature relations using measured data from the WP-1 and other test series of A 533 grade B class 1 steel, and (2) investigating triaxial constraint and the transition from plane-stress to plane-strain-yielding conditions in the crack-tip region.

2.3.4.1 Dynamic fracture-propagation relations for A 533 grade B class 1 steel. Although often unknown or poorly defined for many materials, the relationship between instantaneous crack-tip velocity $\dot{a}$, dynamic stress-intensity factor K, and temperature T is a primary input for predictive "application mode" dynamic-fracture finite-element codes. An estimate of this relationship for A 533 grade B class 1 steel, as inferred from posttest "generation mode" dynamic-fracture analyses of tests WP-1.2, WP-1.3, WP-1.5, and WP-1.6, is presented in Ref. 26. Application-

ORNL PHOTO 3010-88

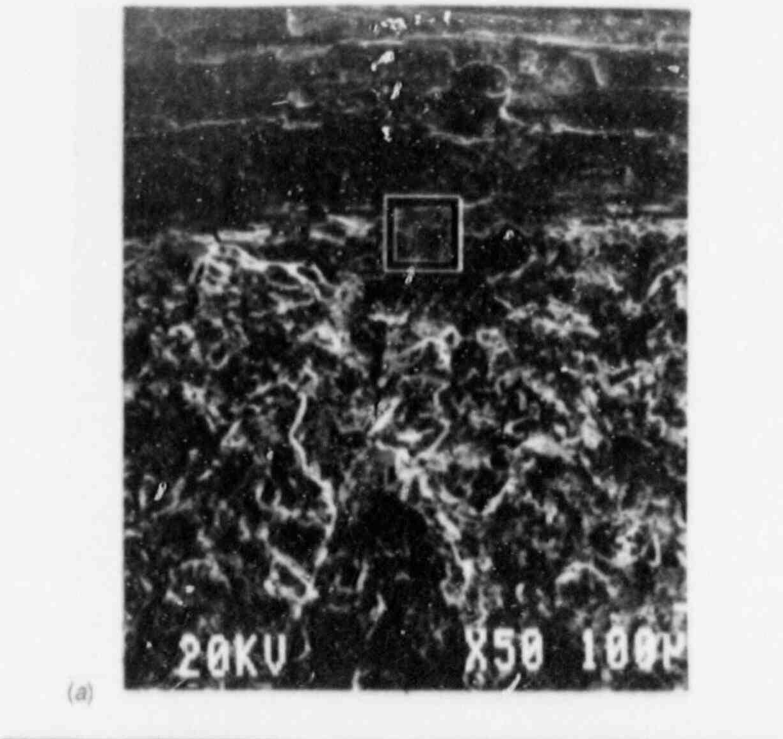

Fig. 2.38. SEM fractographs of cleavage initiation region B (indicated in Fig. 2.37). (*a*) Low magnification SEM fractograph showing the precompression zone (width about 0.5 mm), stretch and ductile fracture zone, and a cleavage initiation region (box area); (*b*) the enlargement of the box area in (*a*) showing ductile fracture zone with a width of about 50 µm and the cleavage initiation origin (x) located at the edge of the ductile fracture zone.

ORNL PHOTO 3011–88

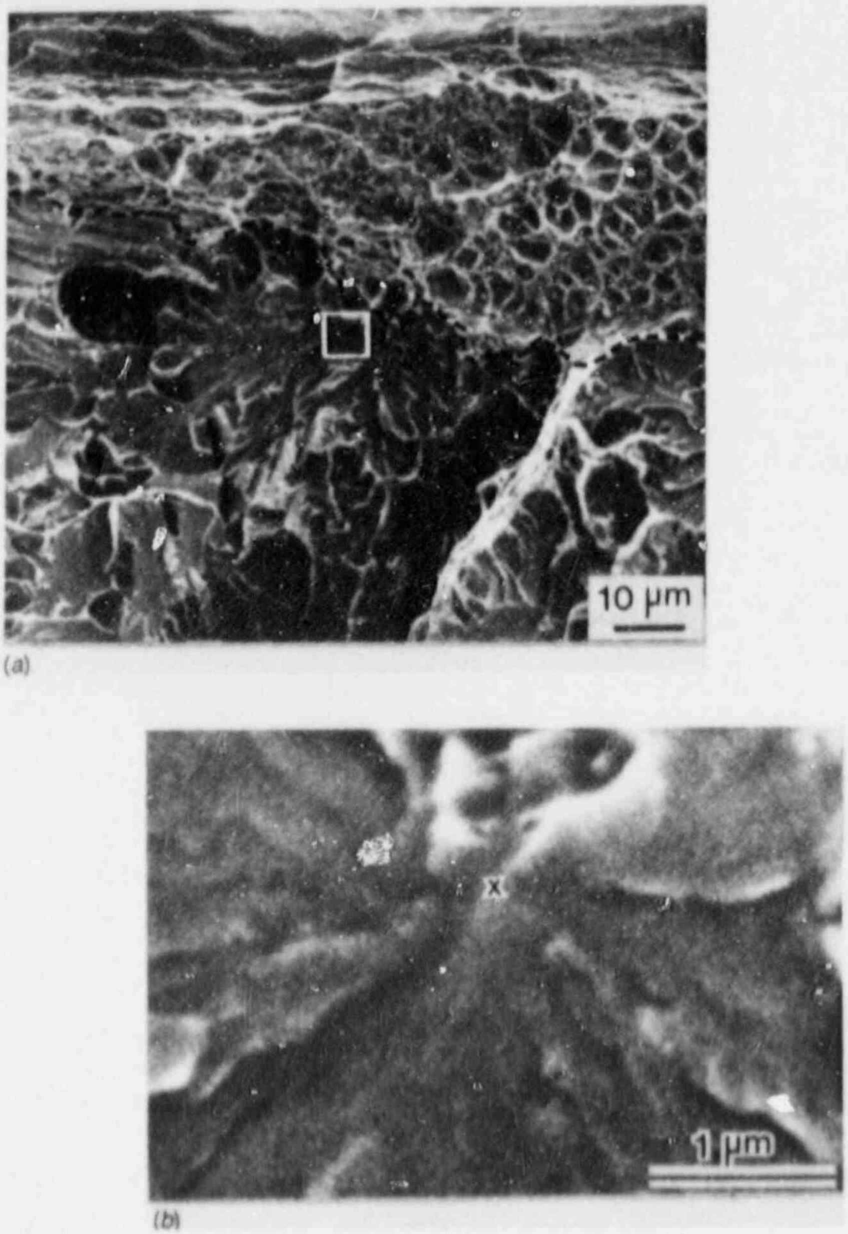

Fig. 2.39. SEM fractographs of cleavage initiation region A (indicated in Fig. 2.37). (*a*) SEM fractograph showing a narrow hole-joining fracture band and a cleavage initiation region (box area), (*b*) an enlargement of box area in (*a*) showing that the cleavage initiation origin (x) is adjacent to a particle clump.

mode analyses of these same tests using the inferred $\dot{a}$ vs K vs T relationship were found to produce results acceptably close to experimental and generation-mode analytical values.

Additional validation of the proposed $\dot{a}$ vs K vs T relationship is now in progress. Application-mode analyses using the proposed relationship have been completed for the 0.15-m-thick WP-1.7 test, and the results are now being interpreted. Similar analyses will also be performed for the recently completed WP-1.8 test (which was also 0.15 m thick). Data from these two tests were not used to infer the $\dot{a}$ vs K vs T relationship and thus provide a fair test of the relationship, at least for the wide-plate test geometry. Validation studies of other specimen geometries are also planned; in particular, data from the small-scale "stub-panel" test specimens at ORNL will be analyzed.

2.3.4.2 Investigation of triaxial constraint and yielding in the crack-tip region. Triaxial constraint effects and the transition from plane-stress to plane-strain-yielding conditions in the crack-tip region are being investigated through a series of fine-mesh static nonlinear three-dimensional (3-D) analyses of a single crack in an infinite plate. The target element size for the analyses is 1/20 of the specimen thickness.

Because of the enormous number of calculations in these fine-mesh analyses, a computationally efficient combined boundary-element—finite-element formulation has been developed for these studies. Finite elements, which are advantageous for modeling nonlinear material behavior, are used in the nonlinear near-crack-tip regions; boundary elements, which are very advantageous for modeling linear infinite-boundary domains, are used to represent the far-field conditions. This combined formulation permits very fine mesh discretization in the crack-tip region of interest without the overhead of massive numbers of elements and degrees of freedom in the far field. Details of the combined boundary-element—finite-element formulation are presented in Refs. 27 and 28.

Although the fundamentals of the combined boundary-element—finite-element formulation are relatively straightforward, several difficulties have been encountered in its application to the 3-D near-crack-tip fracture problem:

1. The boundary-element formulation for the far-field region is for two-dimensional (2-D) plane-stress conditions; this formulation must be mated to the 3-D finite-element formulation for the near crack-tip region. Inaccuracies caused by this dimension mismatch should be negligible provided that the interface between the finite-element and boundary-element regions is far enough from the crack-tip region. Work by Parsons, Hall, and Rosakis (Ref. 29) for linearly elastic conditions suggests that placing the interface at a distance of one plate thickness from the crack tip should be sufficient; parametric studies designed to verify this suggestion are under way.
2. The traction-free crack faces within the far-field region must be discretized by boundary elements extending from the interface between the finite-element—boundary-element regions to the symmetry line (for mode I fracture) at the center of the crack. However, the crack

faces themselves lie along a symmetry line, creating serious numerical instabilities for the boundary elements along this line. Solutions under investigation for this problem include extending the near-field finite-element region back to the center of the crack.

3. The boundary-element far-field formulation complicates bandwidth optimization for the global stiffness matrix. Modifications to the bandwidth optimization algorithms are being investigated to minimize this problem.

These difficulties with the combined boundary-element—finite-element formulation are surmountable, and work on them is under way. Nevertheless, a parallel but separate approach to the problem has been initiated based solely on a conventional finite-element formulation. This parallel approach, which necessitates coarser meshes than desired and a finite-specimen geometry, will be used to perform scoping analyses and to generate preliminary findings while the difficulties with the combined formulation are resolved.

2.3.5 Acknowledgments

Computational resources for this work were provided partly by the San Diego Supercomputer Center, which is administered and operated by GA Technologies, Inc. with major funding from the National Science Foundation.

2.4 High Strain Rate Testing of A 533 Grade B Class 1 Steel at Various Temperatures

A. Gilat*

2.4.1 Introduction

The mechanical behavior of A 533 grade B class 1 steel at high rates of deformation in pure shear is being studied. Tests have been conducted at strain rates of ~800 and 5000 s^{-1} and at temperatures of 20, −60, and −150°C. The results summarized below show that both temperature and strain rate have a significant effect on the material response.

2.4.2 Experimental procedure

The torsional split-Hopkinson bar technique is used for the tests. In this technique, a short material specimen (thin-walled tube) is placed between two bars, as shown schematically in Fig. 2.40. The specimen is loaded by a torsional wave that is generated in the input bar. To generate the wave, a torque is stored in the section between the clamp and the

---

*Engineering Mechanics Department, Ohio State University, Columbus, Ohio.

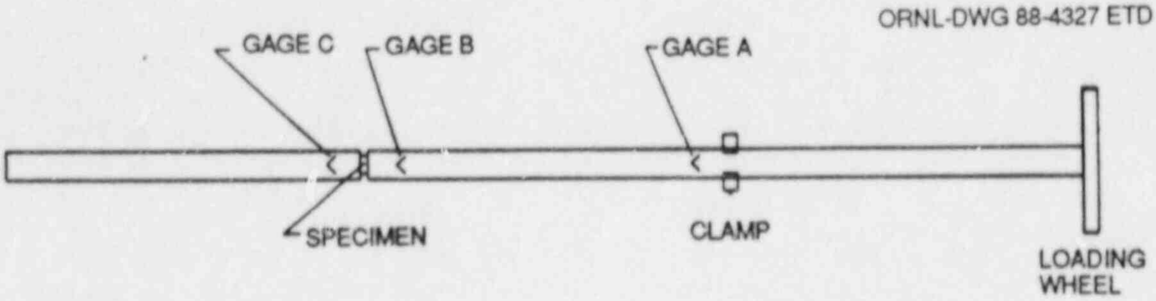

Fig. 2.40. Schematic diagram of torsional split-Hopkinson bar, used in high-strain-rate tests of A 533 grade B class 1 steel.

loading wheel by first tightening the clamp and then turning the loading wheel by a hydraulic system of cables and pulleys. When the clamp is released, a torsional wave propagates toward the specimen. Once the specimen is loaded, part of the loading wave reflects back to the input bar and the remainder is transmitted to the output bar. The history of the load and deformation in the specimen is determined by monitoring the stress waves in the bars that remain elastic during the test. A drawing of the specimen is shown in Fig. 2.41. The specimen itself is the thin-walled tube machined in the middle section. The outside diameter of the flanges on both sides of the specimen is selected so that the impedance of the flanges will match that of the input and output bars. This match ensures a smooth propagation of the waves without reflections. The flanges are glued to the bars with TRA-CON 2106T epoxy. A detailed description of the torsional split-Hopkinson bar technique and the equations used in the analysis of a test are given, for example, in Ref. 30.

In the low-temperature tests, a small chamber is placed around the specimen, and liquid nitrogen is sprayed into the chamber. The temperature is measured with a thermocouple that touches the inner wall of the specimen.

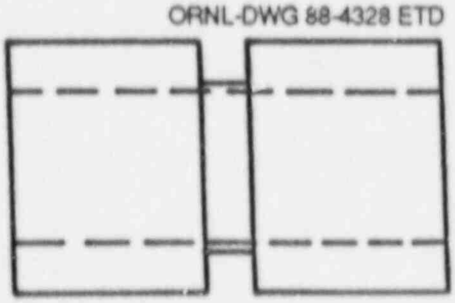

Fig. 2.41. Specimen for the torsional split-Hopkinson bar tests of A 533 grade B class 1 steel.

2.4.3 Results and discussion

Details of 16 successful tests are summarized in Table 2.6. As an example of data obtained in a test, the wave signals recorded at the three gage locations shown in Fig. 2.40 for test OR-22 are shown in Fig. 2.42. The records show a rise time of <50 μs in the input wave. The history of the strain rate in the specimen, obtained by manipulating the recorded signals, is shown in Fig. 2.43. For all of the tests listed in Table 2.6, the stress-strain curves are shown in Figs. 2.44–2.49.

Table 2.6. Summary of test conditions for high-strain-rate tests of A 533 grade B class 1 steel

Experiment No.	Shear strain rate (s^{-1})	Temperature (°C)
OR-16	5000	20
OR-17	4900	20
OR-18	850	20
OR-19	790	20
OR-20	900	20
OR-22	5000	20
OR-27	900	−60
OR-28	5100	−60
OR-29	5000	−60
OR-32	850	−60
OR-33	950	−150
OR-35	910	−150
OR-36	5000	−150
OR-37	5000	−150
OR-38	5000	−150
OR-39	5000	−60

The effects of strain rate and temperature on the flow stress are shown in Figs. 2.50–2.53. In these figures, the data from all of the tests are presented in shear-stress vs shear strain-rate diagrams. The effects of the temperature are also shown separately in Figs. 2.54 and 2.55, which present the lower-yield stress as a function of temperature for tests at strain rates of 800 and 5000 s^{-1}, respectively.

The following two major observations can be made from examining the test results.

1. The material response is affected by the strain rate, and the strain-rate sensitivity increases as the strain rate increases. At room temperature, for example, the lower-yield stress increases by 45 MPa

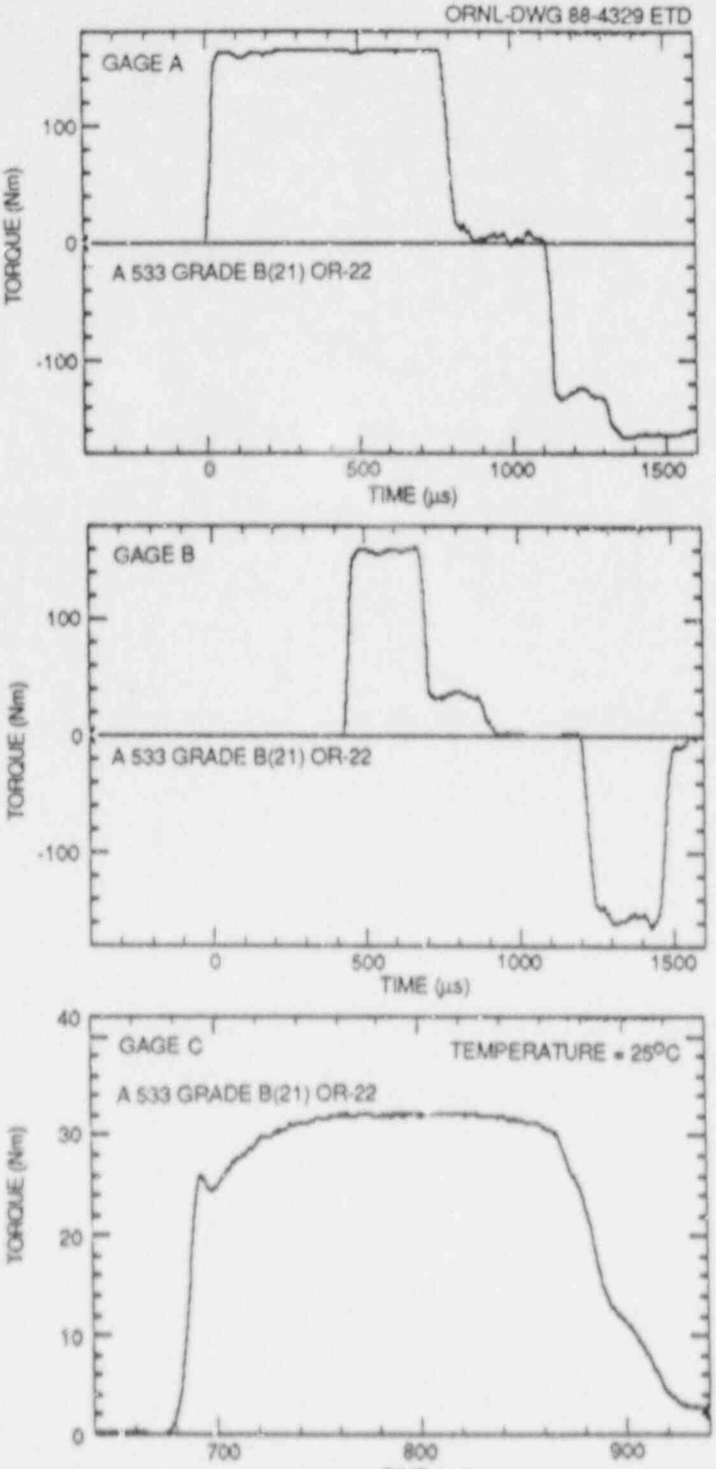

Fig. 2.42. Recorded waves at three gage locations on torsional split-Hopkinson bar (A, B, and C in Fig. 2.40).

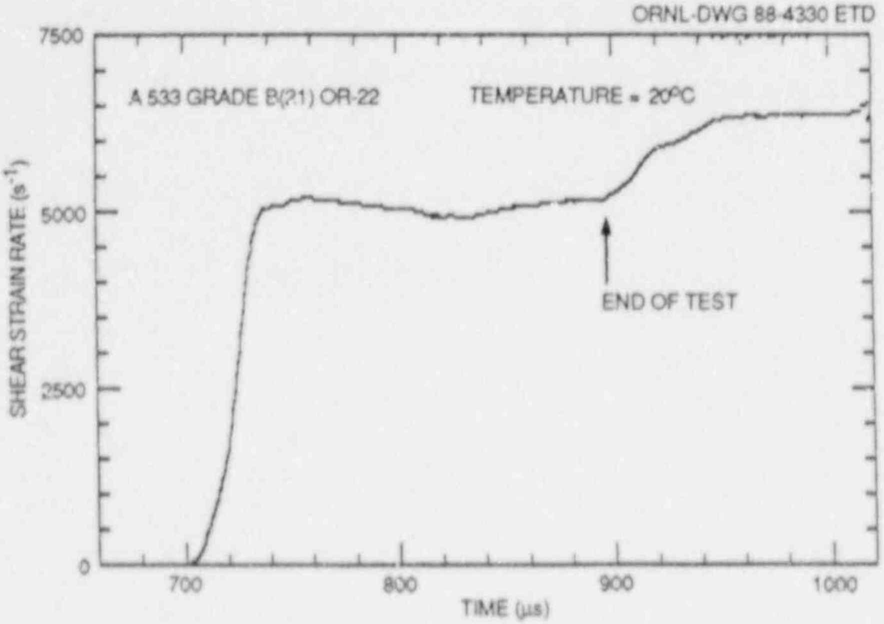

Fig. 2.43. History of strain rate in specimen of A 533 grade B class 1 steel tested at strain rate of 5000 s^{-1} and temperature of 20°C.

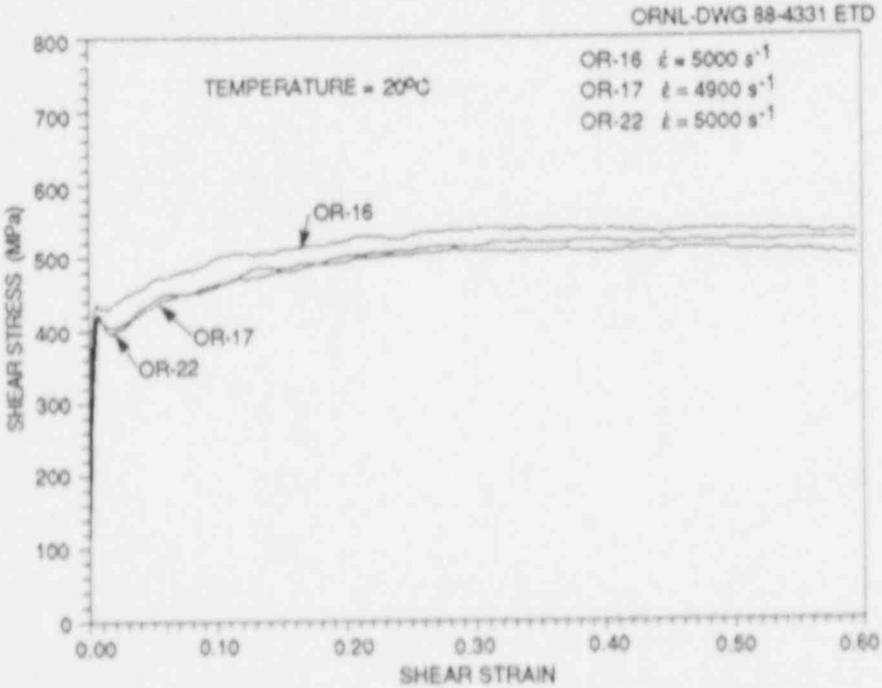

Fig. 2.44. Shear stress-shear strain curves for specimens of A 533 grade B class 1 steel tested at nominal strain rate of 5000 s^{-1} and temperature of 20°C (tests OR-16, -17, and -22 in Table 2.6).

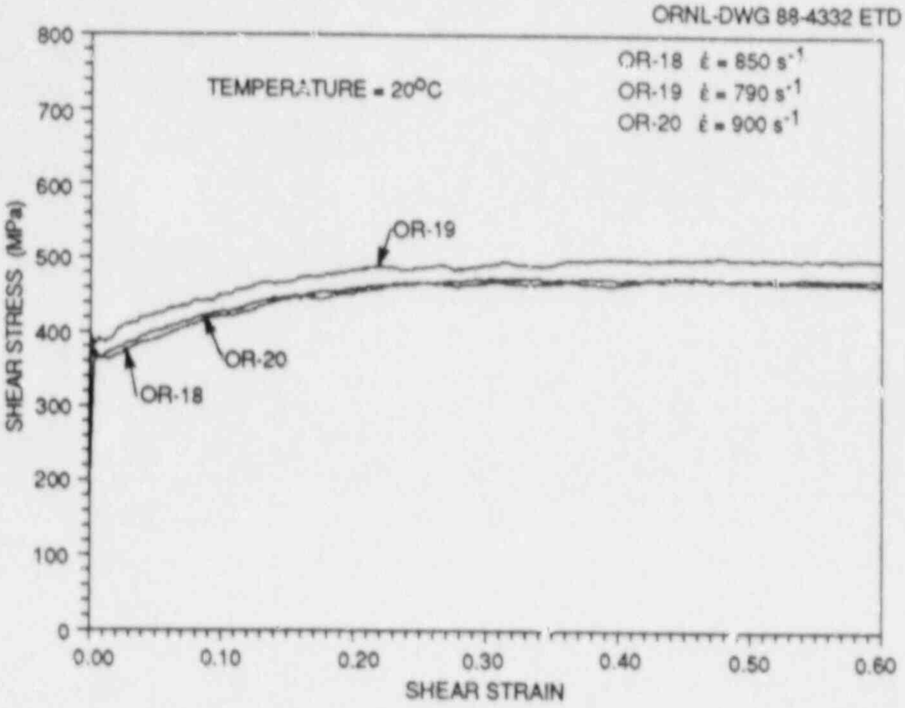

Fig. 2.45. Shear stress-shear strain curves for specimens of A 533 grade B class 1 steel tested at nominal strain rate of 800 s^{-1} and temperature of 20°C (tests OR-18, -19, and -20 in Table 2.6).

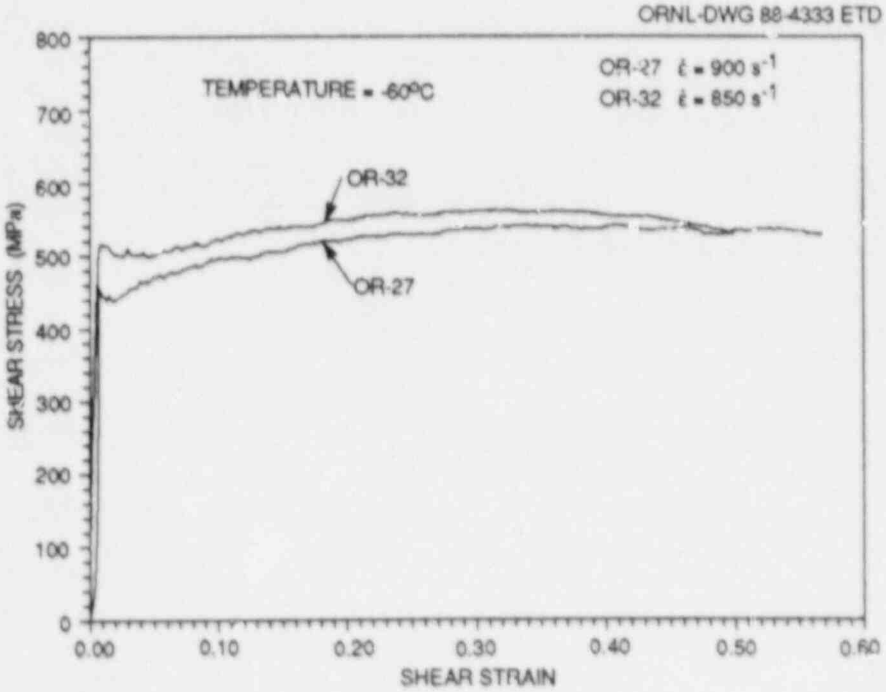

Fig. 2.46. Shear stress-shear strain curves for specimens of A 533 grade B class 1 steel tested at nominal strain rate of 800 s^{-1} and temperature of −60°C (tests OR-27 and -32 in Table 2.6).

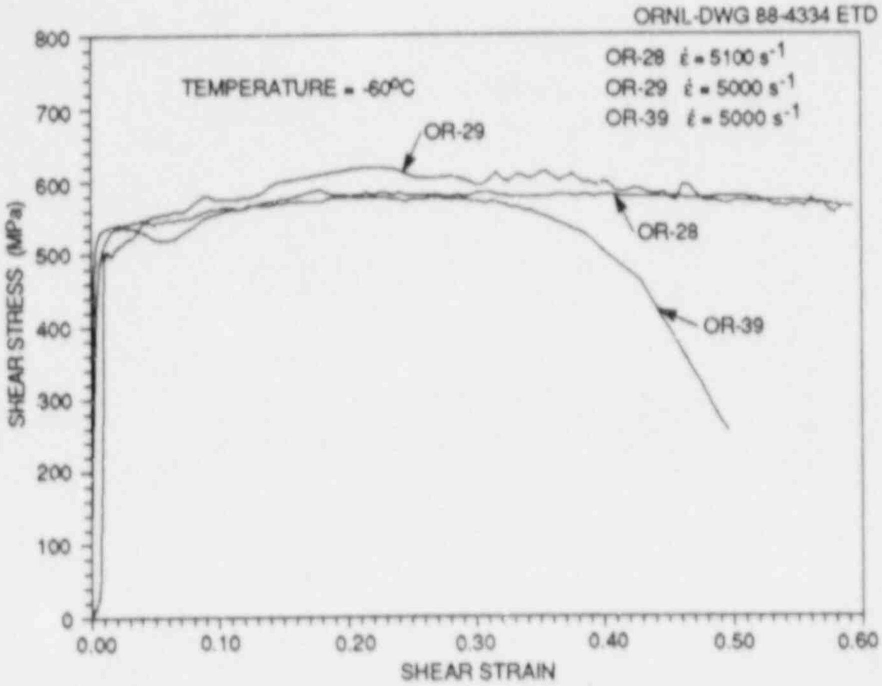

Fig. 2.47. Shear stress-shear strain curves from specimens of A 533 grade B class 1 steel tested at nominal strain rate of 5000 s^{-1} and temperature −60°C (tests OR-28, -29, and -39 in Table 2.6).

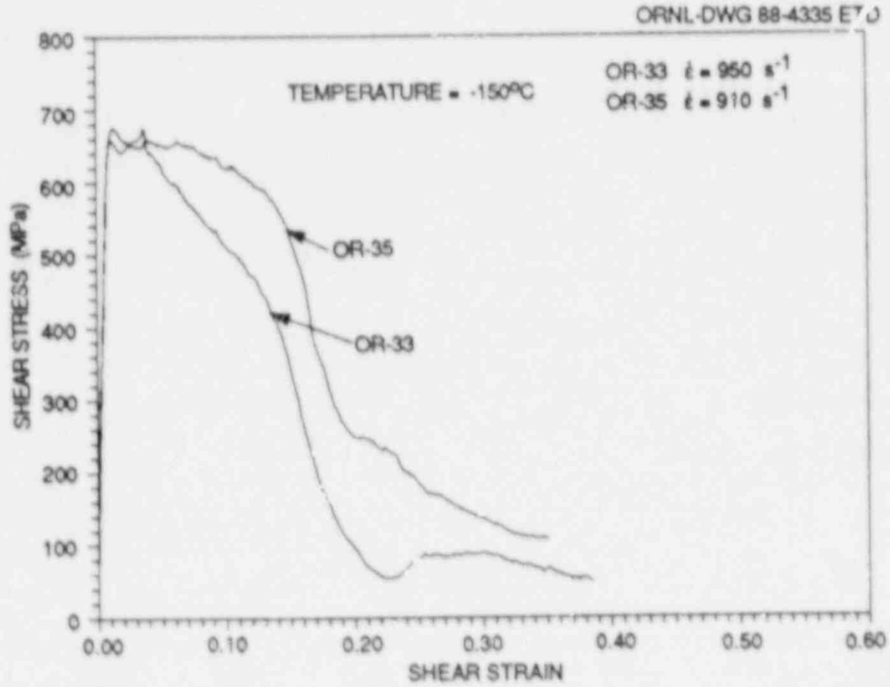

Fig. 2.48. Shear stress-shear strain curves from specimens of A 533 grade B class 1 steel tested at nominal strain rate of 800 s^{-1} and temperature of −150°C (tests OR-33 and -35 in Table 2.6).

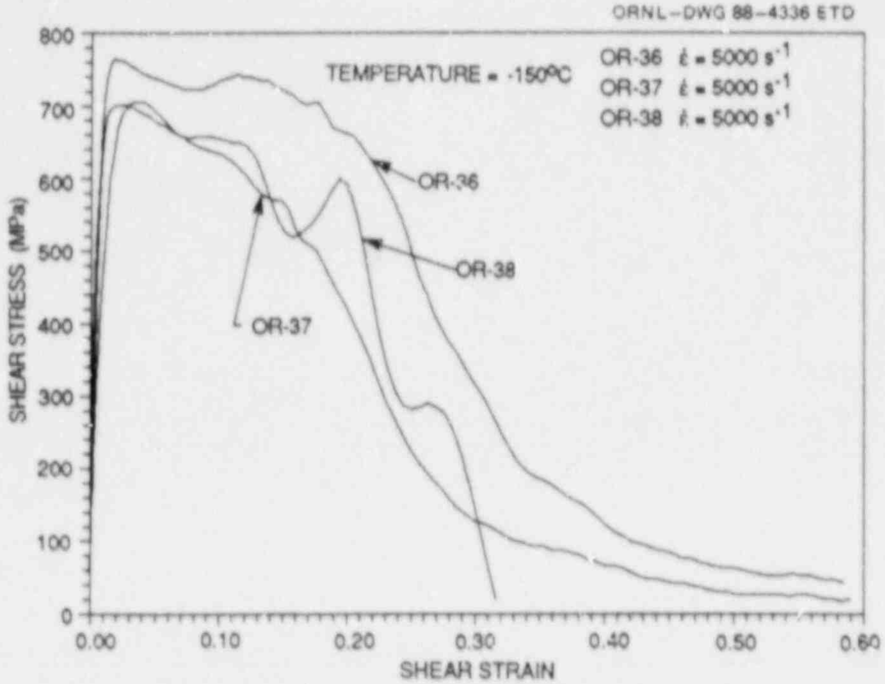

Fig. 2.49. Shear stress-shear strain curves from specimens of A 533 grade B class 1 steel tested at nominal strain rate of 5000 s^{-1} and temperature of −150°C (tests OR-36, -37, and -38 in Table 2.6).

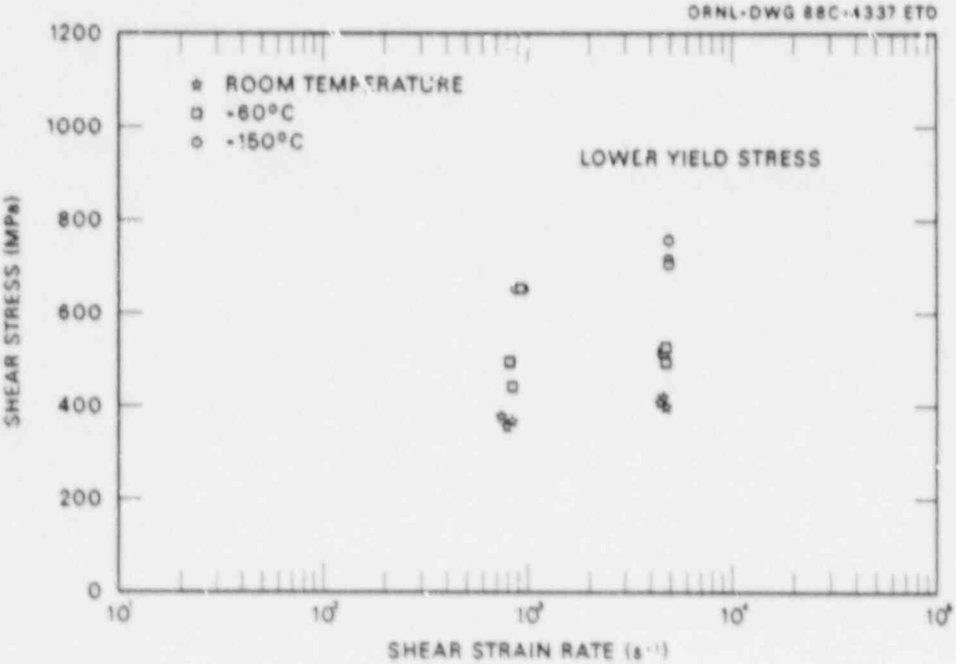

Fig. 2.50. Variation of lower yield stress with strain rate for A 533 grade B class 1 steel.

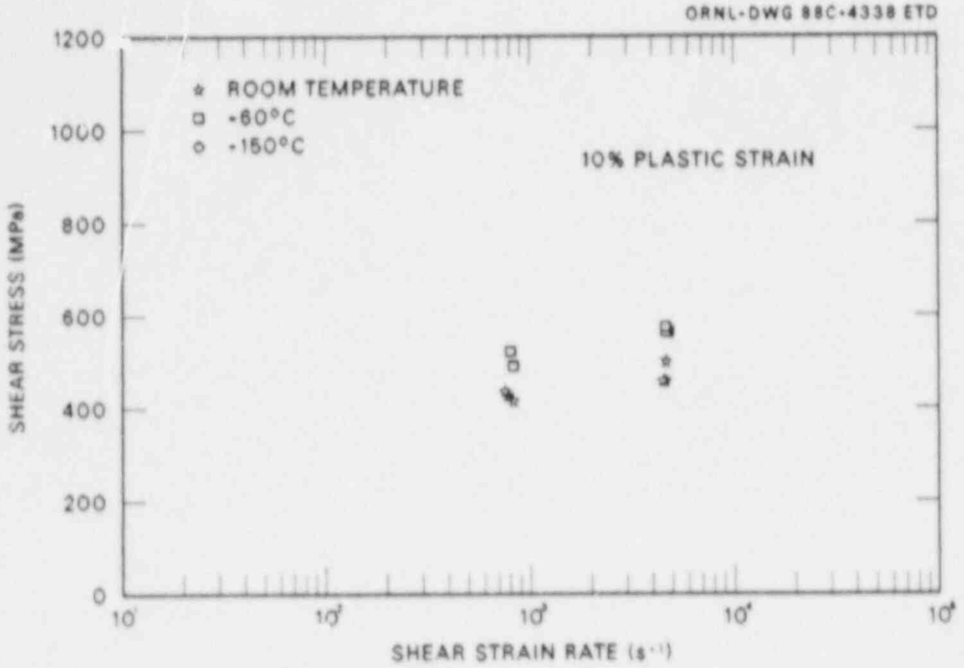

Fig. 2.51. Variation of shear stress with strain rate at 10% plastic strain for A 533 grade B class 1 steel.

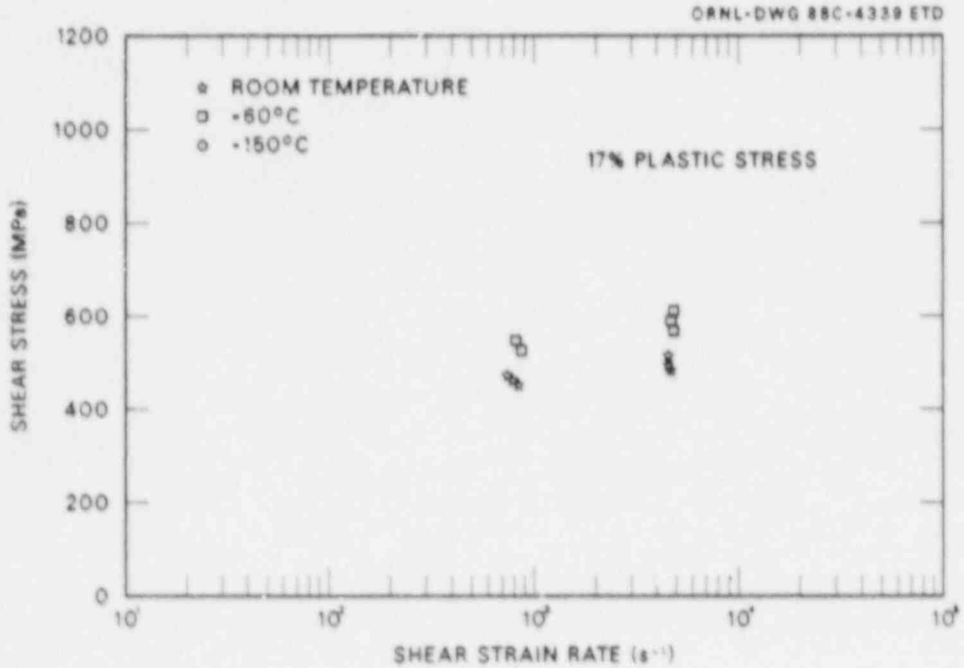

Fig. 2.52. Variation of shear stress with strain rate at 17% plastic strain for A 533 grade B class 1 steel.

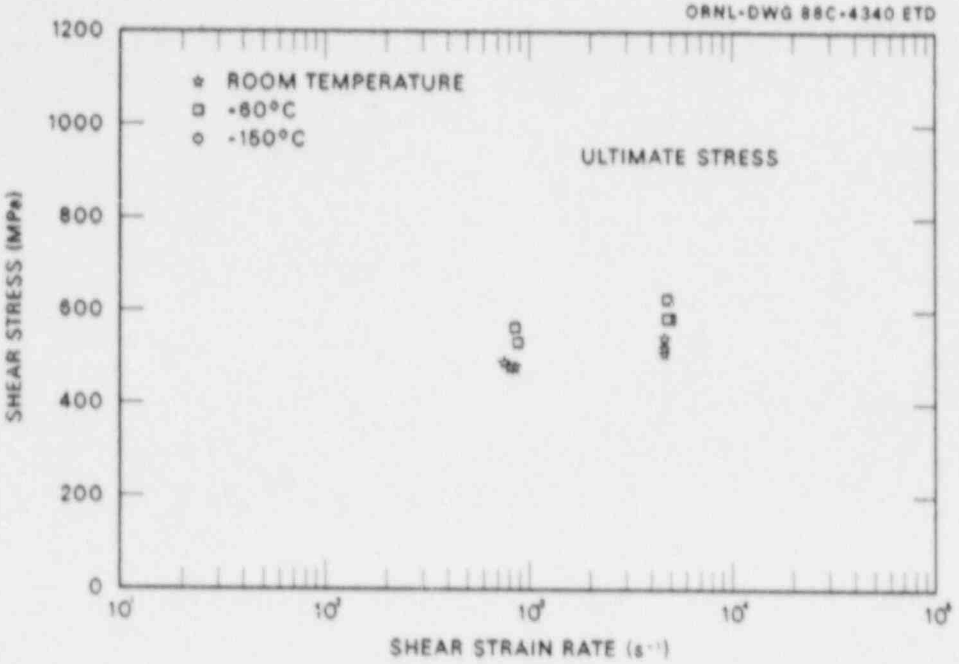

Fig. 2.53. Variation of ultimate shear stress with strain rate for A 533 grade B class 1 steel.

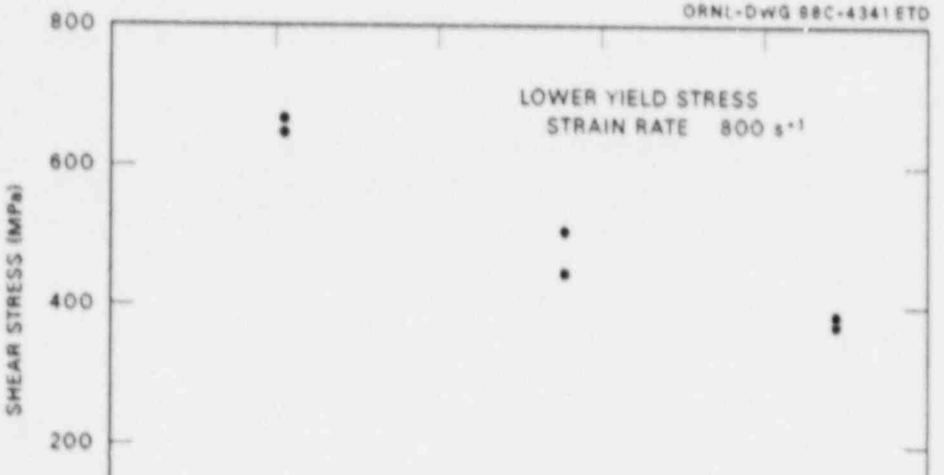

Fig. 2.54. Variation of lower yield stress with temperature for A 533 grade B class 1 steel tested at strain rate of 800 s^{-1}.

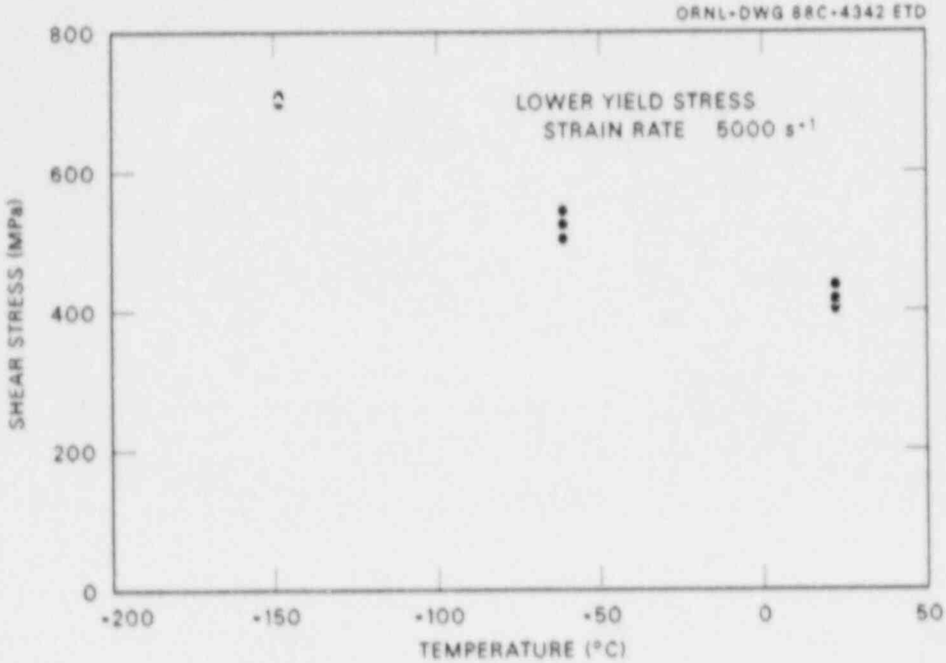

Fig. 2.55. Variation of lower yield stress with temperature for A 533 grade B class 1 steel tested at strain rate of 5000 s^{-1}.

(12%) when the strain rate increases from 900 to 5000 s^{-1}. In comparison, the data from SwRI show an increase of ~17 MPa (6%) when the strain rate increases from 10^{-3} to 10^{-1} s^{-1} and an increase of 48 MPa (16%) when the strain rate increases from 1.7 to 900 s^{-1}. (The comparison is made by transforming the compression data of SwRI to shear data.)

2. The temperature has a significant effect on the material response. In tests at a strain rate of 5000 s^{-1}, for example, the lower yield stress at −150°C is ~300 MPa higher than at room temperature. This is an increase of 75%. Figures 2.54 and 2.55 also show that the increase in stress with decreasing temperature is not linear. The stress increases more rapidly as the temperature decreases. The temperature also has a significant effect on hardening behavior following yield. A comparison of the stress-strain curves at room temperature with the curves at −60°C shows that the amount of hardening (the difference between the yield stress and the ultimate stress) is smaller at the lower temperature. The curves from tests at −150°C show that at this temperature there is no hardening at all after yielding. Following yielding, the material softens as the stress-strain curves gradually decline. The reason for this behavior is not yet clear. Possible explanations may be the formation of twins that are likely to exist at low temperatures or localization of plastic flow that will appear as softening on the macroscopic stress-strain curve. Microscopic examination of the specimens is now being conducted to better understand this observation.

2.5 ORNL Unified Inelastic Deformation Model

S.-J. Chang

The unified inelastic deformation model formulated by Robinson[31-33] has been shown in other R&D programs to be capable of mathematically describing many aspects of the viscoplastic deformation behavior of several structural alloys at high temperatures. Those studies have been aimed primarily at providing equations for use in component design calculations that included monotonic and cyclic loadings. In that formulation, creep and plastic deformation have been represented indistinctively and interactively. The model was first tested for 2 1/4 Cr-1 Mo steel and demonstrated a high degree of success. ORNL has recently extended the basic Robinson model for describing strain-aging effects[34,35] as exhibited by the phenomena of yield drop for Inconel 617 at 950°C and the reverse strain-rate effect for type 304 stainless steel at 550°C. The model can also describe creep-plasticity interactions, such as creep-induced strain hardening, described by Pugh and Robinson.[33]

In the present HSST study, the extended Robinson model is being applied to represent the viscoplastic deformation behavior of A 533 grade B class 1 steel for use in dynamic fracture analyses. The equations have effectively modeled similar phenomena of yield drop and strain-rate sensitivity at 100°C. Some of the preliminary results are shown in Fig. 2.56, which compares theoretical predictions with test data. In general, note that the strain-rate dependence of tensile curves is often influenced by the effect of strain-aging that can be defined as time-delayed effects caused by the interaction between dislocations and solute atoms. Different alloys show different degrees of influence by the strain-aging effect. This effect can lead to various rate sensitivities, even reverse rate sensitivity.

Numerical implementation of a recent version of Robinson's model[32] into a finite-element program was made recently by Hornberger.[36] The current ORNL work will be combined with Hornberger's capabilities, while Dr. Hornberger is on assignment to the HSST program from July to November 1988 from KfK, Karlshrue, Federal Republic of Germany.

The basic equations of the unified deformation model follow.

Flow equation for inelastic strain $\tilde{\varepsilon}$:

$$
\begin{aligned}
2\mu \times \dot{\tilde{\varepsilon}} &= \Phi(|\tilde{\varepsilon}|) \times F^{n} \cdot (\tilde{S} - \tilde{\alpha})/\sqrt{J_2} \,, \qquad F > 0 \text{ and } \tilde{S}(\tilde{S} + \tilde{\alpha}) > 0 \\
&= 0 \,, \qquad F < 0 \text{ or } F > 0 \text{ and } \tilde{S}(\tilde{S} - \tilde{\alpha}) < 0, \qquad (2.2)
\end{aligned}
$$

where

$$
F^2 = J_2/K_o^2 - [K(|\tilde{\varepsilon}|]^2 \quad \text{and} \quad J_2 = (\tilde{S} - \tilde{\alpha})\,(\tilde{S} - \tilde{\alpha})/2 \,. \qquad (2.3)
$$

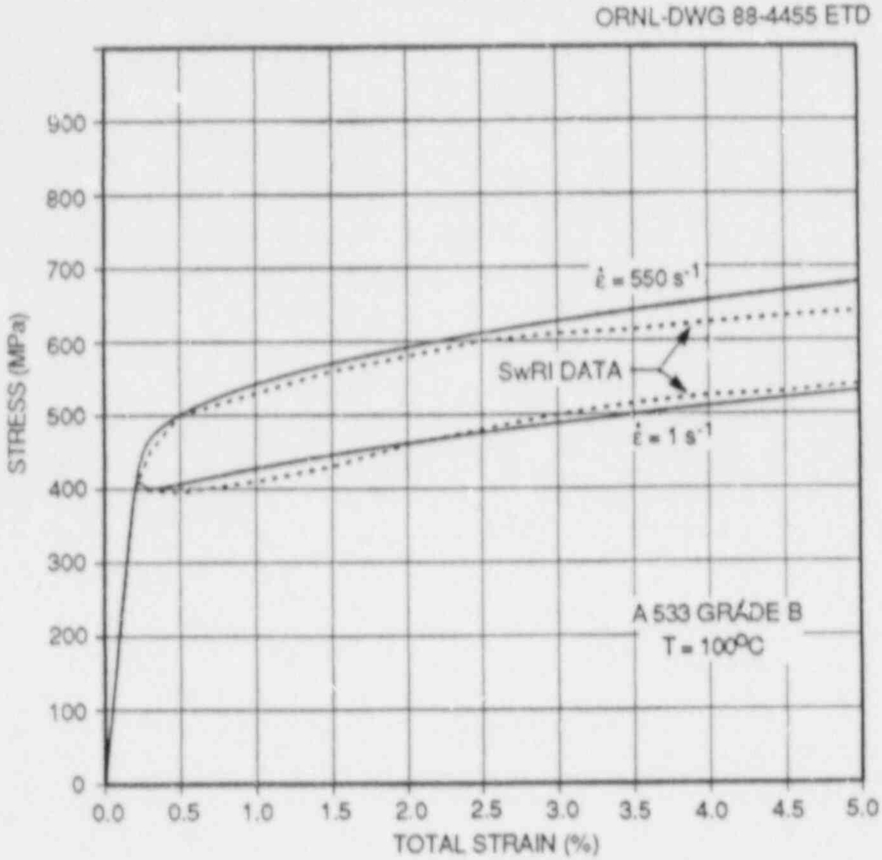

Fig. 2.56. Unified constitutive equation's capability to represent presence of strain-aging effects at low strain rate and its absence at a higher strain rate. (HSST plate 13-A, A 533 grade B class 1 steel at 100°C.)

Growth equation for kinematic variable $\tilde{\alpha}$:

$$\left.\begin{array}{ll} G^{\beta} \times \dot{\tilde{\alpha}} = 2\mu H(|\dot{\tilde{\varepsilon}}|) \times \dot{\tilde{\varepsilon}} - R \times G^{m} \times \tilde{\alpha}/\sqrt{I_2} & , \quad G > G_o \text{ and } \tilde{S}\ \tilde{\alpha} > 0 \\ G_o^{\beta} \times \dot{\tilde{\alpha}} = 2\mu H(|\dot{\tilde{\varepsilon}}|) \times \dot{\tilde{\varepsilon}} - R \times G_o^{m} \times \tilde{\alpha}/\sqrt{I_2} & , \quad G \leq G_o \text{ or } \hat{S}\ \tilde{\alpha} \leq 0 \end{array}\right\} , \qquad (2.4)$$

where

$$G^2 = I_2/K_o^2 \quad \text{and} \quad I_2 = \tilde{\alpha}\ \tilde{\alpha}/2 . \qquad (2.5)$$

$\Phi(|\tilde{\varepsilon}|) = 1 + C|\tilde{\varepsilon}|^{\gamma}$ and $K(|\bar{\varepsilon}|)$ are material functions to model yield stress drop, strain-rate sensitivity, and creep-plasticity interaction. These material functions and coefficients have been evaluated for the data obtained earlier by SwRI for A 533 grade B class 1 steel at strain rates of 1 and 550 s^{-1} and at 100°C (see Table 2.7).

Table 2.7. Unified constitutive equation material constants for A 533 grade B class 1 steel at T = 100°C

n	m	β	G_o	K_o (MPa)	K	$\lvert\dot{\tilde{\varepsilon}}\rvert$ (1/s)	μ (h)	$\mu H/K_o$	R/K_o (1/h)	C	γ
10	7	1.5	$0.01/\sqrt{3}$	100	$0.4/\sqrt{3}$	1	2.224	14.916	2.5×10^{-5}	$10^{3.5}$	0.75
						550	0.159	14.916	3.5×10^{-4}	$10^{2.15}$	0.075

References

1. B. R. Bass et al., *Viscoplastic Dynamic Fracture Analyses of the WP-1 Series of Wide Plate Crack-Arrest Tests*, ORNL/TM- , Martin Marietta Energy Systems, Inc., Oak Ridge Natl. Lab., to be published.

2. K. J. Bathe, *ADINA — A Finite Element Program for Automatic Dynamic Incremental Nonlinear Analysis*, Report AE 84-1, Massachusetts Institute of Technology, Cambridge, Mass., December 1984.

3. R. J. Dexter et al., "Dynamic-Viscoplastic Analysis and Small-Specimen Experimental Methods for the Study of Fracture in A533B Steel," pp. 173–90 in *Proceedings of the Fourth International Conference on Numerical Methods in Fracture Mechanics, San Antonio, Tex.*, March 23–27, 1987, ed. A. R. Luxmoor et al., Pineridge Press, Swansea, U.K., 1987.

4. S. R. Bodner and Y. Partom, "Constitutive Equations for Elastic Viscoplastic Strain Hardening Materials," *J. Appl. Mech.* 42, 385 (1975).

5. P. Perzyna, "Fundamental Problems in Visco-Plasticity," pp. 244–368 in *Recent Advances in Applied Mechanics*, Vol. 9, ed. G. Kuerti, Academic Press, New York, 1966.

6. D. J. Naus et al., *Crack-Arrest Behavior in SEN Wide Plates of Quenched and Tempered A 533 Grade B Steel Tested under Nonisothermal Conditions*, NUREG/CR-4930 (ORNL-6388), Martin Marietta Energy Systems, Inc., Oak Ridge Natl. Lab., September 1987.

7. B. R. Bass et al., "Late-Event Viscoplasticity in Wide-Plate Crack Arrest Tests," accepted for publication in *International Journal of Pressure Vessels and Piping*, 1988.

8. M. F. Kanninen et al., "Viscoplastic Characterization of A 533 Grade B Steel," in *Heavy-Section Steel Technology Program Semiann. Prog. Rep. April–September 1986*, NUREG/CR-4219, Vol. 3, No. 2 (ORNL/TM-9593/V3&N2), Martin Marietta Energy Systems, Inc., Oak Ridge Natl. Lab.

9. S. N. Atluri, T. Nishioka, and M. Nakagaki, "Incremental Path Independent Integrals in Inelastic and Dynamic Fracture Mechanics," *Eng. Fract. Mech.* 20-2, 209–44 (1984).

10. K. Kishimoto, S. Aoki, and M. Sakata, "On the Path-Independent Integral — Ĵ," *Eng. Fract. Mech.* 13, 841–50 (1980).

11. B. Brickstad, "A Viscoplastic Analysis of Rapid Crack Propagation Experiments in Steel," *J. Mech. Phys. Solids* 31, 307–27 (1983).

12. R. deWit and R. J. Fields, "Preliminary Results from the Eleventh Wide-Plate Test: WP-1.7," Letter report from National Bureau of Standards to D. J. Naus, Martin Marietta Energy Systems, Inc., Oak Ridge Natl. Lab., August 20, 1987.

13. B. R. Bass, J. Keeney-Walker, and C. W. Schwartz, "Computational Methods Development for Dynamic-Fracture Analysis," pp. 18–31 in *Heavy-Section Steel Technology Program Semiann. Prog. Rep. April–September 1987*, NUREG/CR-4219, Vol. 4, No. 2 (ORNL/TM-9593/V4&N2), Martin Marietta Energy Systems, Inc., Oak Ridge Natl. Lab.

14. M. F. Kanninen et al., "Elastodynamic and Viscoplastic-Dynamic Fracture Mechanics," pp. 35–52 in *Heavy-Section Steel Technology Program Semiann. Prog. Rep. April–September 1987*, NUREG/CR-4219, Vol. 4, No. 2 (ORNL/TM-9593/V4&N2), Martin Marietta Energy Systems, Inc., Oak Ridge Natl. Lab.

15. M. F. Kanninen et al., "Viscoplastic-Dynamic Analyses of Small-Scale Fracture Tests to Obtain Crack Arrest Toughness Values for PTS Conditions," pp. 93–112 in *Proceedings of the Fifteenth Water Reactor Safety Information Meeting, Gaithersburg, Md., October 1987*, ed. A. J. Weiss, NUREG/CP-0091, Vol. 2, Nuclear Regulatory Commission, February 1988.

16. R. J. Dexter, "Sources of Error in Finite Element Computations of the Stress Intensity Factor for Running Cracks," p. 173 in *Numerical Methods in Fracture Mechanics*, ed. A. R. Luxmoor et al., Pineridge Press, Swansea, U.K., 1987.

17. X. J. Zhang, R. W. Armstrong, and G. R. Irwin, *J. of Mat. Sci. Letters* 5, 961–64, 1986.

18. G. R. Irwin, *Brittle-Ductile Transition Behavior in Reactor Vessel Steels*, ed. A. J. Weiss, NUREG/CP-0082, Vol. 2, Nuclear Regulatory Commission, February 1987, pp. 251–72.

19. A. R. Rosenfield and C. W. Marshall, "Ductile-to-Brittle Fracture Transition", pp. 66–71 in Vol. 11, *Metals Handbook*, 9th ed., American Society for Metals, 1986.

20. X. J. Zhang and A. Kumar, "Fracture Initiation in Wide Plate Test WP-2.4 Using Optical Topography," Letter Report to Martin Marietta Energy Systems, Inc., Oak Ridge Natl. Lab., from the University of Maryland, January 1987.

21. T. Kobayashi, G. R. Irwin, and X. J. Zhang, "Topographic Examination of Fracture Surfaces in Fibrous-Cleavage Transition Behavior," pp. 234–51 in *Fractography of Ceramic and Metal Failure*, ASTM STP 827, ed. J. J. Mecholsky, Jr. and S. R. Powell, Jr., American Society for Testing and Materials, Philadelphia, 1984.

22. D. J. Naus et al., "Summary of the Twelfth Heavy-Section Steel Technology (HSST) Wide-Plate Crack-Arrest Test (WP-CE-1)," attachment to letter, "HSST Wide-Plate Crack-Arrest Test WP-CE-1," from W. R. Corwin, Oak Ridge Natl. Lab., to M. Mayfield, Nuclear Regulatory Commission, December 30, 1987.

23. A. A. Wells, Houdremont Lecture, *British Welding Jnl.* 12(1), (January 1965).

24. D. J. Naus et al., "Summary of the Eleventh HSST Wide-Plate Crack-Arrest Test (WP-1.7)," attachment to letter from W. R. Corwin, Oak Ridge Natl. Lab., to M. Mayfield, Nuclear Regulatory Commission, Dec. 7, 1987.

25. A. T. Zehnder and A. J. Rosakis, "Dynamic Initiation and Propagation in 4340 Steel Under Impact Loading," GALCIT Report SM 86-6, California Institute of Technology, 1986.

26. C. W. Schwartz, H. C. Lee, and B. R. Bass, "Dynamic Fracture Propagation Relations Inferred from Wide-Plate Crack Arrest Tests of A 533 Grade B Steel," pp. 66–71 in *Proceedings of the Fall 1987 Meeting of the Society for Experimental Mechanics, Savannah, Ga., October 1987.*

27. C. W. Schwartz and B. R. Bass, "Evaluation of the Presence of Constraint in Crack Run/Arrest Events," *Proceedings of the 15th Water Reactor Safety Meeting, Gaithersburg, Md., October 1987*, ed. A. J. Weiss, NUREG/CP-0091, Vols. 1–6, Nuclear Regulatory Commission, February 1988.

28. C. W. Schwartz and B. R. Bass, "Coupled Finite Element-Boundary Element Analysis for Nonlinear Fracture Problems," pp. 9.ii.1–4 in *Proceedings of the International Conference on Computational Engineering Science, Atlanta, Ga., April 10–14, 1987*, Springer-Verlag, New York, 1988.

29. I. D. Parsons, J. F. Hall, and A. J. Rosakis, "A Finite Element Investigation of the Elastostatic State Near a Three-Dimensional Edge Crack," Report No. SM 86-29, Division of Engineering and Applied Science, California Institute of Technology, Pasadena, Calif., 1986.

30. *Metals Handbook*, 9th Ed., Vol. 8.

31. D. N. Robinson, *A Unified Creep-Plasticity Model for Structural Metals at High Temperature*, ORNL/TM-5969, Union Carbide Corp. Nuclear Div., Oak Ridge Natl. Lab., October 1978.

32. D. N. Robinson and P. A. Bartolotta, *Viscoplastic Constitutive Relationship with Dependence on Thermomechanical History*, NASA CR 174836, NASA-Lewis, March 1985.

33. C. E. Pugh and D. N. Robinson, "Some Trends in Constitutive Equation Model Development for High-Temperature Behavior of Fast-Reactor Structural Alloys," *Journal of Nuclear Engineering and Design* 48, 269–76 (1978).

34. S.-J. Chang, "Deformation of Inconel 617," pp 126–35 in *High-Temperature Gas-Cooled Reactor Program Progress Report Ending Dec. 31, 1986*, DOE-HTGR-87-17, Martin Marietta Energy Systems, Inc., Oak Ridge Natl. Lab., 1987.

35. S.-J. Chang, *Inelastic Analysis and Testing of SUS 304 Stainless Steel*, by J. J. Blass et al., EPRI 2658-21, pp. 38–43, EPRI, Palo Alto, Calif., 1988.

36. K. Hornberger et al., "Numerical Integration and Implementation of Viscoplastic Models into Finite Element Codes," pp. 477–90, *Proc. of Third International Conference on Computational Plasticity, Barcelona, Spain, April 6–10, 1987*, Pineridge Press, Swansea, U.K.

3. MATERIAL CHARACTERIZATION AND PROPERTIES

R. K. Nanstad

Primarily for internal management and budgetary control, the Heavy-Section Steel Technology (HSST) Program created a separate task (Task H.3) for the work on material characterization and properties determinations. However, for the reader's convenience some contributions to this report are placed within other chapters according to the larger tasks that correspond to the particular material studies. For example, in addition to the work reported here, refer to Sect. 7.1 for crack-arrest studies in clad plates and Sect. 7.2 for nondestructive examination studies in support of cladding evaluations.

3.1 Crack-Arrest Toughness of Clad-Plate Base Metal

S. K. Iskander E. T. Manneschmidt
R. L. Swain

The pretest and posttest material characterization performed to date has been reported in Refs. 1 and 2, respectively. All eight clad-plate test specimens were machined from a single, specially heat-treated A 533 grade B chemistry plate. In this section, the results of crack-arrest toughness tests performed on base metal of the clad plates are presented.

Pretest material characterization consisted of tensile and Charpy V-notch (CVN) tests of base metal, heat-affected zone (HAZ) and cladding, and a J-R curve at room temperature for the stainless steel cladding.[1] Posttest material characterizations reported in Ref. 2 included Young's modulus and stress-strain curves for all three metallurgical zones, as well as results of room temperature tensile testing that had been performed on the HAZ from one of the broken halves of the first plate tested. The reference nil-ductility-transition (RT_{NDT}) temperature of the base metal, the variation of hardness across the thickness of the plate, and metallographic examinations have also been reported in Ref. 2.

Crack-arrest specimens were machined from the base metal of clad plate CP-18, with an L-T orientation, corresponding to the electron-beam (EB)-induced flaw propagating along the surface. The base metal is A 533 grade B with a special heat treatment to raise its RT_{NDT}. Besides characterizing the crack-arrest toughness properties, the specimens were also used to check a special fixture that will be used in the hot cells. The specimens to be tested in the hot cells are the Sixth Irradiation Series and are in three sizes — 25 × 76 × 76 mm, 25 × 152 × 152 mm, and 33 × 152 × 152 mm. Special jigs will be used with each size, and thus crack arrest specimens of each of these sizes were fabricated. The starting notches were weld embrittled (WE).

The material drop-weight nil-ductility transition (NDT) temperature is 36°C. The RT_{NDT} determined according to NB-2331 of the *ASME Boiler and Pressure Vessel Code*, Sect. III (which specifies the use of T-L orientation CVN specimens) is 72°C. Thus, it is the T-L orientation that controlled the RT_{NDT} determination. However, the orientation for surface crack propagation in the clad plates is L-T (which incidently fulfills both the 68-J and 0.89-mm requirements). Accordingly, the results of the crack-arrest tests have been normalized using the NDT temperature rather than RT_{NDT}.

The crack-arrest toughness K_{Ia} was measured according to American Society for Testing and Materials (ASTM) Standard Test Method for Determining the Plane-Strain Crack Arrest Toughness (E1221-88). The results are shown in Table 3.1. Figure 3.1 shows K_{Ia} plotted vs the test temperature T. Also plotted on the same figure is the ASME Sect. III K_{IR} curve, plotted relative to the NDT of this material. All three results at −25°C, as well as one of the results at room temperature for the

Table 3.1. Crack-arrest test results from L-T orientation specimens fabricated from base material of clad plate CP-18

Nominal specimen size (mm)	Specimen No.	Test temperature (°C)	K_{Ia} (MPa•√m)	K_{Ia}/K_{IR}
33 × 152 × 152	CP8	23	66	1.69
	CP9	23	73	1.86
	CP7	50	81	1.65
	CP10	75	83	1.23
	CP11	75	86	1.28
33 × 152 × 152	K_{Ia}/K_{IR} (mean) ± 1σ = 1.54 ± 0.27			
25 × 152 × 152	CP1	23	80	2.04
	CP2	23	87	2.22
	CP3	−25	80	2.49
	CP4	−25	52[a]	1/62[a]
25 × 152 × 152	K_{Ia}/K_{IR} (mean) ± 1σ = 2.09 ± 0.37			
25 × 76 × 76	CP13	−25	24[b]	0.75
	CP15	−25	23[b]	0.71
	CP18	23	79[a]	2.02
For all valid specimens: K_{Ia}/K_{IR} (mean) ± 1σ = 1.81 ± 0.40				

[a] Invalid according to ASTM E1221-88 [remaining ligament too small, but used in analysis of data, not included in calculation of K_{Ia}/K_{IR} (mean)].

[b] Invalid [remaining ligament does not meet ASTM E-1221-88, not included in calculation of K_{Ia}/K_{IR} (mean)].

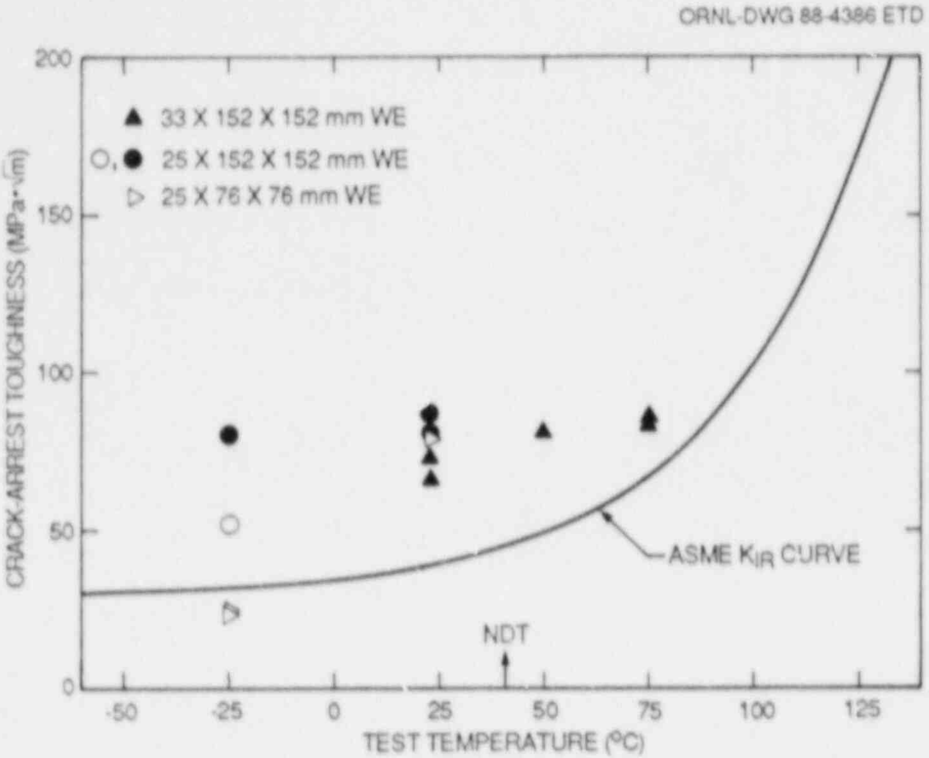

Fig. 3.1. Results of crack-arrest tests on special heat-treated clad plate A 533 grade B base material compared to ASME K_{Ia} curve. Open symbols are invalid according to ASTM Method E1221-88.

smallest specimen size, were invalid according to ASTM Method E1221-88 because the remaining ligament was too small. In earlier tests, also at −25°C, using the smallest size specimens, the crack ran almost the entire ligament. It therefore appears that the WE starter notch induces too large a driving force K_o. To reduce the driving force, a machined, sharp starter notch with no brittle weld, perhaps fatigue precracked and/or warm prestressed (WPS), will be used to obtain data at low temperatures.

Table 3.1 gives the ratio of K_{Ia}/K_{IR}, the mean and standard deviation for the two groups of specimen sizes, as well as for all usable results. The results below the K_{IR} curve are obviously outliers and have been disregarded in the analysis of the data. Two "invalid" values were included in the computations because previous studies have shown that the validity criteria of E1221-88 may be too restrictive.[3] Although the number of test results in this case are too small to enable definite conclusions, it is instructive to compare these averages to those obtained in the characterization of the A 533 grade B class 1 steel (HSST Plate 13A) used in Series 1 of the wide-plate tests. The averages and standard deviation from earlier Oak Ridge National Laboratory (ORNL) tests[4] are 1.46 and 0.20, respectively; while the corresponding values from a Battelle Columbus Laboratory (BCL) study[5] on the same HSST Plate 13A are 1.55 and 0.20, respectively. In the latter study, unusually high K_{Ia}/K_{IR}

ratios were not included in the averages as they were considered outliers. Thus, the mean of the K_{Ia}/K_{IR} ratio and standard deviation from the present study (1.81 and 0.40, respectively) seem to be higher than those obtained in the two previous investigations on the same material. However, the scatter of values from each specimen size group in the present investigation, as measured by the standard deviation, is smaller. The higher K_{Ia}/K_{IR} ratio from the present study may result from the unusual heat treatment that the clad-plate base material has been subjected to in order to raise its RT_{NDT}. On the basis of the limited number of results, it seems that K_{Ia} for this material and in the temperature range −25 to 75°C is only mildly dependent on temperature. These results will be used in the analysis of the tests on clad plates (see Sect. 7.1 for a description of the tests).

3.2 Development of 50-mm-Thick Duplex Crack-Arrest Specimens

S. K. Iskander E. T. Manneschmidt
R. L. Swain J. F. King

Successful crack-arrest testing at temperatures 20 to 40 K above the NDT is difficult to achieve with WE specimens. Duplex specimens 25 to 35 mm thick, with A 533 grade B and 2 1/4 Cr-1 Mo test sections, have been used for this purpose.[4,5] Also successfully tested were 50-mm-thick 2 1/4 Cr-1 Mo specimens.[3,6] However, thus far, the number of successful tests on 50-mm-thick A 533 grade B or weldments at temperatures 20 to 40 K above NDT has been small. In general, unsuccessful tests on duplex specimens are characterized by the running flaw either arresting or making a right-angle turn and propagating along the HAZ of the 4340 steel.

To increase the number of successful tests on 50-mm-thick specimens, the EB-welding parameters have been optimized to reduce the width of the fusion region as well as its porosity to increase the probability of the crack jumping across the tough HAZ.

Figure 3.2 shows micrographs of a typical EB-weld of 4340 steel to the test section. The plane of the picture is parallel to the crack plane. The specimen (No. PI300) from which this micrograph was prepared is one of several successful 50-mm-thick specimens tested.[5] The test section is 2 1/4 Cr-1 Mo material used in the second pressurized thermal shock test (PTSE-2) as well as in the second series of wide-plate tests. Figure 3.3 shows a closeup of the midthickness and the porosity that is common in specimens of this thickness caused by the two EB-weld passes, one from either side. The crack-arrest test was successful, and the lack of fusion apparently did not hinder the crack propagation in this case.

Figure 3.4 shows the variation of microhardness across the fusion zone at three locations, each characterizing about a third of the specimen thickness (see Fig. 3.2). Hardness "peaks" in A 533 grade B HAZ are known to be associated with higher toughness than its base metal[2] and have indeed arrested propagating flaws in the clad-plate tests (see Sect. 7). It is not known whether the hardness peaks observed here are also associated with higher toughness than those of 4340 base metal. The

ORNL PHOTO 3621-88

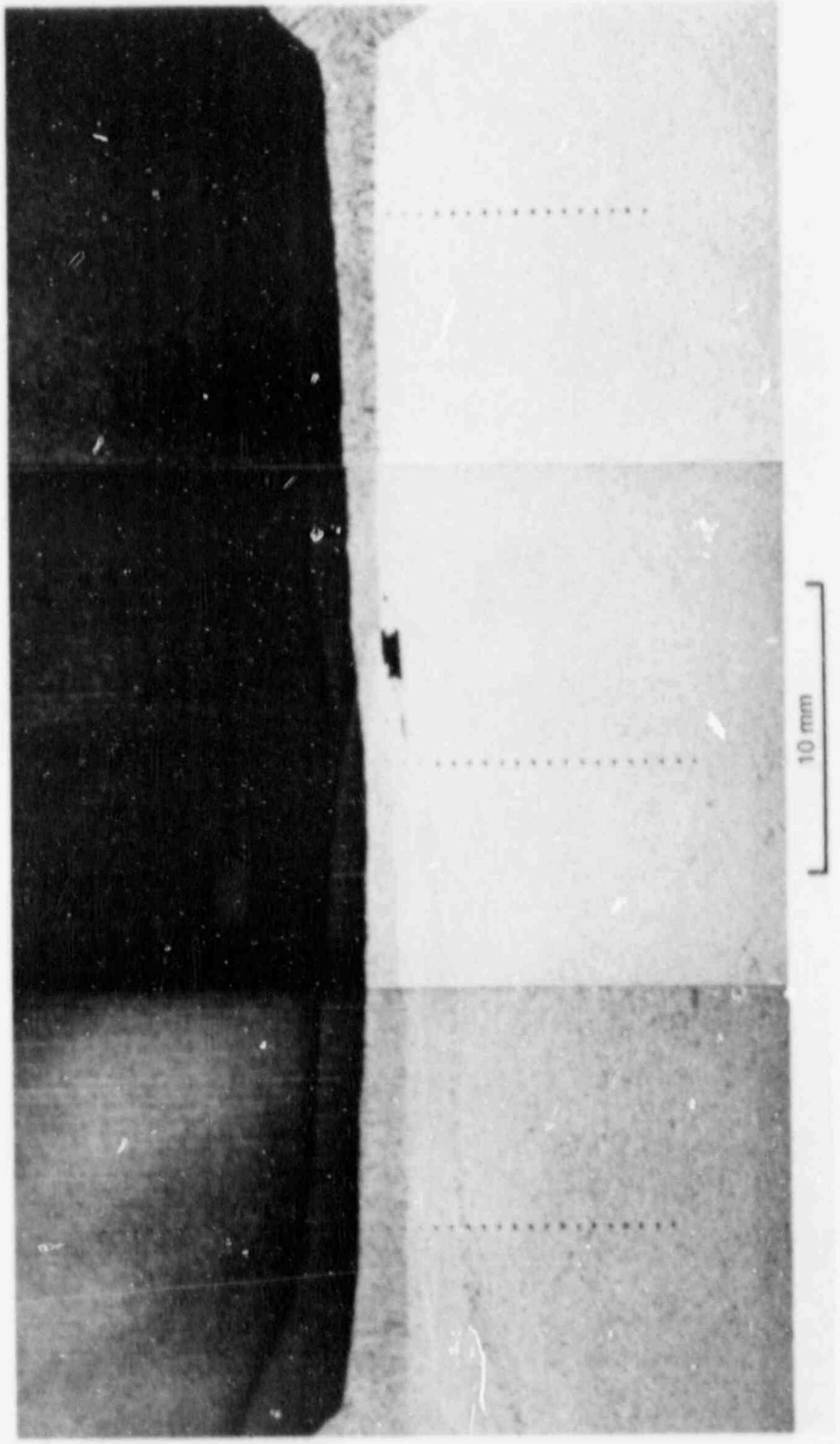

Fig. 3.2. Micrographs of typical EB-weld of 434Q steel Cr-1 Mo material from successful, 50-mm-thick, crack-arrest test of specimen PI300.

M&C PHOTO Y211107

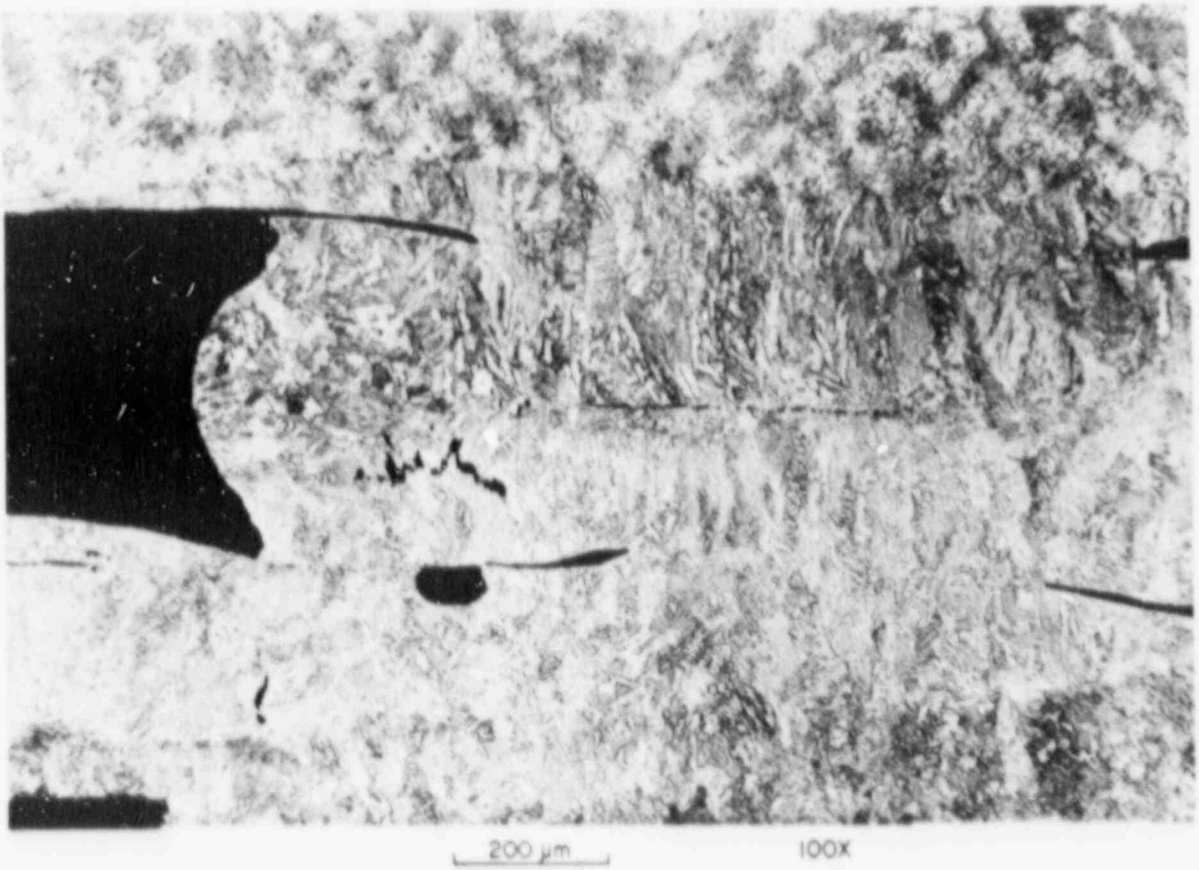

Fig. 3.3. Closeup of midthickness of same specimen shown in Fig. 3.2. The porosity did not hinder the crack propagation in this case.

hardness peaks in the 4340 HAZ, together with the porosity of the midthickness region, may be the cause of the difficulty of the cracks penetrating the fusion zone.

In the case of 2 1/4 Cr-1 Mo, 50-mm duplex specimens, the tests were successful. However, for two other materials, A 533 grade B and its weld metal (designated A73W), the crack-arrest tests on 50-mm duplex specimens were not successful, again because of flaws arresting/diverting in the HAZ of the 4340. Figure 3.5 shows the variation of hardness across midthickness of duplex specimens from two such unsuccessful tests (on specimen WP15BP and A73W73, A 533 grade B base and weld metal, respectively). The variation of hardness in each of these specimens is similar to that in the successful test. Thus, the reasons for the arrest in the HAZ of the 4340 of duplex specimens made of one material and not in those made from another is unknown at this time. Note that the thermal properties of all three above materials are similar.

ORNL-DWG 88-4387 ETD

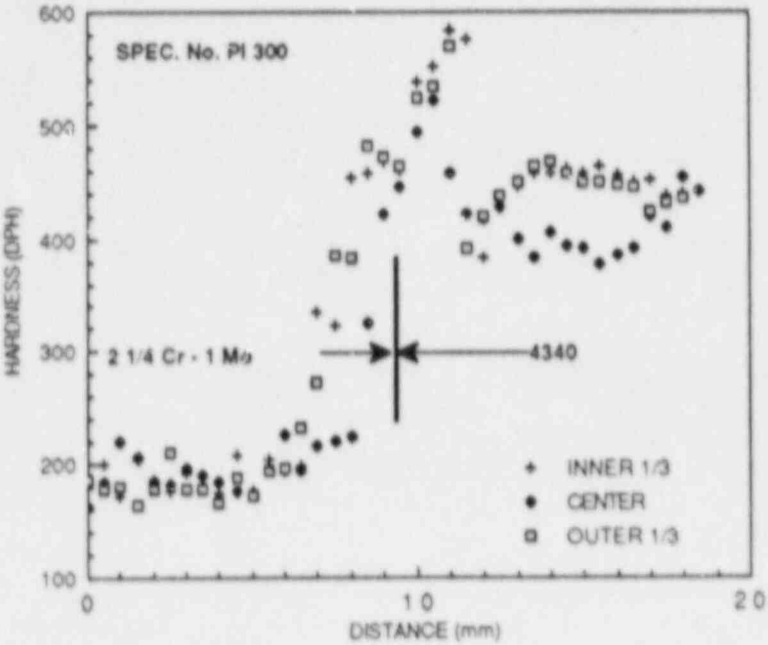

Fig. 3.4. Variation of microhardness across fusion zone at three locations, each characterizing about one-third of the thickness of specimen shown in Fig. 3.2.

ORNL-DWG 88-4388 ETD

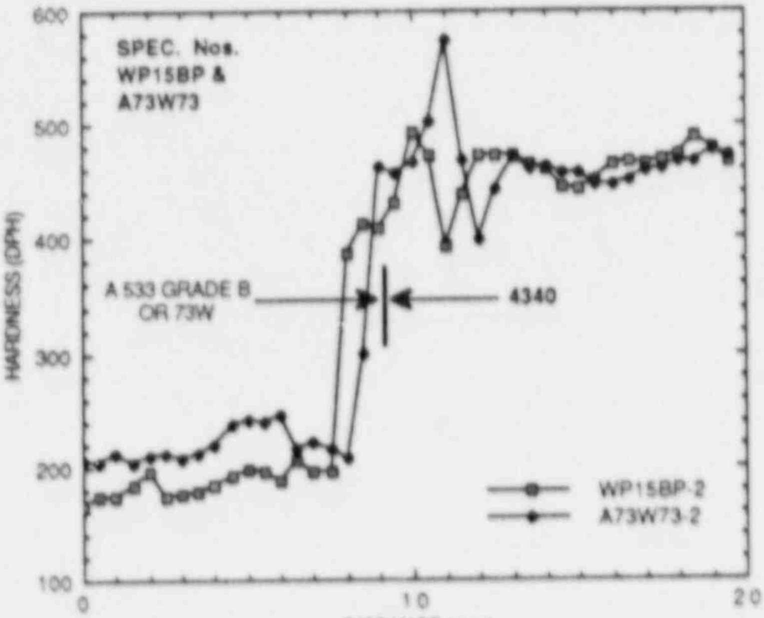

Fig. 3.5. Variation of hardness across midthickness of unsuccessful 50-mm-thick A 533 grade B base and weld metal duplex specimens (WP15BP and A73W73, respectively). In [illegible]h cases the flaw either arrested completely and/or was divert[illegible]irection normal to its original one.

The potential gains to be made by optimizing the EB-weld are diminishing. There is probably more to be gained by optimizing the specimen geometry. One approach to be explored is the side-groove geometry, for example, reducing its sharpness so that crack initiation is moved from the edges toward the center. The initiation site for duplex specimens generally seems to be at the intersection of the side grooves and the crack starter hole in the 4340 material. After initiation, the crack tends toward midthickness and arrests upon reaching the porous midthickness. If the effective toughness of the material towards the surface is smaller than that at midthickness (conditions similar to those of specimens with no side grooves), the available energy could be used in "tunnelling" across the fusion zone. This may increase the chances for a successful test.

References

1. W. R. Corwin, "Stainless Steel Cladding Investigations," pp. 70–79 in *Heavy-Section Steel Technology Program Semiann. Prog. Rep. October 1985–March 1986*, NUREG/CR-4219, Vol. 3, No. 1 (ORNL/TM-9593/V3&N1), Martin Marietta Energy Systems, Inc., Oak Ridge Natl. Lab.

2. S. K. Iskander et al., "Posttest Material Characterization of Clad Plate Materials," pp. 115–26 in *Heavy-Section Steel Technology Program Semiann. Prog. Rep. April–September 1987*, NUREG/CR-4219, Vol. 4, No. 2 (ORNL/TM-9593/V4&N2), Martin Marietta Energy Systems, Inc., Oak Ridge Natl. Lab.

3. R. K. Nanstad et al., "Low-Upper-Shelf Material Characterization," pp. 51–54 in *Heavy-Section Steel Technology Program Semiann. Prog. Rep. October 1986–March 1987*, NUREG/CR-4219, Vol. 4, No. 1 (ORNL/TM-9593/V4&N1), Martin Marietta Energy Systems, Inc., Oak Ridge Natl. Lab.

4. W. R. Corwin et al., "Crack-Arrest Test Results in Support of Wide Plate Testing," pp. 54–56 in *Heavy-Section Steel Technology Program Semiann. Prog. Rep. April–September 1985*, NUREG/CR-4219, Vol. 2 (ORNL/TM-9593/V2), Martin Marietta Energy Systems, Inc., Oak Ridge Natl. Lab.

5. A. R. Rosenfield et al., "Crack Arrest Studies at Battelle Columbus," pp. 102–9 in *Heavy-Section Steel Technology Program Semiann. Prog. Rep. April–September 1984*, NUREG/CR-3744, Vol. 2 (ORNL/TM-9154/V2), Martin Marietta Energy Systems, Inc., Oak Ridge Natl. Lab.

6. A. R. Rosenfield and P. N. Mincer, "Battelle HSST Support Program," pp. 166–69 in *Heavy-Section Steel Technology Program Semiann. Prog. Rep. April–September 1986*, NUREG/CR-4219, Vol. 3, No. 2 (ORNL/TM-9593/V3&N2), Martin Marietta Energy Systems, Inc., Oak Ridge Natl. Lab.

4. SPECIAL TECHNICAL ASSISTANCE

4.1 LWR Vessel Supports

R. D. Cheverton F. B. Kam
R. K. Nanstad G. C. Robinson

4.1.1 Introduction

Late in 1986, a reevaluation of the integrity of the High Flux Isotope Reactor (HFIR)[1] pressure vessel (Fig. 4.1) was begun in an effort to extend the permissible life of this vessel.[2] Vessel surveillance data,[3]

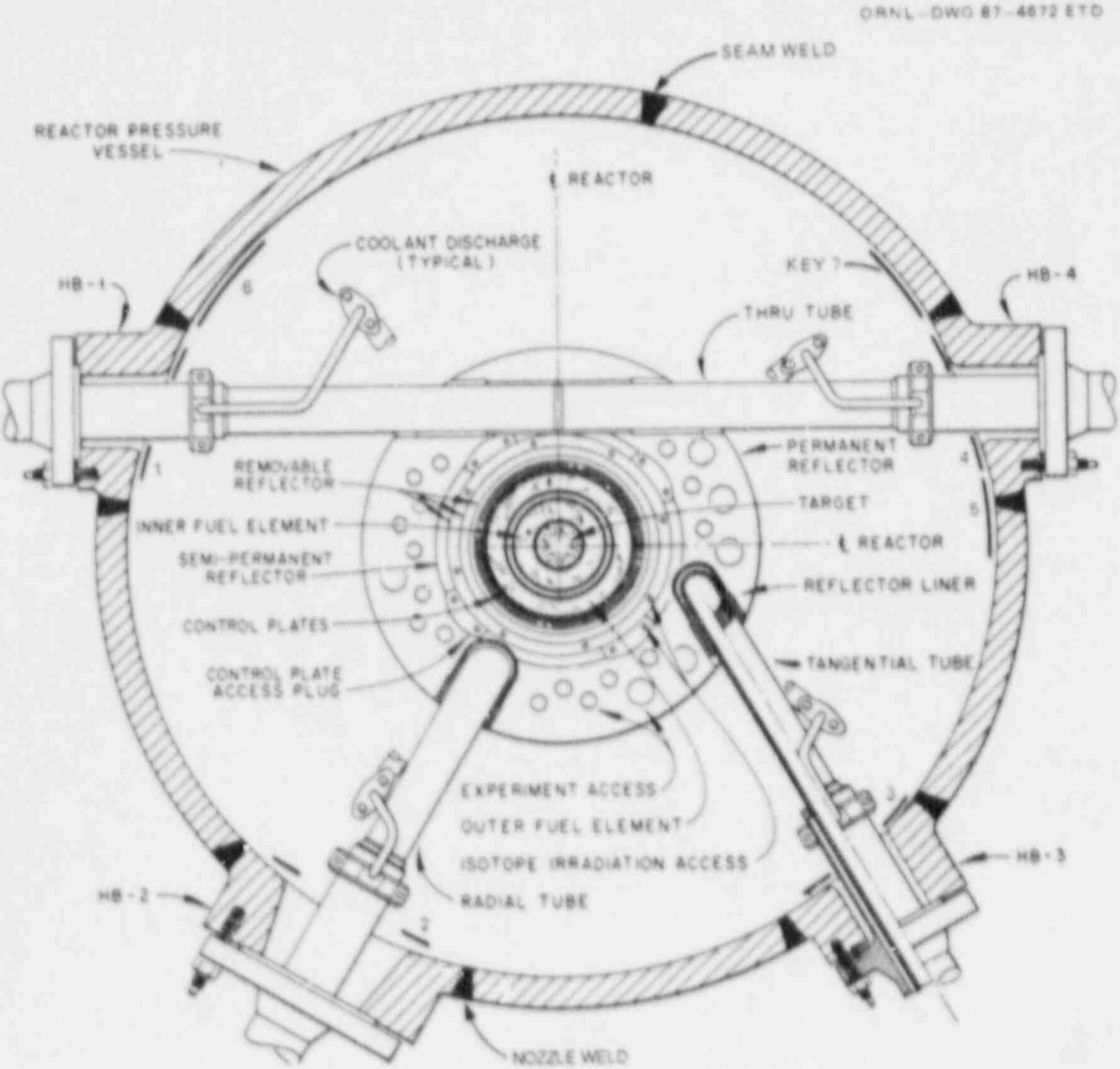

Fig. 4.1. Cross section of HFIR vessel and core at midheight of core, indicating locations of vessel surveillance specimens (Keys 1–7).

which had not been carefully examined since 1974, indicated that the embrittlement rate was significantly greater than had been anticipated on the basis of data obtained from materials testing reactors (MTRs) in the early 1960s. The neutron energy spectra and the irradiation temperatures for the HFIR surveillance specimens and for specimens in the MTRs were believed to be essentially the same, and the materials were very similar; however, the fast-neutron flux (ϕ) in the MTRs was about 10^4 times that in the HFIR specimens. Thus, it appeared that the lower flux in HFIR was responsible for the relatively large amount of embrittlement per neutron; that is, there appeared to be a negative fluence-rate effect ("rate" effect): the lower the fluence rate (ϕ), the greater the embrittlement per neutron.

Soon after this discovery, it was realized that the rate effect might significantly impact the life expectancy for some light-water-reactor (LWR) vessel supports because the temperatures and fast fluxes associated with supports, which are located in the cavity between the vessel wall and biological shield (Fig. 4.2), are about the same as for the HFIR vessel. Thus, a study was initiated at the Oak Ridge National Laboratory (ORNL), as a part of the Nuclear Regulatory Commission's (NRC's) Heavy-Section Steel Technology (HSST) Program, to evaluate the impact.

ORNL-DWG 88-3862A ETD

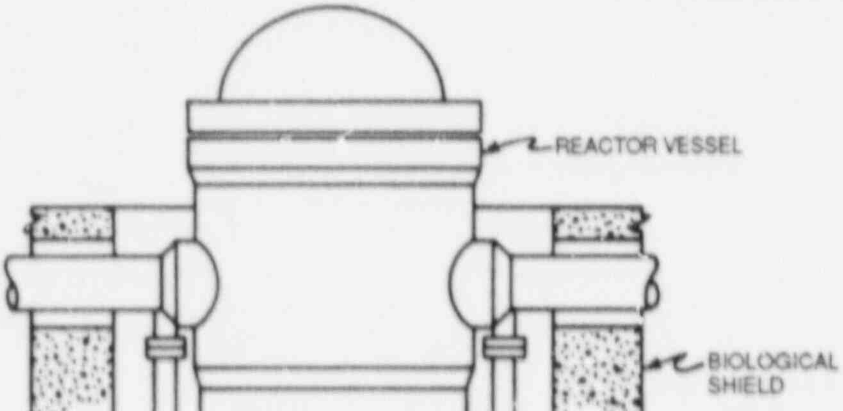

Fig. 4.2. Schematic of PWR vessel indicating location of one type of vessel support in cavity.

4.1.2 Embrittlement rate

The portion of the HFIR vessel that is subjected to the highest fast-neutron fluxes is close to the beam tubes (Fig. 4.1) because the beam tubes displace beryllium and water that otherwise constitute shielding for the vessel wall. Thus, both shell material (A 212 grade B) and nozzle materials (A 105 grade II and A 350 grade LF3) were included in the HFIR vessel materials surveillance program, and the surveillance capsules, each containing three Charpy V-notch (CVN) specimens and a flux monitor, were located close to the beam tubes (keys 1—7, Fig. 4.1).

The design of the HFIR vessel considered radiation embrittlement to the extent that the vessel and nozzle diameters were large enough and the nozzle materials initially tough enough that a vessel life of 20 equivalent full-power years (EFPY) could be achieved. The criterion that had to be satisfied was

$$\mathrm{NDTT} + 33°\mathrm{C} < T \ ,$$

where NDTT is the nil ductility transition temperature (a measure of the extent of embrittlement), and T is the temperature of the vessel. The minimum value of T was 21°C, which was specified as the minimum permissible value for pressurization (normal operating temperature for the vessel is ~49°C). The available embrittlement data used in the design of the vessel were obtained from MTRs, included data for A 212 grade B steel, and corresponded to appropriate irradiation temperatures, that is, <93°C (Fig. 4.3).[4]

HFIR surveillance specimens of A 212 grade B were removed for testing after 15.0 and 17.5 EFPY, and A 105 and A 350 specimens were removed after 2.3, 6.5, 15.0, and 17.5 EFPY. The results, in the form of ΔNDTT vs fluence (Φ), for neutron energy (E) > 1 MeV, are compared with the MTR data in Fig. 4.4. If it is assumed that spectrum and chemistry effects are not responsible for the incongruity of the three sets of data, the comparison indicates a rate effect. To evaluate the possible effects of the chemistry and spectrum, HFIR archive A 212 grade B material was recently irradiated in the Oak Ridge Research Reactor (ORR), a typical MTR, and the HFIR and ORR A 212 grade B data were plotted as a function of displacements per atom (dpa) for E > 0.1 MeV (Fig. 4.5).* Although the HFIR spectrum is somewhat harder, the incongruity still exists. Furthermore, the ORR data point for the HFIR A 212 grade B archive material falls in the scatter band of the MTR data (Fig. 4.4), and surveillance data from army reactors PM-1 and PM-1A (Fig. 4.6) (Ref. 5) indicate no significant differences in sensitivity between A 212 grade B and A 350 grade LF3. These later data also indicate that for the relatively high fluxes in the PM-1 reactors, the increase in NDTT for A 212 grade B at a fluence of 1 to 2×10^{17} neutrons/cm^2 is much less than that obtained from HFIR. Thus, it appears that the rate effect indicated in Fig. 4.4 is a real phenomenon.

---

*To obtain the MTR curve, it was assumed that the calculated spectrum for the ORR was appropriate for the MTR data.

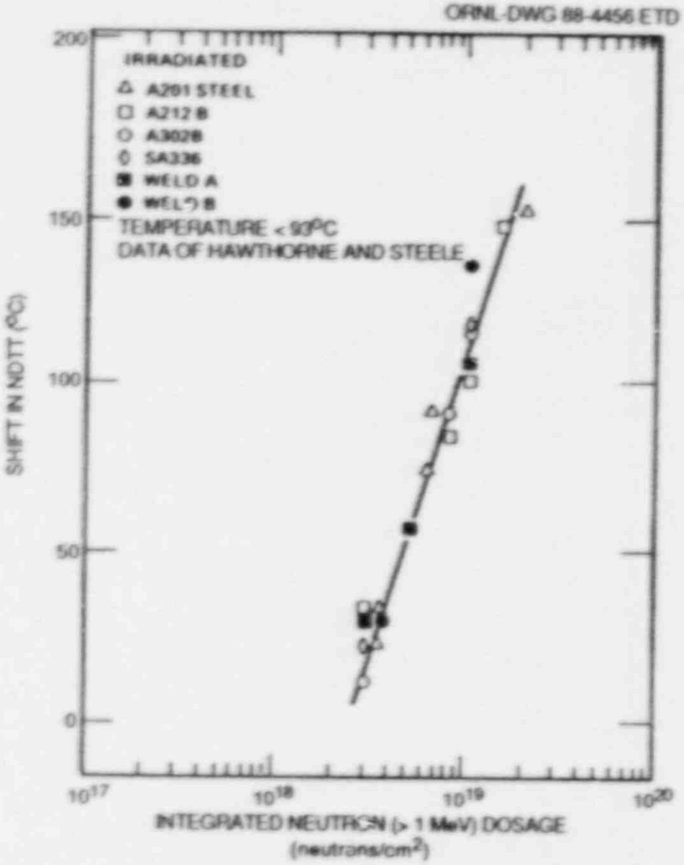

Fig. 4.3. Increase in NDTT with fluence (E > 1 MeV) for pressure-vessel materials irradiated in MTRs.

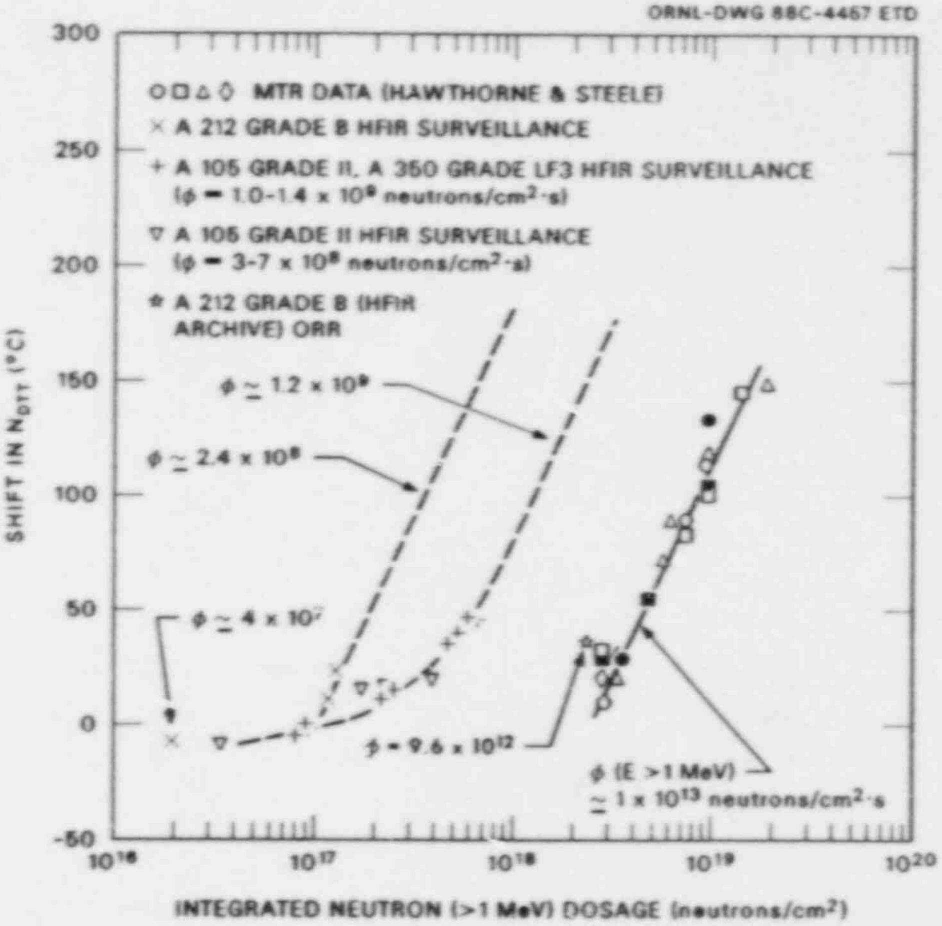

Fig. 4.4. Increase in NDTT with fluence (E > 1 MeV) for irradiations in HFIR (vessel surveillance positions) and MTRs.

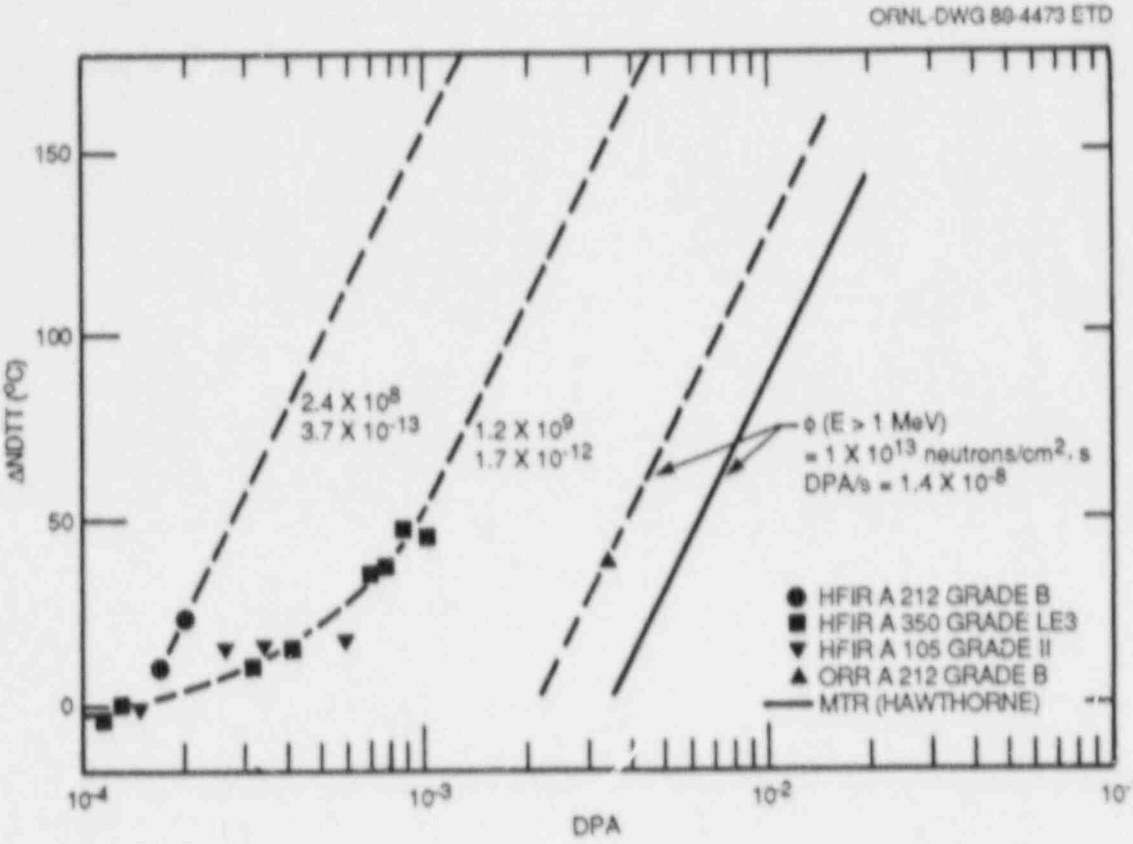

Fig. 4.5. Increase in NDTT with DPA for irradiations in HFIR (vessel surveillance positions) and ORR.

4.1.3 Application of rate effect to LWR vessel supports

A preliminary evaluation of the impact of the rate effect on life expectancy of LWR vessel supports was conducted by estimating the increase in NDTT, at 32 EFPY, corresponding to the cavity fluxes in specific Babcock and Wilcox (B&W), Combustion Engineering (CE), Westinghouse (W), and General Electric (GE) reactors for which calculated multigroup cavity fluxes were available.[6,7] Displacements per atom (E > 0.1 MeV) was used in lieu of fluence to account for the different neutron spectra in HFIR, ORR, and LWR cavities.* As indicated in Figs. 4.4 and 4.5, it was assumed that curves drawn through the HFIR data points corresponding to different flux values were parallel to the MTR curve and that they adequately represent vessel support materials. Furthermore, it was assumed that for a given value of ΔNDTT, there is a linear relationship

---

*The lower limit for E of 0.1 MeV was considered to be adequate for the purpose of this study.

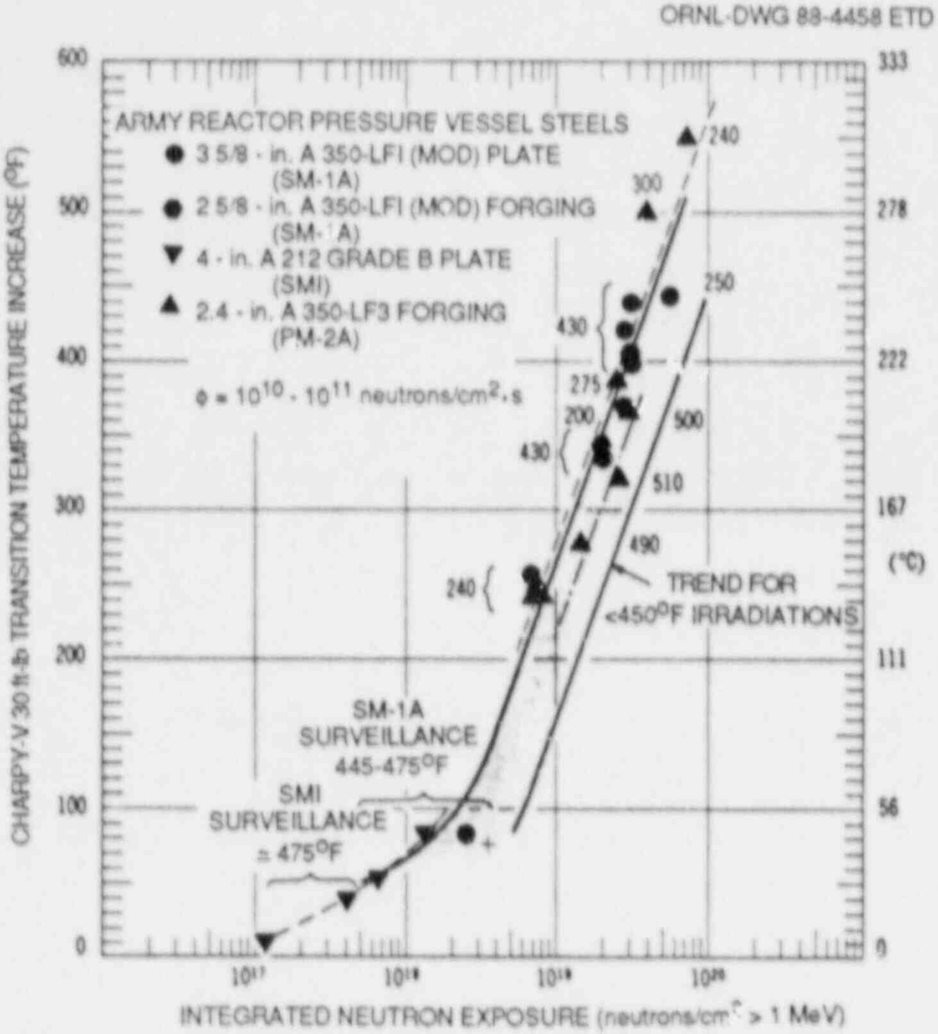

Fig. 4.6. Effects of neutron radiation on Charpy-V transition temperature behavior of Army reactor pressure vessel steels. Numbers adjacent to data points indicate exposure temperatures. *Source*: Ref. 5.

between log dpa and log (dpa rate) over a limited range (Fig. 4.7).* Based on these assumptions, the results presented in Table 4.1 were obtained.

In terms of ΔNDTT, the impact of the rate effect *is* quite large, except for the GE reactors, which have more water shielding and thus a much lower flux in the cavity. However, it is not intended to imply that all pressurized-water-reactor (PWR) vessel supports will experience these large shifts. Many of the supports do not extend vertically into the

---

*Figure 4.7 was obtained by cross-plotting data in Fig. 4.5 for $\phi = 2.4 \times 10^8$ and 1.2×10^9 neutrons/cm^2·s. The extent of extrapolation required is evident from Fig. 4.5.

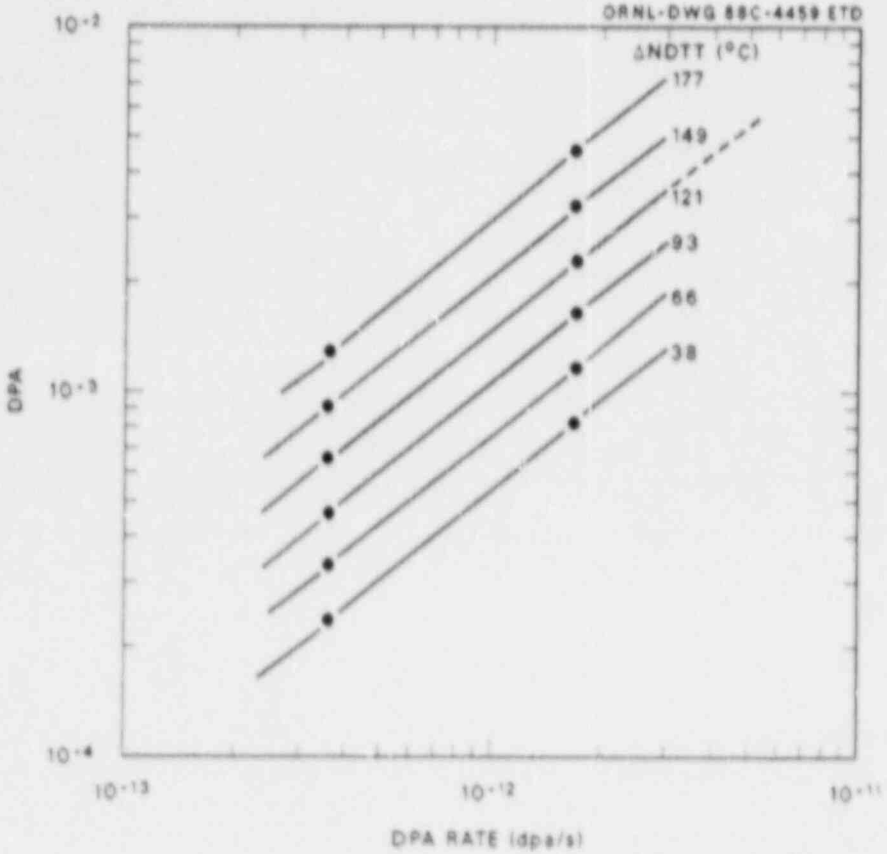

Fig. 4.7. DPA vs DPA rate with ΔNDTT as parameter (deduced from HFIR vessel surveillance data).

Table 4.1. Estimates of 32-EFPY ΔNDTT values corresponding to cavity fluxes at core midheight for "typical" LWR plants

NSSS designer (type reactor)	$\phi(E > 1$ MeV) (neutrons/cm^2·s)	dpa rate ($E > 0.1$ MeV) (dpa/s)	dpa ($E > 0.1$ MeV)	ΔNDTT[a] (°F)	
				MTR[b]	HFIR[c]
GE (BWR)[d]	2.9×10^7	5.8×10^{-14}	5.8×10^{-5}	0	[e]
B&W (PWR)[f]	2.0×10^8	6.1×10^{-13}	6.1×10^{-4}	~20	180
W (PWR)	5.9×10^8	3.9×10^{-12}	3.9×10^{-3}	50	240
CE (PWR)	1.8×10^9	4.5×10^{-12}	4.5×10^{-3}	70	240

[a] Applies only to plants with vessel supports that extend vertically to midheight of core.

[b] MTR curve in Fig. 4.5.

[c] See Fig. 4.7.

[d] Boiling-water reactor.

[e] No attempt made to extrapolate to dpa $<1 \times 10^{-4}$.

[f] Pressurized-water reactor.

high-flux region opposite the core. For example, all but one of the vessels in B&W plants are supported by skirts at the bottom of the vessel, well away from the core (vessels in GE plants are supported on skirts, also). On the other hand, shield-tank and long-column-type supports (Fig. 4.2) do extend the full length of the core, and some others extend to and below the top of the core.

The concern over embrittlement is that the probability of support failure as a result of propagation of sharp, cracklike defects (flaws) increases with increasing embrittlement (increasing NDTT). Most supports are nominally loaded in compression, and this tends to minimize the chances of flaw propagation. However, some supports are in bending, at least under some loading conditions; some are exposed to thermal gradients that induce significant thermal tensile stresses; and some contain welds that introduce residual tensile stresses. Thus, assuming flaws to exist, presumably the ingredients (flaws, tensile stress, and low toughness) do exist in some supports for flaw propagation. Therefore, it appears that the embrittlement rate effect deduced from the HFIR surveillance program may significantly impact the life expectancy of some PWR vessel supports.

4.1.4 Summary and conclusions

Data from the HFIR pressure vessel surveillance program indicate an embrittlement rate effect that may have a significant impact on the life expectancy of some PWR vessel supports. However, the necessity for extensive extrapolation of the HFIR data and the correlation of data with neutron energies only above 0.1 MeV introduce substantial uncertainties. Furthermore, it is premature to state what the effect of embrittlement is on the life expectancy of the vessel supports. There is, however, sufficient evidence of an embrittlement rate effect to justify a continuing effort to obtain more definitive answers. This effort is under way at the request of the NRC.

4.2 BWR Vessel Integrity Assessment

R. D. Cheverton   D. G. Ball

In November 1987 the NRC requested that ORNL begin to evaluate the integrity of BWR vessels when subjected to pressurized-thermal-shock (PTS) loading. Two specific reasons for concern are that (1) surveillance data from BWRs indicate that the embrittlement rate may be greater than expected and (2) the 10-year inspection for flaws specified by the ASME code is not required by the NRC for boiling-water-reactor (BWR) vessels. Previously it was believed that radiation-induced embrittlement of BWR vessels and thus the potential for propagation of flaws in the belt-line region of these vessels were essentially negligible.

The approach selected for the present evaluation involves the calculation of the conditional probability of vessel failure in accordance with the methodologies developed for the Integrated Pressurized-Thermal

Shock (IPTS) Program.[8] This approach permits consideration of the influence of in-service inspection on the calculated probability of failure, because it is necessary to specify flaw density and flaw size distribution. For the analyses conducted thus far, values of these parameters are consistent with no in-service inspection. Details of the method of analysis for estimating the conditional probability of vessel "failure" [$P(F|E)$] and of the parameters simulated are discussed in Refs. 8–10.

Accident scenarios were discussed with S. Hodge (ORNL) and W. Hodges (NRC), and a more specific transient, the design basis accident (DBA), is described in Ref. 11. This latter transient involves complete circumferential failure of one of the recirculation loops (Fig. 4.8) while the reactor is at full power. As indicated in Fig. 4.9, the vessel will depressurize in ~30 s. The low pressure activates the core spray systems and the low-pressure coolant injection (LPCI) system. Cold water is injected through the core spray system onto the top of the core and through the LPCI system to the bottom of the core (Fig. 4.10). Within 85 s, the LPCI cold water, which enters through half of the jet pumps, spills over the top of the jet pumps, coming in contact with the vessel wall. Thus, the vessel wall is exposed to a low-temperature coolant, and the vessel pressure and bulk coolant temperatures are further reduced (Figs. 4.11 and 4.12). Table 4.2 shows the "conservative" estimates of the bulk coolant temperatures and heat transfer coefficient adjacent to the vessel wall.[11] As indicated, within 30 s the coolant temperature is down to 138 from 288°C, and during this time the heat transfer coefficient is very

Table 4.2. Bulk-fluid temperatures and fluid-film heat transfer coefficient at inner surface of vessel wall for DBA[11]

Time after DBA (s)	Bulk-fluid temperatures		Heat transfer coefficients	
	Region II T_F [°C (°F)]	Region III T_F [°C (°F)]	Region II h [W/cm^2·°C (Btu/h·ft^2·°F)]	Region III h [W/cm^2·°C (Btu/h·ft^2·°F)]
0	228 (550)	288 (550)	5.68×10^4 (10,000)	5.68×10^4 (10,000)
10	260 (500)	260 (500)	5.68×10^4 (10,000)	5.68×10^4 (10,000)
20	199 (390)	199 (390)	5.68×10^4 (10,000)	5.68×10^4 (10,000)
25	149 (300)	154 (310)	5.68×10^4 (10,000)	5.68×10^4 (10,000)
30	138 (280)	138 (280)	5.68 (10)	56.8 (10)
40	132 (270)	132 (270)	5.68 (10)	56.8 (10)
80	132 (270)	132 (270)	5.68 (10)	56.8 (10)
85	21 (70)	132 (270)	2.84×10^3 (500)	56.8 (10)
175	21 (70)	127 (260)	2.84×10^3 (500)	56.8 (10)
500	21 (70)	121 (250)	2.84×10^3 (500)	56.8 (10)
700	21 (70)	116 (240)	2.84×10^3 (500)	56.8 (10)
1000	21 (70)	110 (230)	2.84×10^3 (500)	56.8 (10)
2000	21 (70)	107 (225)	2.84×10^3 (500)	56.8 (10)
3000	21 (70)	107 (224)	2.84×10^3 (500)	56.8 (10)

ORNL-DWG 88-4460 ETD

	PRESSURE (psia)	FLOW (lb/h)	TEMPERATURE (°F)	ENTHALPY (Btu/lb)
1. CORE INLET	1060	77×10^6	532	526.9
2. CORE OUTLET	1033	77×10^6	548	634.9
3. SEPARATOR OUTLET (STEAM DOME)	1020	10.5×10^6	547	1191.5
4. STEAM LINE (2nd ISOLATION VALVE)	985	10.5×10^6	543	1191.5
5. FEEDWATER INLET (INCLUDES CLEANUP RETURN FLOW)	1045	10.5×10^6	420	397.8
6. RECIRCULATION PUMP SUCTION	1032	34.2×10^6	532	526.8
7. RECIRCULATION PUMP DISCHARGE	1206	34.2×10^6	533	527.6

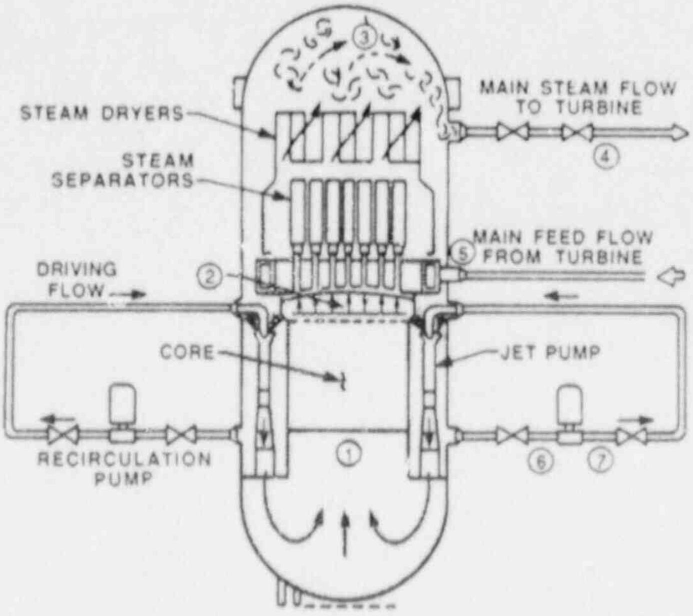

Fig. 4.8. Schematic of BWR pressure vessel internals and recirculating system. *Source*: Ref. 11.

large. There is a brief period of steam blanketing (~50 s); at 85 s the coolant temperature is 21°C, and the heat transfer coefficient 2.84×10^3 $W/m^2 \cdot {}^\circ C$.

On the basis of the discussions with Hodge and Hodges and the previous description of the DBA, it was tentatively concluded that BWR vessels may be subjected to thermal-shock loading as a result of sudden loss of pressure, but presumably there is no means for rapid repressurization. Thus, the conditional probability of failure [P(F|E)] was calculated for thermal-shock loading conditions only. An exponential decrease in coolant temperature of the form $T_c = T_F + (288 - T_F)e^{-\beta t}$ was considered, and calculations were made for $\beta = \infty$ (step change in temperature from 288°C

ORNL-DWG 88-4461 ETD

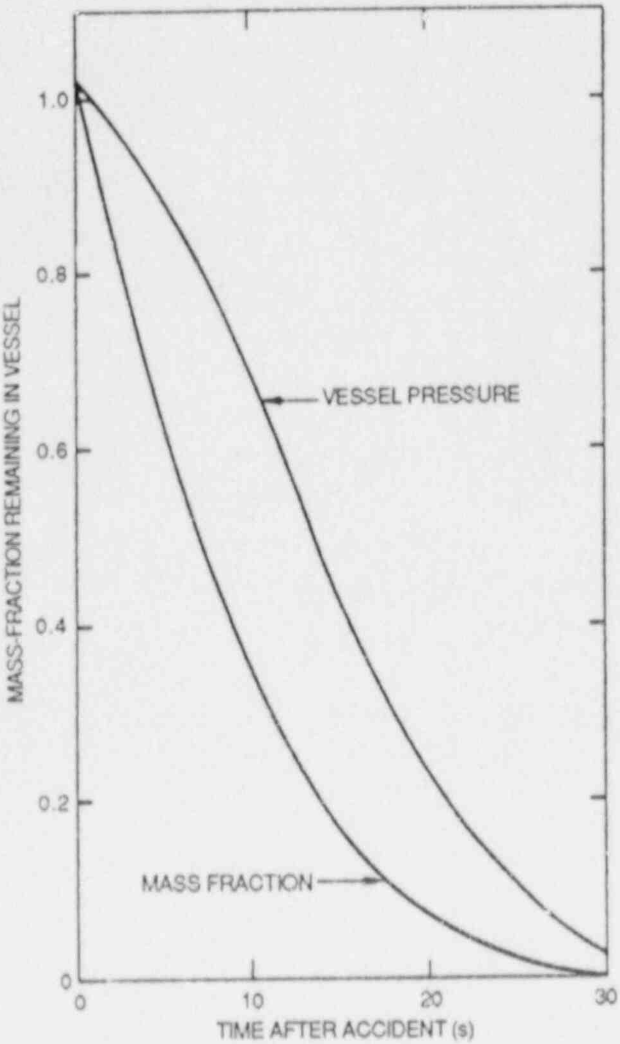

Fig. 4.9. Vessel pressure and mass fraction following DBA. *Source*: Ref. 11.

to T_F), β = 0.15 min^{-1} (ΔT = 167°C for t = 13 min), and T_F = 93 and 121°C. For all cases, the pressure was assumed to be essentially atmospheric. Two values of the fluid-film, heat-transfer coefficient were used (1.70×10^3 and 3.41×10^3 $W/m^2 \cdot °C$), the lower value representing natural convection and the higher value moderate forced convection.

Thus far, two sets of calculations have been made. For the first set, radiation embrittlement was deduced from the PTS embrittlement trend curve used for the IPTS studies;[8] fluence data[12] were taken from a very early compilation (Table 4.3); copper (Cu) and nickle (Ni) concentrations of 0.35 and 0.80% were used; and the initial value of RT_{NDT} was 18°C. For both sets of calculations the flaws were axially oriented and two dimensional (2 D), and the vessel dimensions were 6.50-m inside diameter,

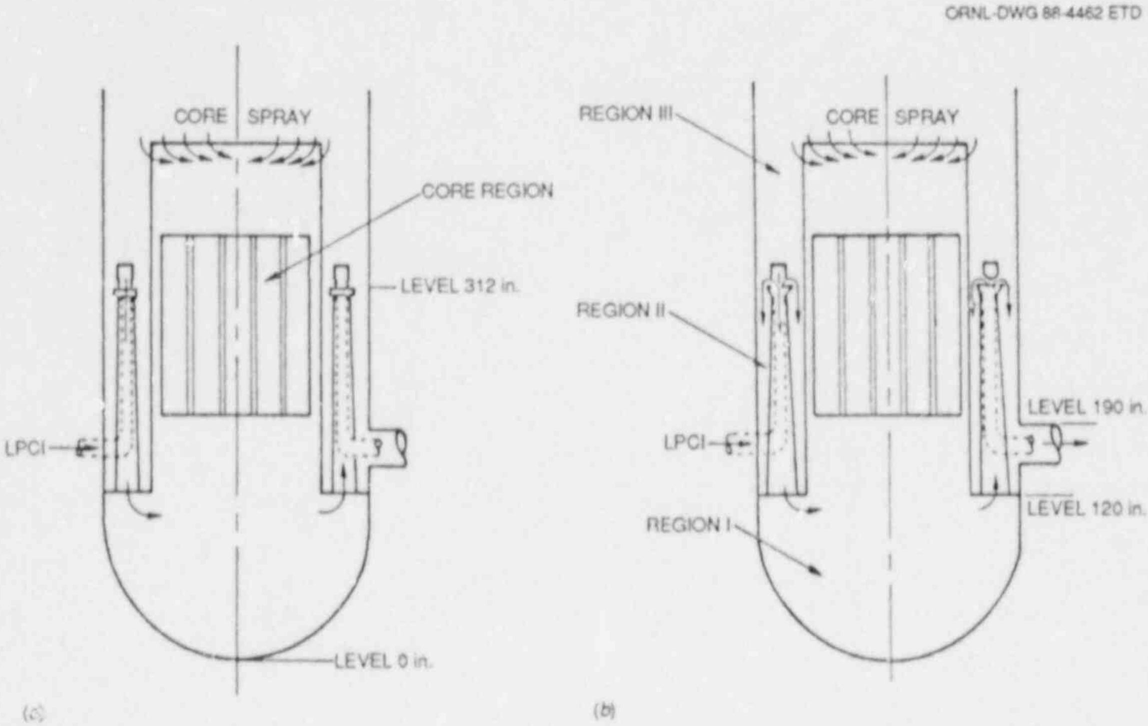

Fig. 4.10. Cooling water injection into BWR vessel. *Source*: Ref. 11.

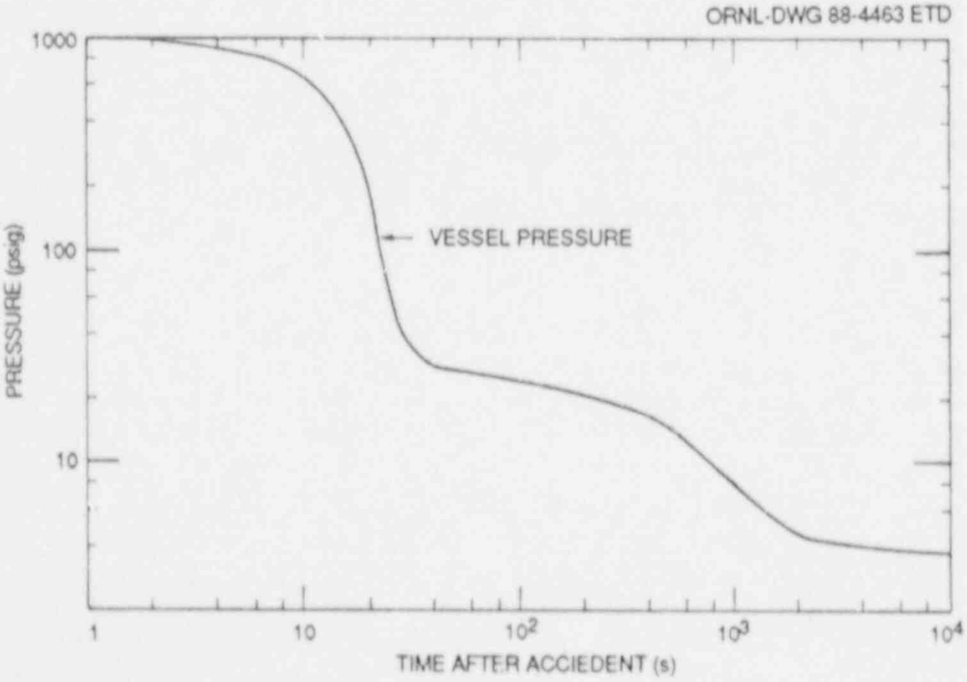

Fig. 4.11. Vessel internal pressure after DBA. *Source*: Ref. 11.

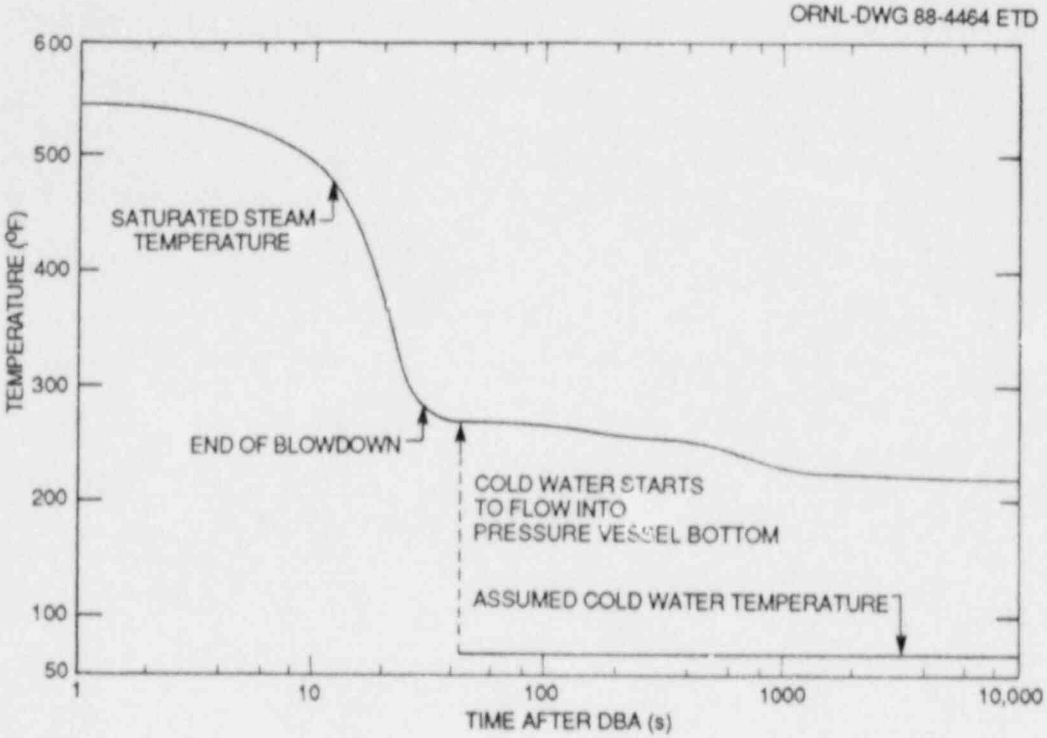

Fig. 4.12. Bulk fluid temperature after DBA. *Source*: Ref. 11.

Table 4.3. Fast-neutron fluence for several BWR vessels at end of life[a] (preliminary data)

Reactor	Thermal power (MW)	Reactor life (years)	Fluence (E > 1 MeV) (neutrons/cm^2)
Big Rock Point	157	40	4×10^{18}
La Crosse	165	20	1×10^{19}
Oyster Creek	1600	40	9×10^{17}
Nine-Mile Point	1500	40	7×10^{17}
Dresden-2	2300	40	2×10^{17}
Millstone Point	1700	40	4×10^{17}
Browns Ferry	3300	40	4×10^{17}
Dresden-3	2500	40	2×10^{17}
Quad Cities-1	2500	40	2×10^{17}
Monticello	1700	40	5×10^{17}
Vermont Yankee	1600	40	1×10^{17}

[a] Data taken from Ref. 12. Fluences for BWRs not listed are reported in FSARs to be $<10^{19}$ neutrons/cm^2.

0.156-m wall, and 3.81 mm of cladding. Also, for both sets of calculations, the flaw density was assumed to be 0.1 flaws/vessel, consistent with what was considered to be reasonable for the IPTS studies.[8]

Results for the first set of calculations are presented in Table 4.4. As indicated for a fluence (Φ) of 1×10^{19} neutrons/cm^2, the conditional probability of crack initiation [P(I|E)] ranges from 4×10^{-6} to 8×10^{-4}, and the conditional probability of a flaw initiating and not arresting within the inner 95% of the wall [P(F|E)] ranges from 2×10^{-7} to 7×10^{-5}. [Of course, the slower the thermal transient and the smaller the value of the surface heat transfer coefficient (h), the lower the probability of "failure."] For fluences of 3×10^{18} and 1×10^{18} neutrons/cm^2, the probabilities are about 2 and 5 orders of magnitude less, respectively.

Table 4.4. Calculated values of P(I|E) and P(F|E) corresponding to two postulated transients and a flaw density of 0.1 flaw/vessel

Transient[a]	h[b] (W/m^2·°C)	Fluence (E > 1 MeV) (neutrons/cm^2)			
		P(I|E)[c]			P(F|E)[d]
		1×10^{18}	3×10^{18}	1×10^{19}	1×10^{19}
1	1.70×10^3			4×10^{-5}	2×10^{-6}
1	3.41×10^2	5×10^{-9}	5×10^{-6}	8×10^{-4}	7×10^{-5}
2	1.70×10^3			4×10^{-6}	2×10^{-7}
2	3.41×10^3			4×10^{-5}	5×10^{-6}

[a] Transient 1: step change in coolant temperature from 288 to 93°C and in pressure from normal operating pressure to essentially atmospheric.

Transient 2: exponential decrease in coolant temperature ($T = 93°\text{C} + 194e^{-\beta t}$, $\beta = 0.15\ \text{min}^{-1}$, T in °C) and step change in pressure to essentially atmospheric.

[b] Surface heat transfer coefficient.

[c] Conditional probability of crack initiation.

[d] Conditional probability of crack initiation without crack arrest within the inner 95% of the wall.

Preliminary information from the NRC (W. Hodges) indicates that ~50 depressurization transients have occurred at BWR plants. There are ~30 BWR plants, and they have an average operating time of ~10 years. Thus, the frequency of "failure" associated with the depressurization transients is about a factor of 5 less than the values of P(F|E). It is apparent that even for the very severe conditions considered, all of the plants except possibly Big Rock Point and La Crosse have very low estimated frequencies of failure.

For the second set of calculations an updated compilation of vessel chemistry, initial RT_{NDT}, and fluence data were used;[13] on the basis of information in Ref. 14 and discussions with Neil Randall,[15] *Regulatory Guide 1.99* Rev. 2 was used in lieu of the PTS trend curve. (As indicated by Figs. 4.13 and 4.14, even *Regulatory Guide 1.99* Rev. 2 may underestimate the damage rate in BWRs.)

For the first set of calculations referred to above, copper and Φ were simulated and used as independent variables. In the most recent study, ΔRT_{NDT} was used as an independent variable instead, and the distribution for ΔRT_{NDT} was obtained using the *Regulatory Guide 1.99* Rev. 2 trend curve and Monte Carlo techniques. In this study Cu, Ni, and Φ were used as independent variables, and ΔRT_{NDT} was, of course, the dependent variable. A typical distribution for ΔRT_{NDT} with Cu = 0.30%, Ni = 1.0%, and $\Phi = 3 \times 10^{18}$ neutrons/cm^2 is shown in Fig. 4.15. The distribution is not quite normal, but the use of a normal distribution tends to be conservative. As indicated in Table 4.5, the standard deviation is a mild

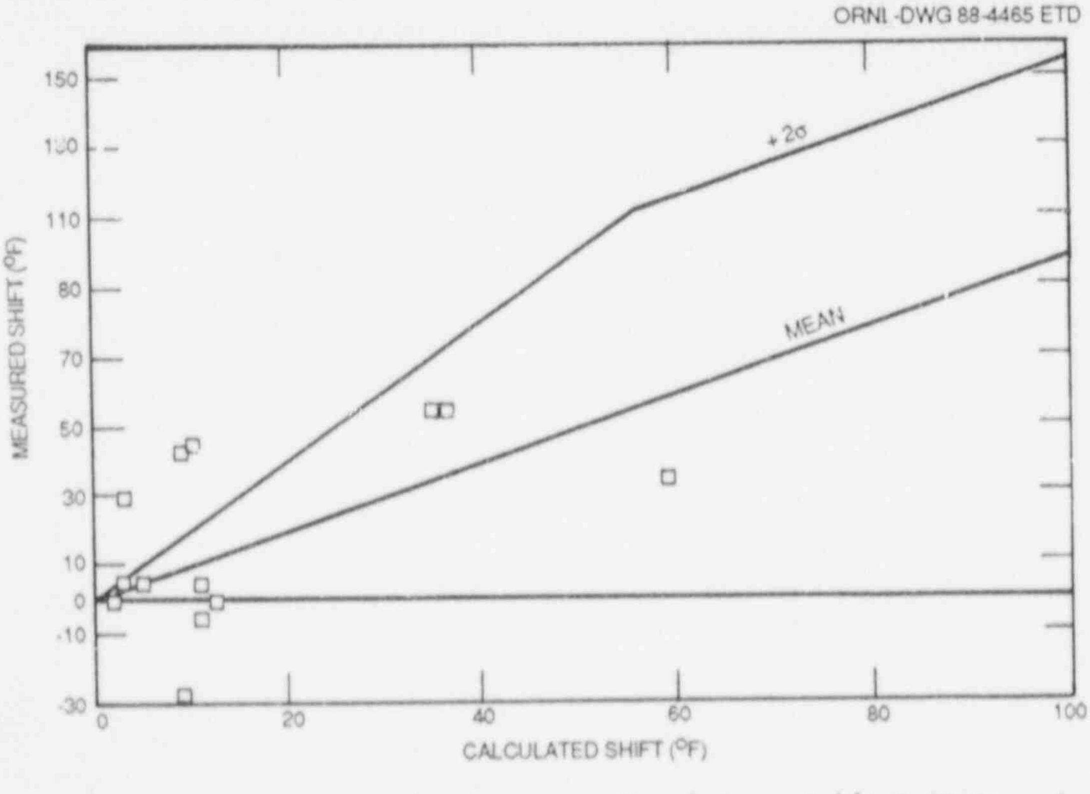

Fig. 4.13. BWR weld shift data vs *Regulatory Guide 1.99* Rev. 2. *Source*: Ref. 14.

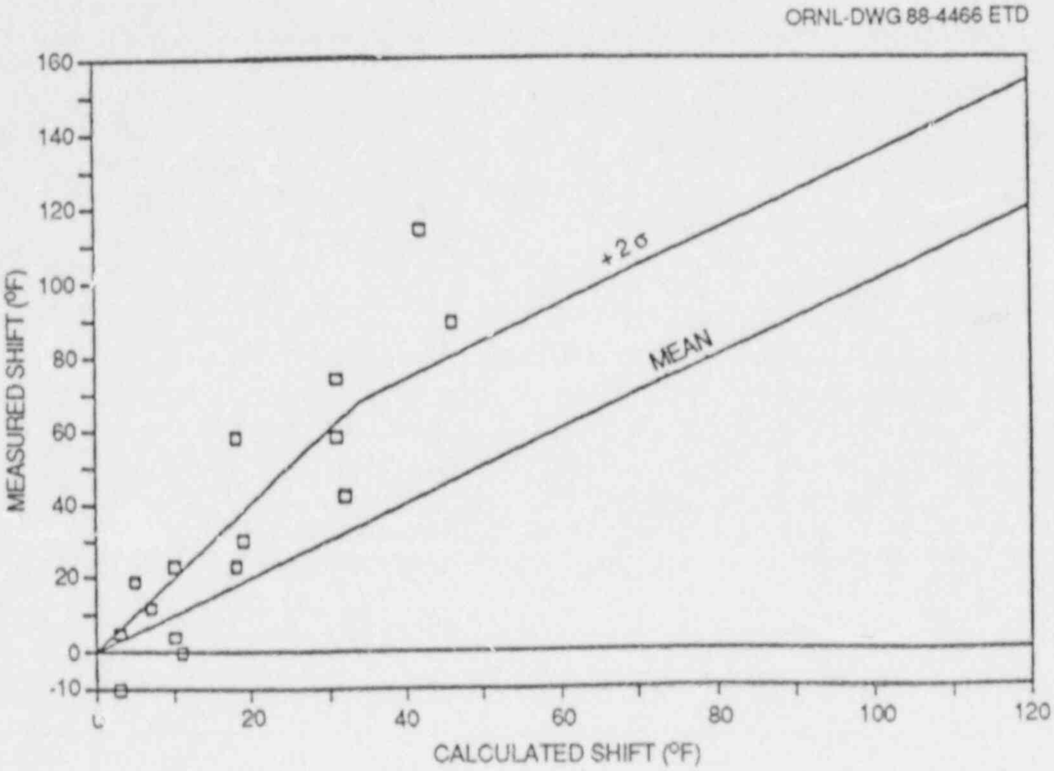

Fig. 4.14. BWR plate shift data vs *Regulatory Guide 1.99* Rev. 2. *Source*: Ref. 14.

Table 4.5. Calculated ΔRT_{NDT} standard deviation as a function of fluence (Φ) (based on *Regulatory Guide 1.99* Rev. 2 with copper = 0.30%, nickle = 1.0%)

Fluence	Standard deviation (% of mean)
2E19	9
1E19	10
3E18	13
1E18	16

ORNL-DWG 88-4467 ETD

```
235+*                                                        8
225 |*                                                      78
    |***                                                   547
205 |************                                         2249
    |***************************                          5431
185 |*******************************************          8617
    |************************************************     9743
165 |*******************************************          8654
    |******************************                       6063
145 |********************                                 3889
    |***********                                          2169
125 |******                                               1154
    |***                                                   596
105 |**                                                    335
    |*                                                     173
 85 |*                                                     124
    |*                                                      62
 65 |*                                                      29
    |*                                                      23
 45 |*                                                      15
    |*                                                       6
 25 |*                                                       7
    |*                                                       3
  5 |*                                                      25
    ----+----+----+----+----+----+----+----+----+---
```

ΔRT_{NDT}

DEPENDENT VARIABLE: ΔRT_{NDT}

INDEPENDENT VARIABLE:	MEAN	STANDARD DEVIATION	TRUNCATION
FLUENCE	3×10^{18}	9×10^{17}	>= 0.0
% COPPER	0.3	0.025	<= 0.4
% NICKEL	1.0	0.0	

Fig. 4.15. Distribution for ΔRT_{NDT} based on *Regulatory Guide 1.99* Rev. 2.

function of the mean value of the fluence. For this second set of calculations of P(F|E), a normal distribution with a standard deviation of 16% of the mean was used for ΔRT_{NDT}.

Thus far, calculated values of P(F|E) and P(I|E), based on *Regulatory Guide 1.99* Rev. 2 and using ΔRT_{NDT} as the independent variable, have been obtained for step changes in coolant temperature from 288 to 93°C and from 288 to 121°C, a fluid-film heat transfer coefficient of 3.4×10^3 $W/m^2 \cdot °C$, and three valves of RT_{NDT_0} (−40, −18, 4°C). The results are presented in Figs. 4.16 and 4.17 for P(F|E) and Figs. 4.18 and 4.19 for P(I|E).

The results in Figs. 4.16–4.19 are based on one flaw per vessel. As mentioned previously, based on the studies in Ref. 8, a flaw density of 0.1 flaw/vessel is more realistic. Thus, the values in Figs. 4.16–4.19 can be multiplied by 10^{-1}.

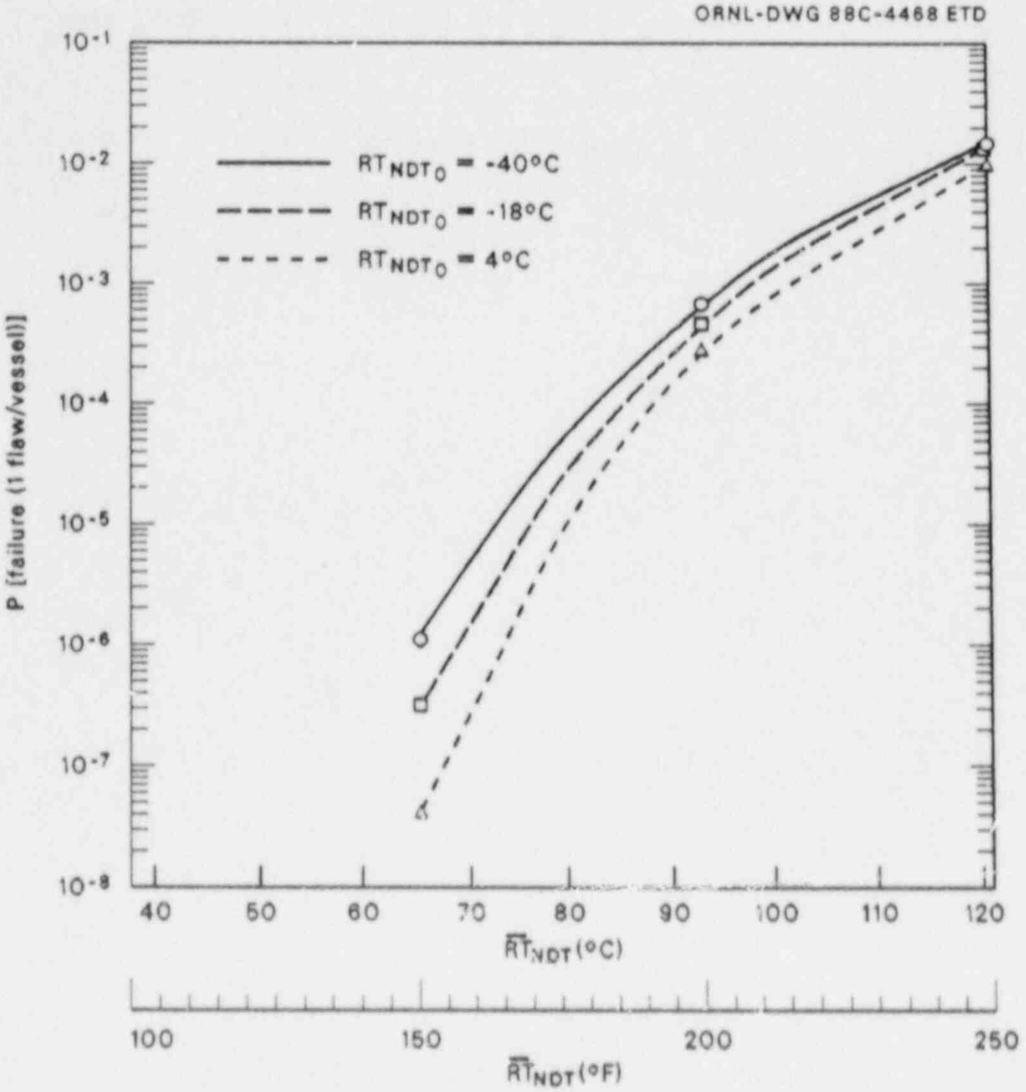

Fig. 4.16. P(F|E) vs RT_{NDT} for step change in coolant temperature from 288 to 93°C and for one flaw per vessel.

Based on the recent compilation of chemistry, RT_{NDT_0} and 32-EFPY fluences for all BWR vessels[13] and the information in Figs. 4.16–4.19, it appears that the most susceptible BWR vessel is one with RT_{NDT} = 157°C and RT_{NDT_0} = +4°C. For this vessel and a step change in coolant temperature of 194°C, P(F|E) < 1×10^{-9}, and P(I|E) ≈ 1×10^{-7}; for a step change of 167°C, P(F|E) < 1×10^{-9}, and P(I|E) < 1×10^{-9}.

If the actual time dependence of the coolant temperature were included, the results would not be significantly different because the initial decrease in temperature (Figs. 4.9 and 4.12) is so rapid. However, if the lower value of T_F indicated in Table 4.2 were used (21°C), P(I|E) would be substantially greater.

ORNL-DWG 88C-4469 ETD

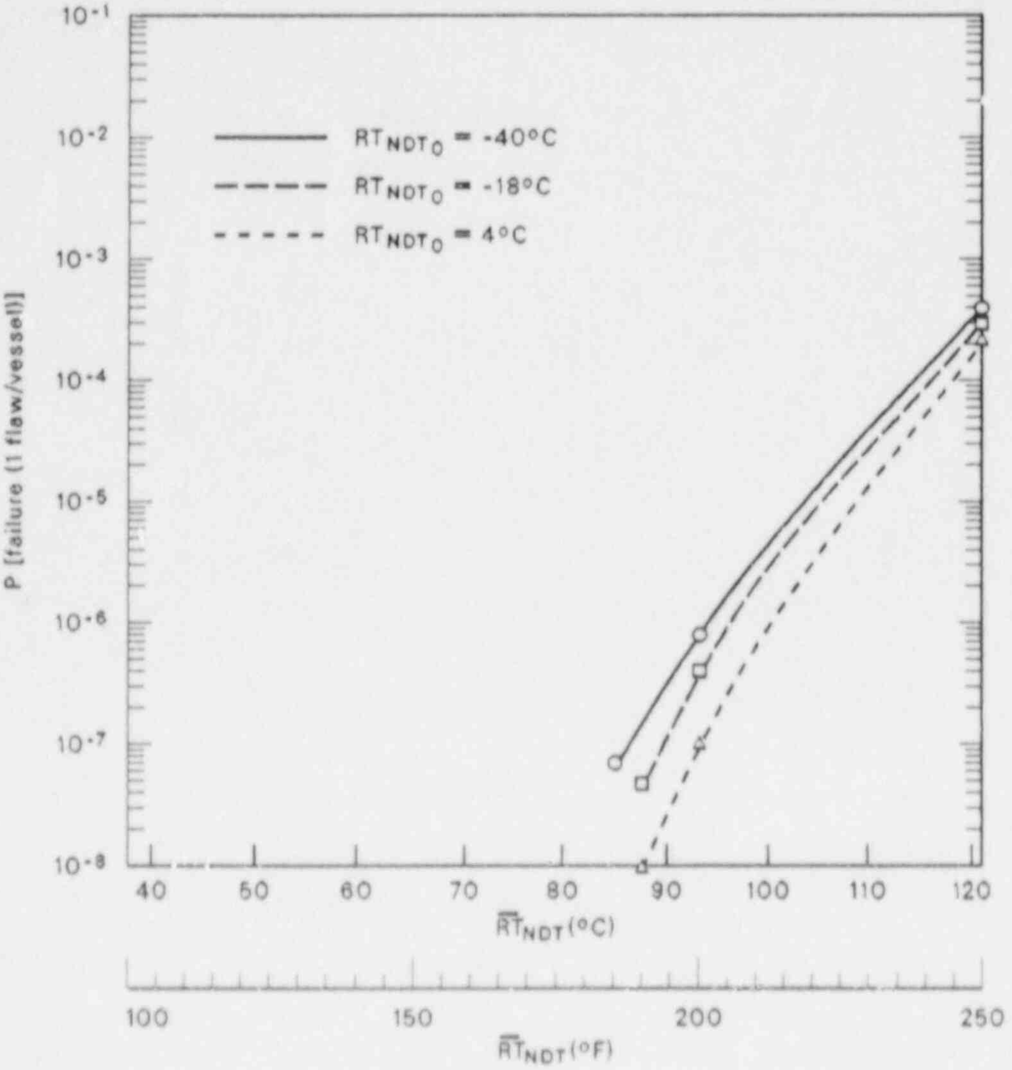

Fig. 4.17. P(F|E) vs RT_{NDT} for step change in coolant temperature from 288 to 121°C and for one flaw per vessel.

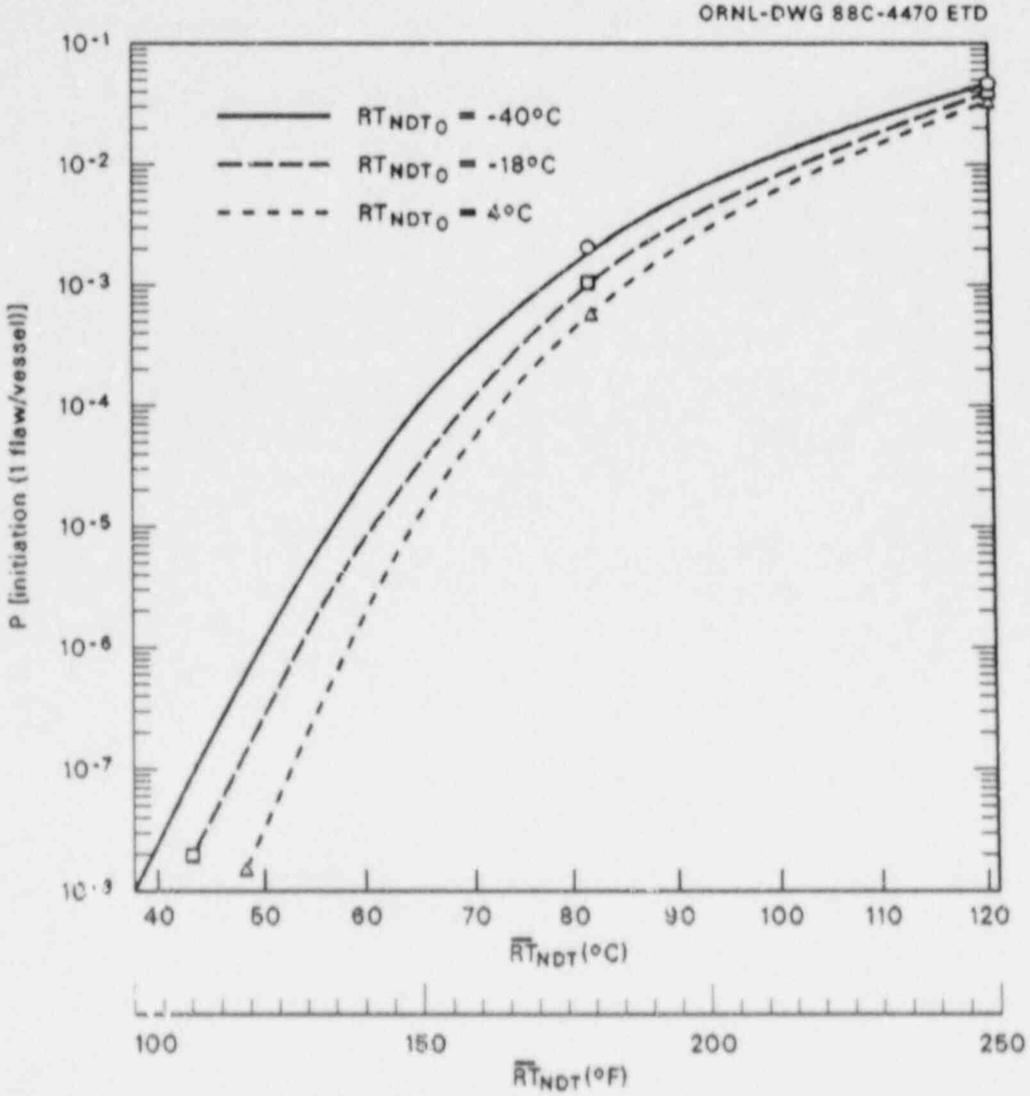

Fig. 4.18. P(I|E) vs $\overline{RT}_{NDT}$ for step change in coolant temperature from 288 to 93°C and for one flaw per vessel.

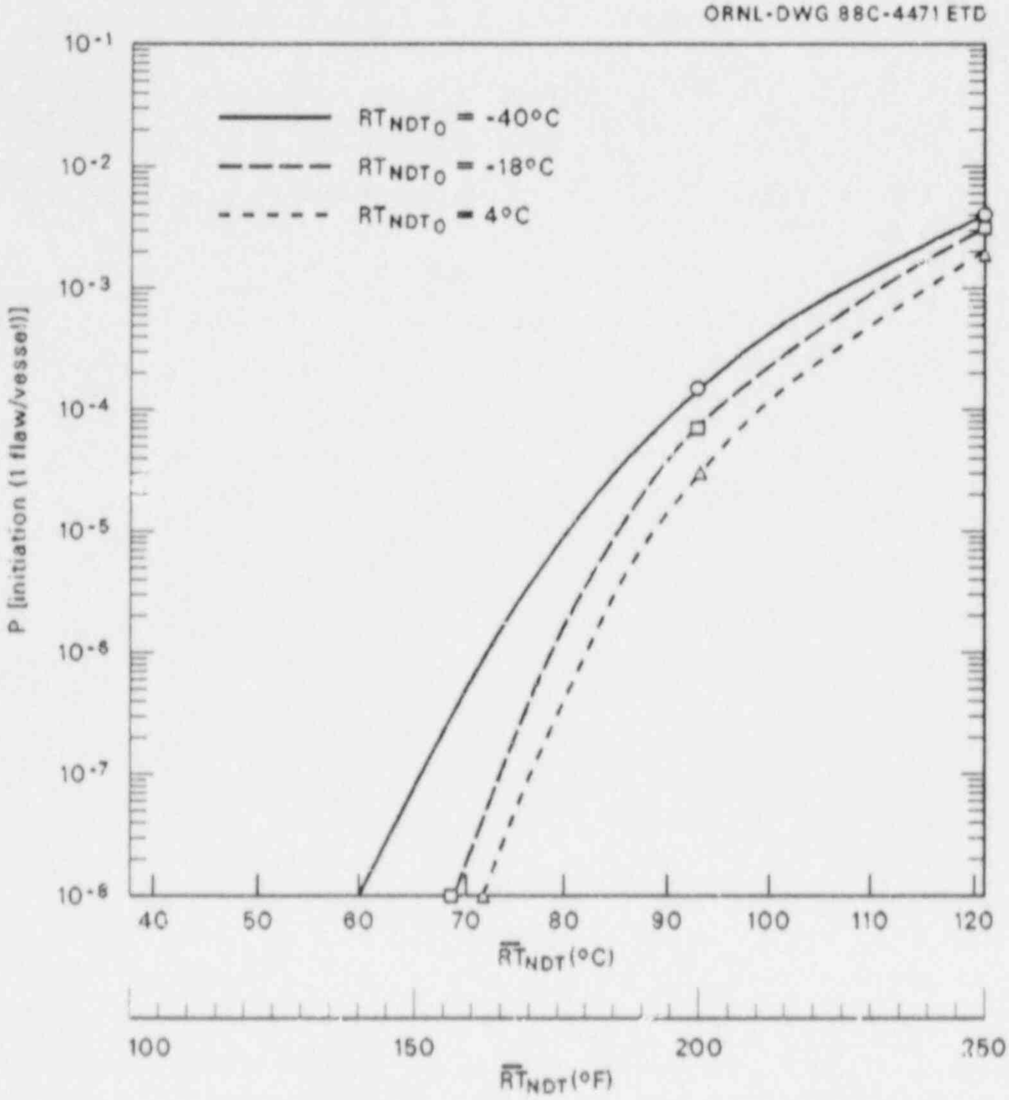

Fig. 4.19. P(I|E) for step change in coolant temperature from 288 to 121°C and for one flaw per vessel.

A decrease in P(F|E) can be achieved by using a more realistic flaw shape [three dimensional (3 D) as opposed to 2 D]. However, results of the IPTS studies[8] indicated that the effect was not large. Perhaps the greatest reduction in the calculated frequency of failure can be achieved by thoroughly examining the frequency of events.

4.3 Evaluation of J-R Curve Validity Requirements

R. K. Nanstad J. G. Merkle
S. Druce

The specific problem concerns the continued operation of PWRs with low-upper-shelf weld toughness. Already, 2 plants have fallen below the legal screening limit of 68 J, and it is anticipated that an additional 15 plants will do so before reaching the end of their original design lives. It is intended that continued operation below the 68-J limit can be justified using an instability (J-T) analysis demonstrating that unstable crack propagation will not occur. A draft ASME document using this approach suggests that crack extensions up to 0.7 in. (18 mm) may be required. Furthermore, it is proposed that J_{mod} should be used rather than the conventional deformation J (J_D). However, the use of J_{mod} may be premature, because some J-delta a data are known to exhibit an upward curvature that is physically unacceptable. Further doubts arise from an analysis of the HSST intermediate test vessel V-8A where the experimentally observed instability is predicted using J_D but not using J_{mod}.

A series of ad hoc working group meetings have been held to pursue informal discussion with two objectives:

1. examine which J parameter is the more correct and define ranges of validity, in particular, the allowable amount of crack extension; and
2. determine how small specimen data may be extrapolated and applied to structures.

Means for extrapolation of data are required as surveillance specimens, even when available, are generally either 0.5T or 1T compacts. A specimen size effect program is being conducted at Materials Engineering Associates using a plate of A 302 grade B steel with homogeneous properties and a low-upper-shelf energy of ~68 J. The tests are to be controlled to the highest capability of modern unloading compliance techniques to provide an accurate data set on appropriate material for the evaluation of the previous two issues.

Apart from the specific problem that requires some progress on a short time scale, the questions being addressed are generic to most structural integrity problems. In particular, the questions are germane to leak-before-break situations. Conclusions from the discussions to date are summarized as follows.

1. There remains considerable uncertainty regarding which J-like parameter is fundamentally more correct and its range of applicability.
2. At present, for conservatism, it would appear prudent to continue with deformation theory J, although with further advances in defining limits of applicability J_{mod} may be preferred.
3. For many materials, existing crack growth (delta a) limits in testing standards now appear unduly conservative: 30% of the remaining ligament appears more appropriate.

4. In testing high-toughness materials, it is more difficult to obtain "valid" data covering a fixed amount of crack extension. For these materials, J limitations are likely to be more restrictive than crack extension limits; thus, it is unlikely that any increase in allowable crack extension would be of particular benefit. This is likely to be the case with modern high-purity reactor pressure vessel steels and austenitic stainless steels.
5. There is a continuing need for development of elastic-plastic fracture-mechanics (EPFM) testing techniques to assist in the evaluation of different EPFM parameters, their ranges of applicability, and means of extrapolation to larger crack extensions.
6. Current approaches to defining allowable J and delta a limits are incomplete because they do not include a material sensitivity factor relating crack growth to changes in crack-tip constraint.

During the next report period, participation in the working group will continue, and a summary report will be compiled on the current state-of-the-art assessment methods for low-upper-shelf welds in general.

References

1. R. D. Cheverton and T. M. Sims, *HFIR Core Nuclear Design*, ORNL-4621, Union Carbide Corp. Nuclear Div., Oak Ridge Natl. Lab., July 1971.

2. R. D. Cheverton, J. G. Merkle, and R. K. Nanstad, eds., *Evaluation of HFIR Pressure-Vessel Integrity Considering Radiation Embrittlement*, ORNL/TM-10444, Martin Marietta Energy Systems, Inc., Oak Ridge Natl. Lab., April 1988.

3. J. R. McWherter, R. E. Schappel, and J. R. McGuffey, *HFIR Pressure Vessel and Structural Components Material Surveillance Program*, ORNL/TM-1372, Union Carbide Corp. Nuclear Div., Oak Ridge Natl. Lab., January 1966.

4. J. R. Hawthorne, "Studies of Radiation Effects and Recovery of Notch Ductility of Pressure Vessel Steels," British Nuclear Energy Conference, Iron and Steel Institute, London, England, November 30, 1960.

5. L. E. Steele et al., *Irradiated Materials Evaluation and Reactor Pressure Vessel Surveillance for the Army Nuclear Power Program*, NRL Memorandum Report 1644, September 1, 1965.

6. Nicolas Tsoulfanidis et al., "Neutron Energy Spectrum Calculations in Three PWR's," *Proc. Fifth ASTM-EURATOM Symposium on Reactor Dosimetry*, pp. 693–701, 1985.

7. M. L. Williams, Oak Ridge National Laboratory, personal communication to R. D. Cheverton, Oak Ridge National Laboratory.

8. D. S. Selby et al., *Pressurized Thermal Shock Evaluation of the H. B. Robinson Unit 2 Nuclear Power Plant*, NUREG/CR-4183 (ORNL/TM-9567), Martin Marietta Energy Systems, Inc., Oak Ridge Natl. Lab., September 1985.

9. R. D. Cheverton and D. G. Ball, *OCA-P, A Deterministic and Probabilistic Fracture-Mechanics Code for Application to Pressure Vessels*, NUREG/CR-3618 (ORNL-5991), Martin Marietta Energy Systems, Inc., Oak Ridge Natl. Lab., May 1984.

10. D. G. Ball and R. D. Cheverton, *Adaptation of OCA-P, A Probabilistic Fracture-Mechanics Code, to a Personal Computer*, NUREG/CR-4468 (ORNL/CSD/TM-233), Martin Marietta Energy Systems, Inc., Oak Ridge Natl. Lab., January 1986.

11. L. C. Hsu, *An Analytical Study of Brittle Fracture of GE-BWR Vessels Subjected to the Design Basis Accident*, NEDO-10029, June 1969.

12. G. D. Whitman, G. C. Robinson, and A. W. Savolainen, ed., *Technology of Steel Pressure Vessels for Water-Cooled Nuclear Reactors*, ORNL-NSIC-21, Union Carbide Corp. Nuclear Div., Oak Ridge Natl. Lab., December 1967.

13. Personal communication from M. Mayfield (Nuclear Regulatory Commission) to R. D. Cheverton (Oak Ridge National Laboratory), March 22, 1988.

14. P. P. Stancavage, *US BWR Vessel Aging Mitigation*, NEA/UNIPEDE Specialist Meeting on Life-Limiting and Regulatory Aspects of Core Internals and Pressure Vessels, Stockholm, Sweden, paper No. 12, October 14–16, 1987.

15. Personal communication from P. N. Randall (Nuclear Regulatory Commission) to R. D. Cheverton (Oak Ridge National Laboratory).

5. CRACK-ARREST TECHNOLOGY

D. J. Naus

5.1 Background

The primary objective of the crack-arrest studies under the Heavy-Section Steel Technology (HSST) Program is to generate data for understanding the crack-arrest behavior of prototypical pressure-vessel steels at temperatures near and above the onset of the Charpy upper-shelf region. Program goals include (1) extending the existing K_{Ia} data bases beyond those associated with the upper limit in the *American Society of Mechanical Engineers Boiler and Pressure Vessel Code (ASME B&PVC)*; (2) clearly establishing that crack arrest occurs before fracture-mode conversion; (3) observing the relationship between arrest data and machine/specimen compliance behavior; and (4) validating the predictability of crack arrest, stable tearing, or unstable tearing sequences for ductile materials. Also, the tests and analyses provide bases for obtaining and interpreting dynamic fracture data (with relatively long crack runs) and for validating viscoplastic fracture models and analysis methods. During this report period, the program objectives and goals were investigated for a prototypical pressure-vessel material, A 533 grade B class 1 steel.

The wide-plate tests are being conducted at the National Bureau of Standards (NBS), Gaithersburg, Maryland, under an interagency agreement. The tests are designed to provide fracture-toughness measurements at temperatures approaching or above the onset of the Charpy upper-shelf regime in a rising toughness region and with an increasing driving force. In addition to providing crack-arrest data, the wide-plate tests provide information on dynamic fracture (run and arrest) processes that are being used by researchers at Oak Ridge National Laboratory (ORNL), Southwest Research Institute (SwRI), and the University of Maryland (UM) to develop and evaluate improved fracture-analysis methods (see Chap. 2).

Crack-arrest work is also being conducted at ORNL to develop the capabilities to perform small-specimen high-K_{Ia} tests. These activities are reported in Sect. 5.6.

5.2 Wide-Plate Crack-Arrest Testing*

R. deWit[†] S. R. Low[†]
R. J. Fields[†]

5.2.1 Introduction

The HSST wide-plate crack-arrest tests are being performed with the 27-MN-capacity testing machine at NBS. The first series of six tests

---

*Work sponsored by the HSST Program under Interagency Agreement No. DE-A105-840R21432 between the U.S. Department of Energy and the National Bureau of Standards.

[†] Fracture and Deformation Division, National Bureau of Standards, Gaithersburg, Maryland.

(WP-1.1 through WP-1.6) has been completed using specimens made from HSST plate 13A of A 533 grade B class 1 steel. The first four tests using a low-upper-shelf base material (WP-2.4, WP-2.1, WP-2.5, and WP-2.3) have also been completed. During this report period, analyses were completed for two additional tests that used A 533 grade B class 1 materials (WP-1.7 and WP-CE-1). Each test used a single-edge notched (SEN) plate specimen that was subjected to a thermal gradient along the plane of crack propagation. The linear thermal gradient, which provides a rising toughness field, was achieved by cooling the notched edge of the plate and heating the other edge. During each test, strain and temperature were obtained as functions of time and position. Also, load, crack-opening-displacement (COD), acoustic-emission (AE), and accelerometer data were obtained during each test as functions of time. Figure 5.1 presents a schematic of a wide-plate crack-arrest specimen, and Fig. 5.2

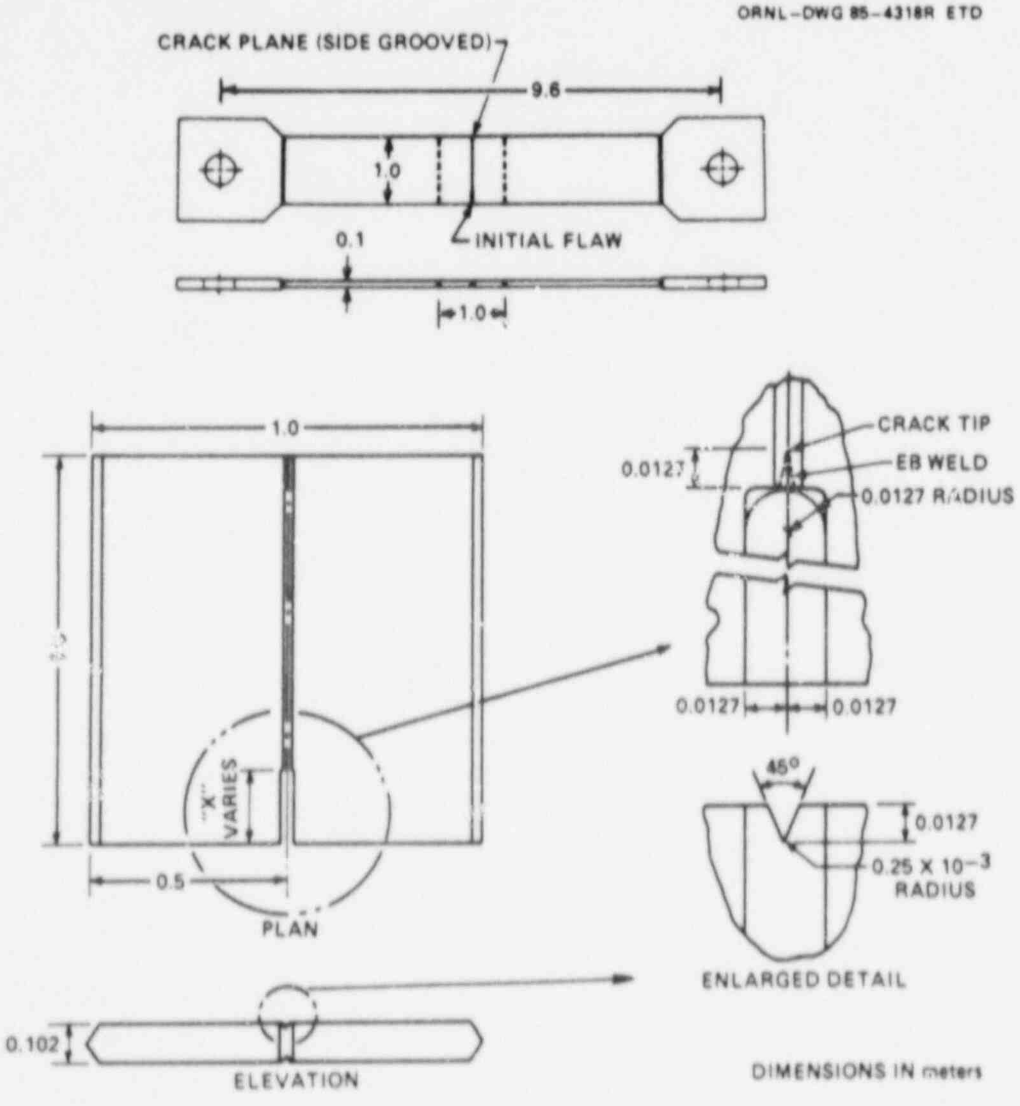

Fig. 5.1. Schematic of HSST wide-plate crack-arrest specimen.

ORNL-PHOTO 6718-85

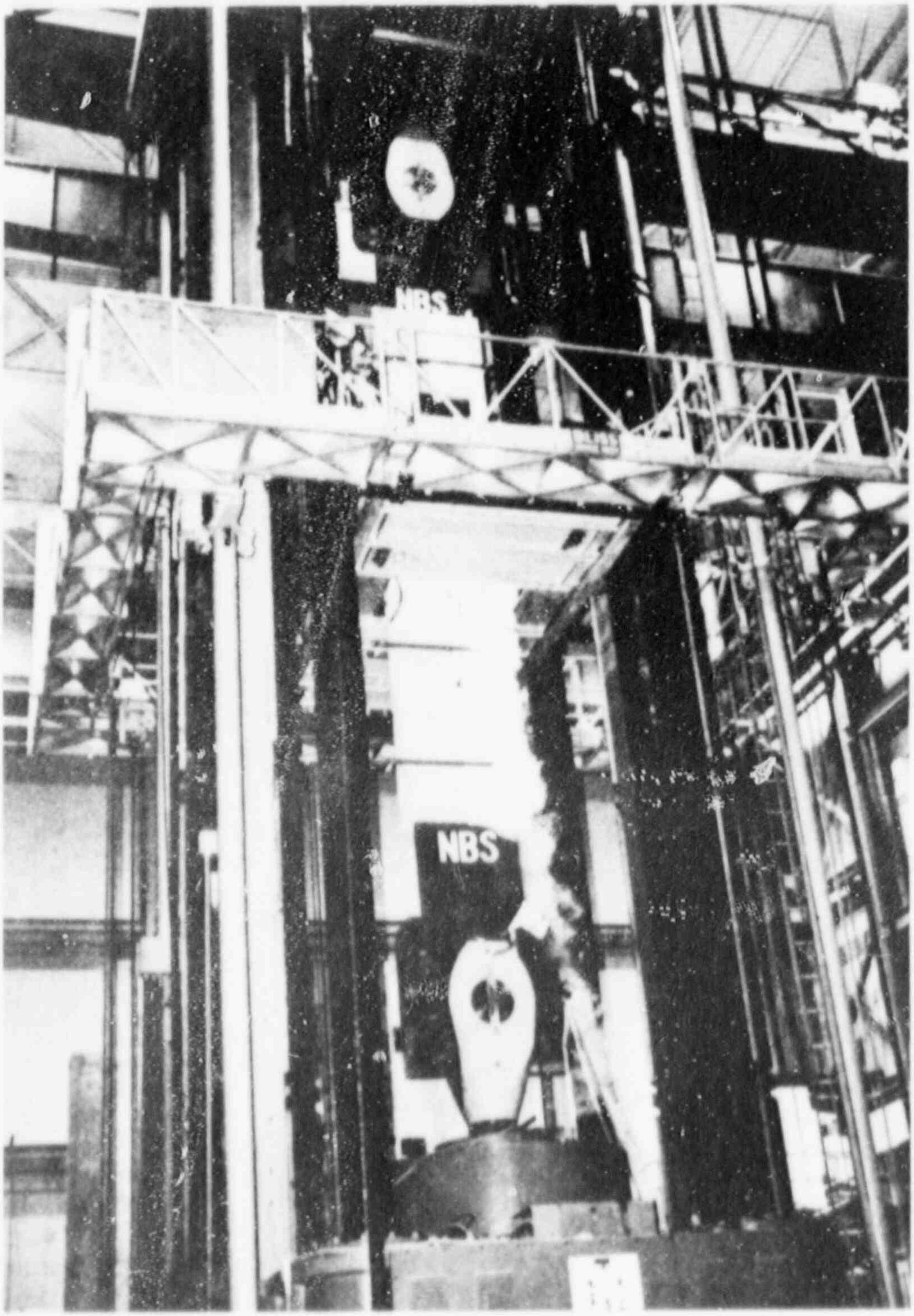

Fig. 5.2. Wide-plate crack-arrest test in progress using the 27-MN capacity tensile machine at NBS (Gaithersburg) fracture laboratory.

shows a specimen positioned in the NBS testing machine. More details on the specimen assembly are included in Ref. 1.

Tests WP-1.7 and WP-CE-1 were conducted on July 23, 1987, and September 14, 1987, respectively. The 1 × 1 × 0.15 m specimens (0.1 m for specimen WP-CE-1) were provided by ORNL. The specimens had been precracked by hydrogen charging an electron-beam (EB) weld located at the base of a premachined notch in the plate (Fig. 5.1). The crack front of specimens WP-1.7 and WP-CE-1 had also been cut into the chevron configuration shown schematically in Fig. 5.3. Table 5.1 presents specific dimensions for each of the plate specimens.

Table 5.1. Detailed dimensions of wide-plate crack-arrest specimens

Specimen feature	Symbol[a]	Dimension (mm)	
		WP-1.7	WP-CE-1
Initial crack length	a_o	202	200
Thickness	B	152.4	101.7
Notch thickness	B_N	114.3	76.3
Chevron thickness (thickness a_o)	B_C	61.0	40.0
Width	W	1000	1000
Pop-in crack length	a_o	NA	NA

[a] See Fig. 5.3.

5.2.2 Instrumentation and testing procedure

NBS welded the plate specimen to pull plates; the overall specimen dimensions for WP-1.7 and WP-CE-1 are presented in Fig. 5.4. (The length of pull plates changed from test to test because of the cutting procedure used to remove a specimen before the welding of the next specimen.) The specimens were then instrumented with 40 thermocouples positioned as shown in Fig. 5.5. Biaxial and uniaxial strain gages were placed on the specimen and pull plates as shown in Fig. 5.6. Additional instrumentation included (1) two COD gages installed on the front (F-COD) and back (B-COD) plate faces at $a/w = 0.150$ (the gages measured the displacement between points 30 mm above and 30 mm below the crack plane), (2) an AE transducer located on the lower pull tab, and (3) two accelerometers mounted at the top and bottom pull plates near the pull tabs. A measurement of tensile load applied to the specimen was obtained from the testing machine load cell.

ORNL–DWG 86–4106 ETD

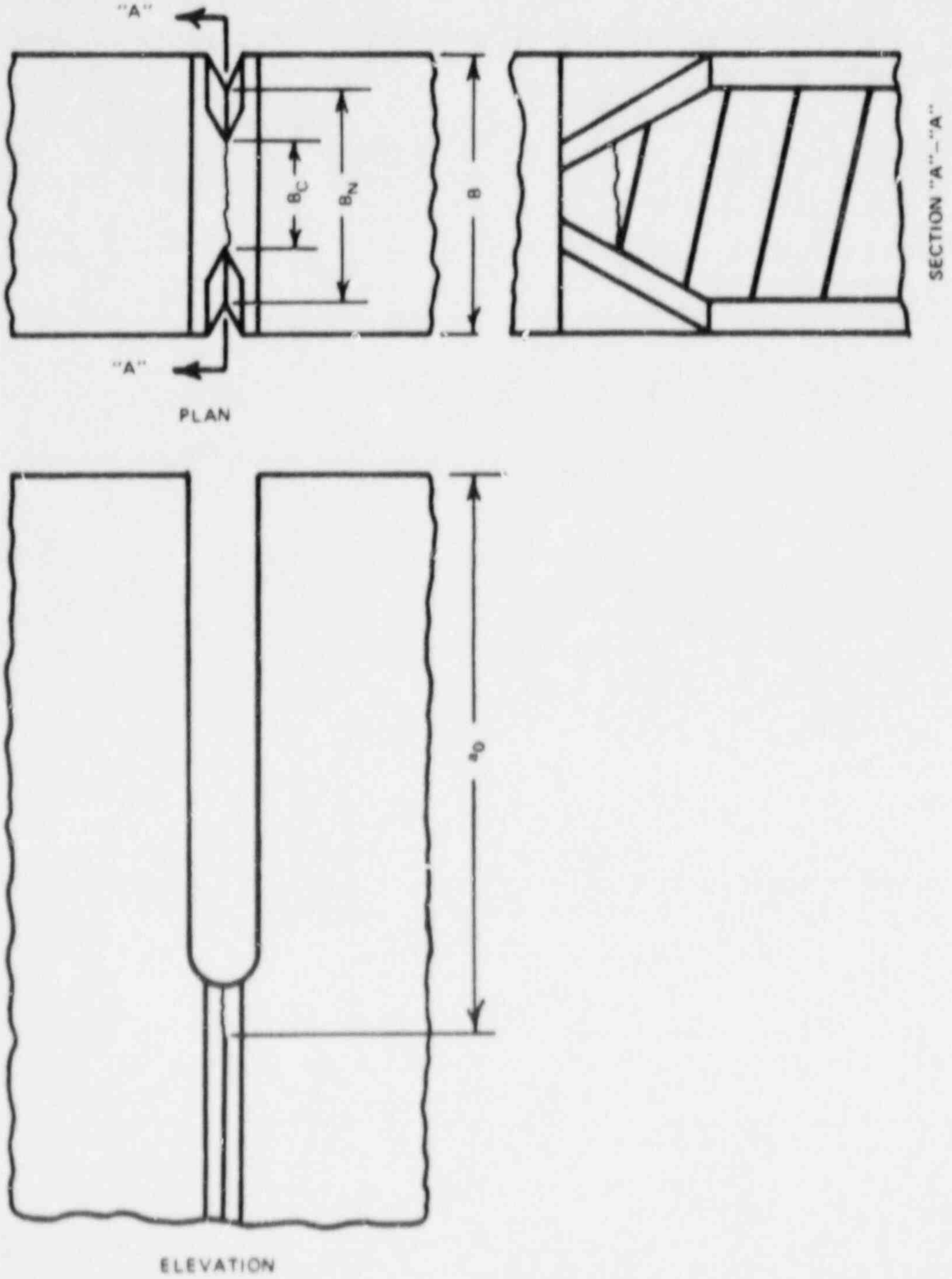

Fig. 5.3. Schematic of chevron configuration of crack front.

ORNL-DWG 88-4194 ETD

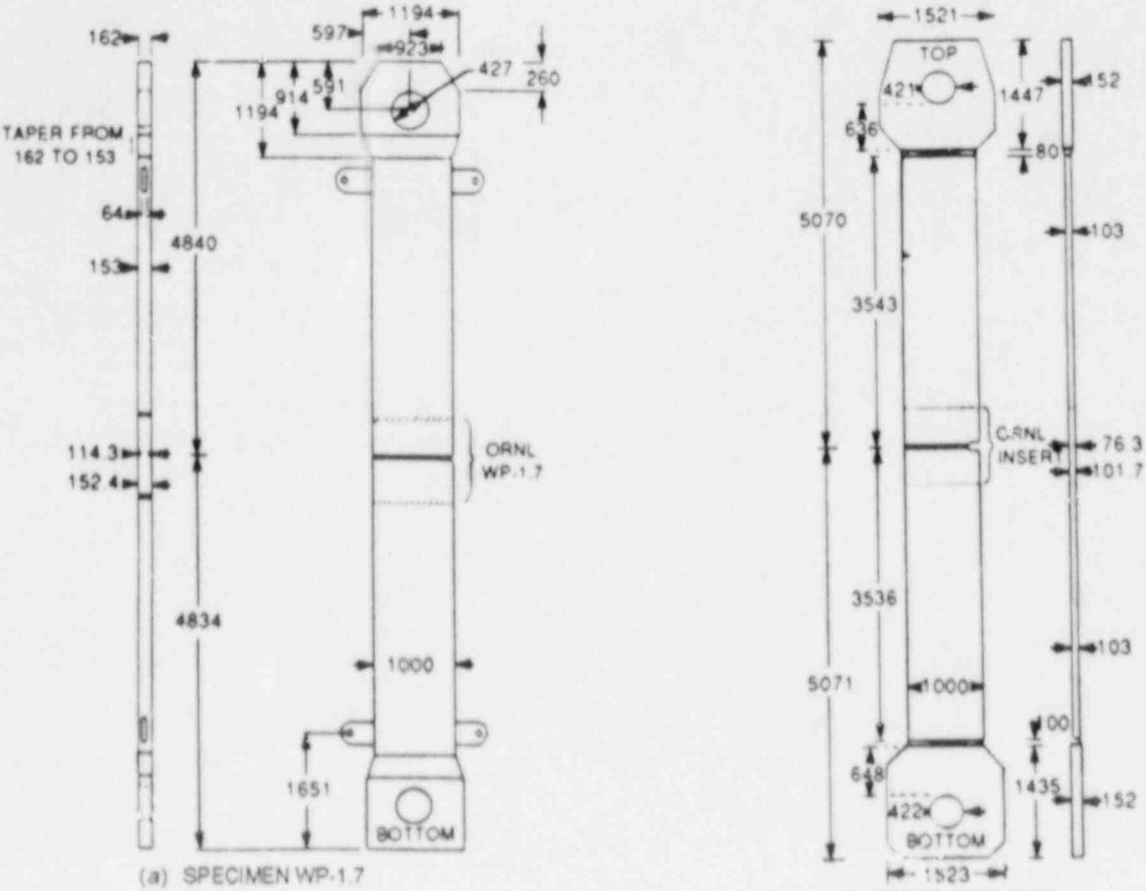

(*a*) SPECIMEN WP-1.7

ALL DIMENSIONS IN millimeters ± 2 mm

(*b*) SPECIMEN WP-CE-1

Fig. 5.4. Overall dimensions of HSST wide-plate crack-arrest specimens and pull-plates for (*a*) specimen WP-1.7 and (*b*) specimen WP-CE-1.

After being instrumented, the specimen was placed into the testing machine and insulated. A temperature gradient was then imposed across the plate by cooling the notched edge with liquid nitrogen while the other edge was heated. Liquid nitrogen flow and power to the heaters were continuously adjusted to obtain the desired thermal gradient. Final calibrations of the strain gages, CODs, and load were completed just before specimen loading. The specimen was then loaded until crack propagation occurred.

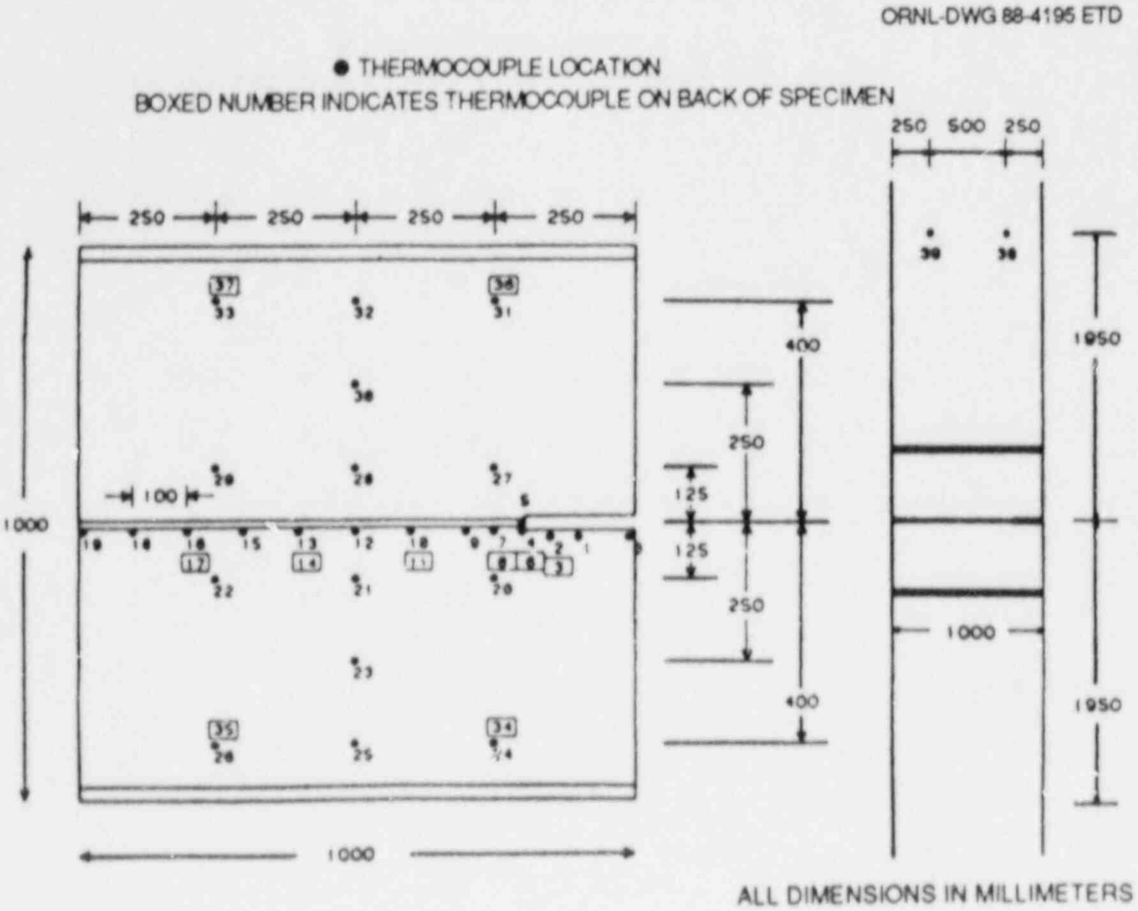

Fig. 5.5. Thermocouple locations for HSST wide-plate crack-arrest test specimens WP-1.7 and WP-CE-1.

5.2.3 Test description summary*

5.2.3.1 Test WP-1.7. The WP-1.7 test was performed at NBS on July 23, 1987.[2] This seventh test in the WP-1 series was the first to use a 152-mm-thick plate. After a satisfactory thermal gradient was obtained (Fig. 5.7), the specimen was loaded at an average rate of 17 kN/s (Fig. 5.8). At the testing machine's 26.7-MN tensile-load capacity, the crack run-arrest event(s) did not occur, so the load was held constant for 176 s. During this constant load period, the crack run-arrest event(s) still did not occur, so the specimen was rapidly unloaded in an effort to sharpen the crack tip before applying a second load cycle. Also before that cycle two changes were made in the testing procedure. The crack-tip temperature was lowered ~5°C to −23.7°C (Fig. 5.9), and the specimen

---

*Although the WP-1.7 and WP-CE-1 tests were described in the previous semiannual progress report, a summary of the material is repeated as background for the posttest analyses that are described later in this chapter.

ORNL-DWG 88-4196 ETD

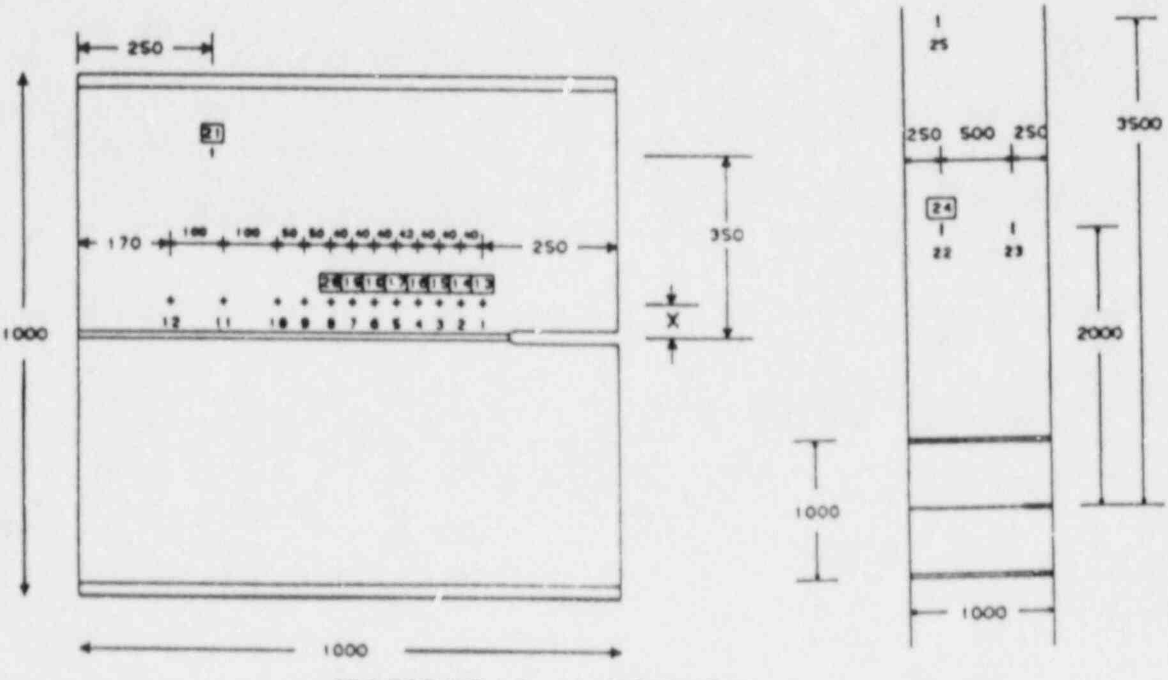

x = 97.5 FOR WP-1.7   x = 65 FOR WP-CE-1

ALL DIMENSIONS IN MILLIMETERS

Fig. 5.6. Strain-gage locations for HSST wide-plate crack-arrest test specimens WP-1.7 and WP-CE-1.

ORNL-DWG 88-4197 ETD

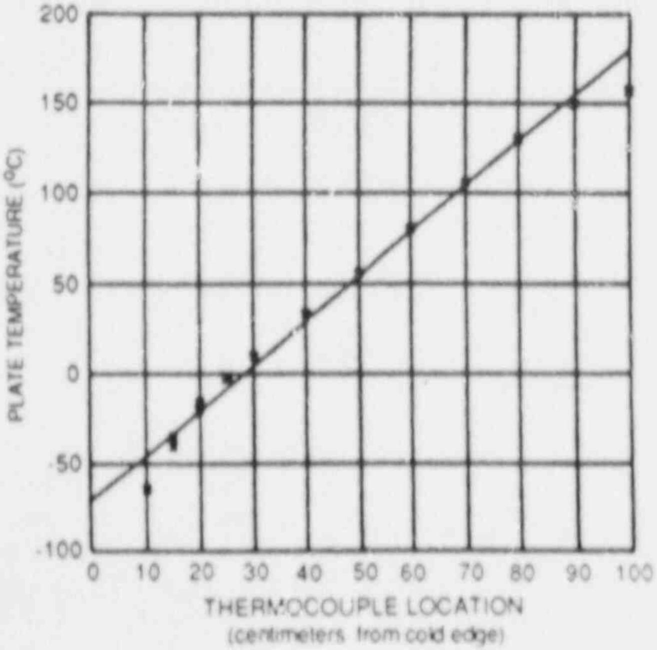

CENTIMETERS	TEMPERATURE (°C)	
	REAL	IDEAL
0	-119	-70
10	-65	-46
15	-40	-33
15	-35	-33
20	-20	-21
20	-16	-21
20	-17	-21
25	-3	-8
25	-1	-8
30	10	4
40	33	29
40	33	29
50	56	55
60	80	79
60	80	79
70	106	104
80	130	129
80	130	129
90	150	154
100	157	180

Fig. 5.7. Actual and ideal temperature distributions across specimen width at machine maximum load during first loading cycle: Test WP-1.7.

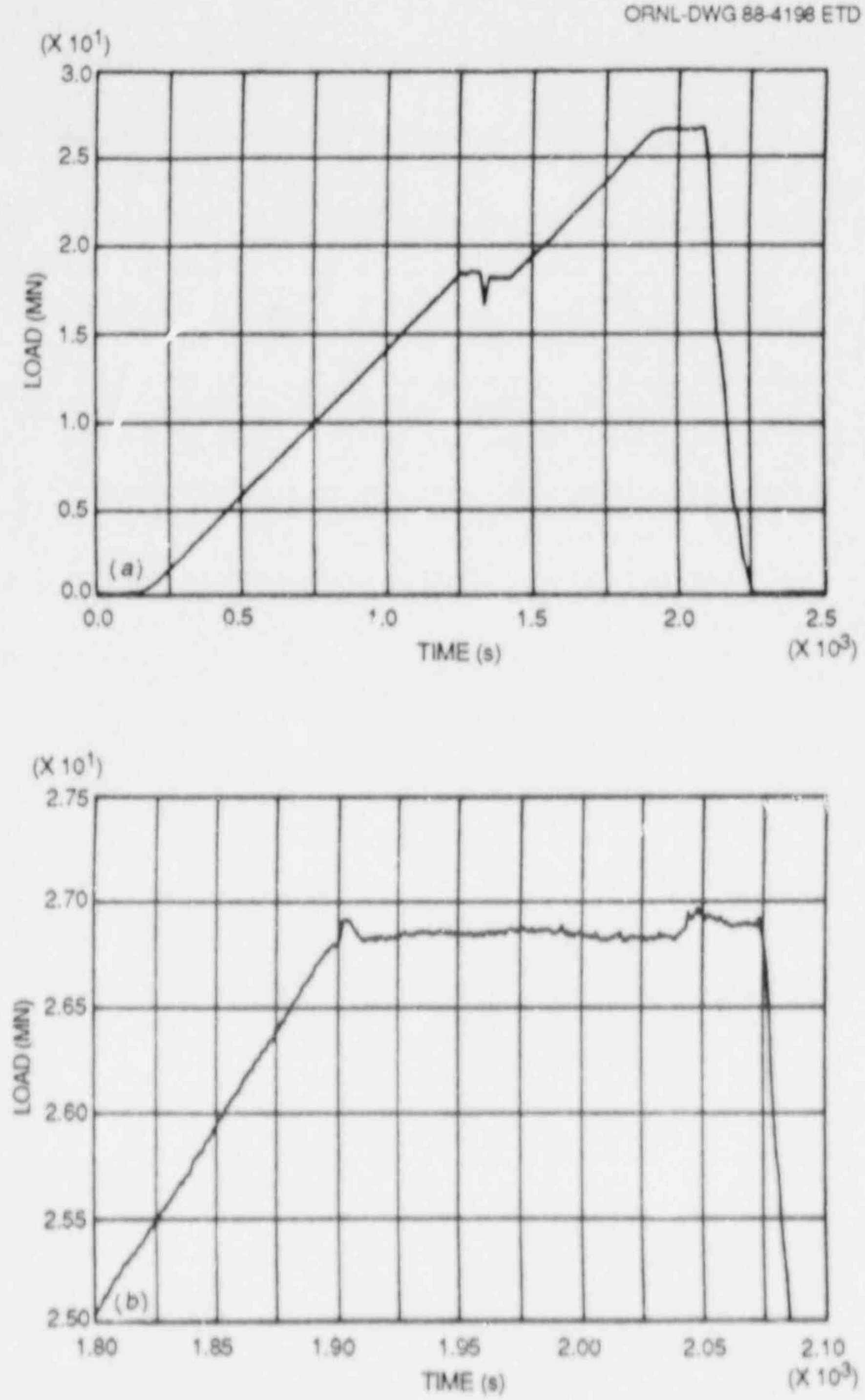

Fig. 5.8. Load vs time relationship during (*a*) first load cycle and (*b*) constant load period of 176 s: Test WP-1.7.

ORNL-DWG 88-4199 ETD

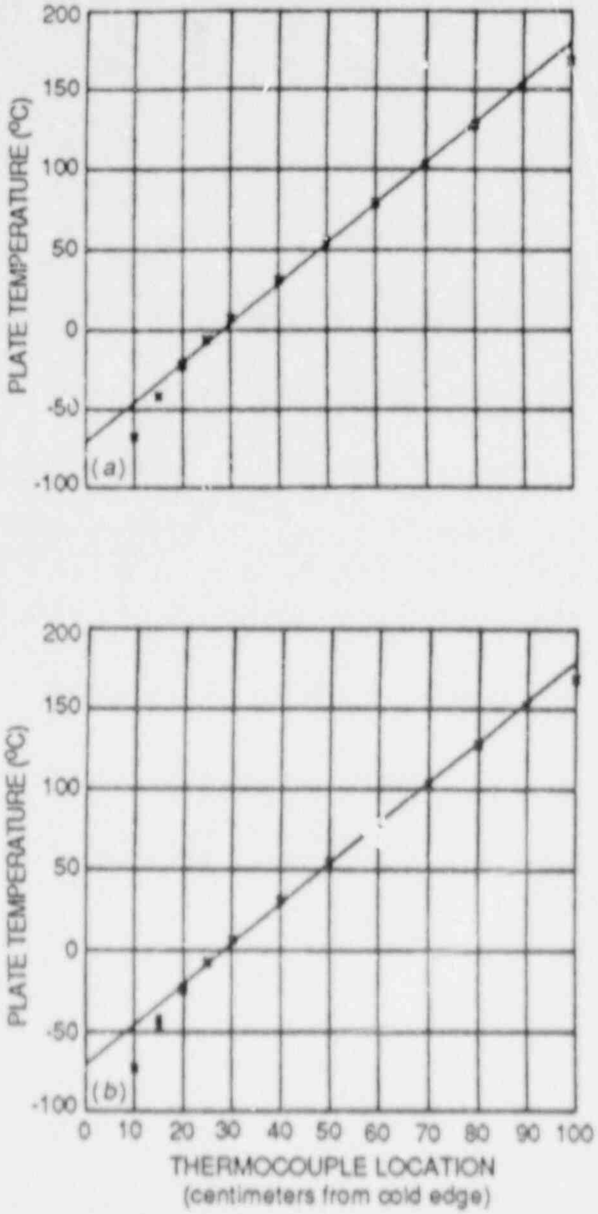

CENTIMETERS	TEMPERATURE (°C) REAL	TEMPERATURE (°C) IDEAL
0	-132	-70
10	-67	-46
15	-42	-33
15	-41	-33
20	-22	-21
20	-21	-21
20	-21	-21
25	-6	-8
25	-6	-8
30	7	4
40	31	29
40	32	29
50	55	55
60	79	79
60	79	79
70	104	104
80	128	129
80	128	129
90	152	154
100	168	180

CENTIMETERS	TEMPERATURE (°C) REAL	TEMPERATURE (°C) IDEAL
0	-132	-70
10	-73	-46
15	-46	-33
15	-42	-33
20	-25	-21
20	-23	-21
20	-22	-21
25	-8	-8
25	-7	-8
30	6	4
40	31	29
40	31	29
50	54	55
60	79	79
60	79	79
70	104	104
80	128	129
80	128	129
90	152	154
100	169	180

Fig. 5.9. Actual and ideal temperature distributions across specimen width at (*a*) start of second load cycle and (*b*) just before initiation of crack run-arrest events: Test WP-1.7.

loading rate was increased by a factor of ~5. Approximately 4700 s after the beginning of the first load cycle, specimen loading was reinitiated at a rate of 90 kN/s. At a load of 26.2 MN (Fig. 5.10), the crack run-arrest events and ductile tearing initiated and lasted ~27.5 ms. Examining the strain-gage records and fracture surface indicated that two cleavage crack run-arrest events occurred.

5.2.3.2 Test WP-CE-1. Test WP-CE-1 was the twelfth wide-plate crack-arrest test and the first that used the A 533 grade B class 1 material provided by Combustion Engineering, Inc.[3] After obtaining a satisfactory thermal gradient (Fig. 5.11), the specimen was loaded at an average rate of 24 kN/s. At a load of 10.14 MN, cleavage crack propagation initiated with a stable arrest occurring at a/w = 0.37 on the plate front face and at a/w = 0.42 on the plate back face. After holding the load constant for 150 s, loading was reinitiated at 24 kN/s. At a load of 15.26 MN, fibrous crack propagation began and was then followed by a rapid drop in load to about 4.4 MN (Fig. 5.12). After maintaining the load at this value for about 30 s, loading was reinitiated at 24 kN/s until at a load of 6.34 MN, complete separation of the plate occurred. Examining the fracture surface and strain-gage records indicated that one

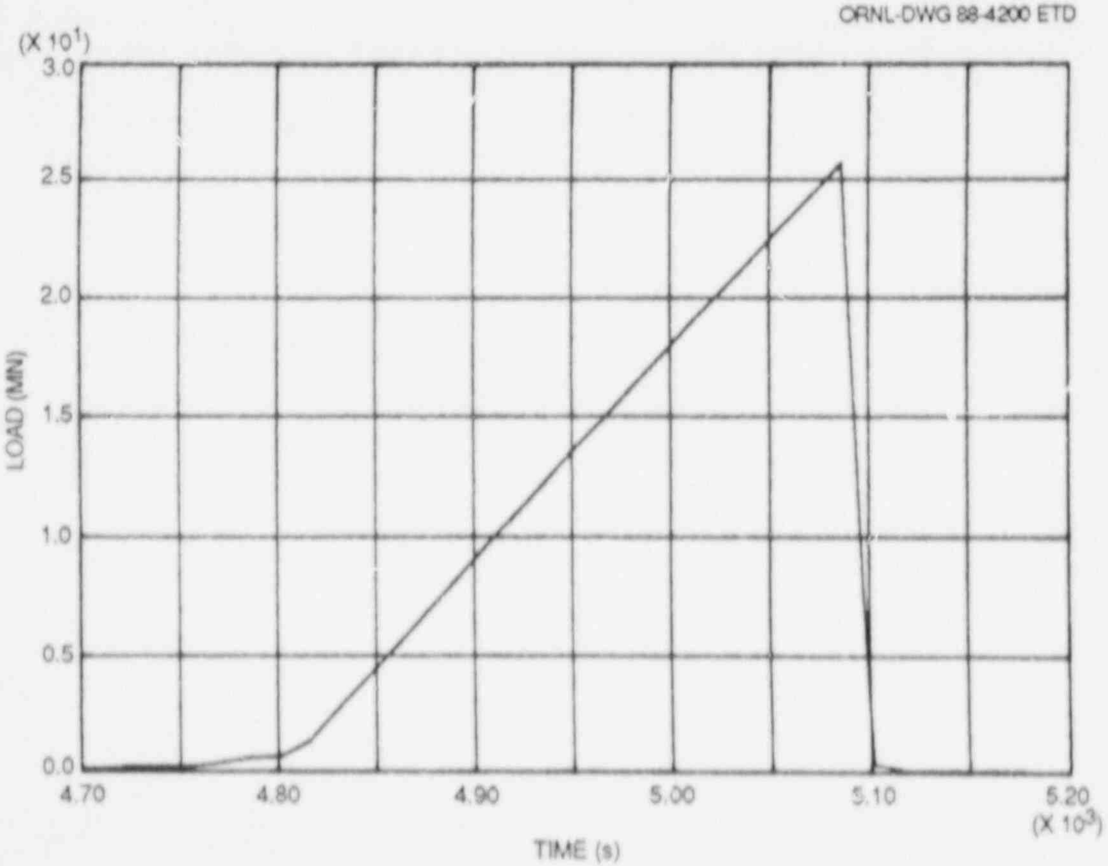

Fig. 5.10. Load vs time relationship during second load cycle: Test WP-1.7.

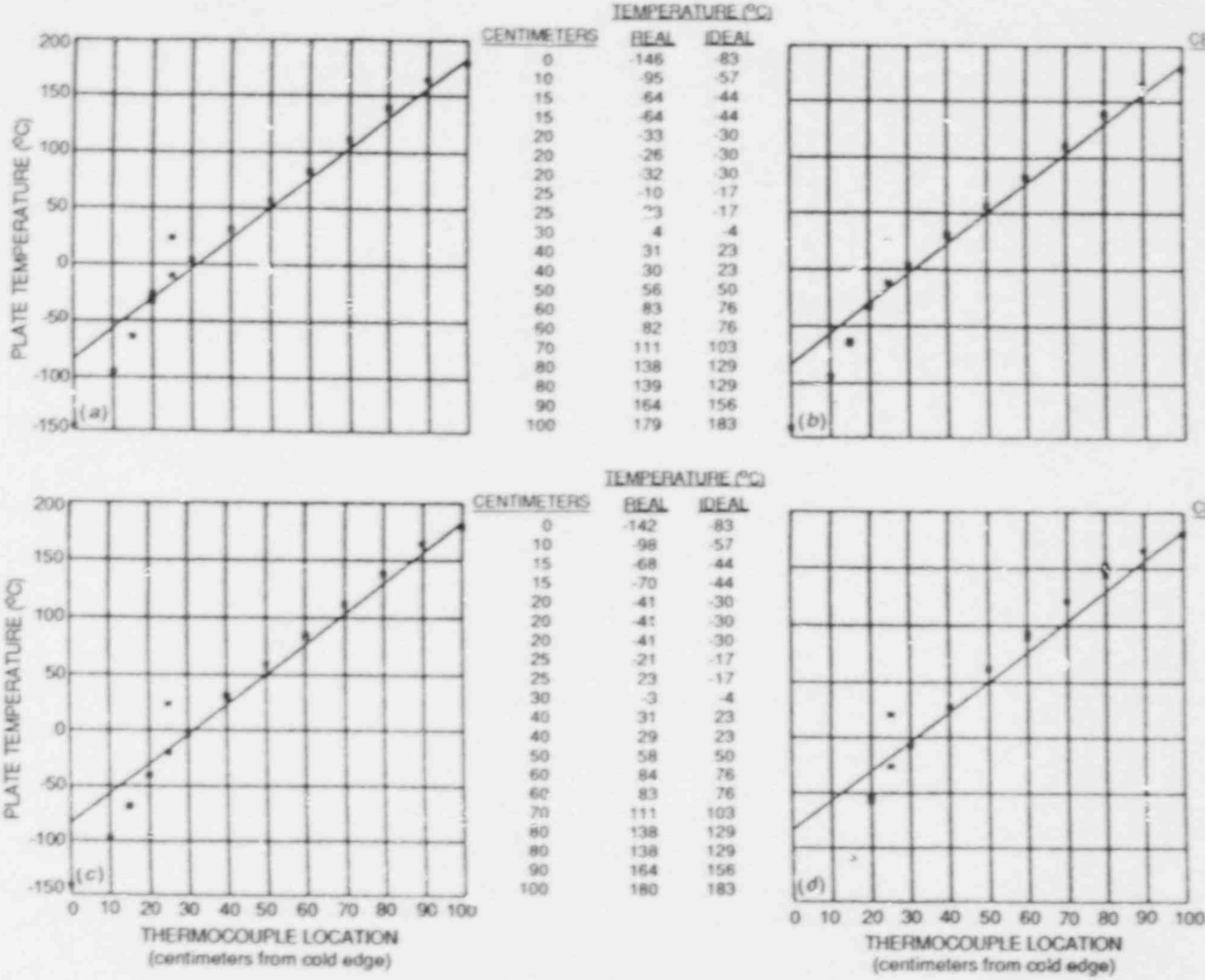

(a)

CENTIMETERS	TEMPERATURE (°C) REAL	TEMPERATURE (°C) IDEAL
0	-146	-83
10	-95	-57
15	-64	-44
15	-64	-44
20	-33	-30
20	-26	-30
20	-32	-30
25	-10	-17
25	23	-17
30	4	-4
40	31	23
40	30	23
50	56	50
60	83	76
60	82	76
70	111	103
80	138	129
80	139	129
90	164	156
100	179	183

(b)

CENTIMETERS	TEMPERATURE (°C) REAL	TEMPERATURE (°C) IDEAL
0	-142	-83
10	-95	-57
15	-63	-44
15	-66	-44
20	-34	-30
20	-33	-30
20	-34	-30
25	-12	-17
25	23	-17
30	[illegible]	-4
40	31	23
40	30	23
50	56	50
60	83	76
60	82	76
70	111	103
80	138	129
80	139	129
90	164	156
100	190	183

(c)

CENTIMETERS	TEMPERATURE (°C) REAL	TEMPERATURE (°C) IDEAL
0	-142	-83
10	-98	-57
15	-68	-44
15	-70	-44
20	-41	-30
20	-41	-30
20	-41	-30
25	-21	-17
25	23	-17
30	-3	-4
40	31	23
40	29	23
50	58	50
60	84	76
60	83	76
70	111	103
80	138	129
80	138	129
90	164	156
100	180	183

(d)

CENTIMETERS	TEMPERATURE (°C) REAL	TEMPERATURE (°C) IDEAL
0	-190	-83
[illegible]	BAD	-57
15	-154	-44
15	-110	-44
20	BAD	-30
20	-54	-30
20	-59	-30
25	-26	-17
25	21	-17
30	-8	-4
40	28	23
40	28	23
50	61	50
60	93	76
60	89	76
70	121	103
80	144	129
80	152	129
90	166	156
100	181	183

Fig. 5.11. Actual and ideal temperature distributions across specimen width at (*a*) start of loading, (*b*) initiation of cleavage crack run-arrest event, (*c*) onset of ductile fracture, and (*d*) final separation of plate: Test WP-CE-1 (thermocouple No. 8 at $a/w = 0.25$ was defective).

ORNL-DWG 88-4202 ETD

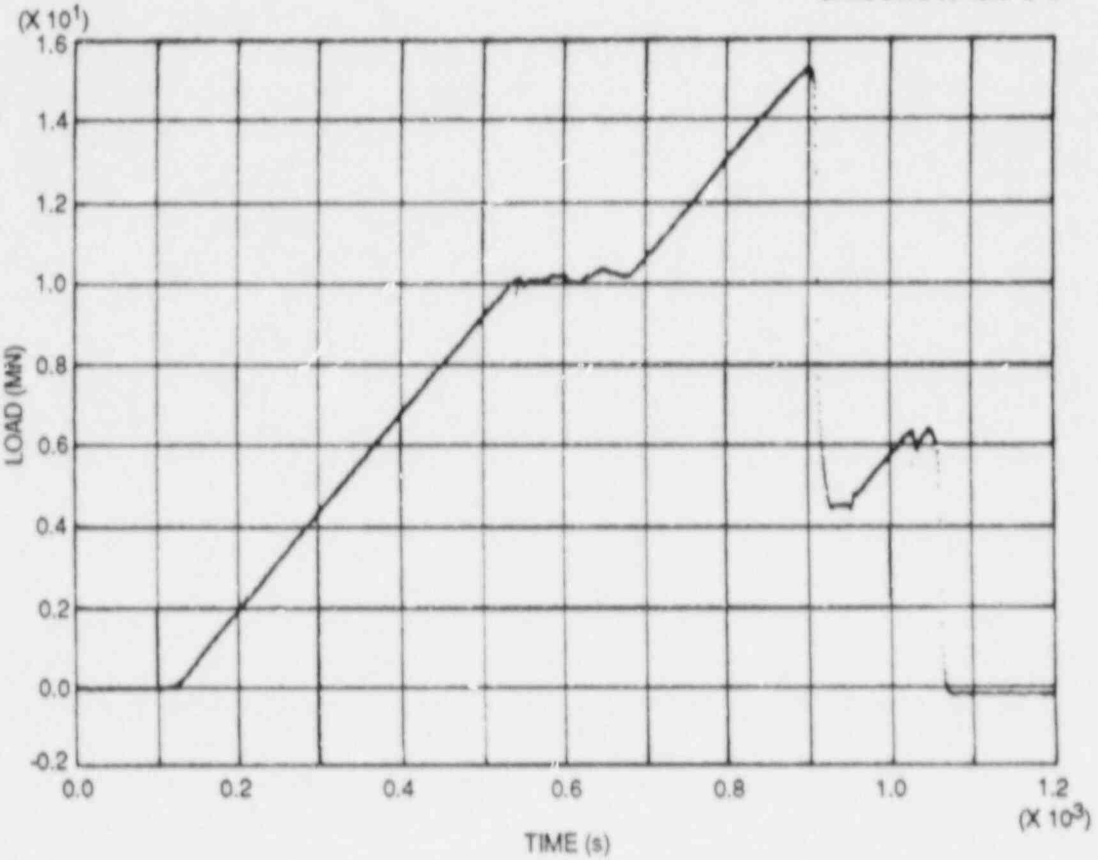

Fig. 5.12. Load vs time relationship: Test WP-CE-1.

cleavage crack run-arrest event occurred before the onset of ductile tearing.

5.2.4 Test result summary

5.2.4.1 Test WP-1.7. The entire fracture surface of WP-1.7 is shown in Fig. 5.13(*a*), and a close-up of the cleavage and loss-of-cleavage regions is presented in Fig. 5.13(*b*). As noted in the figure, two cleavage crack run-arrest events occurred during the test. A region of fibrous fracture averaging 10 mm in width separates the two events. Also, there is a significant island of cleavage beyond the second arrest. It is about 30 mm in diameter and extends to a point 673 mm from the cold edge of the plate (i.e., to a point where the plate temperature was about 97°C). The cleavage crack started in the plane of the side grooves; however, as it progressed, it deviated from this plane. The maximum deviation was 15 mm below the plane of the side grooves in the lower half of the plate at a position corresponding to the second arrest point.

Figures 5.14–5.17 present strain histories for common crack-line gages mounted on the front and back surfaces of the plate specimen.

ORNL-PHOTO 2588-88

Fig. 5.13. Fracture surface for specimen WP-1.7. (*a*) Overall fracture surface and (*b*) close-up of initial crack, cleavage run-arrests, and loss-of-cleavage region (the scale is at the specimen back surface).

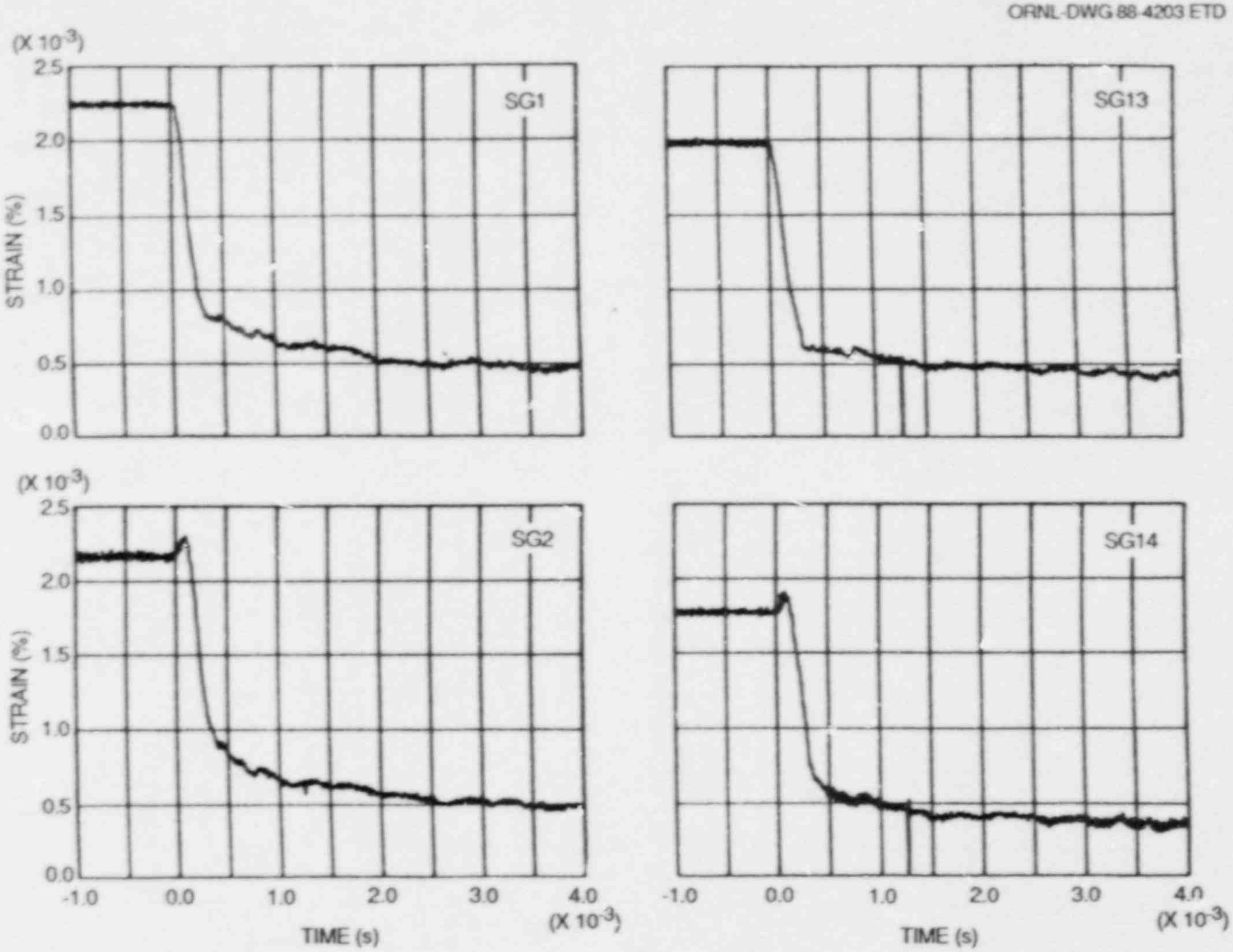

Fig. 5.14. Strain histories during second load cycle for companion crack-line gages: Test WP-1.7. (Strain values from first loading cycle have been subtracted.)

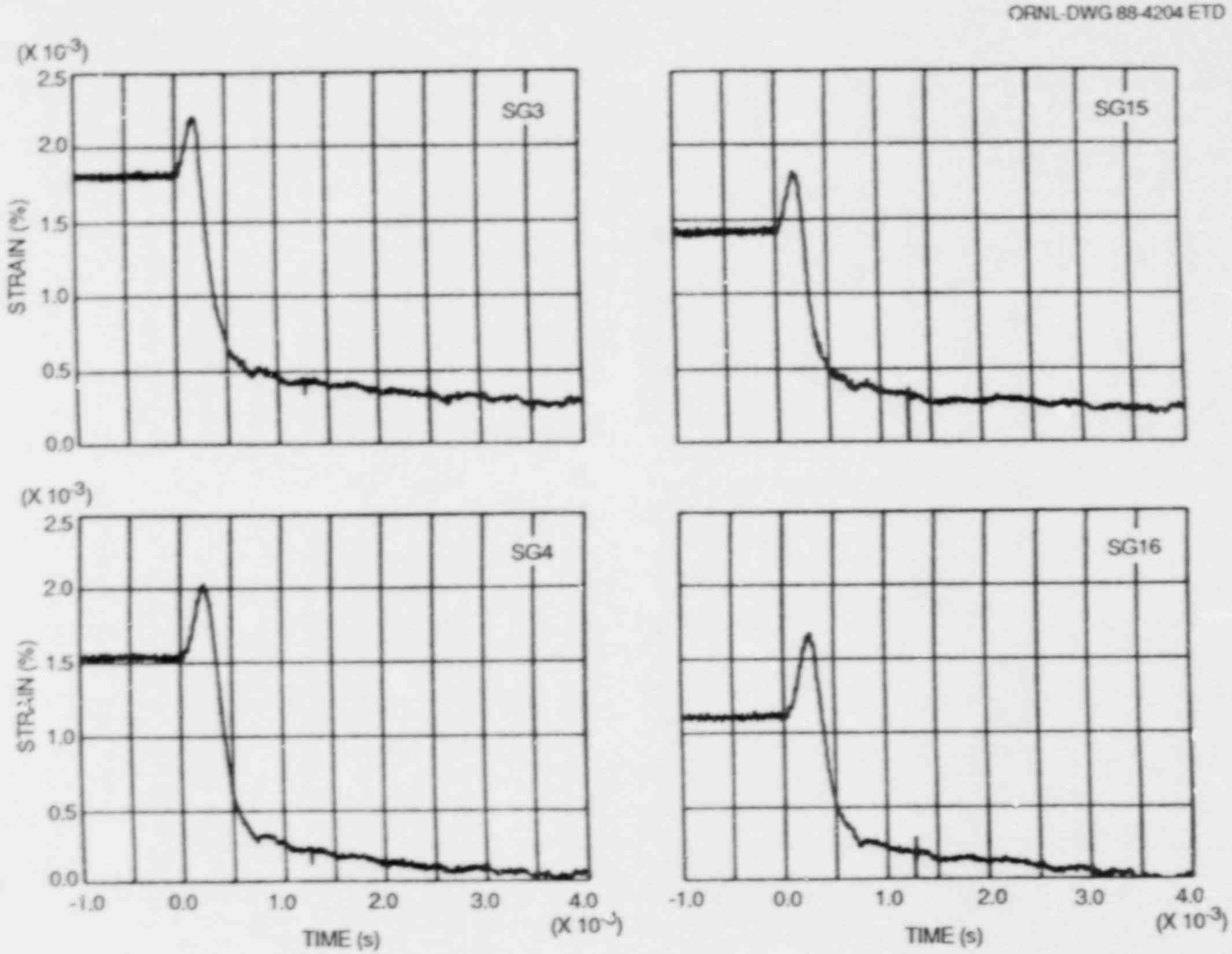

Fig. 5.15. Strain histories during second load cycle for companion crack-line gages: Test WP-1.7. (Strain values from first loading cycle have been subtracted.)

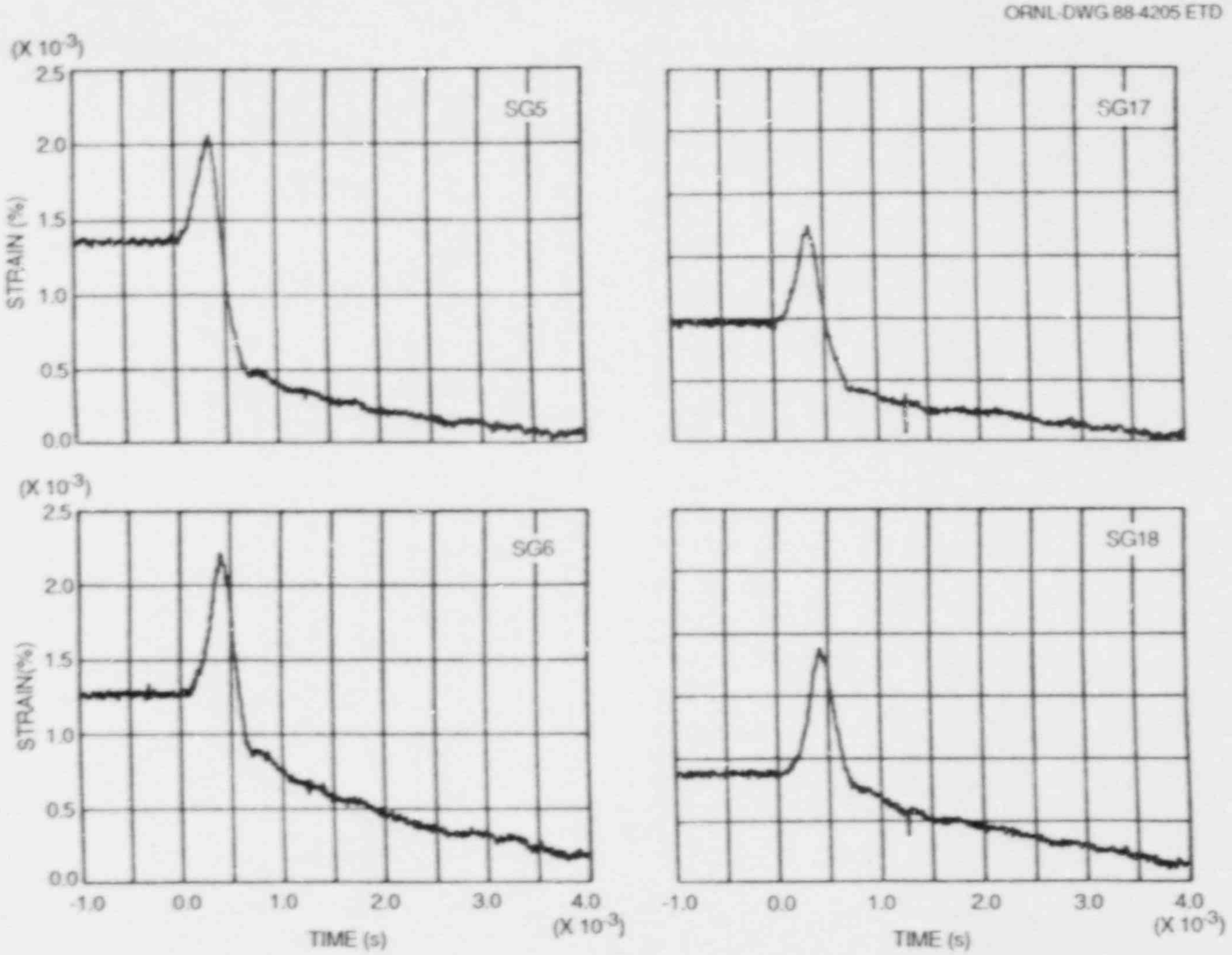

Fig. 5.16. Strain histories during second load cycle for companion crack-line gages: Test WP-1.7. (Strain values from first loading cycle have been subtracted.)

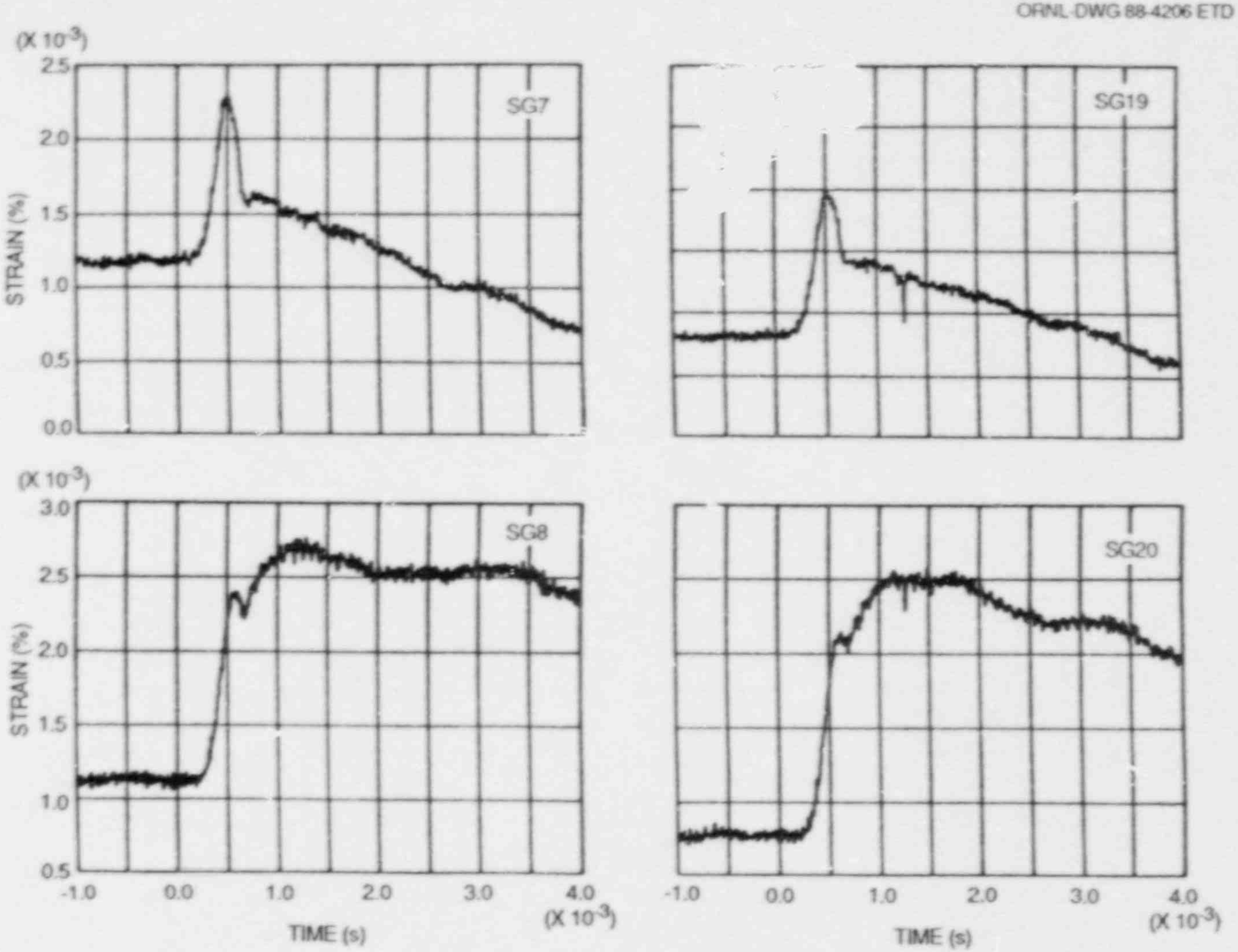

Fig. 5.17. Strain histories during second load cycle for companion crack-line gages: Test WP-1.7. (Strain values from first loading cycle have been subtracted.)

Figure 5.17 shows the cleavage crack passing gage No. 7 and arresting just past gage No. 8. Figure 5.18 shows reinitiation followed by the second crack run-arrest event as detected by companion crack-line gage Nos. 7 and 8 on the plate front face and 19 and 20 on the plate back face. The second cleavage crack run-arrest event as detected by gage Nos. 9 and 10 followed by fibrous fracture past crack-line gage Nos. 10–12 is shown in Fig. 5.19. The response of near- and far-field strain gages is presented in Figs. 5.20–5.22.

Dynamic displacement of the specimen as measured 3.539 m below the crack-line is presented in Fig. 5.23 for two time resolutions. Figure 5.24 presents the AE record at two levels of time resolution for test WP-1.7.

Evaluation of the strain-gage records and fracture surface were also used to deduce the crack length (position of the crack front) during the fracture process, and the results are summarized in Table 5.2. In the table, the strain-gage positions have been modified from those shown in Fig. 5.6 to account for the fact that the peak strain occurs at an angle of 72° in front of the crack tip. A plot of the strain-gage derived crack-front position vs time from the front-face and back-face strain gage results for the first 15 ms of the test is presented in Fig. 5.25(*a*). This figure indicates that the crack-front advance at comparable elapsed times was very uniform across the plate thickness during the cleavage crack run-arrest events. An expanded plot of the strain-gage derived crack-front position vs time from the front-face and back-face strain gage results over the ≈30 ms duration of the test is presented in Fig. 5.25(*b*). The results presented in this plot indicate that the crack-front advance across the plate thickness was uniform throughout the test duration.

5.2.4.2 Test WP-CE-1. Figure 5.26(*a*) shows the entire fracture surface of specimen WP-CE-1. A close-up of the initial crack, the cleavage crack run-arrest region, and the loss-of-cleavage region is shown in Fig. 5.26(*b*). Note that one cleavage crack run-arrest event occurred during the test, with clear delineation of the the cleavage arrest. Also note that the fibrous fracture appearance for this material more closely resembles that obtained with the WP-2 series material (low-upper-shelf) than with the WP-1 series material (A 533 grade B class 1). The entire fracture surface produced by this test remained in the plane of the side grooves. The reduction-in-thickness contour map for the specimen is presented in Fig. 5.27. As noted in the figure, the greatest reduction-in-thickness measured was 10%, the largest value obtained so far in any of the wide-plate crack-arrest tests. Also, as previous tests have shown, significant reductions-in-thickness occur only after the location corresponding to the arrest point (i.e., a/w > 0.37 for test WP-CE-1).

Figures 5.28 and 5.29 present strain histories for companion crack-line gages mounted on the front and back surfaces of the plate. Figure 5.28 shows the cleavage crack passing strain gage Nos. 1–4 and 13–16. Figure 5.29 shows the crack arresting before reaching strain gage No. 5 at the plate front face and passing strain gage No. 17 but arresting before reaching strain gage No. 18 at the plate back face. Figure 5.30 presents highly amplified strain histories for crack-line gage Nos. 9–12 mounted on the plate front face. Strain histories for near- and far-field gage Nos. 21–24 are presented in Fig. 5.31. Long-time (70-ms)

ORNL-DWG 88-4207 ETD

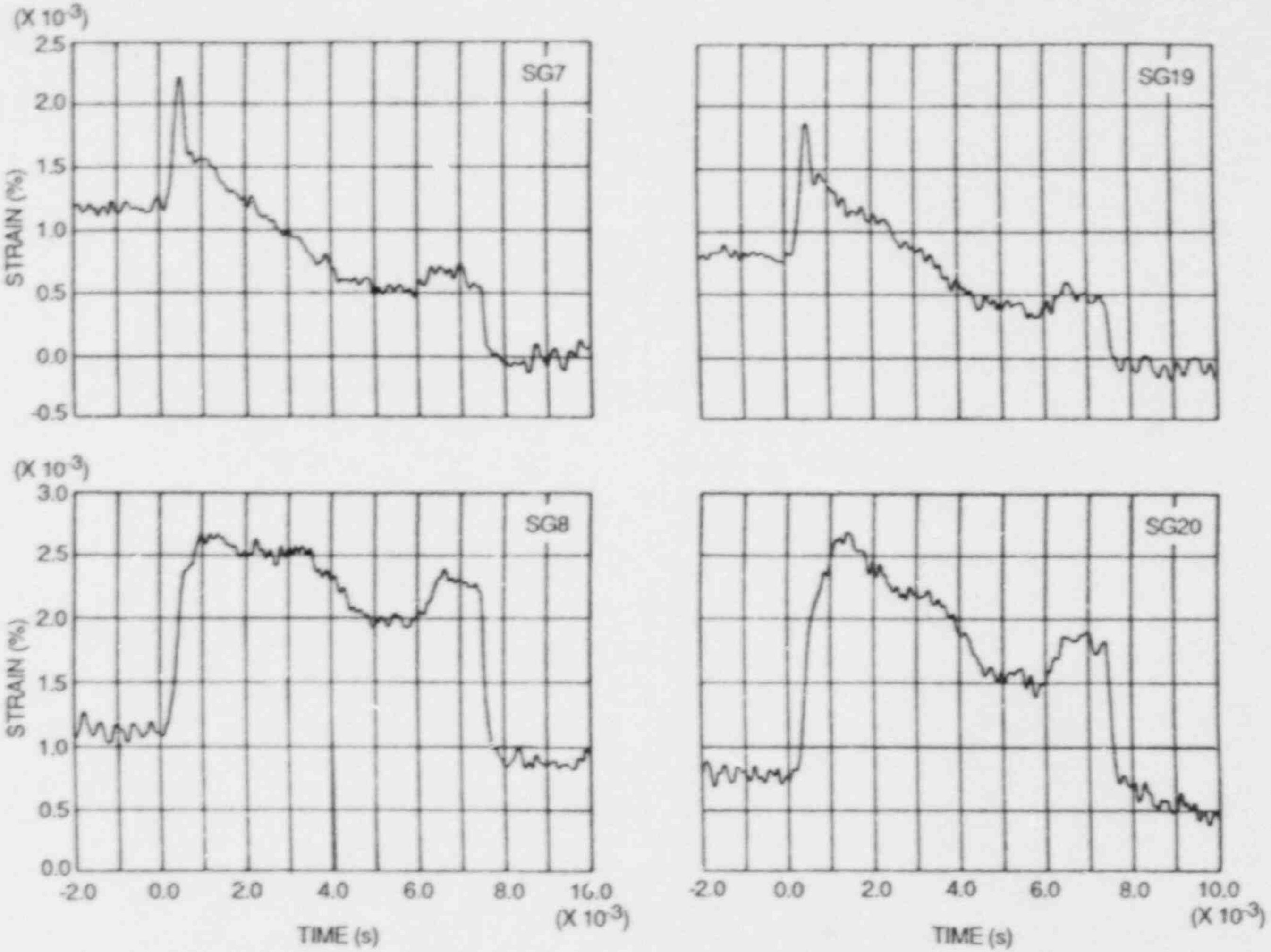

Fig. 5.18. Strain histories (expanded time scale) during second load cycle for companion crack-line gages showing reinitiation followed by the second crack run-arrest event: Test WP-1.7. (Strain values from first loading cycle have been subtracted.)

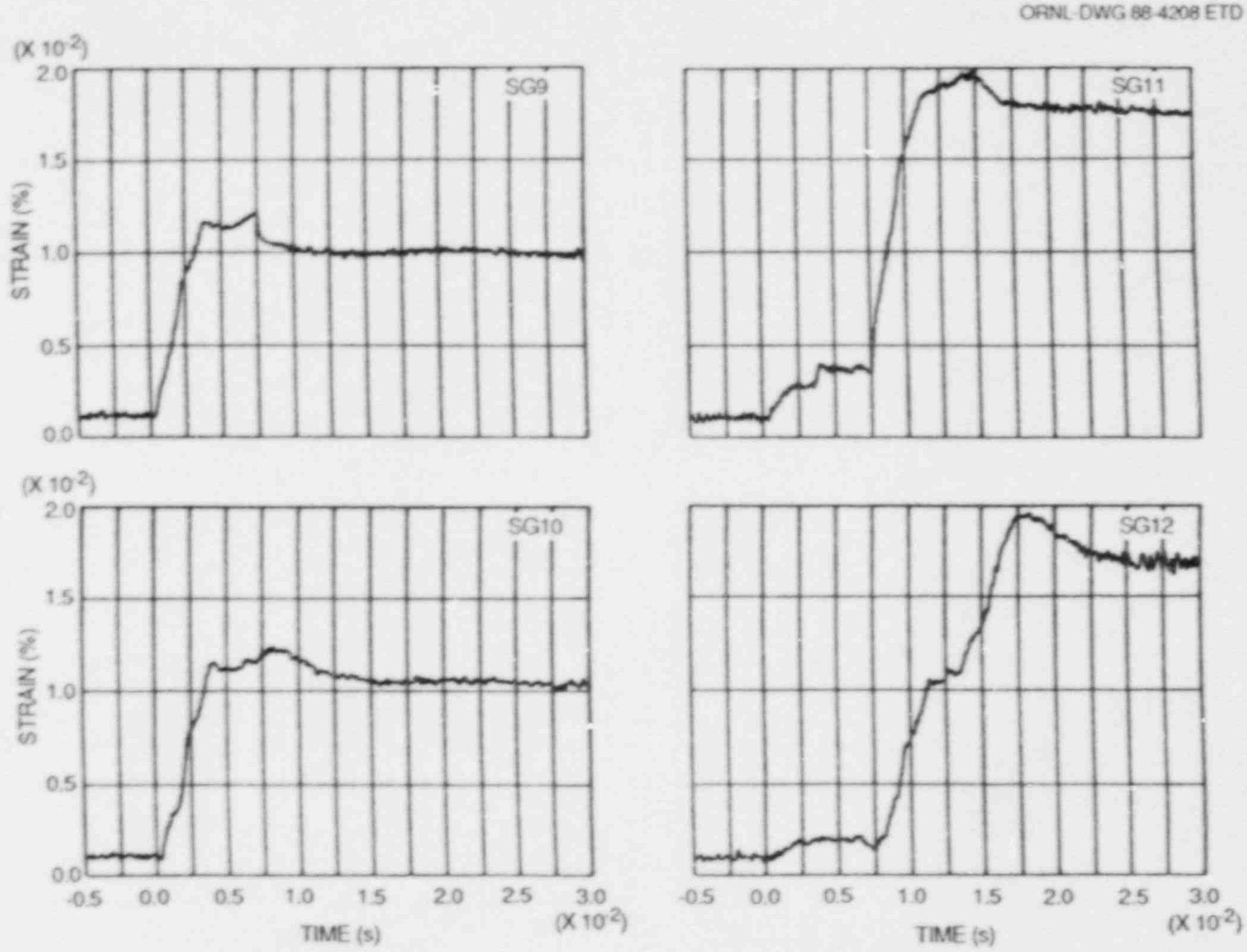

Fig. 5.19. Strain histories during second load cycle for front-face crack-line gages showing the second cleavage crack run-arrest event (gage No. 9) followed by fibrous fracture past gage Nos. 10–12: Test WP-1.7. (Strain values from first loading cycle have been subtracted.)

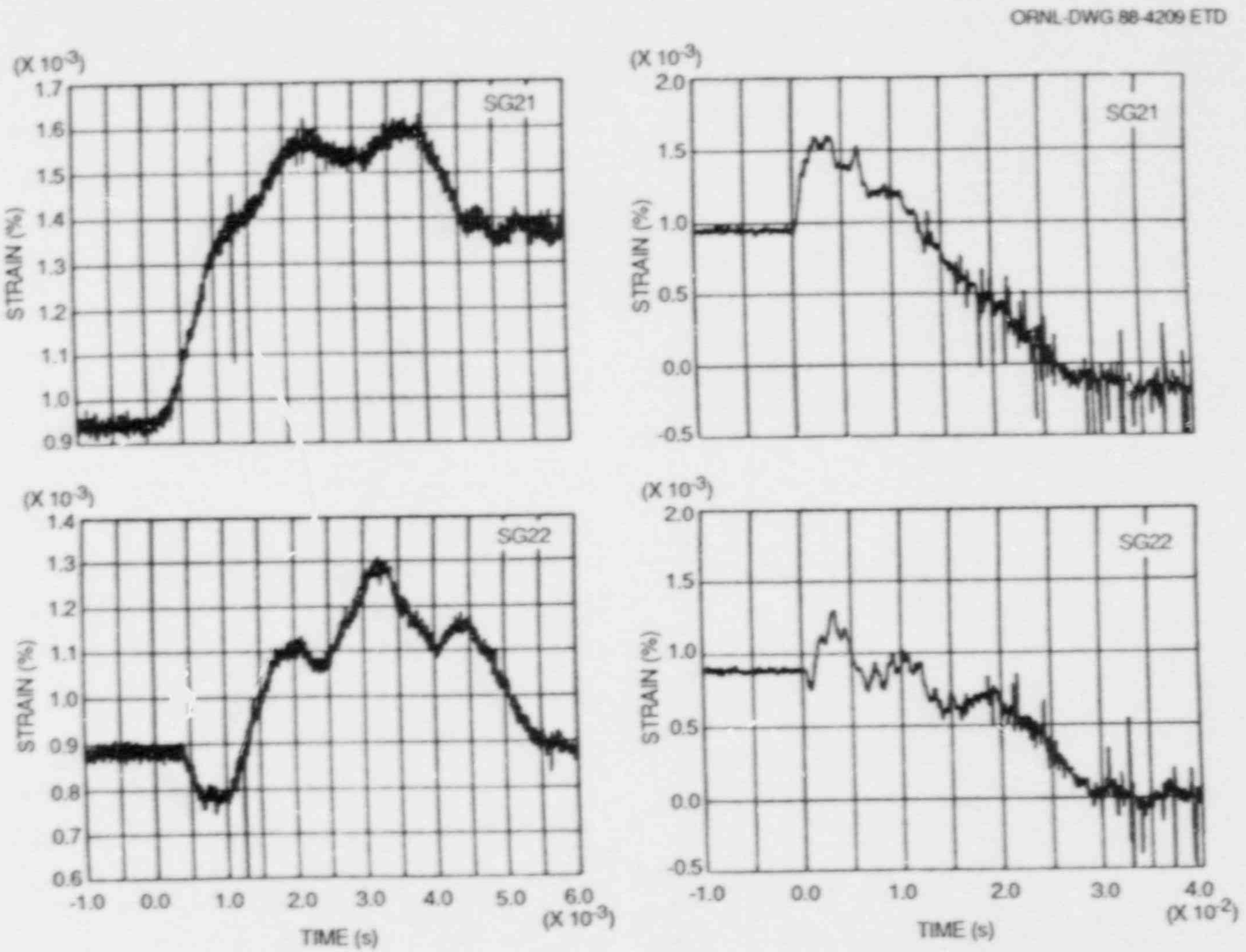

Fig. 5.20. Strain histories at two time resolutions during second load cycle for near- and far-field gages: Test WP-1.7. (Strain values from first loading cycle have been subtracted.)

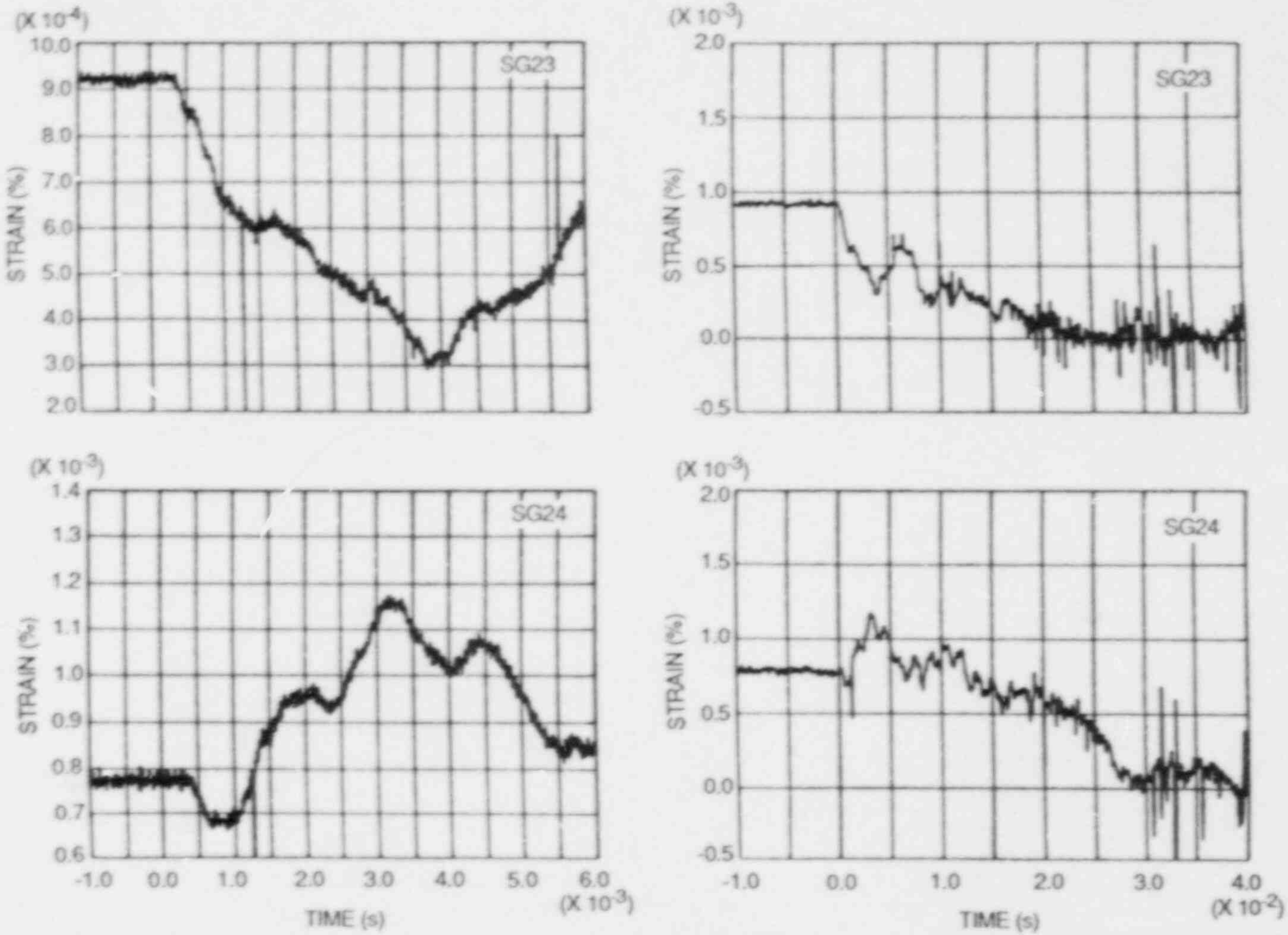

Fig. 5.21. Strain histories at two time resolutions during second load cycle for far-field gages: Test WP-1.7. (Strain values from first loading cycle have been subtracted.)

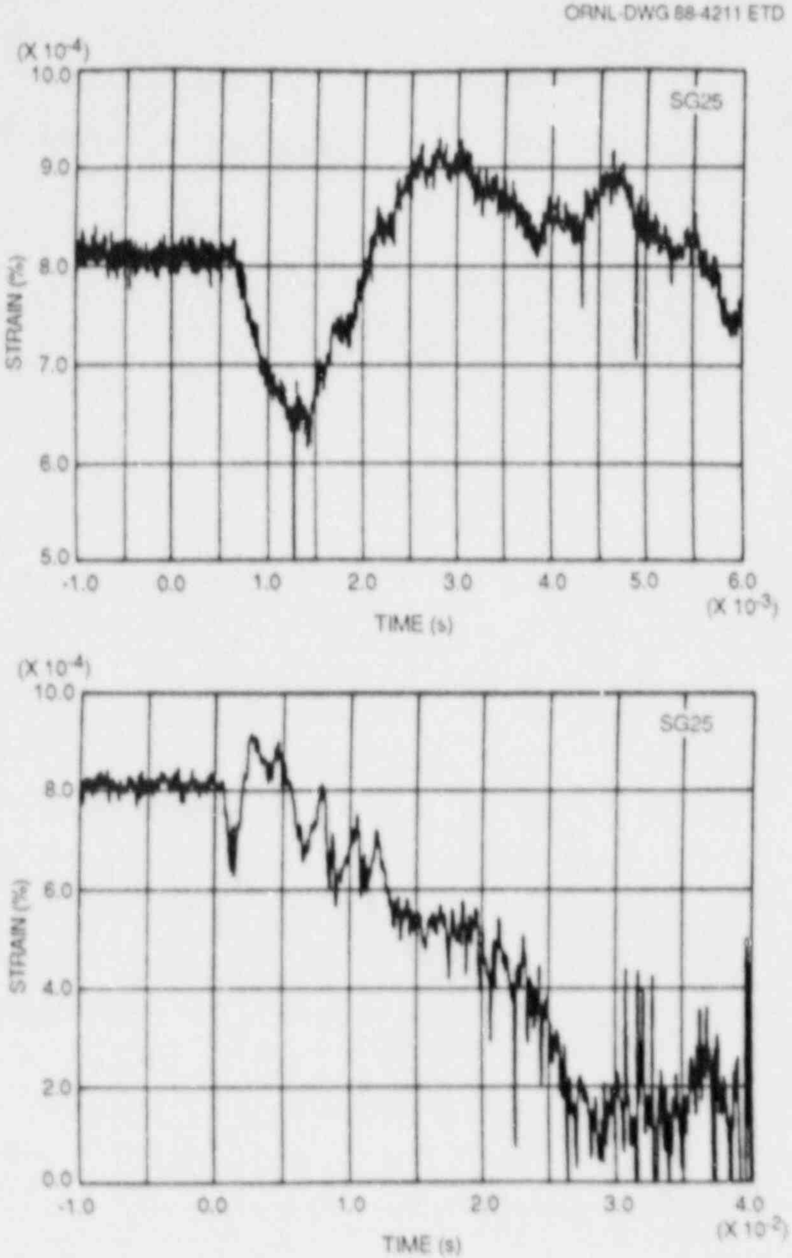

Fig. 5.22. Strain history at two time resolutions during second load cycle for far-field gage: Test WP-1.7. (Strain values from first loading cycle have been subtracted.)

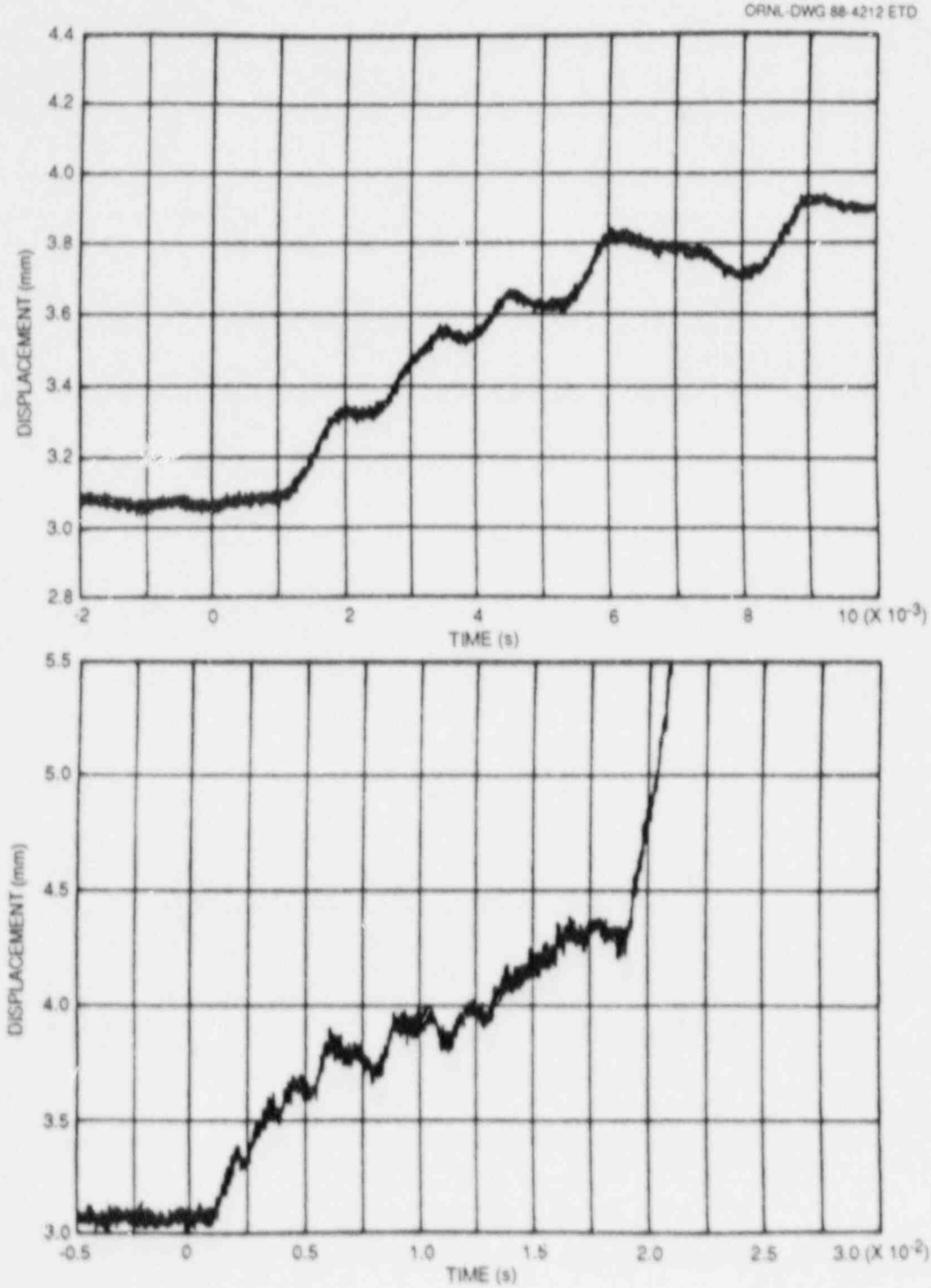

Fig. 5.23. Dynamic displacement history at two time resolutions as measured 3.539 m below the crack-line during the second load cycle: Test WP-1.7.

ORNL-DWG 88-4213 ETD

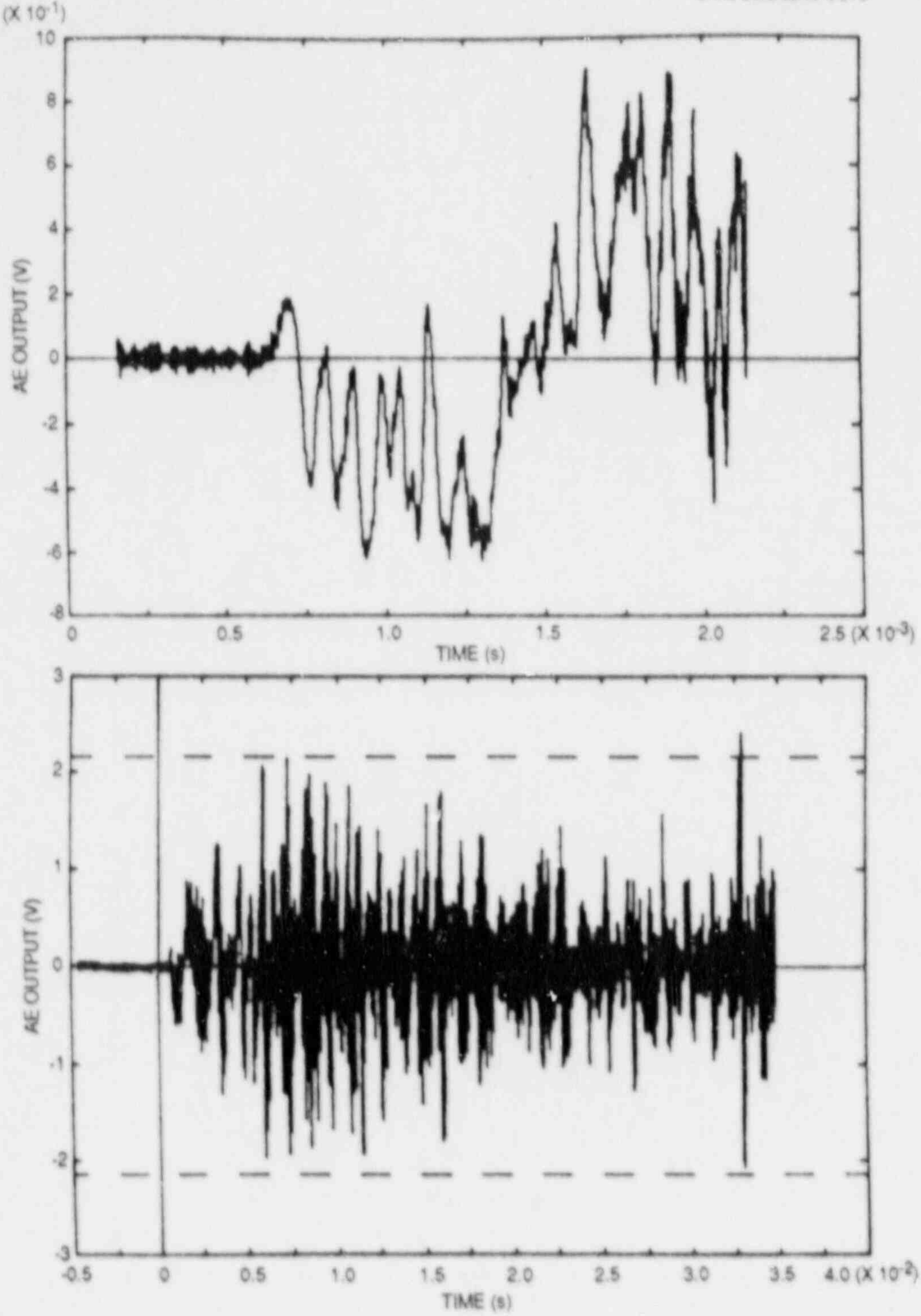

Fig. 5.24. Acoustic-emission history at two time resolutions during the second load cycle: Test WP-1.7.

Table 5.2. Crack position vs time and velocity

Indicator[a]	Position (mm)	Time (ms)	Velocity[b] (m/s)
Front-face measurements: WP-1.7			
Initial crack	202	0	
			471
SG1	218	0.034	
			645
SG2	258	0.096	
			476
SG3	298	0.180	
			800
SG4	338	0.230	
			357
SG5	378	0.342	
			741
SG6	418	0.396	
			377
SG7	458	0.502	
			333
SG8	498	0.622	
			517
Arrest	528	0.680	1.5
Some fibrous growth			
Reinitiation (cleavage)	538	7.442	
			250
SG9	548	7.482	
			833
SG10	598	7.542	
			206
Arrest	635	7.722	
Reinitiation (fibrous)	635	12.342	
			25
SG11	698	14.822	
			29
SG12	798	18.282	
			22
End of plate	1000	27.482	

Table 5.2 (continued)

Indicator[a]	Position (mm)	Time (ms)	Velocity[b] (m/s)
	Back-face measurements:	*WP-1.7*	
Initial crack	202	0	
			533
SG13	218	0.030	
			741
SG14	258	0.084	
			444
SG15	298	0.174	
			444
SG16	338	0.264	
			455
SG17	378	0.352	
			571
SG18	418	0.422	
			541
SG19	458	0.496	
			333
SG20	498	0.616	
			417
Arrest	528	0.688	1.5
Some fibrous growth			
Reinitiation	538	7.402	346
Arrest	635	7.682	
Reinitiation	635	12.362	
			24
End of plate	1000	27.482	

[a] Gage positions in the table are all reduced by 32 mm from the actual gage position shown in Fig. 5.6 to account for the fact that the peak strain occurs at an angle of 72° in front of the crack tip.

[b] Velocity is an average calculated velocity for crack propagation between indicator points.

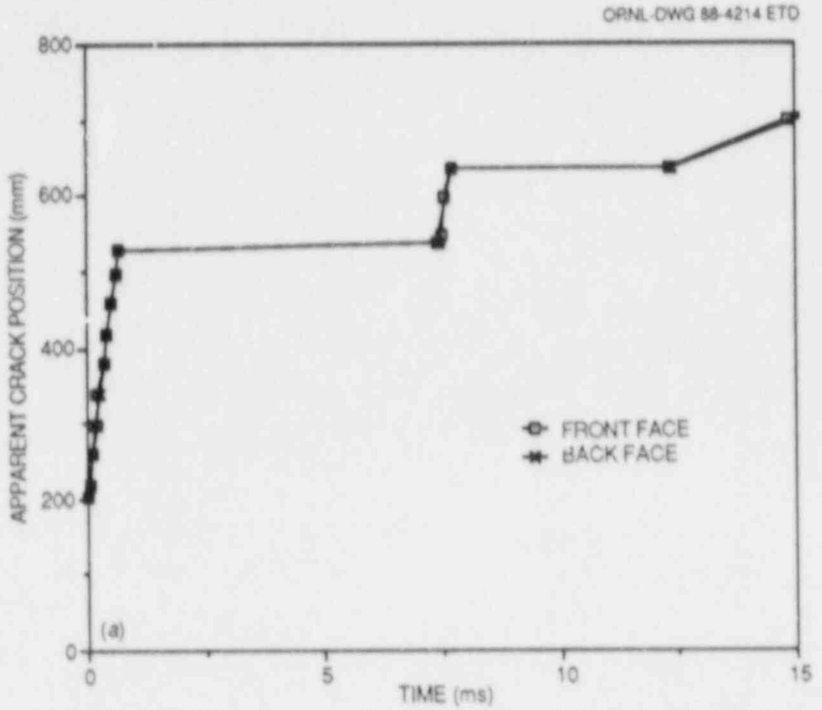

Fig. 5.25. Apparent crack-front position history (*a*) during the first 15 ms of the cleavage crack run-arrest events and (*b*) over the entire test duration: Test WP-1.7.

ORNL PHOTO 8240-88

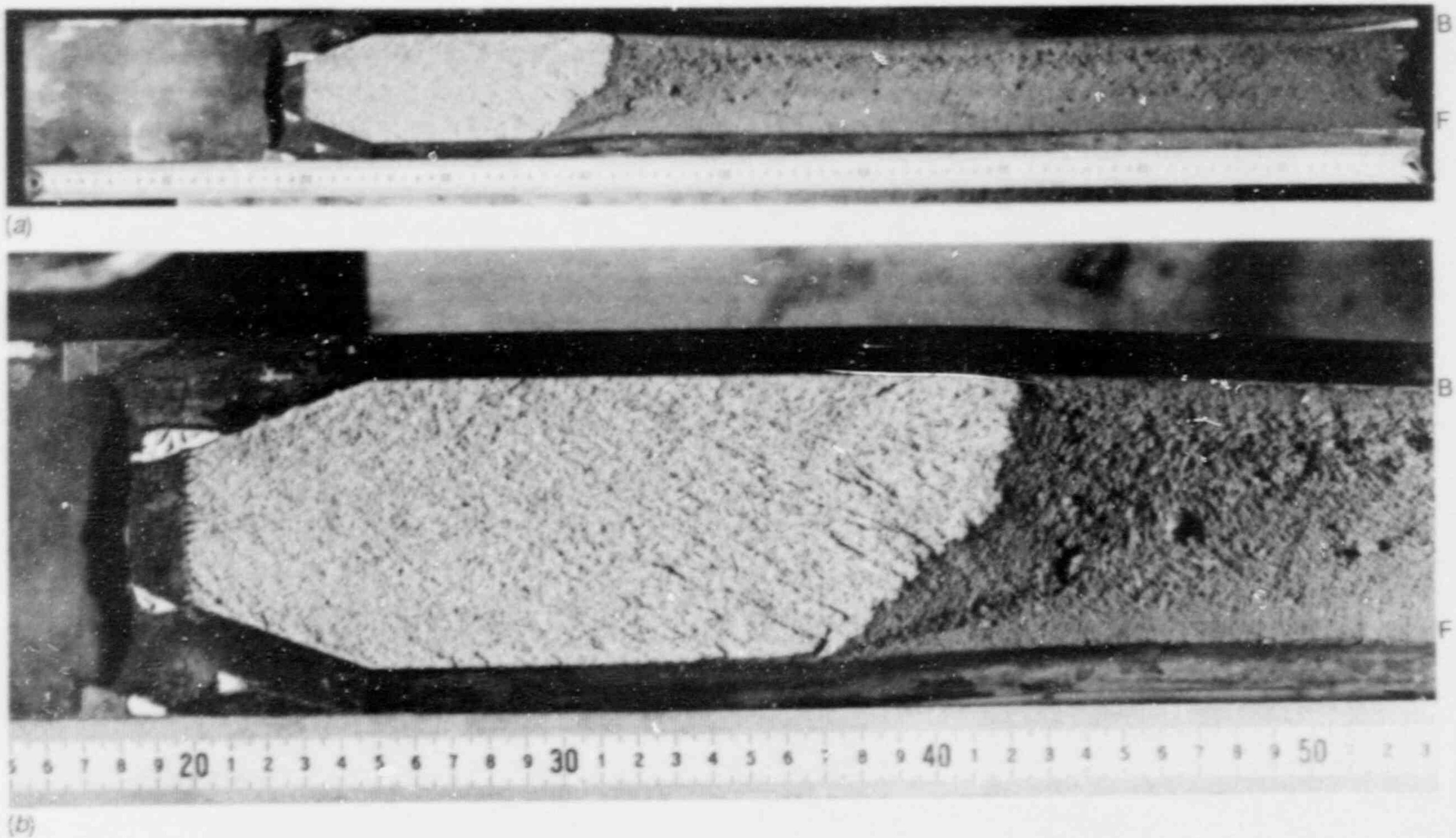

Fig. 5.26. Fracture surface for specimen WP-CE-1. (*a*) Overall fracture surface and (*b*) close-up of initial crack, cleavage run-arrest event, and loss-of-cleavage region. (The scale is at the specimen front face.)

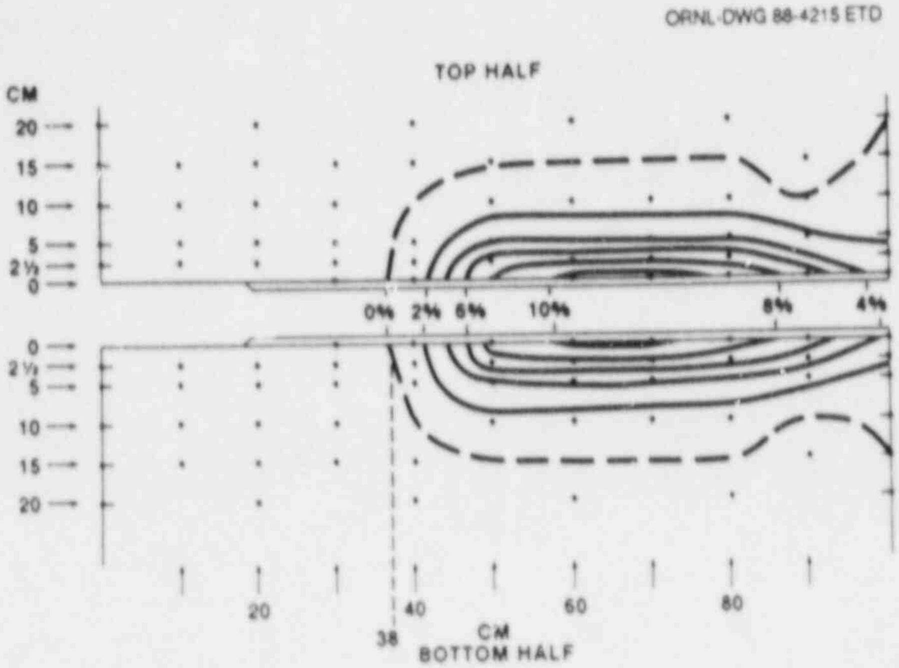

Fig. 5.27. Reduction-in-thickness contour map for specimen WP-CE-1.

strain histories for near- and far-field gage Nos. 21—24 are presented in Fig. 5.32. Short- (6-ms) and long- (60-s) time strain output from far-field gage No. 25 is presented in Fig. 5.33. Long-time records for strain gage Nos. 5—8 in Fig. 5.34 and strain gage Nos. 17—20 in Fig. 5.35 provide some indications of reinitiation and arrest events, but the fracture surface does not clearly reflect their occurrence. Figures 5.36—5.40 present strain histories for selected gages for the period of ductile tearing. (Results for strain gage Nos. 5—10, 15, and 17—20 are not available because of the large amount of plasticity that occurred following arrest to render the gages either inoperable or uninterpretable.) Note that although the time scales in Figs. 5.36—5.40 have been synchronized, the time zero does not necessarily correspond to the onset of ductile fracture because it could not be unambiguously identified.

The strain-gage records and fracture surface were used to deduce the crack length (apparent position of crack front) during the fracture process, and the results are summarized in Table 5.3. In the table, the strain-gage positions are modified from those shown in Fig. 5.6 to account for the fact that the peak strain occurs at an angle of 72° in front of the crack tip. Figure 5.41 presents a plot of crack position vs time derived from the front-face and back-face strain-gage results up to the time corresponding to arrest of the cleavage crack propagation. (Because of the large amount of plasticity that occurred after arrest, many strain gages became inoperative or uninterpretable; therefore, the crack-front position vs time could not be evaluated during fibrous fracture.) Results ($a/w > 0.229$) indicate that the crack front advance at comparable elapsed times during the cleavage crack run-arrest event was more rapid near the back face of the plate than near the front face. As noted earlier, no results are available for the period of ductile tearing.

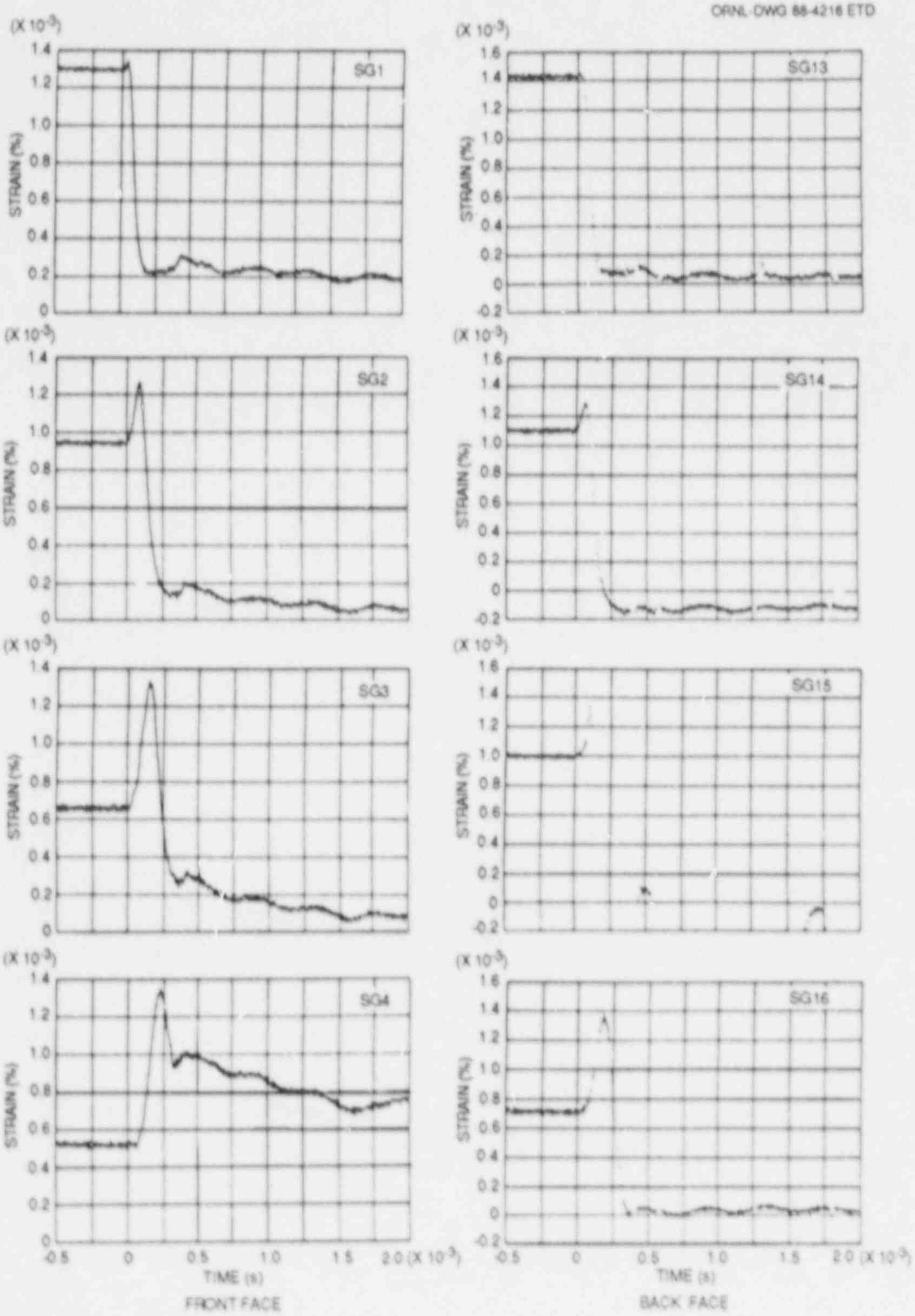

Fig. 5.28. Strain histories for companion crack-line gages showing the cleavage crack passing these gages: Test WP-CE-1.

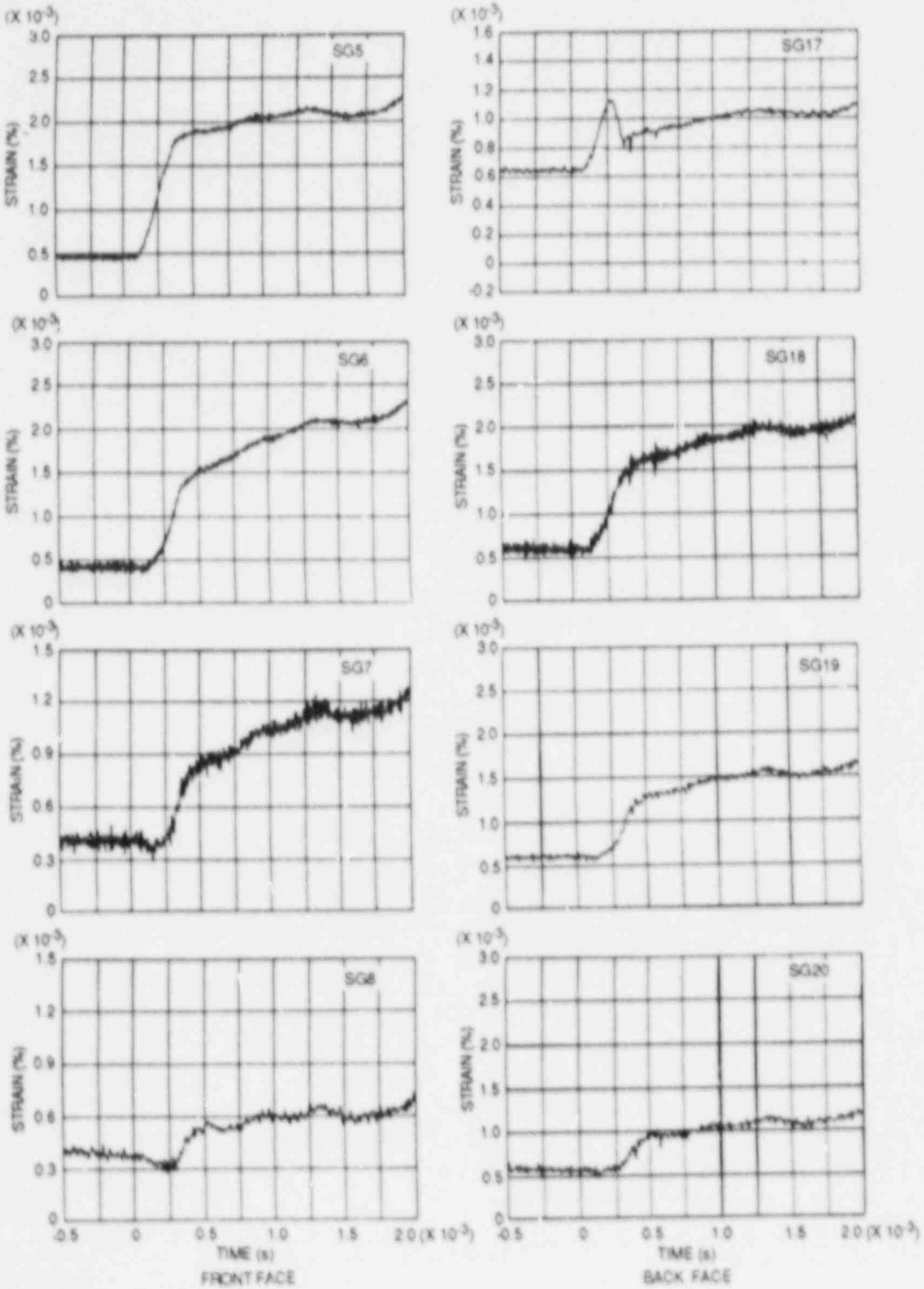

ORNL-DWG 88-4217 ETD

Fig. 5.29. Strain histories for companion crack-line gages showing the crack arresting before reaching gage No. 5 at plate front face and gage No. 18 at plate back face: Test WP-CE-1.

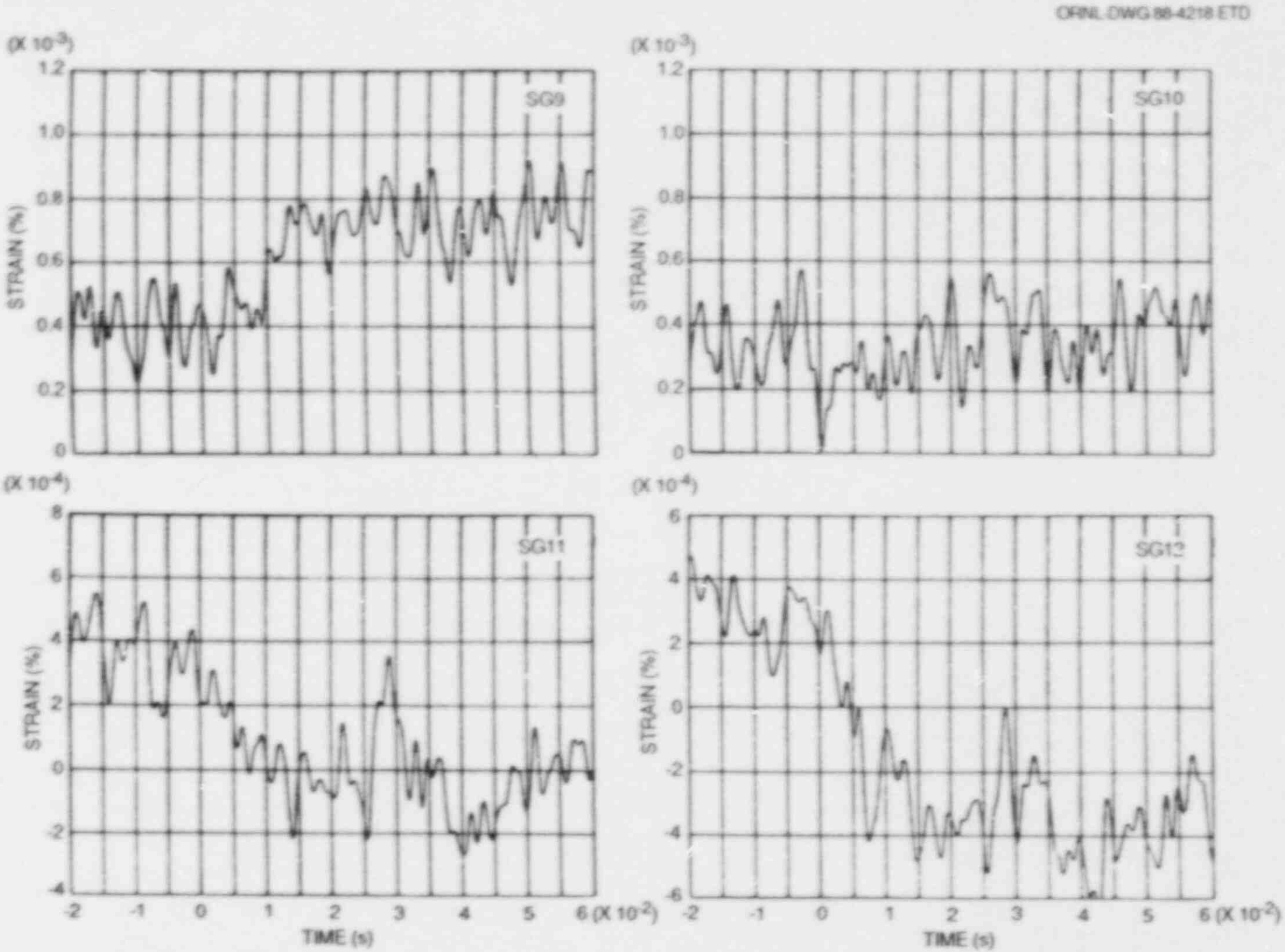

Fig. 5.30. Highly amplified strain histories for front-face gages: Test WP-CE-1. (The noise is caused by the high amplification.)

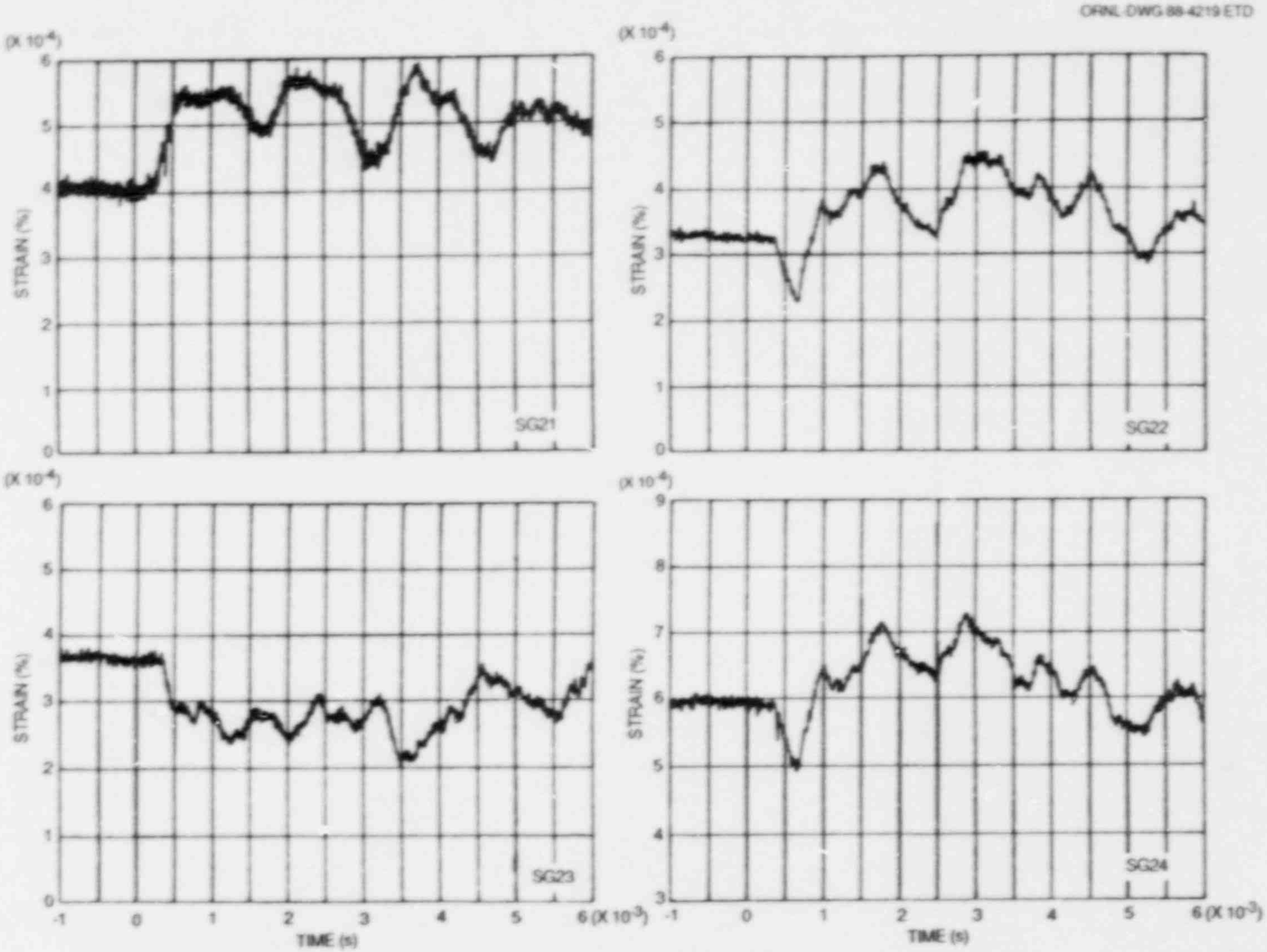

Fig. 5.31. Strain histories for near- and far-field gages recorded just after arrest of the cleavage crack propagation: Test WP-CE-1.

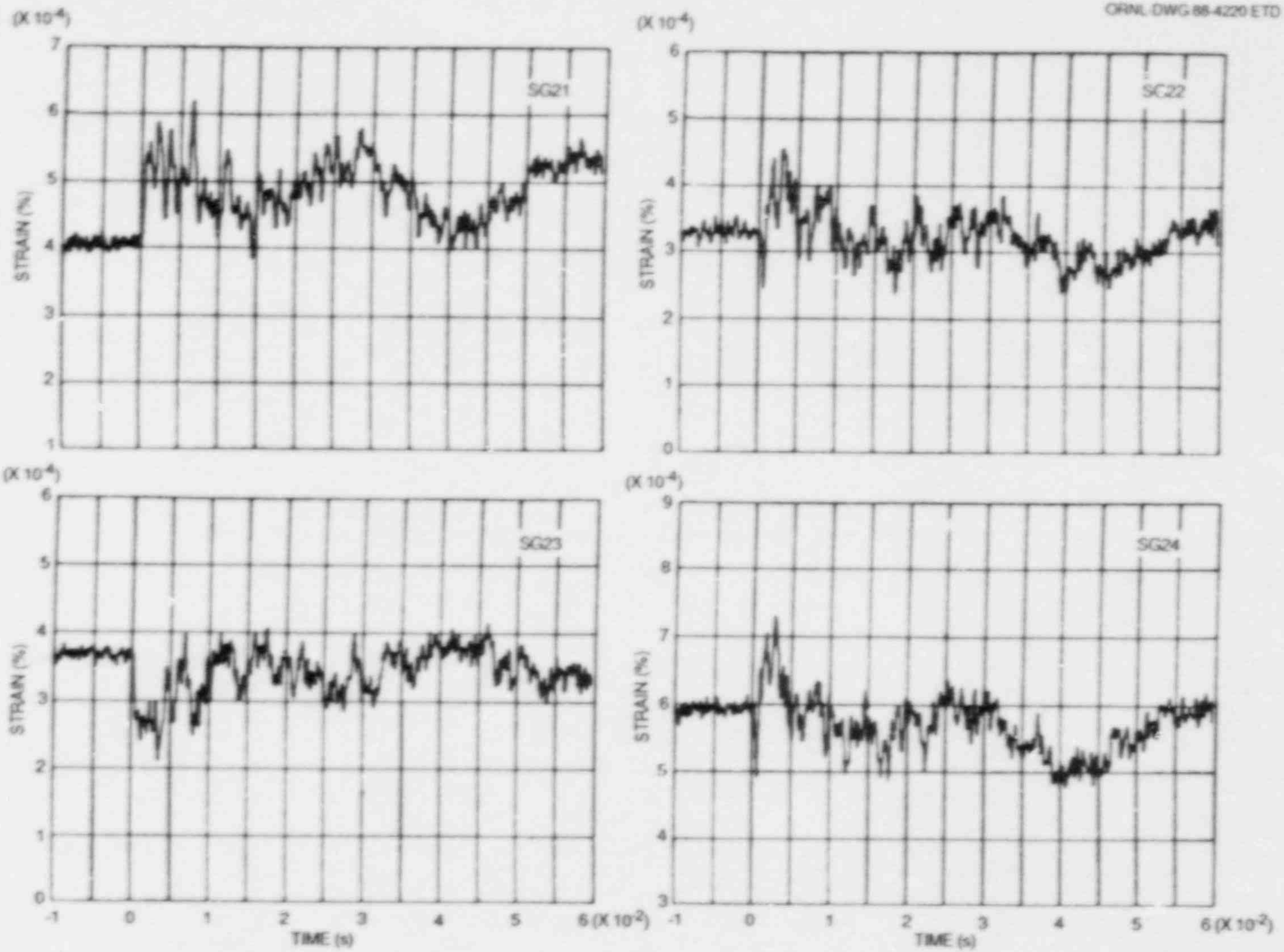

Fig. 5.32. Long-time (70-ms) strain histories for near- and far-field gages: Test WP-CE-1.

ORNL-DWG 88-4221 ETD

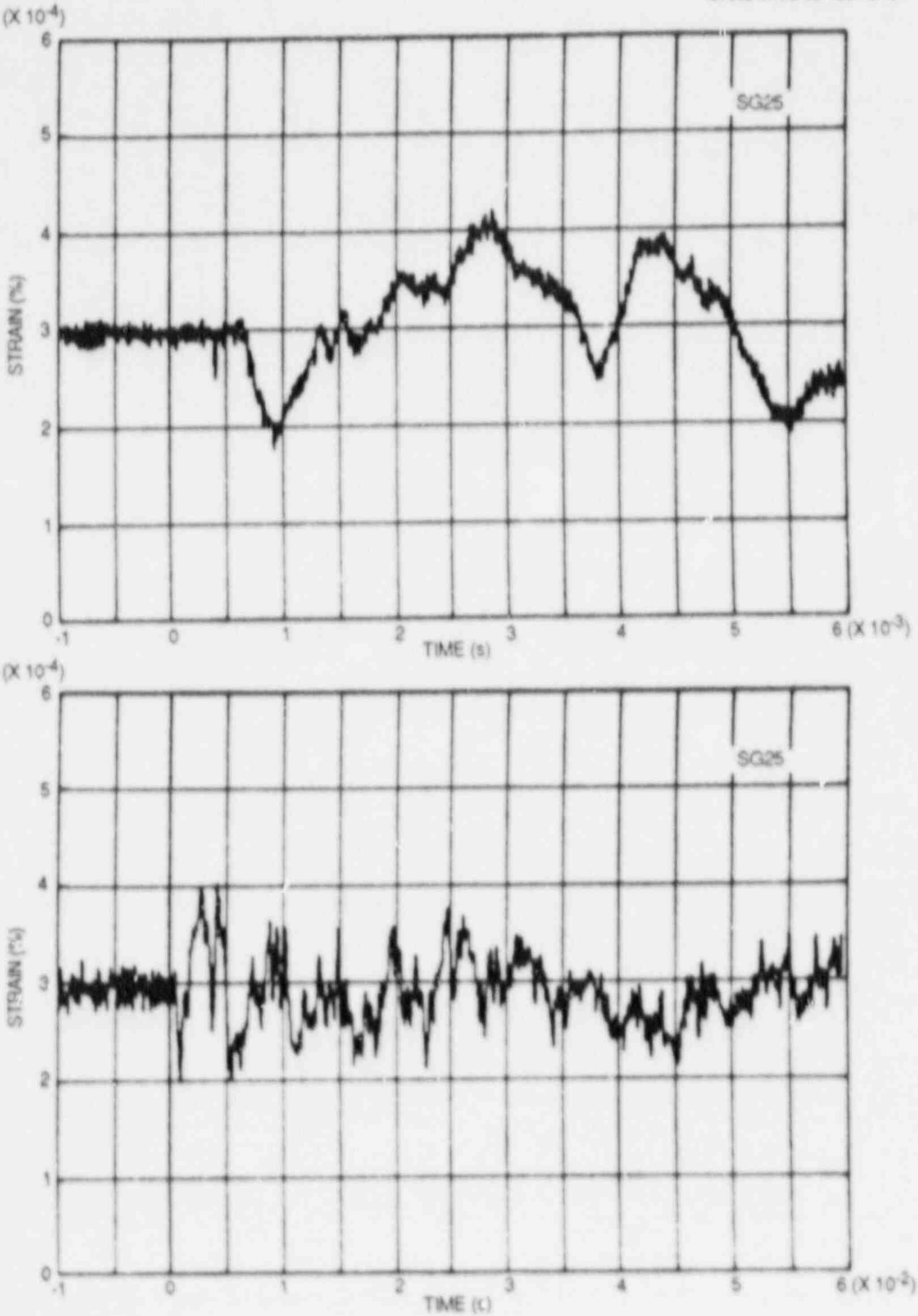

Fig. 5.33. Short- (6-ms) and long- (60-ms) time strain histories for far-field gage No. 25: Test WP-CE-1.

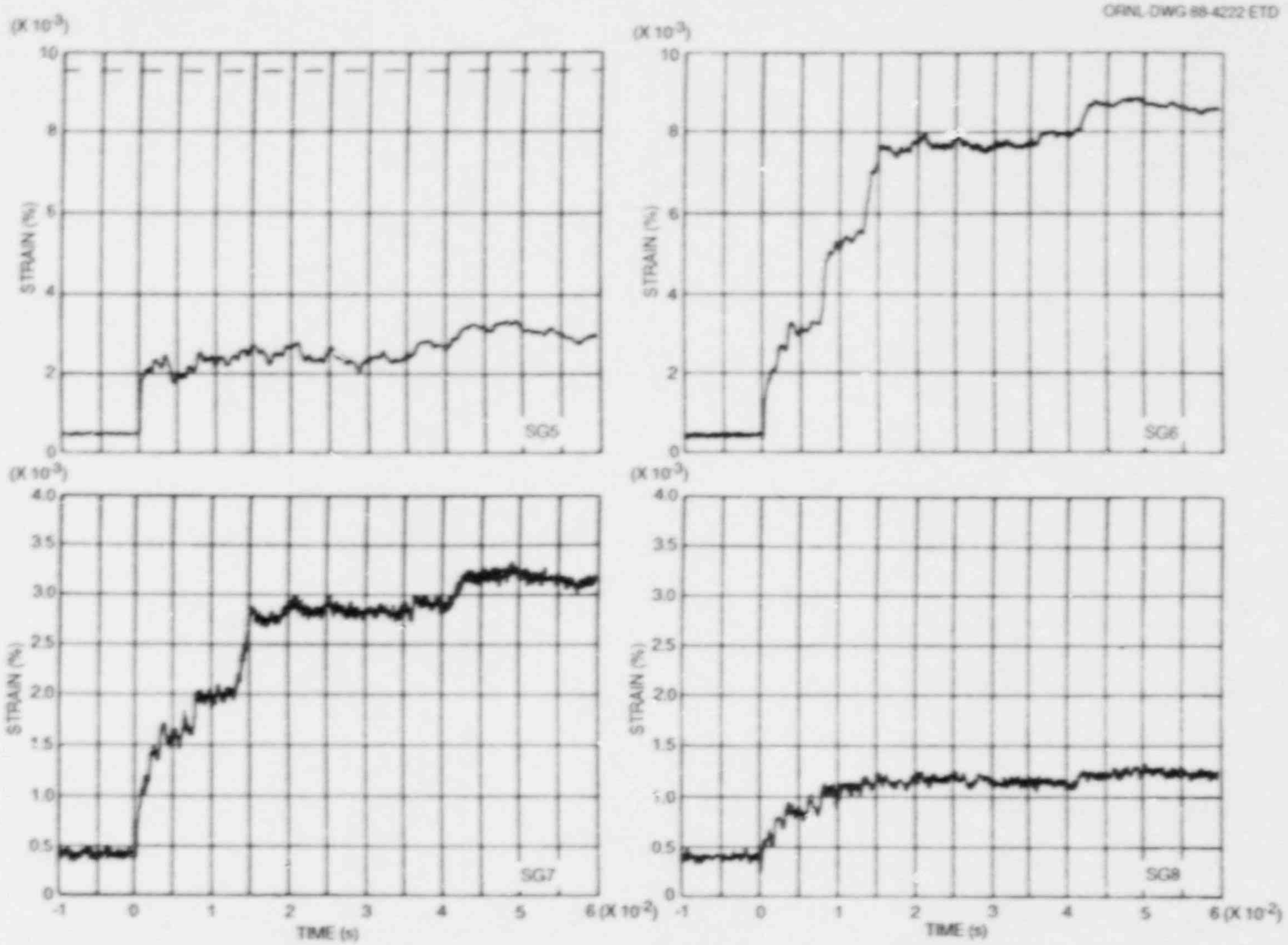

Fig. 5.34. Long-time (60-ms) strain histories for front-face crack-line gages, suggesting some incremental movement of the crack toward gage Nos. 5 and 6: Test WP-CE-1.

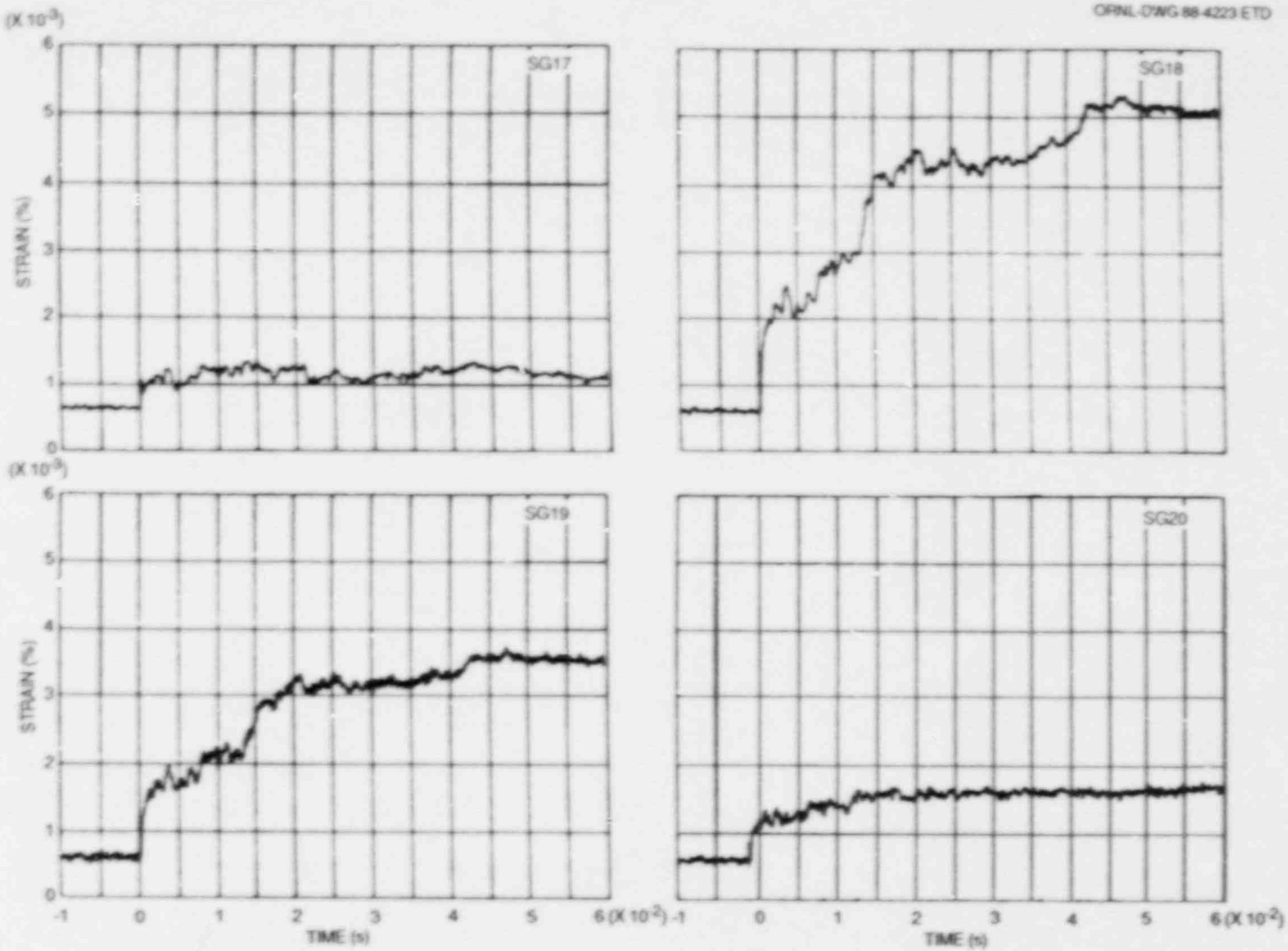

Fig. 5.35. Long-time (60-ms) strain histories for back-face crack-line gages, suggesting some incremental movement of the crack toward gage Nos. 18 and 19: Test WP-CE-1.

ORNL-DWG 88-4224 ETD

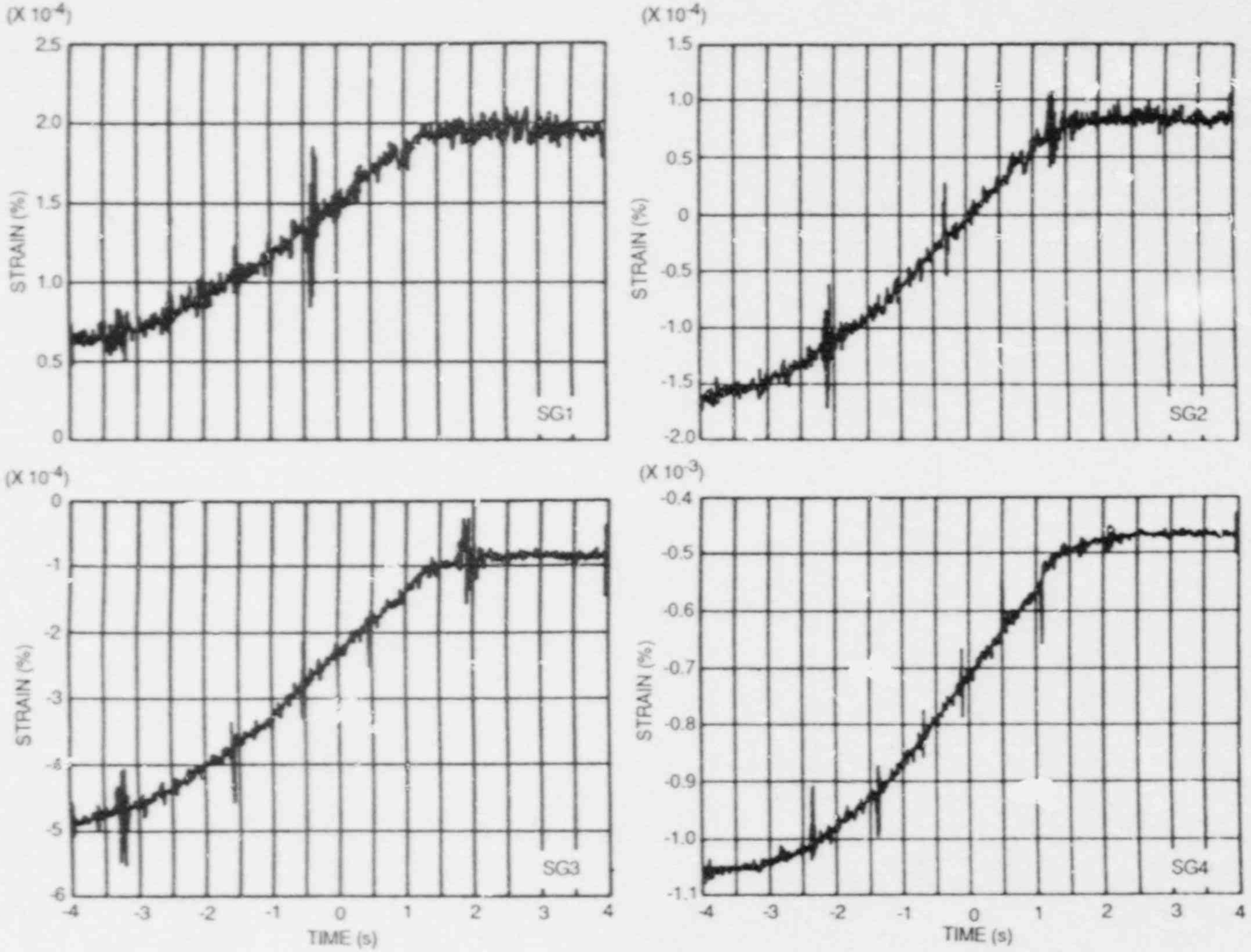

Fig. 5.36. Strain histories for front-face crack-line gages during ductile tearing: WP-CI-1.

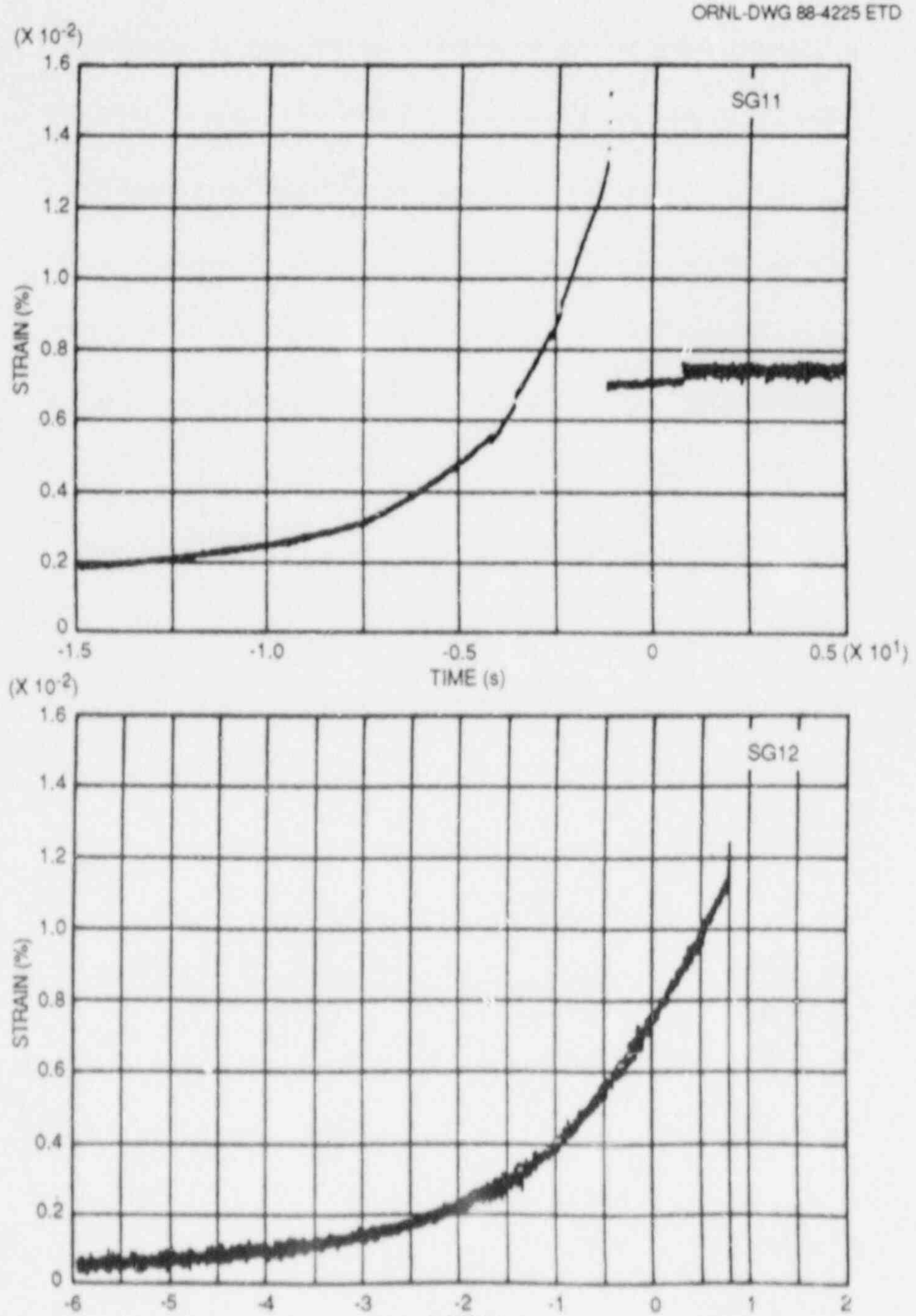

Fig. 5.37. Plasticity and fibrous crack extension as detected by front-face crack-line gages: Test WP-CE-1.

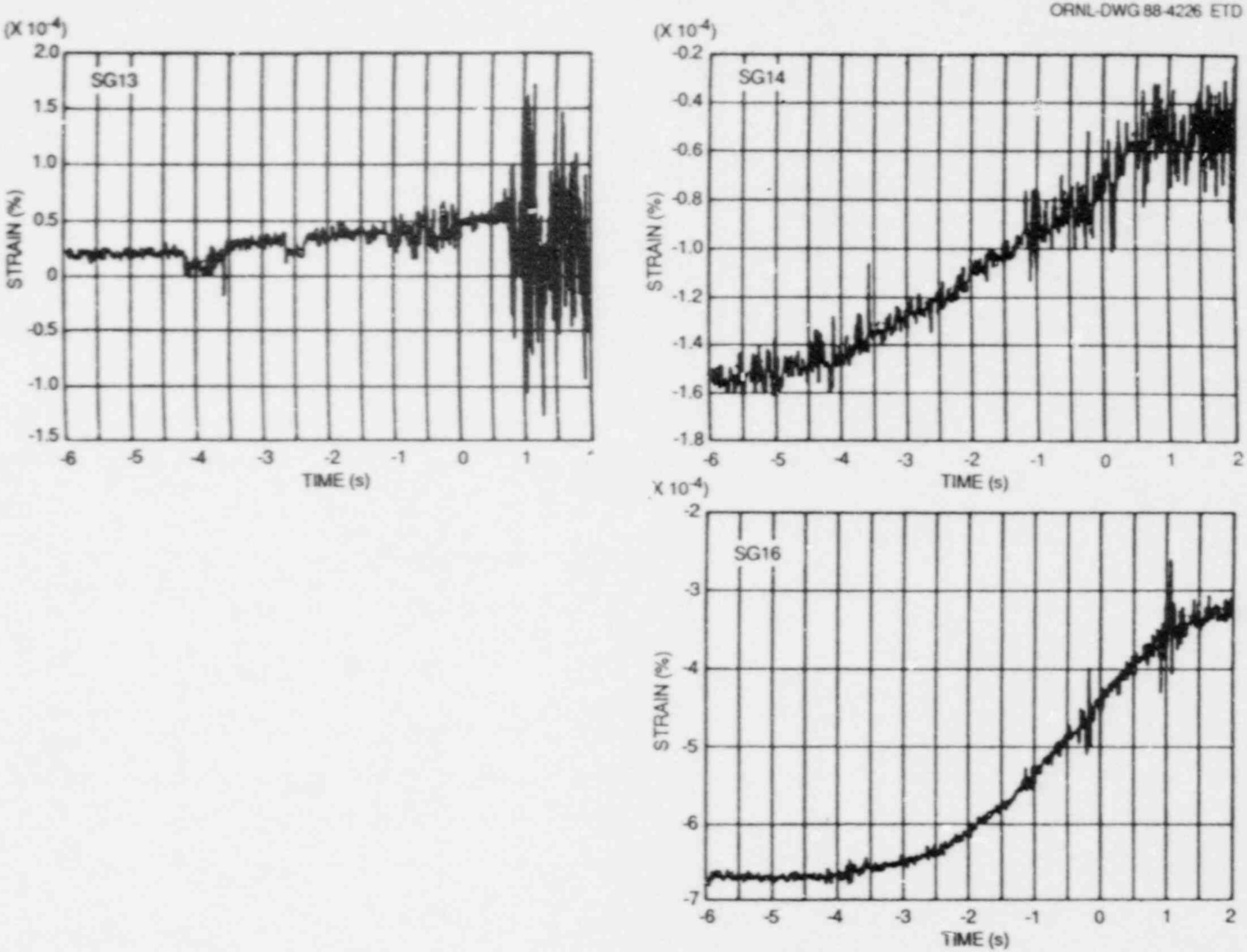

Fig. 5.38. Strain histories for back-face crack-line gages during period while ductile fracture was occurring: Test WP-CE-1.

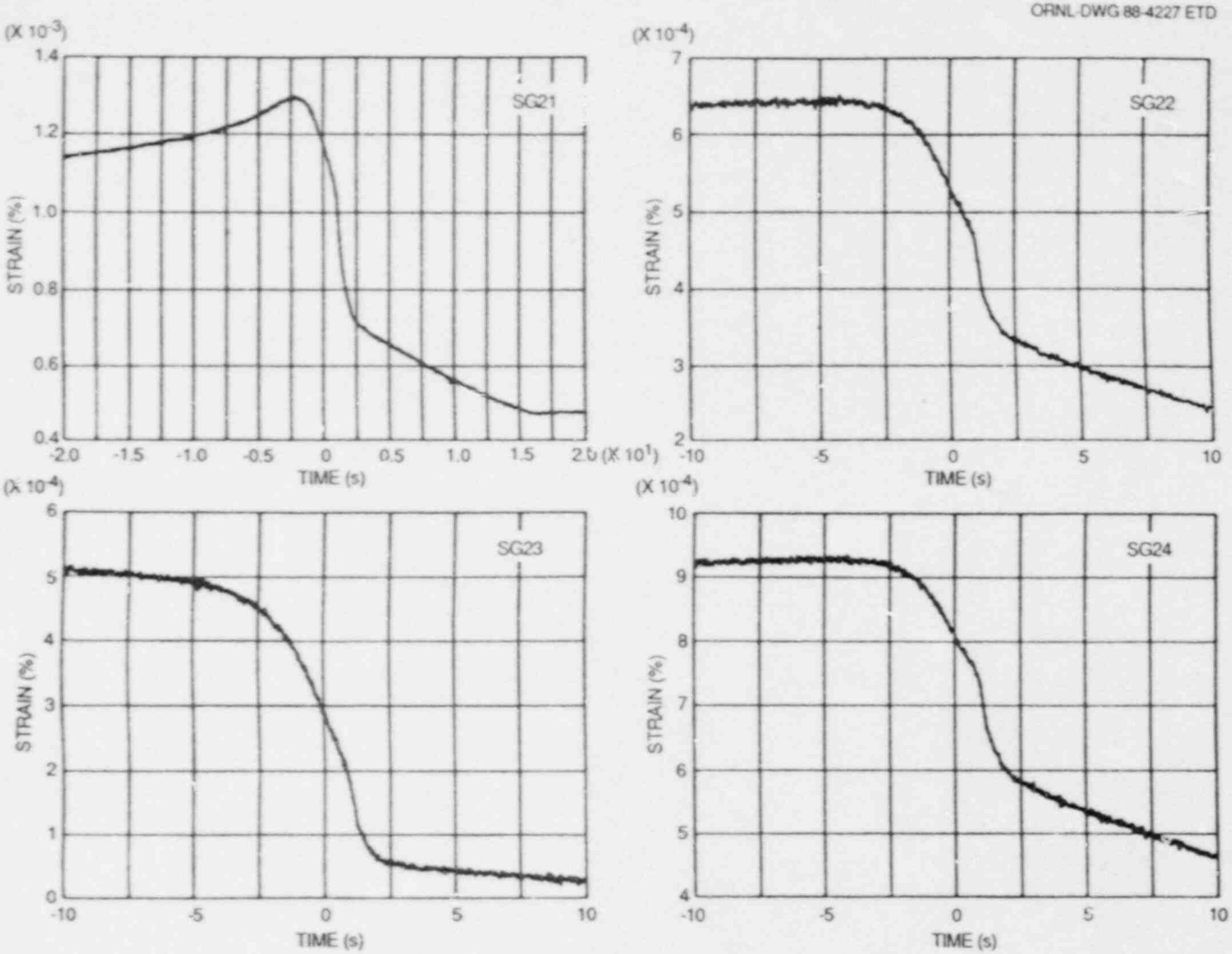

Fig. 5.39. Strain histories for near- and far-field gages during period while ductile fracture was occurring: Test WP-CF-1.

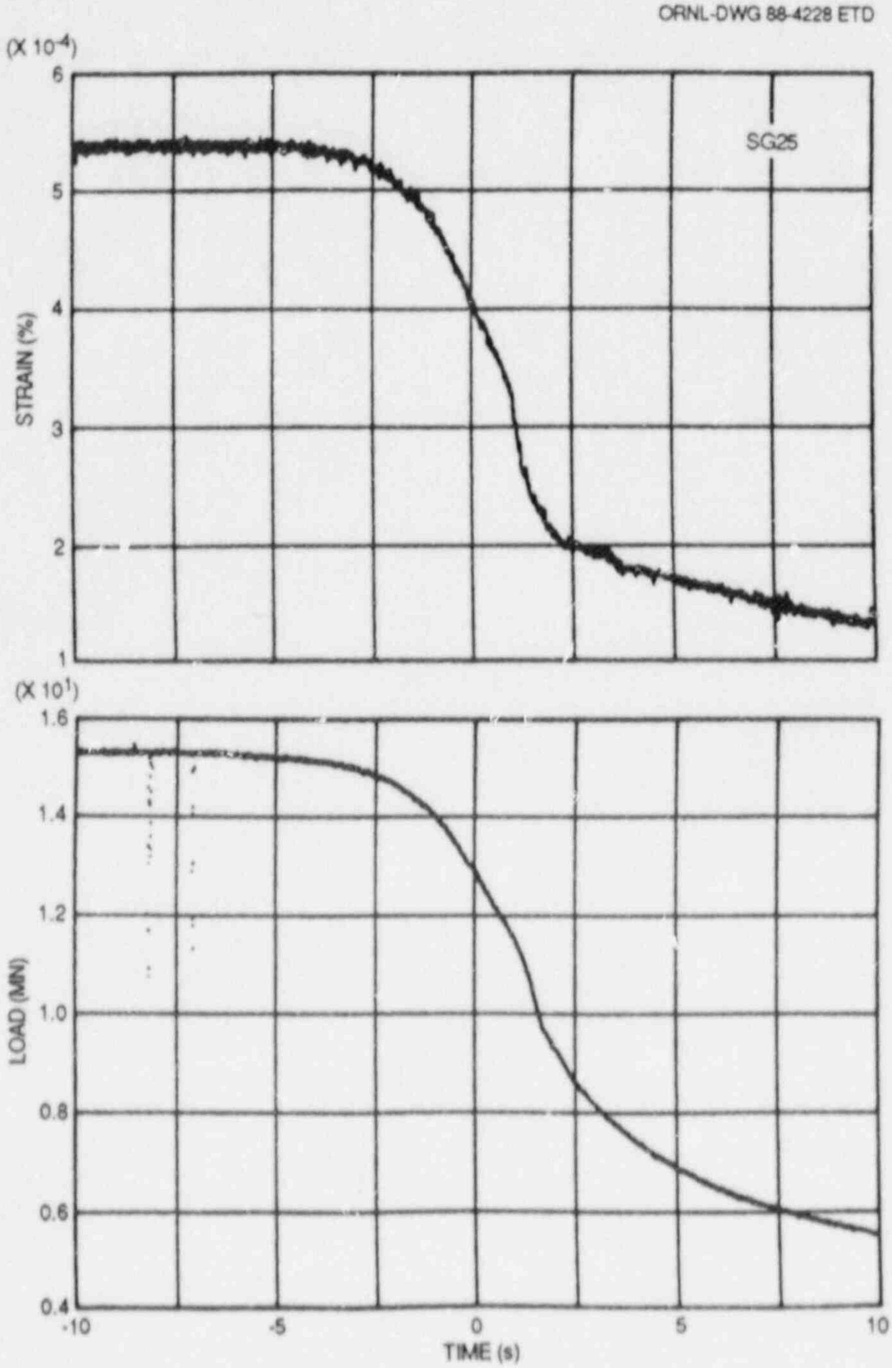

Fig. 5.40. Load and far-field strain histories during the same time period: Test WP-CE-1.

Table 5.3. Crack position vs time and velocity

Indicator[a]	Position (mm)	Time (ms)	Velocity[b] (m/s)
Front-face measurements: WP-CE-1			
Initial crack	200	0	853
SG1	229	0.034	741
SG2	269	0.088	690
SG3	309	0.146	526
SG4	349	0.222	244
Cleavage arrest	370	0.308	
Back-face measurements: WP-CE-1			
Initial crack	200	0	853
SG13	229	0.034	1538
SG14	269	0.060	952
SG15	309	0.102	513
SG16	349	0.180	435
SG17	389	0.272	337
Cleavage arrest	420	0.364	

[a] Strain gage positions in the table are all reduced by 21 mm from the actual gage position shown in Fig. 5.6 to account for the fact that the peak strain occurs at an angle of 72° in front of the crack tip.

[b] Velocity is an average calculated velocity for crack propagation between indicator points.

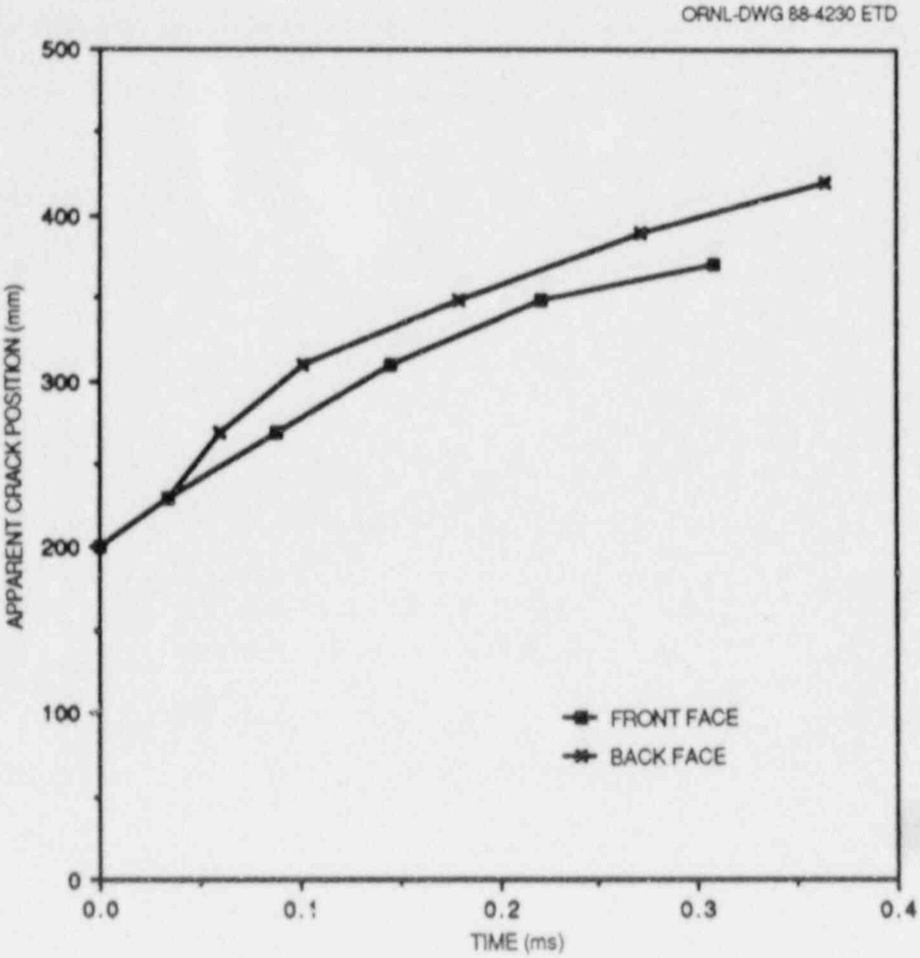

Fig. 5.41. Apparent crack-front position history: Test WP-CE-1.

Front- and back-face COD histories for both short (6 ms) and long (60 ms) times are presented in Fig. 5.42. Longitudinal accelerations recorded by "damped" accelerometers mounted on the specimen's centerline at 3.714 m above (top) and 3.710 m below (bottom) the crack plane are presented in Figs. 5.43 and 5.44, respectively. Dynamic displacement of the specimen, relative to that of the large columns of the testing machine, as measured 3.710 m below the crack plane, is presented in Fig. 5.45 for several time resolutions.

5.3 Properties of Prototypical Pressure Vessel Materials

5.3.1 WP-1 series

The initial series of wide-plate crack-arrest specimens is taken from the central portion of the 18.73-cm-thick HSST plate 13A of A 533 grade B class 1 steel that is in a quenched and tempered condition.

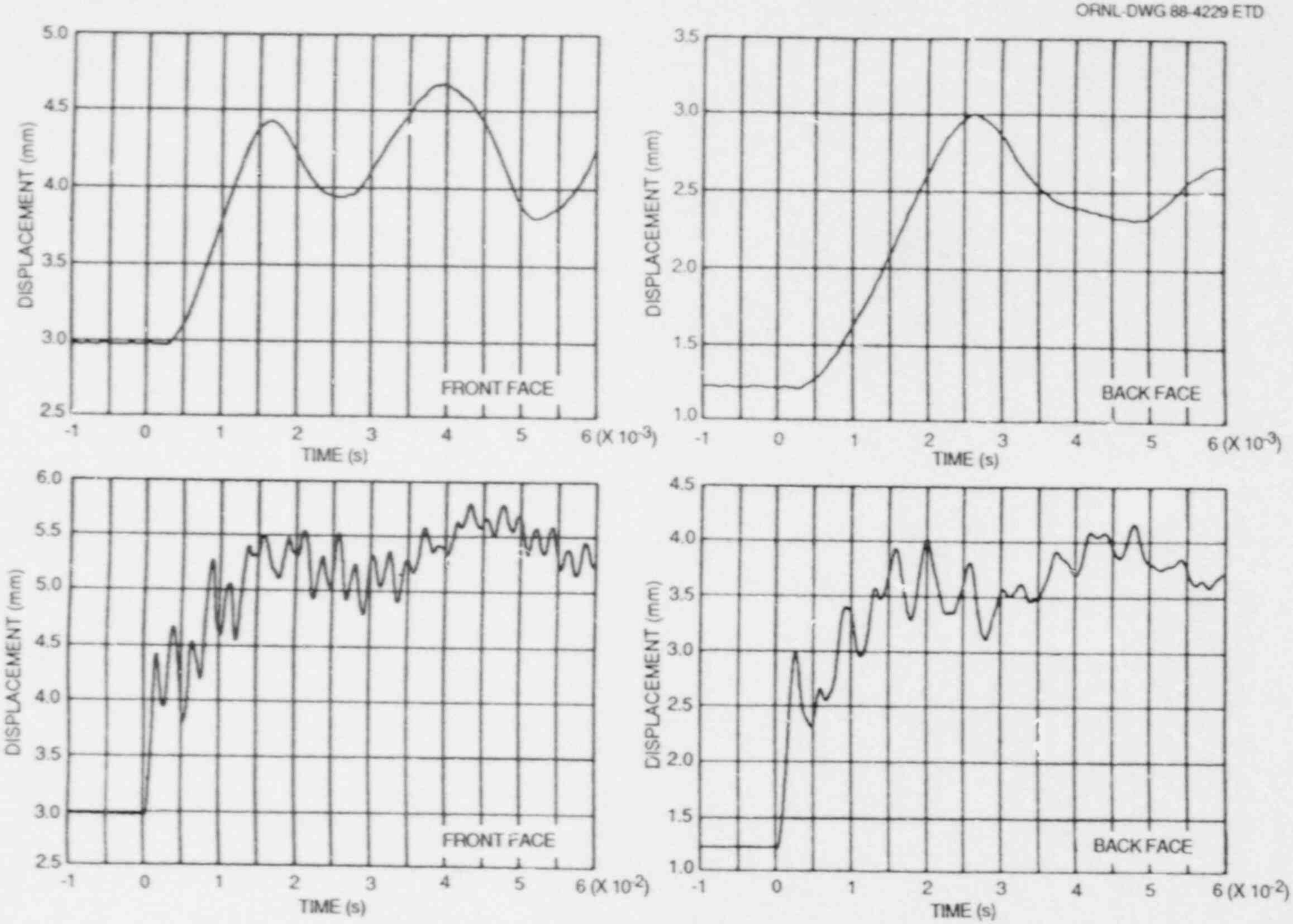

Fig. 5.42. F-COD and B-COD histories for both short- (6-ms) and long- (60-ms) time periods: Test WP-CE-1.

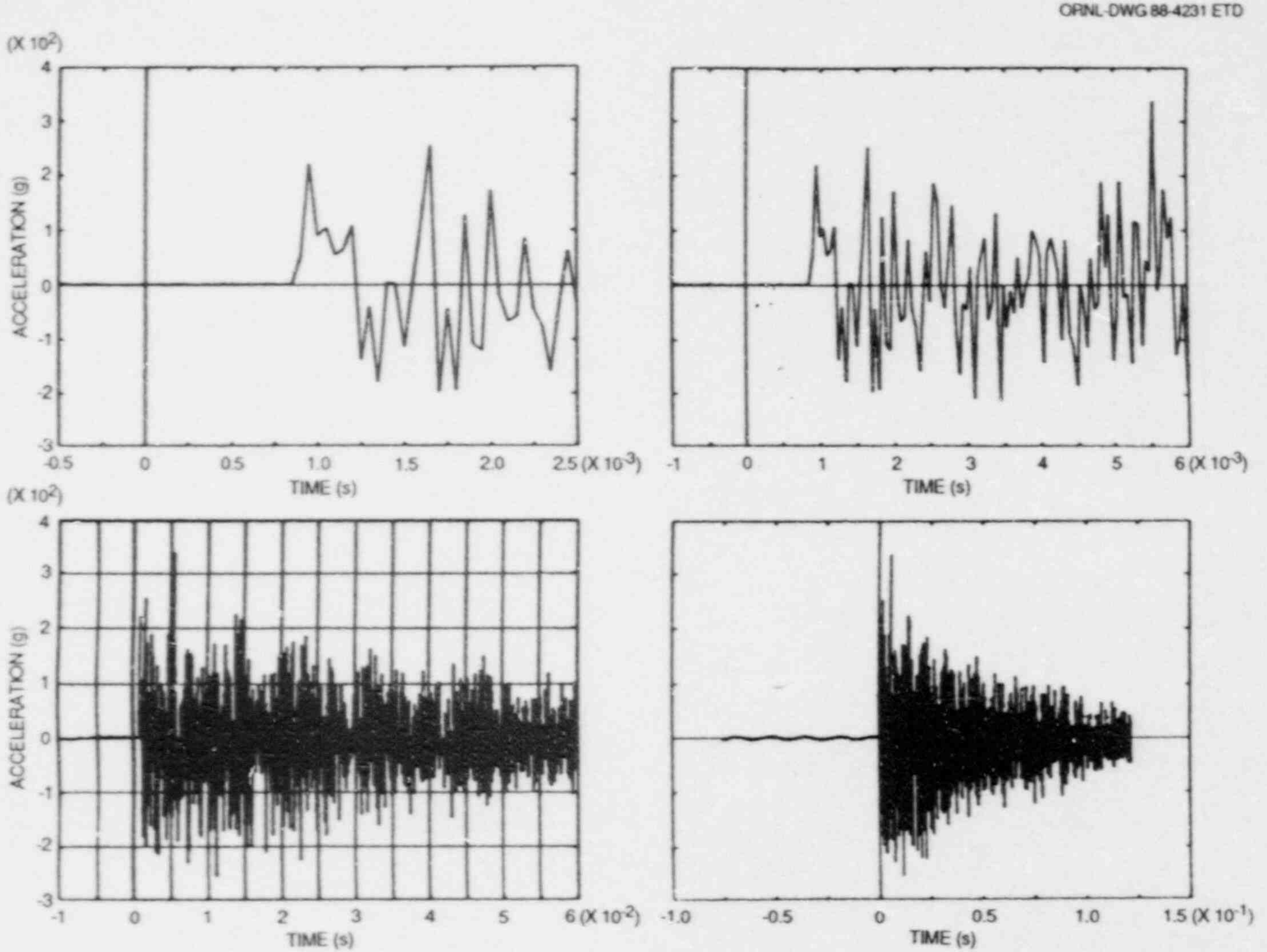

Fig. 5.43. Longitudinal acceleration results at various time resolutions measured by top "damped" accelerometer mounted 3.714 m above the crack plane: Test WP-CE-1.

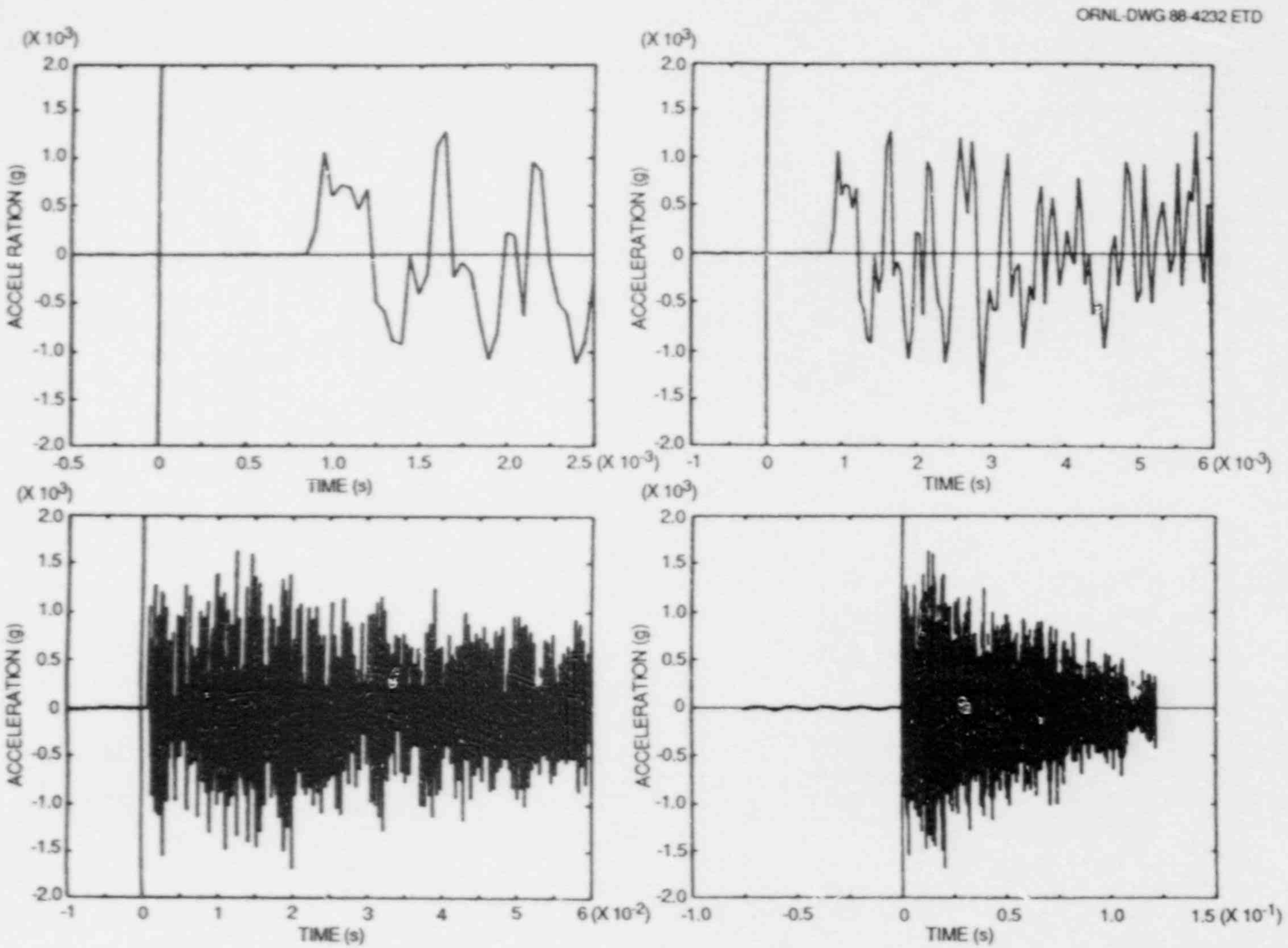

Fig. 5.44. Longitudinal acceleration results at various time resolutions measured by bottom "damped" accelerometer mounted 3.710 m below the crack plane: Test WP-CE-1.

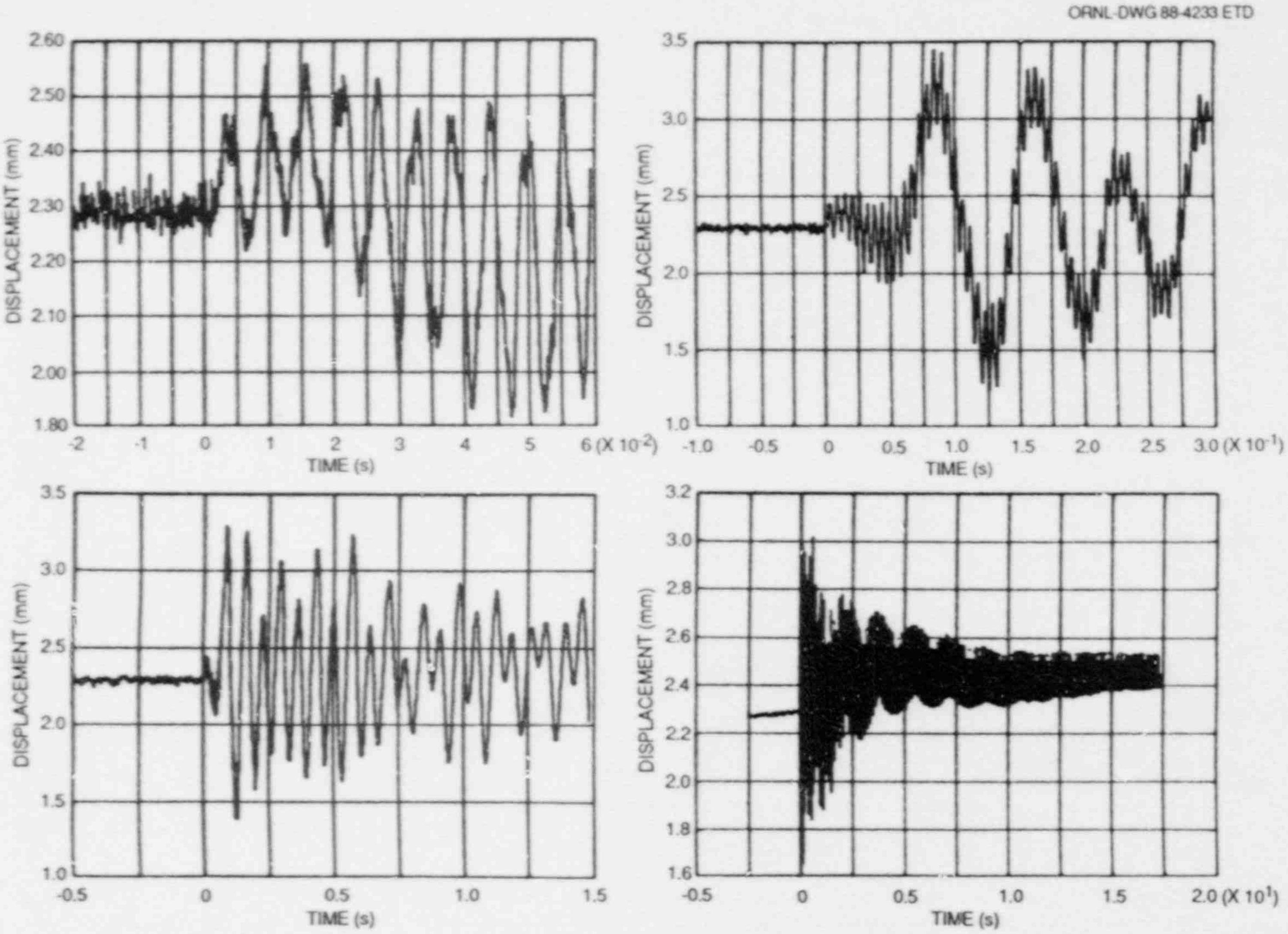

Fig. 5.45. Dynamic displacement results at several time resolutions of specimen relative to that of the large columns of the testing machine as measured 3.710 m below the crack plane: Test WP-CE-1.

Properties of this plate include

1. Young's modulus $E = 206.9$ GPa,
2. Poisson's ratio $\nu = 0.3$,
3. coefficient of thermal expansion $\alpha = 11 \times 10^{-6}/°C$, and
4. density $\rho = 7850\ kg/m^3$.

Temperature-dependent fracture-toughness relations for initiation and arrest, based on small-specimen data, are given by

$$K_{Ic} = 51.276 + 51.897\ e^{0.036(T-RT_{NDT})}\ , \tag{5.1}$$

$$K_{Ia} = 49.957 + 16.878\ e^{0.028738(T-RT_{NDT})}\ , \tag{5.2}$$

with units of K and T being megapascals times root meters and degrees Celsius, respectively. Drop-weight and Charpy V-notch test data indicate that $RT_{NDT} = -23°C$ and that the Charpy upper-shelf energy is 160 J with its onset occurring at 55°C.

Analytical studies have used a dynamic fracture-toughness relation in the following form:

$$K_{ID} = K_{Ia} + A(T)\ \dot{a}^2\ , \tag{5.3}$$

where K_{Ia} is given by Eq. (5.2) and either

$$A(T) = [329.7 + 16.25\ (T - RT_{NDT})] \times 10^{-6}\ , \tag{5.4}$$

or

$$A(T) = [121.71 + 1.296\ (T - RT_{NDT})] \times 10^{-6}\ , \tag{5.5}$$

if $(T - RT_{NDT})$ is greater or less than $-13.9°C$, respectively. Units for K_{ID}, A, $\dot{a}$, and T, respectively, are

1. megapascals times root meters,
2. megapascals times square seconds times meters to the $-3/2$,
3. meters per second, and
4. degrees Celsius.

The form of the K_{ID} expression in Eq. (5.3) and relations for A(T) [Eqs. (5.4) and (5.5)] are derived from Ref. 4 by estimating that $RT_{NDT} = -6.1°C$ for the material used in that study.

5.3.2 WP-CE series

The WP-CE specimens were made from a second heat of A 533 grade B class 1 material that was provided to ORNL by Combustion Engineering (CE), Inc., in the form of a plate 244 × 1016 × 1016 mm. The material was characterized by CE, and the detailed results are presented in Ref. 5. Pertinent material properties include

1. an ultimate tensile strength ranging from ≈580 MPa at room temperature to ≈560 MPa at 66°C to ≈520 MPa at 120°C,
2. a nil-ductility transition temperature from ≈ −34°C to ≈ −23°C,
3. a Charpy upper-shelf energy of ≈180 to ≈203 J, and
4. the minimum temperature for fully ductile behavior occurring at ≈43 to ≈49°C.

Temperature-dependent fracture-toughness relations for the WP-CE material used for pretest planning were the same as Eqs. (5.1) and (5.2) with the RT_{NDT} changed to the appropriate value for the WP-CE material.

5.4 Wide-Plate Analyses at ORNL

B. R. Bass J. Keeney-Walker

5.4.1 Posttest analyses of test WP-1.7

5.4.1.1 Posttest three-dimensional (3-D) static analyses. Three-dimensional static finite-element analyses were performed on the WP-1.7 plate assembly to determine the static-stress intensity factor at the time of crack initiation. These analyses were performed with the ORMGEN/ORVIRT (Refs. 6, 7) fracture analysis system and the ADINA-84 (Ref. 8) finite-element code. The 3-D finite-element model incorporated a segment of the plate assembly that was 4.4595 m in length measured from the crack plane to the top of the load-pin hole. The crack-tip region of the model included the chevron cutout, the side grooving, and the edge notch, the dimensions of which are taken from Table 5.1. From symmetry conditions neglecting out-of-plane eccentricity, one-quarter of the partial pull-plate assembly was modeled using 3751 nodes and 720 20-noded isoparametric elements.

The thermal deformations computed from a posttest two-dimensional (2-D) analysis were superposed on a 3-D finite-element model to account for the in-plane thermal bending effect in the 3-D analyses. The boundary conditions of the 2-D thermoelastic analysis were based on the assumption that the heated and cooled edges of the plate were fixed at T_{max} = 182.7°C and T_{min} = −74.7°C, respectively, along a 2.4-m length (centered relative to the crack plane) and that the pull-tab edges were maintained at T = 20.0°C. The remaining surfaces of the assembly were assumed to be insulated. The in-plane thermal bending produced a load-line eccentricity (through the top of the load-pin hole) of 1.83 cm relative to the geometric center of the plate.

In the 3-D analysis, thermal stress effects were neglected, and a uniform line-load statically equivalent to the WP-1.7 test initiation load of 26.2 MN was applied at the location corresponding to the top of the load-pin hole. This analysis resulted in a static stress-intensity factor of K_I = 280.6 MPa$\cdot\sqrt{m}$ at the center plane of the plate. A ratio of K_I/K_{Ic} = 2.71 results from comparing this computed K_I value with the static initiation value of K_{Ic} = 103.7 MPa$\cdot\sqrt{m}$ evaluated from Eq. (5.1) using the crack-tip temperature of −22.7°C.

5.4.1.2 Posttest two-dimensional (2-D) static and dynamic analyses

Static and stability analyses using Eq. (5.2) for K_{Ia}. Posttest 2-D analyses were done using computer codes based on both quasistatic and elastodynamic techniques. For the quasistatic analyses, the ORNL computer code WPSTAT (Ref. 9) was used to perform both crack-arrest and crack-stability analyses. As described in Ref. 9, the WPSTAT code evaluates static stress-intensity factors as a function of crack length a and temperature differential $\Delta T = T_{max} - T_{min}$ across the plate. These factors are computed for fixed-force conditions K_I^F (a, ΔT) and for fixed load-pin displacement conditions K_I^{DSP} (a, ΔT) by superposing contributions from tension and bending finite-element and handbook solutions. Also, WPSTAT categorizes arrested crack lengths in terms of three types of instability limits that are enumerated below.

For test WP-1.7, the proposed temperature profile was defined by specifying a crack-tip temperature of T_{CT} = −19°C at x = 0.20 m and a midplate temperature of T_{MP} = 57°C at x = 0.5 m, implying that T_{min} = −69.7°C and T_{max} = 183.7°C. As indicated in Fig. 5.9(*b*), the temperature gradient actually achieved at the time of the run-arrest event deviated somewhat from the proposed profile in the region of $0.2 < x < 0.6$. Consequently, the posttest WPSTAT calculations of the static factors K_I^F (a, ΔT) and K_I^{DSP} (a, ΔT) used the actual temperature profile provided in Fig. 5.9(*b*) (i.e., T_{CT} = −22.7°C and T_{mid} = 54°C). For this specified temperature profile, the dependence of the arrested crack length and crack stability on the applied initiation load F_{in} was investigated with WPSTAT, and the results are presented in Fig. 5.46. Figure 5.46 includes the statically calculated final crack length a_{fc}, as well as the instability-limit crack lengths for (1) reinitiation a_{rein} (F_{in}), (2) tensile instability a_{I1} (F_{in}), and (3) tearing instability a_{I2} (F_{in}). The tensile instability calculation is based on the average stress in the remaining ligament equal to an ultimate stress of σ_u = 550 MPa, which represents the lowest value for the temperature range of interest. For the tearing instability calculation, the material tearing resistance is assumed to be represented by a power-law J-resistance curve $J_R = C(\Delta a)^m$, where C = 0.3539, m = 0.4708, and the units J_R and Δa are MJ/m^2 and mm, respectively. In Fig. 5.46, the statically computed arrest length corresponding to the measured initiation load F_{in} = 26.2 MN is given by a_{fc} = 0.635 m. The computed arrest point is above the tensile instability

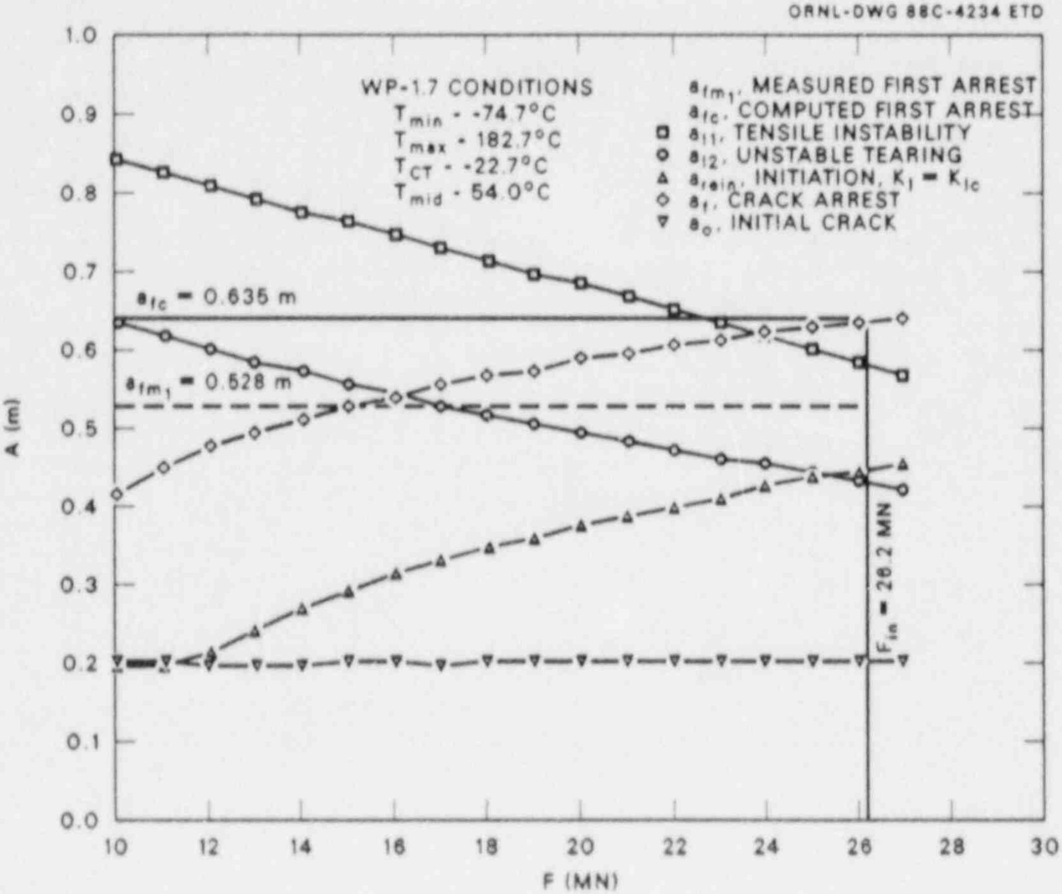

Fig. 5.46. Statically calculated crack lengths [Eq. (5.2)]: Test WP-1.7.

curve a_{I1}, implying an unstable condition. The measured initial arrest point a_{fm_1} = 0.528 m is below the tensile instability curve but above the tearing instability curve a_{I2}. Figure 5.46 indicates that tearing instability is expected when the crack length exceeds ≈0.43 m, which occurs before the first measured arrest position (see Table 5.2).

In Fig. 5.47, the K_{Ia} function presented in Eq. (5.2) is evaluated on the arrest crack-length curve $a_f(F)$, on the incipient tearing-instability curve $a_{I2}(F)$, and on the cleavage-reinitiation curve $a_{rein}(F)$. The K_{Ic} function presented in Eq. (5.1) is evaluated on the curve $a_{rein}(F)$. Evaluation of the $K_{Ia}(a_f)$ curve at the initiation load F_{in} = 26.2 MN yields an arrest toughness of K_{Ia} = 457 MPa$\cdot\sqrt{m}$ at the computed arrest point of a_{fc} = 0.635 m where the crack-tip temperature would be T = 87.7°C.

The complete static fracture mechanics and stability analyses are depicted in Fig. 5.48 for the initiation load of F_{in} = 26.2 MN. Included

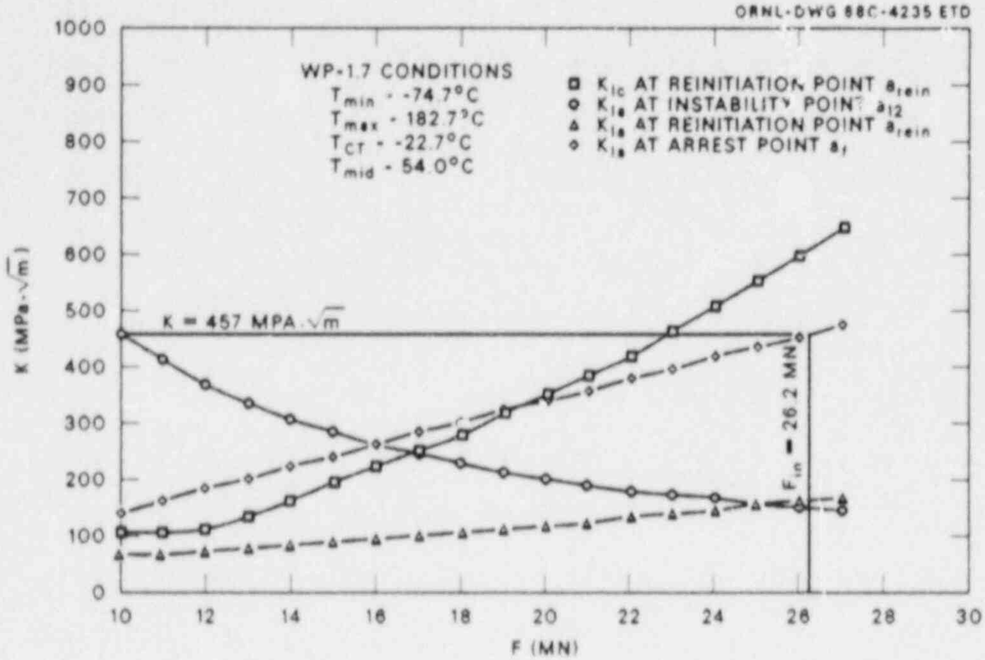

Fig. 5.47. Determination of arrest toughness at initiation load of 26.2 MN [Eq. (5.2)]: Test WP-1.7.

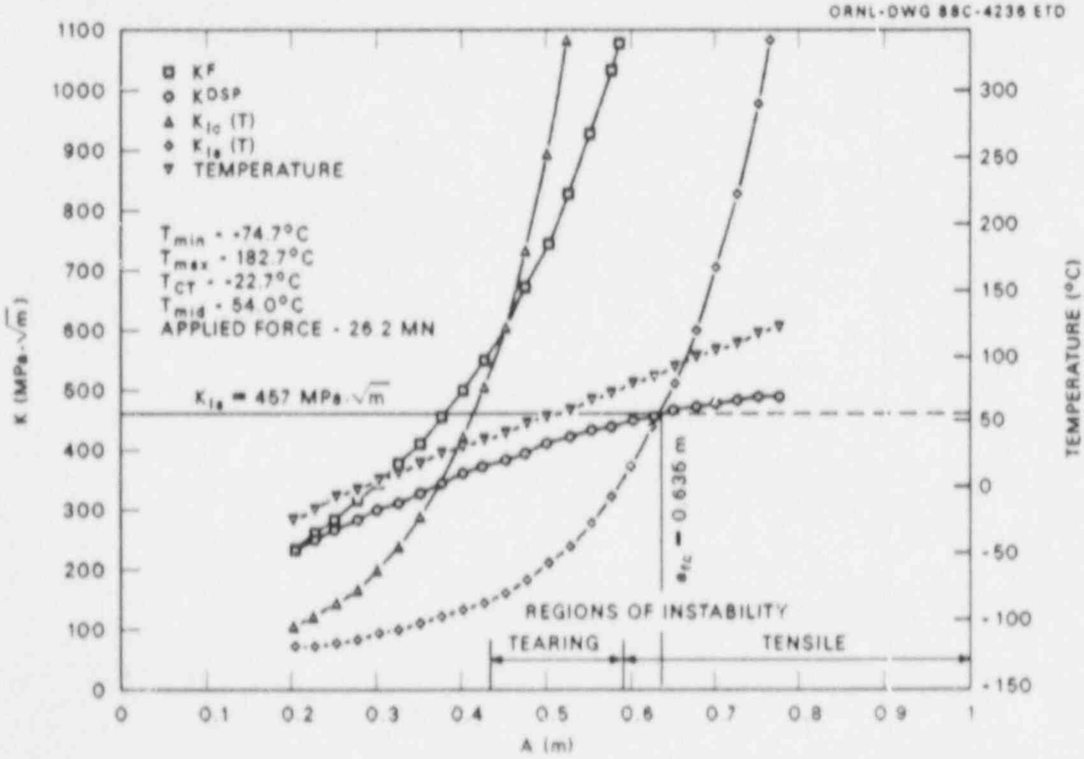

Fig. 5.48. Complete static and stability analyses for initiation load of 26.2 MN [Eq. (5.2)]: Test WP-1.7.

in the figure are curves for initiation toughness K_{Ic}, arrest toughness K_{Ia}, displacement controlled stress-intensity factor K_I^{DSP}, and force-controlled stress-intensity factor K_I^F. The regions of tearing and tensile instability and the computed cleavage arrest point a_{fc} are also identified in Fig. 5.48.

Static and stability analyses using Schwartz function for K_{Ia}. The analysis was repeated using the Schwartz function for K_{Ia}, that is,

$$K_{Ia} = 63.130 + 9.211e^{0.03988(T-RT_{NDT})} . \tag{5.6}$$

In Fig. 5.49, the statically computed arrest length corresponding to the measured initiation load F_{in} = 26.2 MN is given by a_{fc} = 0.562 m, which is closer to the measured initial arrest point of a_{fm_1} = 0.528 m than the results presented in Fig. 5.46. Both the computed arrest point and the

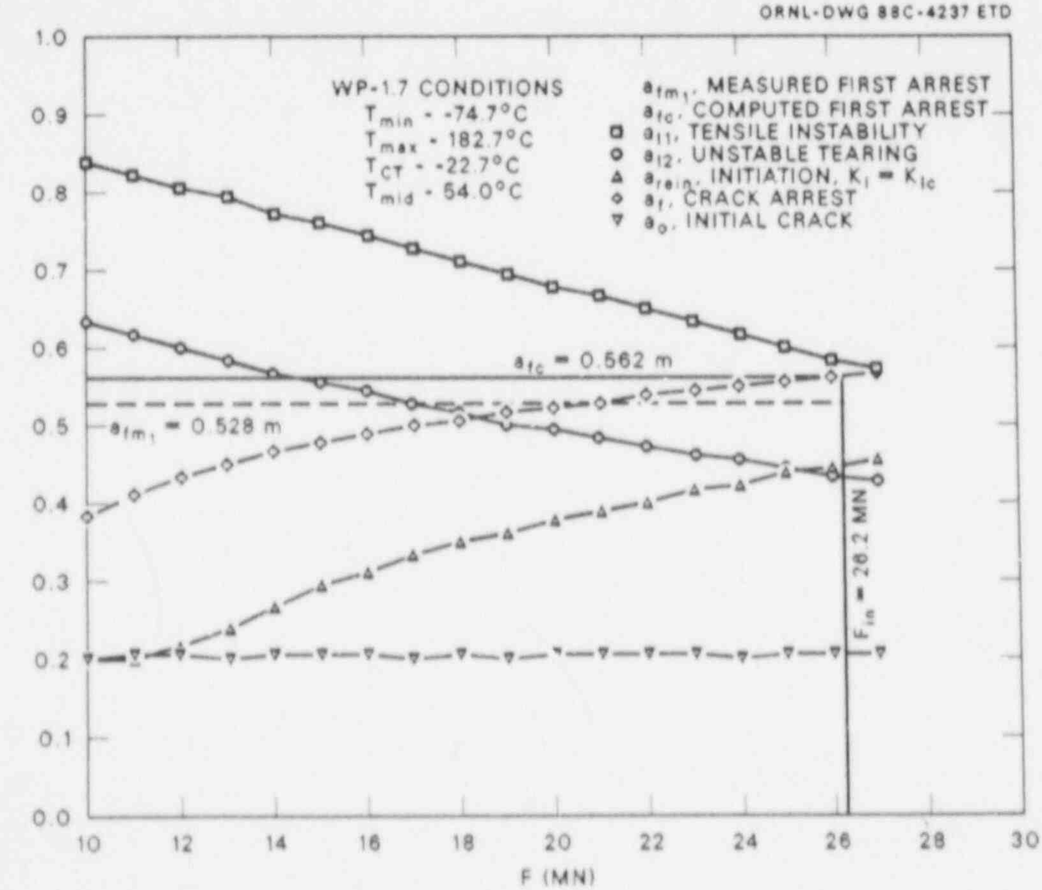

Fig. 5.49. Statically calculated crack lengths [Eq. (5.6)]: Test WP-1.7.

first measured arrest point are now between the tensile instability curve and the tearing instability curve.

In Fig. 5.50, the K_{Ia} function in Eq. (5.6) is evaluated on the (1) arrest crack-length curve $a_f(F)$, (2) incipient tearing instability curve a_{I2}, and (3) cleavage reinitiation curve $a_{rein}(F)$. Evaluation of the $K_{Ia}(a_f)$ curve at the initiation load of F_{in} = 26.2 MN yields an arrest toughness of K_{Ia} = 433 MPa•$\sqrt{m}$ at the computed arrest point of a_{fc} = 0.562 m, where the crack-tip temperature would be T = 69.4°C. The complete static fracture mechanics and stability analyses are presented in Fig. 5.51 for the initiation load of F_{in} = 26.2 MN.

5.4.1.3 Application-mode dynamic analysis (fixed-load boundary condition) Elastodynamic analyses of wide-plate test WP-1.7 were carried out with the ADINA/VPF (Ref. 10) dynamic crack-analysis code. The 2-D plane stress finite-element model of the wide-plate configuration used in the analyses consists of 938 nodes and 277 eight-noded isoparametric elements. A total of 34 spring elements were used in the crack plane to model propagation of the crack tip. Side grooves were taken into account by adjusting the resulting stress-intensity factor calculated in each time-step of the analysis. The in-plane bending of the plate assembly

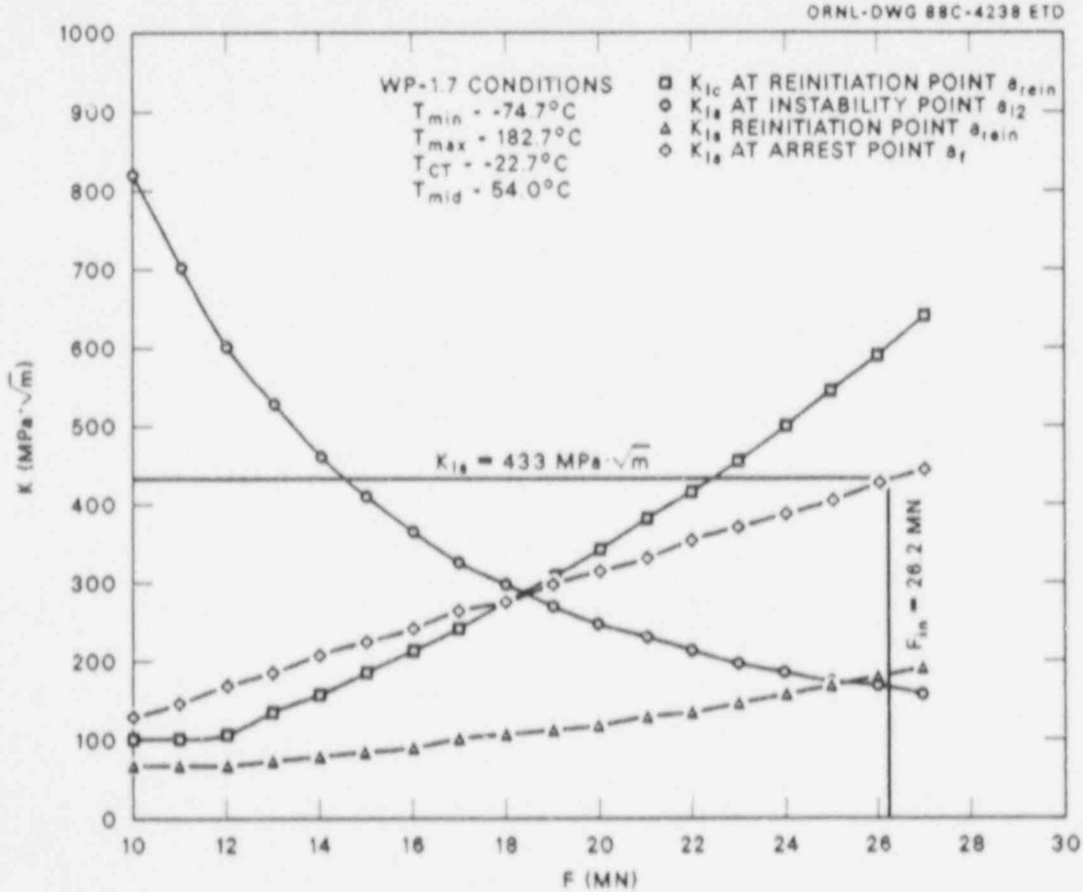

Fig. 5.50. Determination of arrest toughness at initiation load of 26.2 MN [Eq. (5.6)]: Test WP-1.7.

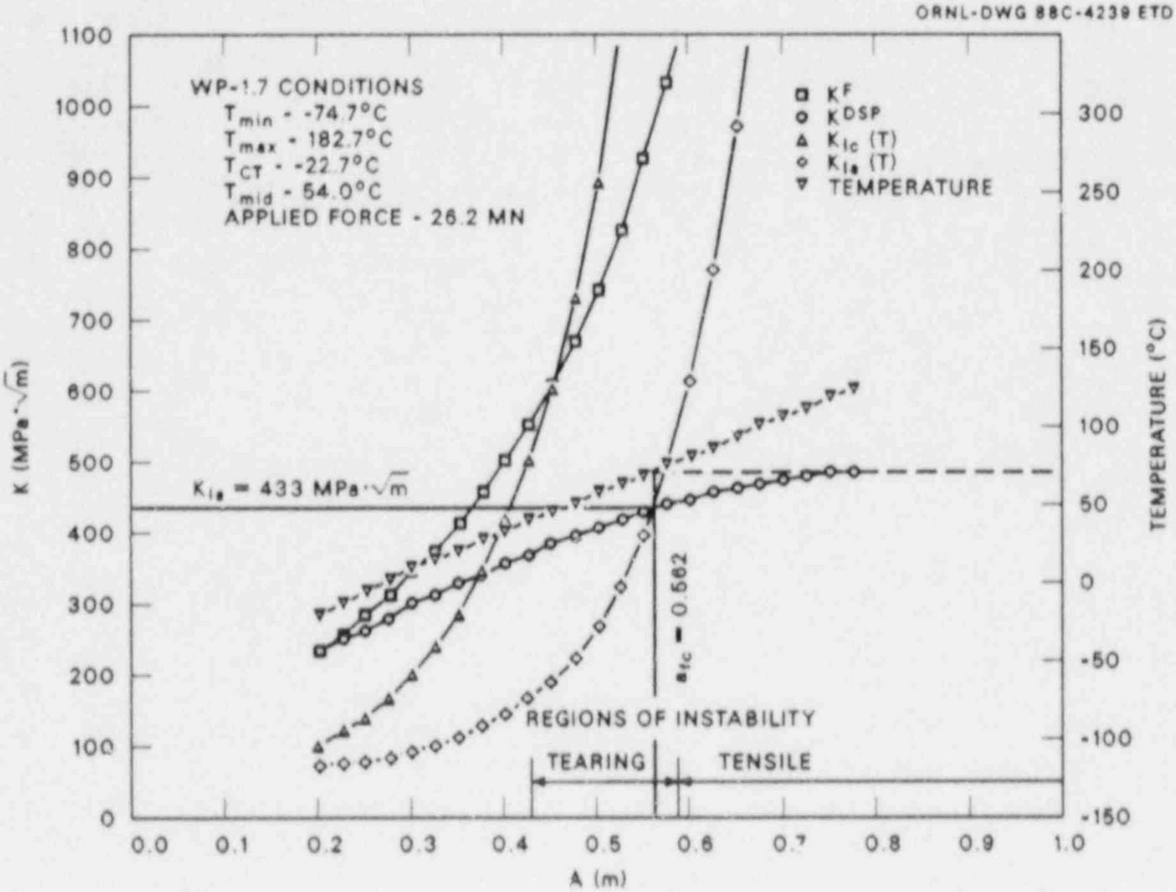

Fig. 5.51. Complete static and stability analyses for initiation load of 26.2 MN [Eq. (5.6)]: Test WP-1.7.

caused by the thermal gradient across the plate was also incorporated into the analyses.

A posttest application-mode analysis of WP-1.7 was performed using the temperature gradient of Fig. 5.9(*b*) and the material properties given in Sect. 5.3.1. For the dynamic analysis, the load point was fixed at the value of the measured fracture load, 26.2 MN, as a prescribed concentrated load. The time step was set at Δt = 5 μs.

Application-mode analysis using Eq. (5.2) for K_{Ia}. The calculated crack-depth history from this analysis is presented in Fig. 5.52 and indicates a predicted arrest of $a_{fp} = 0.748$ m. Figure 5.53 presents the dynamic stress-intensity factor K_I^{DYN}, the static toughness K_{Ia}, and the crack velocity $\dot{a}$ as a function of instantaneous crack length. The crack propagates into a rising K_I field, followed by a predicted arrest at the point where the crack-tip temperature would have been T = 115.6°C. The arrest toughness at the arrest-point temperature was determined to be $K_{Ia} = 863$ MPa·$\sqrt{m}$. The computed arrest length exceeds the measured initial arrest length at $a_{fm_1} = 0.528$ m (arrest A, front face), where the

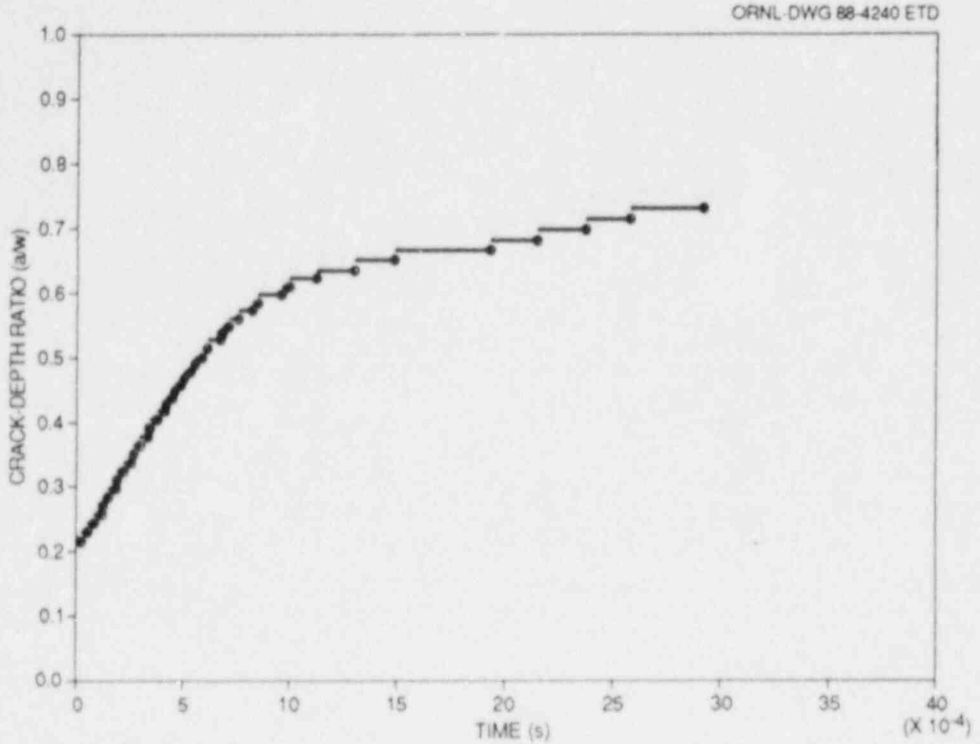

Fig. 5.52. Dynamic-analysis, crack-depth history [Eq. (5.2)]: Test WP-1.7.

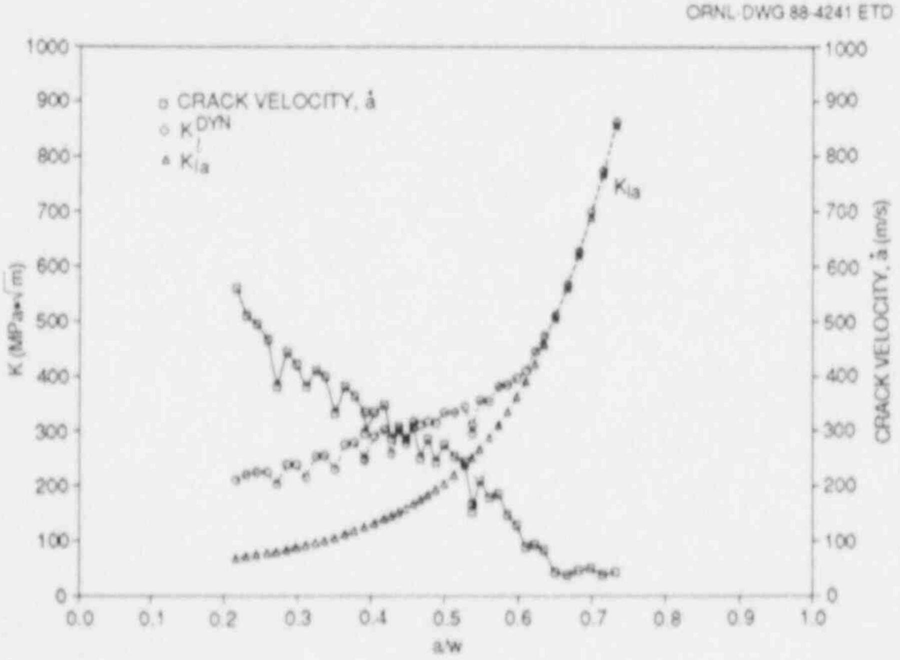

Fig. 5.53. Dynamic factor, static toughness, quasi-static displacement-controlled factor, and crack velocity vs instantaneous crack length [Eq. (5.2)]: Test WP-1.7.

crack-tip temperature T = 61.0°C and the corresponding arrest toughness K_{Ia} = 239 MPa$\cdot\sqrt{m}$. There also appears to be a predicted arrest, a_{fp} = 0.666 m, where the crack-tip temperature would have been T = 95.6°C and the arrest toughness K_{Ia} = 510 MPa$\cdot\sqrt{m}$. Both predicted arrest points exceed the last measured arrest point, a_{fm_2} = 0.635 m, where T = 87.8°C and K_{Ia} = 457 MPa$\cdot\sqrt{m}$. The analyses were terminated at time t = 3 ms, which precludes any prediction from the analysis of the reinitiation that occurred in the test at time t = 7.4 ms.

Application-mode analysis using Eq. (5.6) for K_{Ia}. The calculated crack-depth history from this analysis is presented in Fig. 5.54 and indicates a predicted arrest of a_{fp} = 0.538 m. Figure 5.55 shows the crack propagating into a rising K_I field, followed by a predicted arrest at a point where the crack-tip temperature would have been T = 63.5°C. The arrest toughness at the arrest-point temperature is determined to be K_{Ia} = 330 MPa$\cdot\sqrt{m}$. This prediction is quite close to the measured initial arrest length of a_{fm_1} = 0.528 m, where T = 61.0°C and K_{Ia} = 326 MPa$\cdot\sqrt{m}$. These analyses were also terminated at time t = 3 ms.

ORNL-DWG 88-4242 ETD

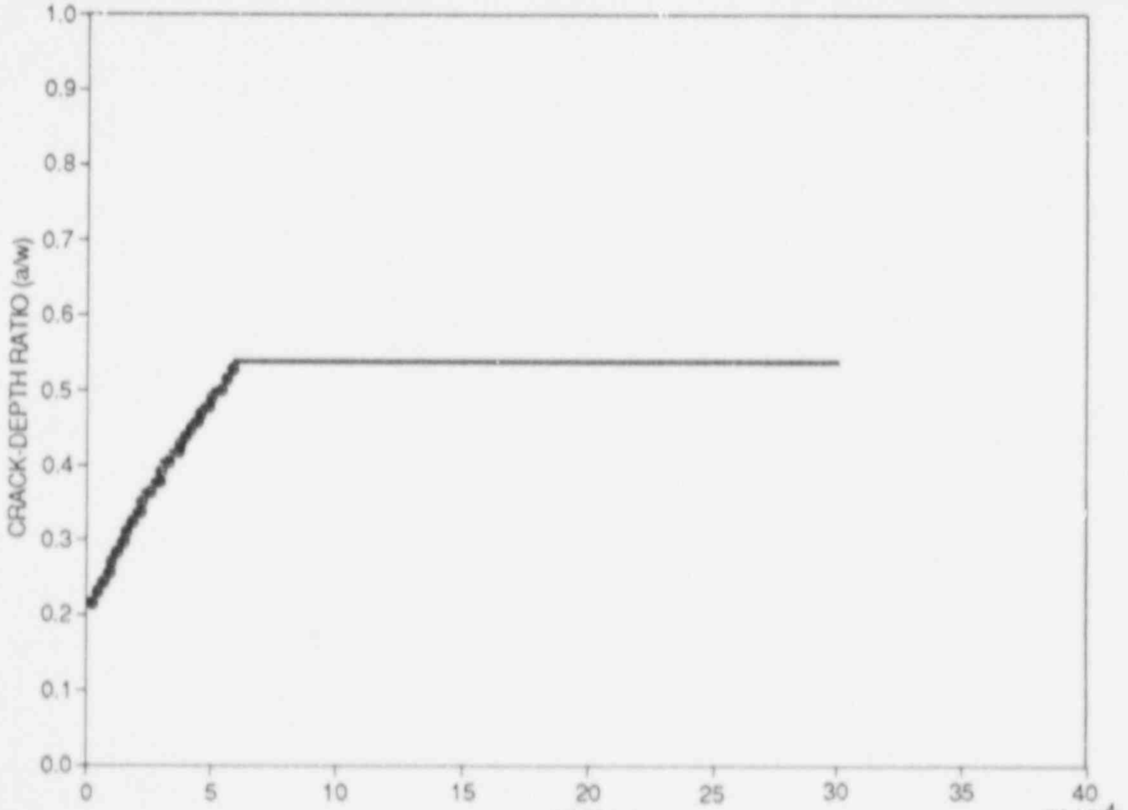

Fig. 5.54. Dynamic-analysis, crack-depth history [Eq. (5.6)]: Test WP-1.7.

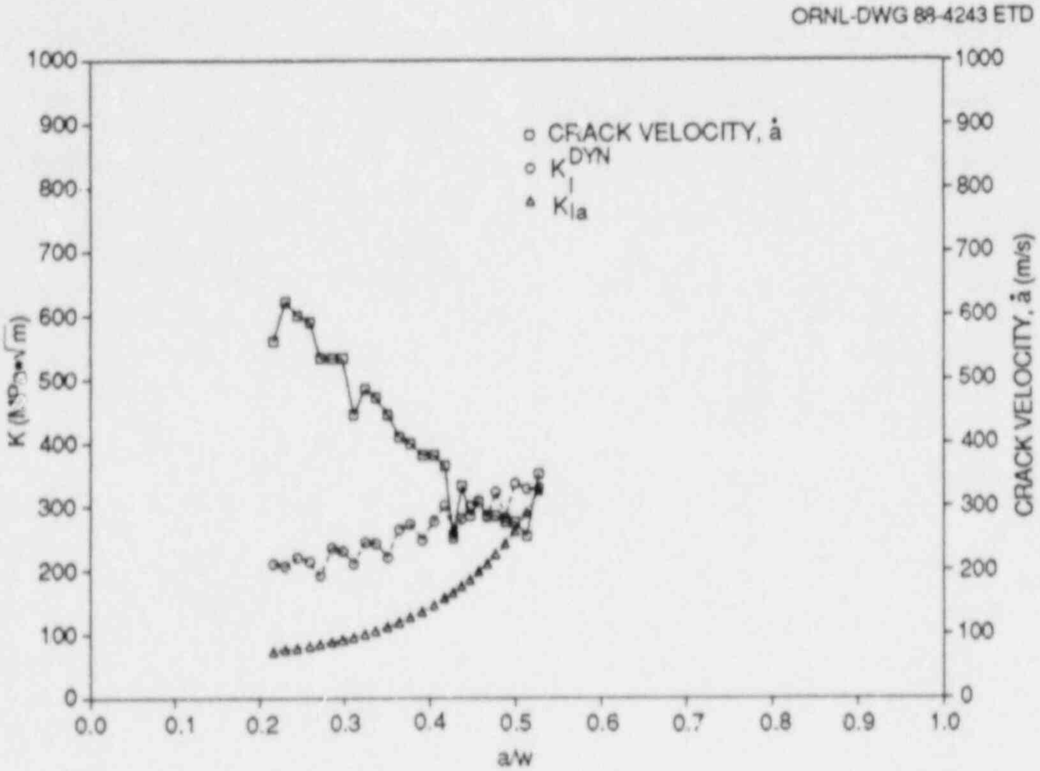

Fig. 5.55. Dynamic factor, static toughness, quasi-static displacement-controlled factor, and crack velocity vs instantaneous crack length [Eq. (5.6)]: Test WP-1.7.

5.4.1.4 Generation-mode dynamic analysis (fixed-load boundary condition). From the output of the crack-line strain gages and from an inspection of the fracture surface, estimates of the crack position as a function of time were constructed and given in Table 5.2 for the front-face and back-face strain gages. Figure 5.56 incorporates the two measured crack arrests as determined from the front-surface strain measurements in Table 5.2. For the dynamic analyses (front-face results), the load point was fixed at the value of the initiation load, 26.2 MN, as a prescribed concentrated load, and the time step was set at $\Delta t = 10$ µs. From these calculations, the stress-intensity factor as a function of time is given in Fig. 5.57. The generation-mode analysis results for the two arrest events are summarized in Table 5.4.

The computed strain histories from selected points close to the companion crack-line strain gage Nos. 1–20 (see Fig. 5.6 for strain-gage locations) are depicted in Figs. 5.58–5.60 for the generation-mode analysis (fixed load) along with measured data from the gages. The sharply defined strain peaks are associated with the fast-running crack passing under a gage point, with the peak being transformed into a more blunted curve as the crack-tip propagation slows down. The comparisons of strain histories in these figures indicate generally good agreement between measured and computed times for the occurrence of the peak-strain values. The transition of the strain pulse from a sharp peak for strain gage Nos. 7 and 8 to a blunted curve for gage Nos. 9 and 10 in Fig. 5.61 reflects

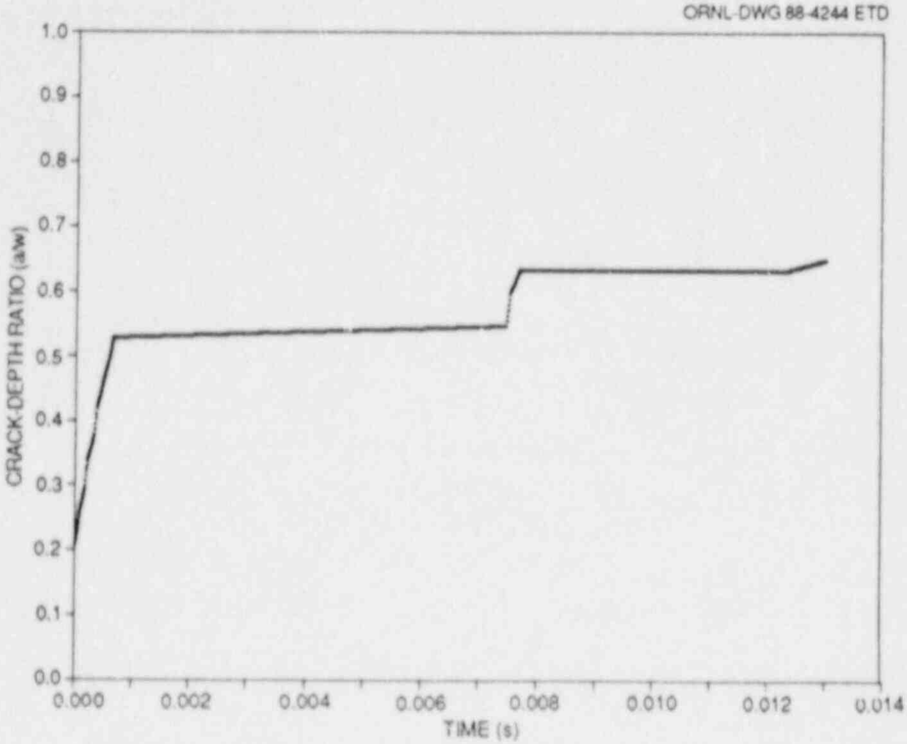

Fig. 5.56. Crack-front position history used as input for generation-mode dynamic analysis: Test WP-1.7.

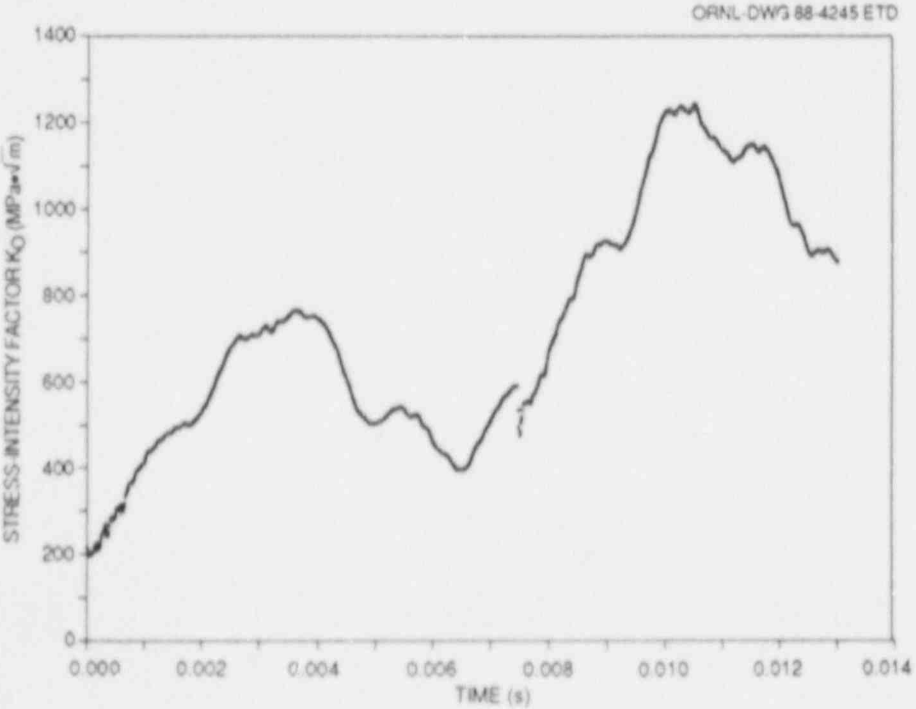

Fig. 5.57. Calculated stress-intensity factor vs time from the generation-mode dynamic analysis (fixed-load case): Test WP-1.7.

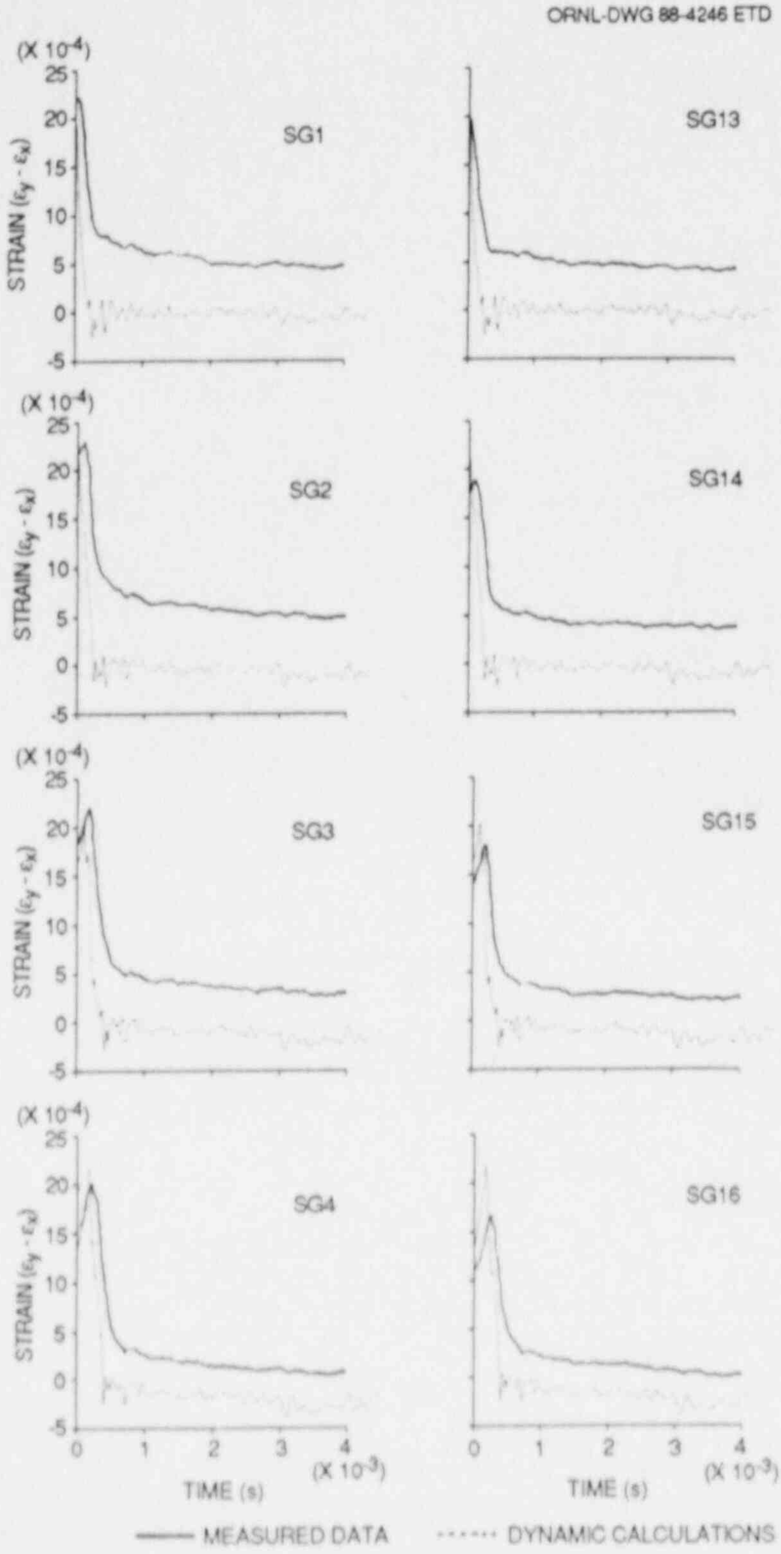

Fig. 5.58. Actual and computed strain histories for companion crack-line gages: Test WP-1.7.

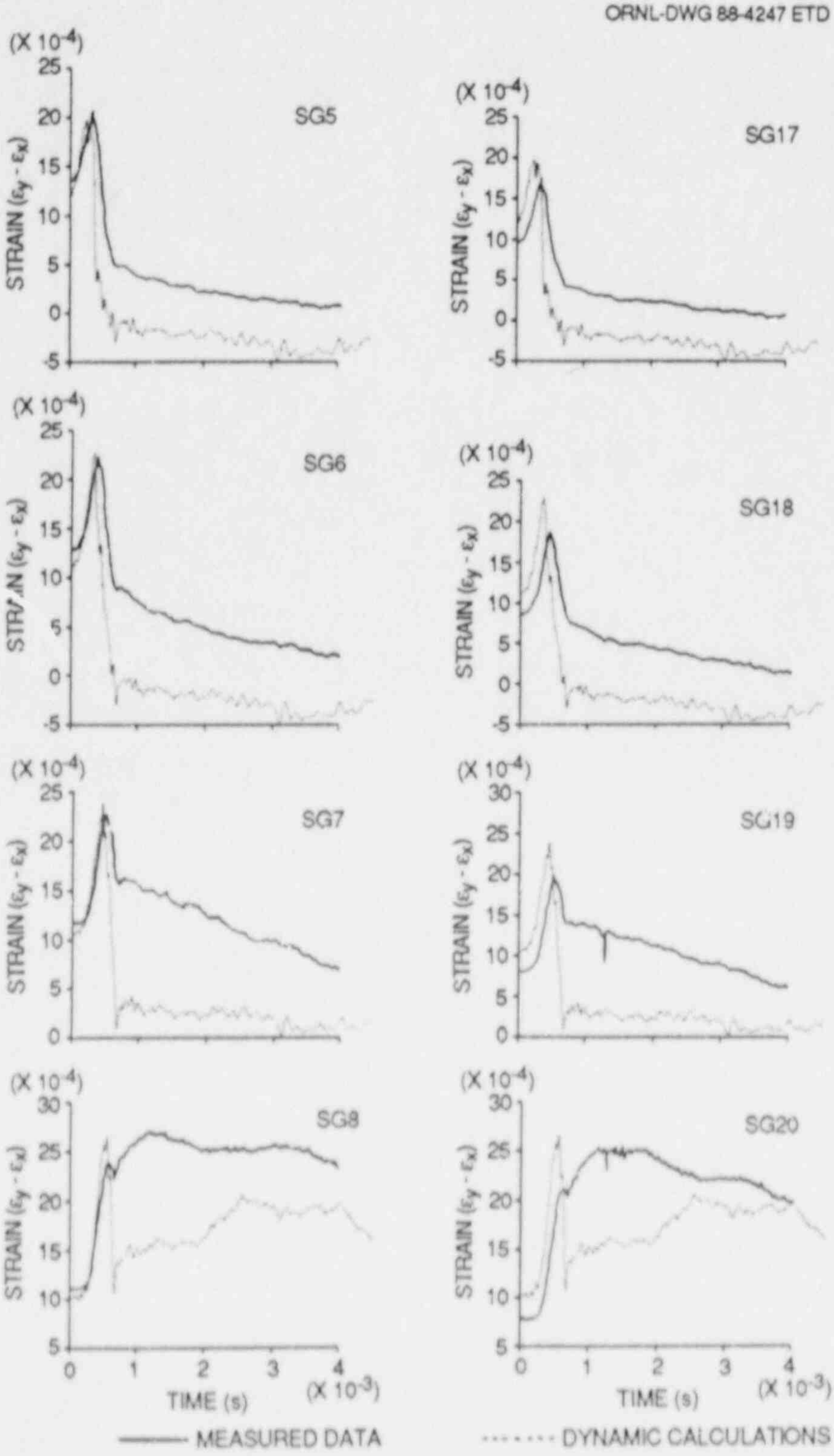

Fig. 5.59. Actual and computed strain histories for companion crack-line gages: Test WP-1.7.

Table 5.4. Summary of computed results for test WP-1.7

Event	Time (ms)	a (m)	K^a $(\mathrm{MPa}\cdot\sqrt{\mathrm{m}})$
Initiation	0.0	0.202	223.06[b]
Arrest A	0.680	0.528	318.82
Reinitiation	7.442	0.538	591.51
Arrest B	7.722	0.635	555.00
Reinitiation	12.342	0.635	960.55

[a] Generation-mode, fixed-load dynamic analysis.

[b] From ADINA static analysis.

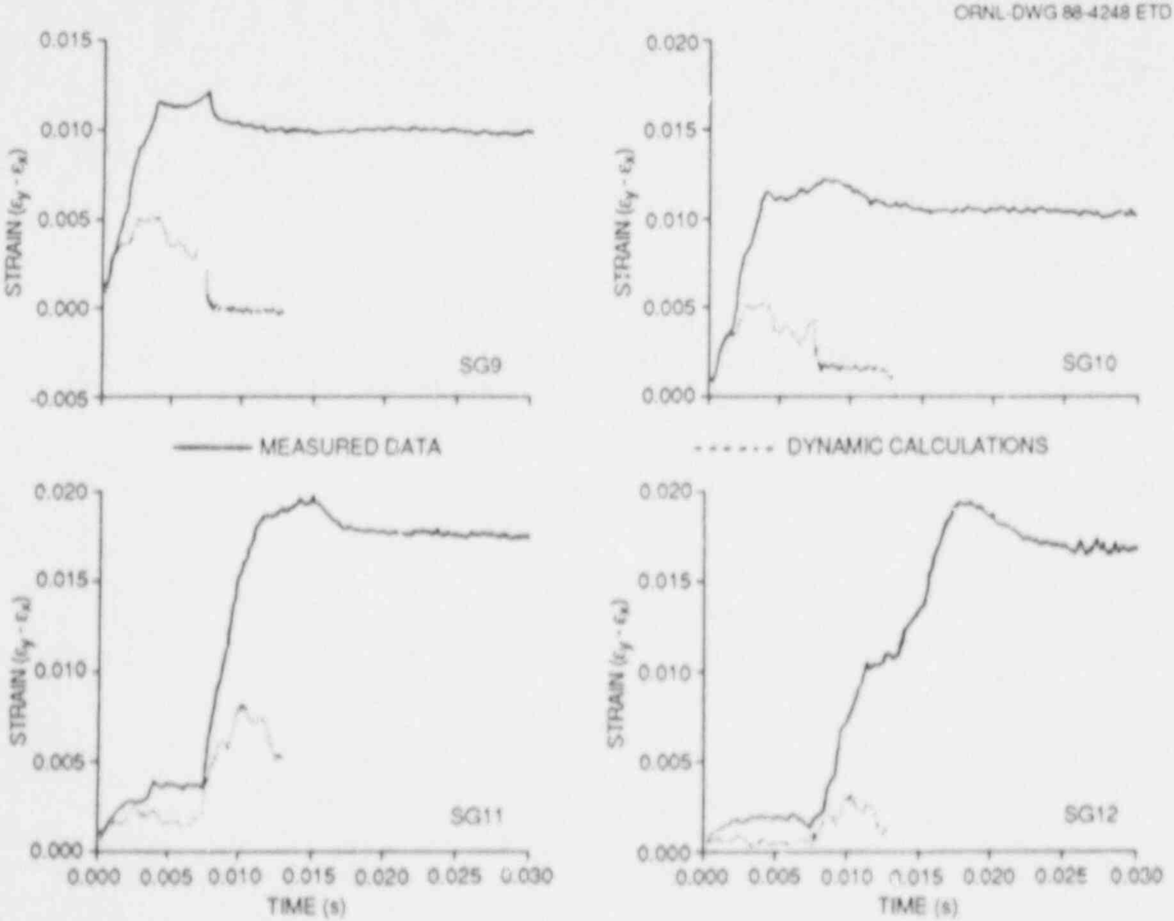

Fig. 5.60. Actual and computed strain histories for front-face crack-line gages: Test WP-1.7.

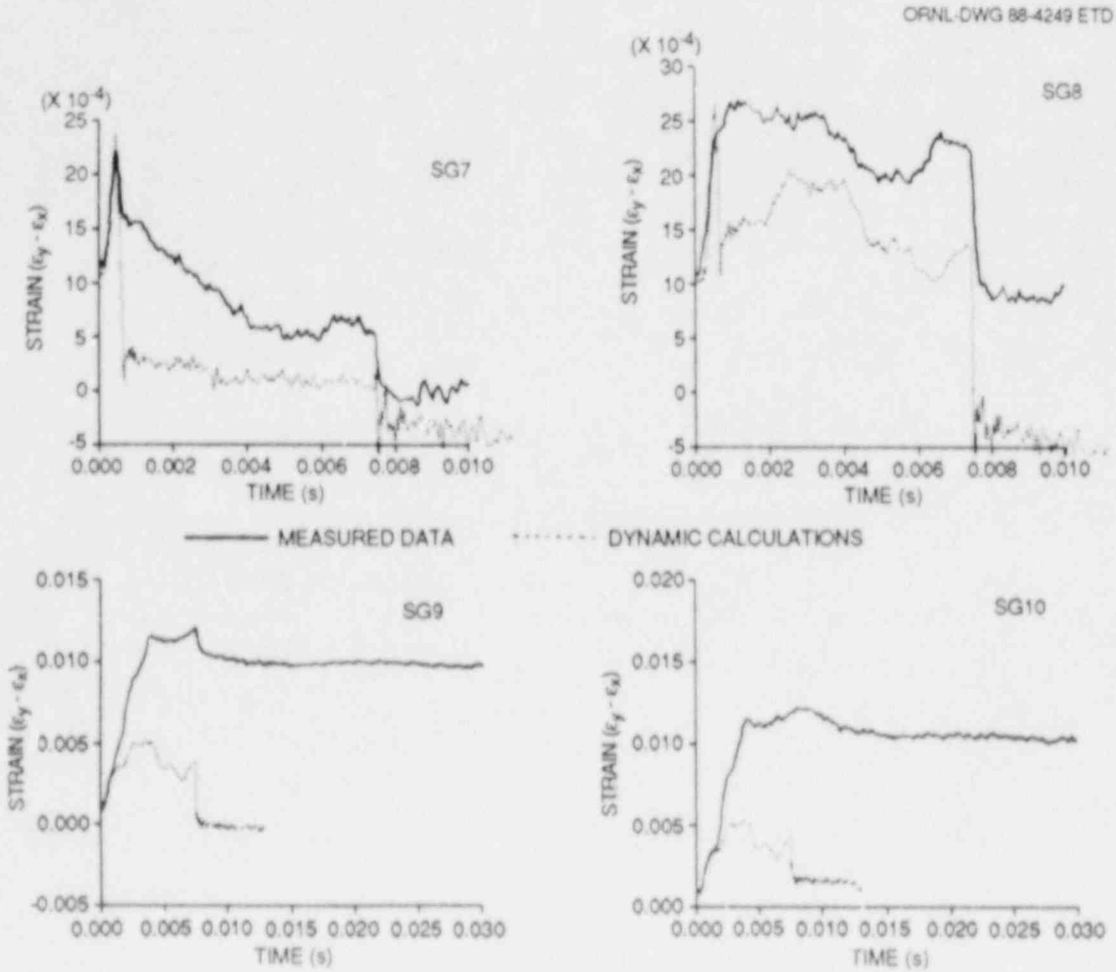

Fig. 5.61. Actual and computed strain histories for front-face crack-line gages showing the first crack run-arrest event between gage Nos. 8 and 9 and reinitiation as detected by gage Nos. 7 and 8: Test WP-1.7.

the arrest event (arrest A) between the front-side crack-line strain gage Nos. 8 and 9. Figure 5.61 also reflects reinitiation of the arrested crack (arrest A), as detected by gage Nos. 7 and 8 at ~7.4 ms. This same occurrence also can be viewed for the second arrest and reinitiation event (Fig. 5.60).

Finally, Fig. 5.62 presents a comparison of displacements that were calculated using a generation-mode analysis at ~3.539 m below the crack plane on the centerline of the plate with the measured data obtained from the displacement gage installed on the plate. The gage measured the displacement of this point on the plate relative to the large columns of the testing machine. The output of the measured data was adjusted in the figure from ~3.1 to 6.1 mm for comparison with the finite-element model. Calculated and measured results did not give good agreement, as indicated by the large oscillations (~3.7 mm) in the calculated displacements.

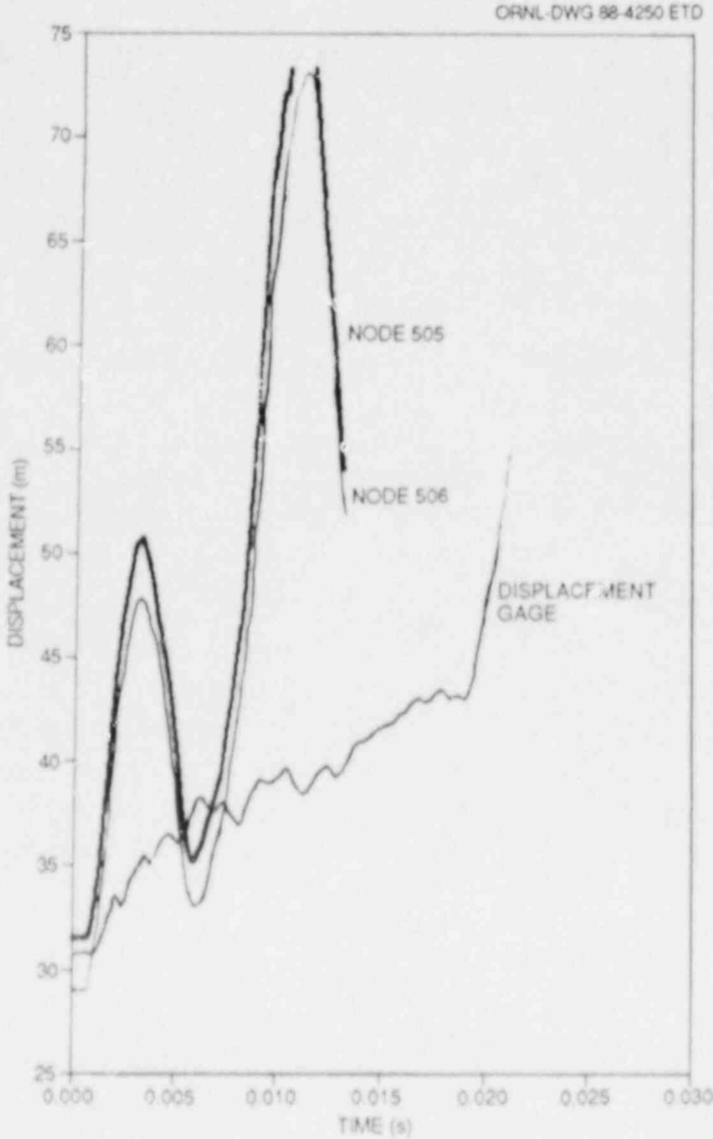

Fig. 5.62. Actual and computed displacement histories determined at a point 3.539 m below the crack plane on the centerline of the plate: Test WP-1.7.

5.4.2 Posttest analyses of test WP-CE-1

5.4.2.1 Posttest 3-D static analyses. The 3-D finite-element model for test WP-CE-1 incorporated a segment of the plate assembly 4.6930 m long measured from the crack plane to the top of the load-pin hole. The crack-tip region of the model included the side grooving and the edge notch, the dimensions of which were taken from Table 5.1. From symmetry conditions neglecting out-of-plane eccentricity, one-quarter of the partial pull-plate assembly was modeled using 3751 nodes and 720 20-noded isoparametric elements.

Thermal deformations to be superposed on the 3-D finite-element model to account for the in-plane bending effect were computed from a 2-D analysis, which assumed that the heated and cooled edges of the plate were fixed at $T_{max} = 205.5°C$ and $T_{min} = -93.5°C$, respectively. The in-plane thermal bending produced a load-line (through the top of the load-pin hole) eccentricity of 2.26 cm relative to the geometric center of the plate.

In the 3-D analysis, thermal stress effects were neglected, and a uniform line-load statically equivalent to the WP-CE-1 test initiation load of 10.14 MN was applied at the location corresponding to the top of the load-pin hole. This analysis produced a static stress-intensity factor of $K_I = 166.2$ MPa•$\sqrt{m}$ at the center plane of the plate. Comparing this computed K_I value with the static initiation value of $K_{Ic} = 104.5$ MPa•$\sqrt{m}$, evaluated from the relationship presented in Eq. (5.1) using the crack-tip temperature of −33.7°C, yields a ratio of $K_I/K_{Ic} = 1.59$. A comparison of initiation stress-intensity factors obtained from this test and previous tests is presented in Table 5.5.

Table 5.5. Initiation stress-intensity factor comparisons

Test designation	Crack-tip temperature (°C)	Calculated static K_I[a] (MPa•$\sqrt{m}$)	Property correlation K_{Ic} (MPa•$\sqrt{m}$)	K_I/K_{Ic}
WP-1.2	−33	251.5	87.5[b]	2.87
WP-1.3	−51	173.5	70.1[b]	2.48
WP-1.4	−62	213.0	63.9[b]	3.33
WP-1.5	−30	179.8	91.6[b]	1.96
WP-1.6	−19	233.8	111.2[b]	2.10
WP-1.7	−22.7	280.6	103.7[b]	2.71
WP-CE-1	−33.7	166.2	104.5[b]	1.59
WP-2.4A	45	123.0	93.9[c]	1.31
WP-2.4B[d]	60.8	143.3	135.7[c]	1.06
WP-2.1	55	126.4	117.6[c]	1.07
WP-2.5	66	119.5	155.5[c]	0.77
WP-2.3	66	136.1	155.5[c]	0.88

[a] Computed from 3-D static analysis using ORMGEN/ADINA/ORVIRT.

[b] Calculated from $K_{Ic} = 51.276 + 51.897\, e^{0.036(T-RT_{NDT})}$ using crack-tip temperature of initial flaw and material RT_{NDT}.

[c] Calculated from $K_{Ic} = 39.53 + 93.47\, e^{0.036(T-DW_{NDT})}$ using crack-tip temperature of initial flaw and material DW_{NDT}.

[d] After crack pop-in.

5.4.2.2 Posttest 2-D static and dynamic analyses

Static and stability analysis. Posttest 2-D analyses for test WP-CE-1 were carried out in the same manner as for WP-1.7. Using a temperature profile as defined by specifying the crack-tip temperature of T_{CT} = −33.7°C and midplate temperature T_{MP} = 56°C, implying that T_{min} = −93.5°C and T_{max} = 205.5°C, the dependence of arrested crack length and crack stability on the applied initiation load F_{in} = 10.14 MN was investigated with WPSTAT; the results are presented in Fig. 5.63. Figure 5.64 presents an evaluation of the K_{Ia} function of Eq. (5.2) on the arrest crack-length curve $a_f(F)$, on the incipient tearing-instability curve $a_{i2}(F)$, and on the reinitiation curve $a_{rein}(F)$. The K_{Ic} function of Eq. (5.1) is also evaluated on the curve $a_{rein}(F)$. Evaluation of the $K_{Ia}(a_f)$ curve at the initiation load F_{in} yields an arrest toughness K_{Ia} = 229.1 MPa$\cdot\sqrt{m}$ at the computed arrest point a_{fc} = 0.467 m, where the crack-tip temperature would be T = 47.7°C. The complete static-fracture mechanics and stability analyses are depicted in Fig. 5.65.

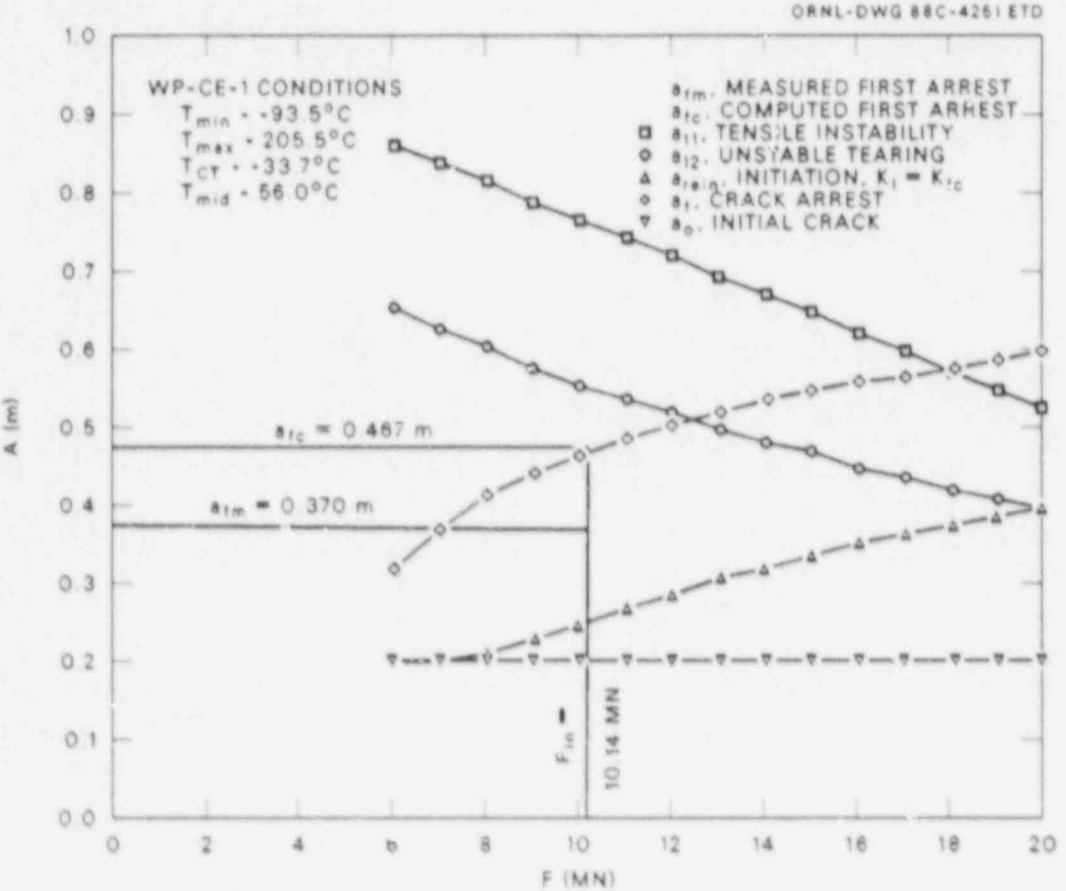

Fig. 5.63. Statically calculated crack lengths: Test WP-CE-1.

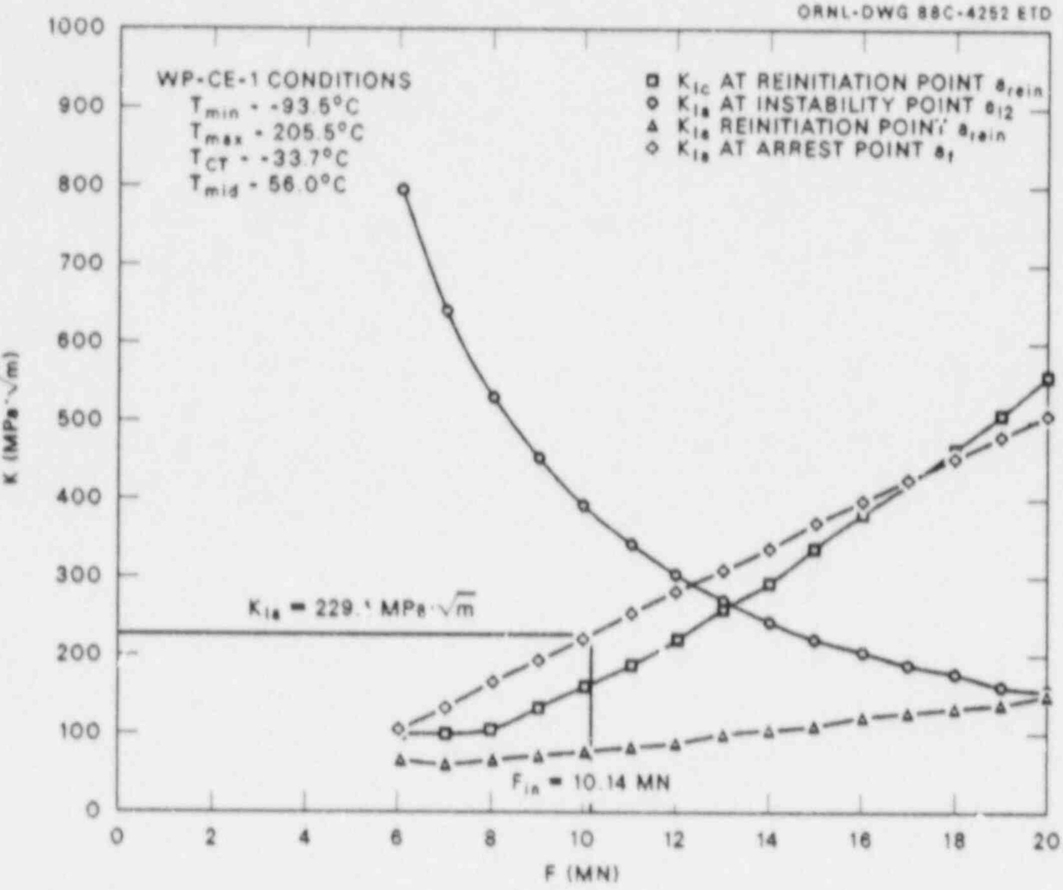

Fig. 5.64. Determination of arrest toughness at initiation load of 10.14 MN: Test WP-CE-1.

<u>Application-mode dynamic analyses (fixed-load boundary condition)</u>. The 2-D plane-stress finite-element model of the wide-plate configuration used in the analyses consisted of 863 nodes and 264 eight-noded isoparametric elements. For the dynamic analysis, the load point was fixed at the value of the measured fracture load, 10.14 MN, as a prescribed concentrated load. The time step was set at $\Delta t = 5\ \mu s$. Figure 5.66 presents the calculated crack-depth history from this analysis and indicates a predicted arrest, $a_{fp} = 0.55$ m. Figure 5.67 presents the dynamic stress-intensity factor K_I^{DYN}, the static toughness K_{Ia}, and the crack velocity $\dot{a}$ as a function of instantaneous crack depth. The crack propagates into a rising K_I field, followed by a predicted arrest at a point where the crack-tip temperature would have been T = 69.3°C. The arrest toughness at the arrest-point temperature was determined to be K_{Ia} = 344.4 MPa·√m. The computed arrest length exceeds the measured arrest point $a_{fm} = 0.370$ (plate front face), where T = 22.3°C and K_{Ia} = 135.9 MPa·√m. There also appears to be a predicted arrest, $a_{fp} = 0.50$ m, where

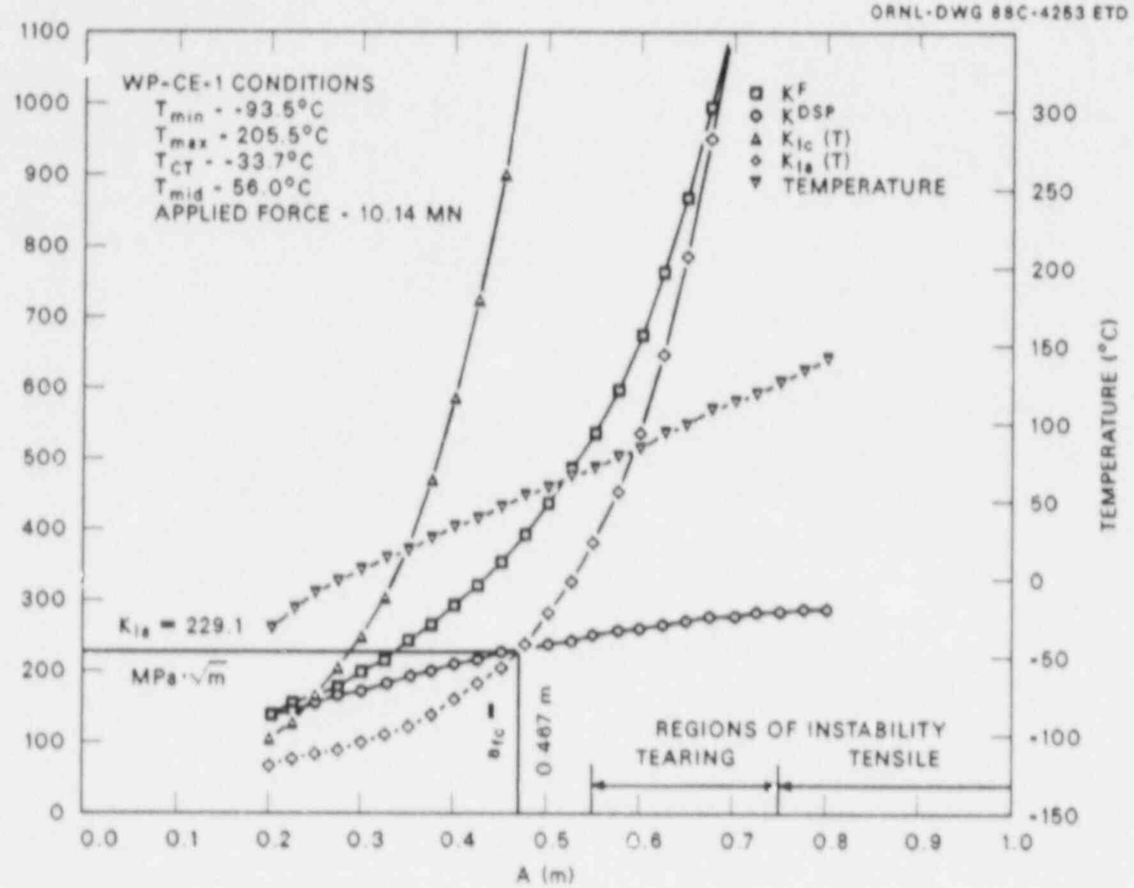

Fig. 5.65. Complete static and stability analyses for initiation load of 10.14 MN: Test WP-CE-1.

the crack-tip temperature would have been T = 56.0°C and the arrest toughness K_{Ia} = 256.4 MPa·√m. This point is much closer to the measured arrest length at the plate back face at a_{fm} = 0.42 m, where the crack-tip temperature T = 35.6°C and the corresponding arrest toughness K_{Ia} = 176.2 MPa·√m. The analysis was terminated at time t = 3 ms.

5.4.2.3 Generation-mode dynamic analysis (fixed-load boundary condition). Figure 5.68 depicts the apparent crack position vs time curve that was used as input for the posttest generation-mode elastodynamic analysis of test WP-CE-1. For these analyses, the load point was fixed at the value of the initiation load, 10.14 MN, as a prescribed concentrated load, and the time step was set at Δt = 5 μs. From these calculations, the stress-intensity factor as a function of time is given in Fig. 5.69. Table 5.6 presents the generation-mode analysis results for the two arrest events (one front face and one back face). Computed strain histories from selected points close to the crack-line strain gage Nos. 1–4, 5 and 13–15, and 16–18 (see Fig. 5.6 for strain-gage locations) are depicted in Figs. 5.70–5.72, respectively, for the generation-mode analysis (fixed load) along with measured data from the gages.

ORNL-DWG 88-4254 ETD

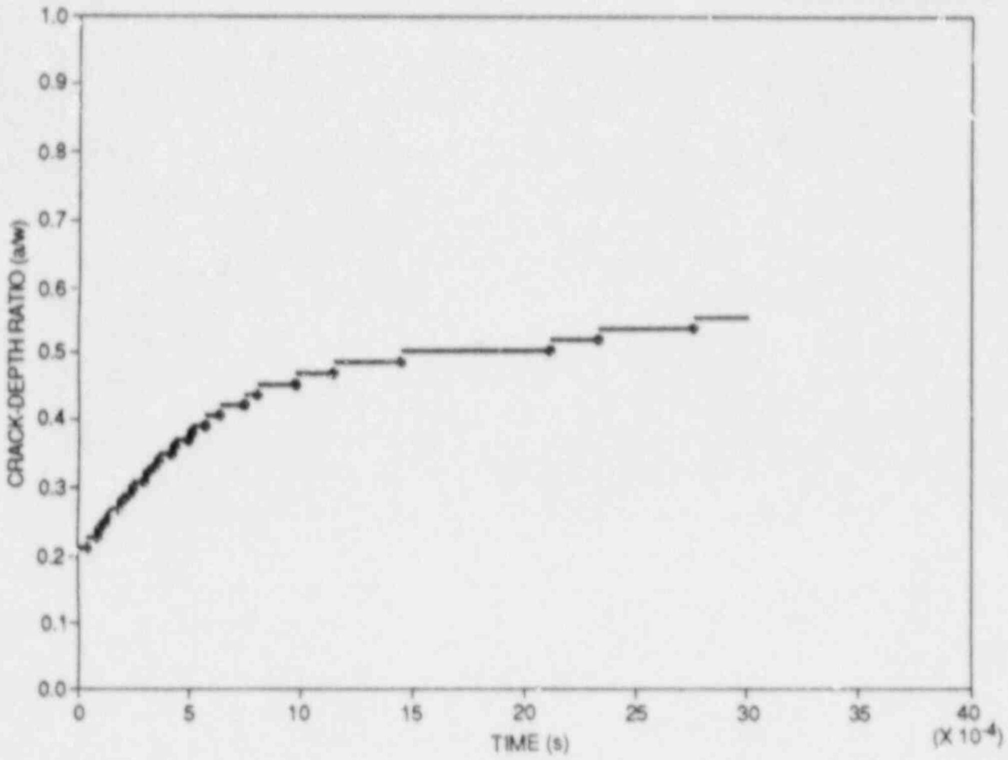

Fig. 5.66. Dynamic-analysis, crack-depth history: Test WP-CE-1.

ORNL-DWG 88-4255 ETD

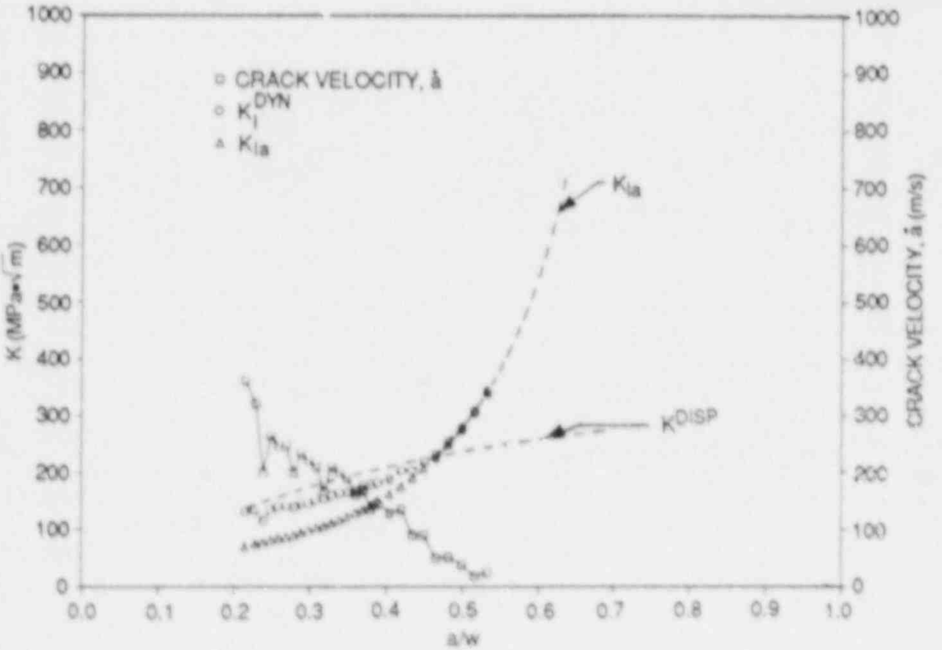

Fig. 5.67. Dynamic factor, static toughness, quasi-static displacement-controlled factor, and crack velocity vs instantaneous crack length: Test WP-CE-1.

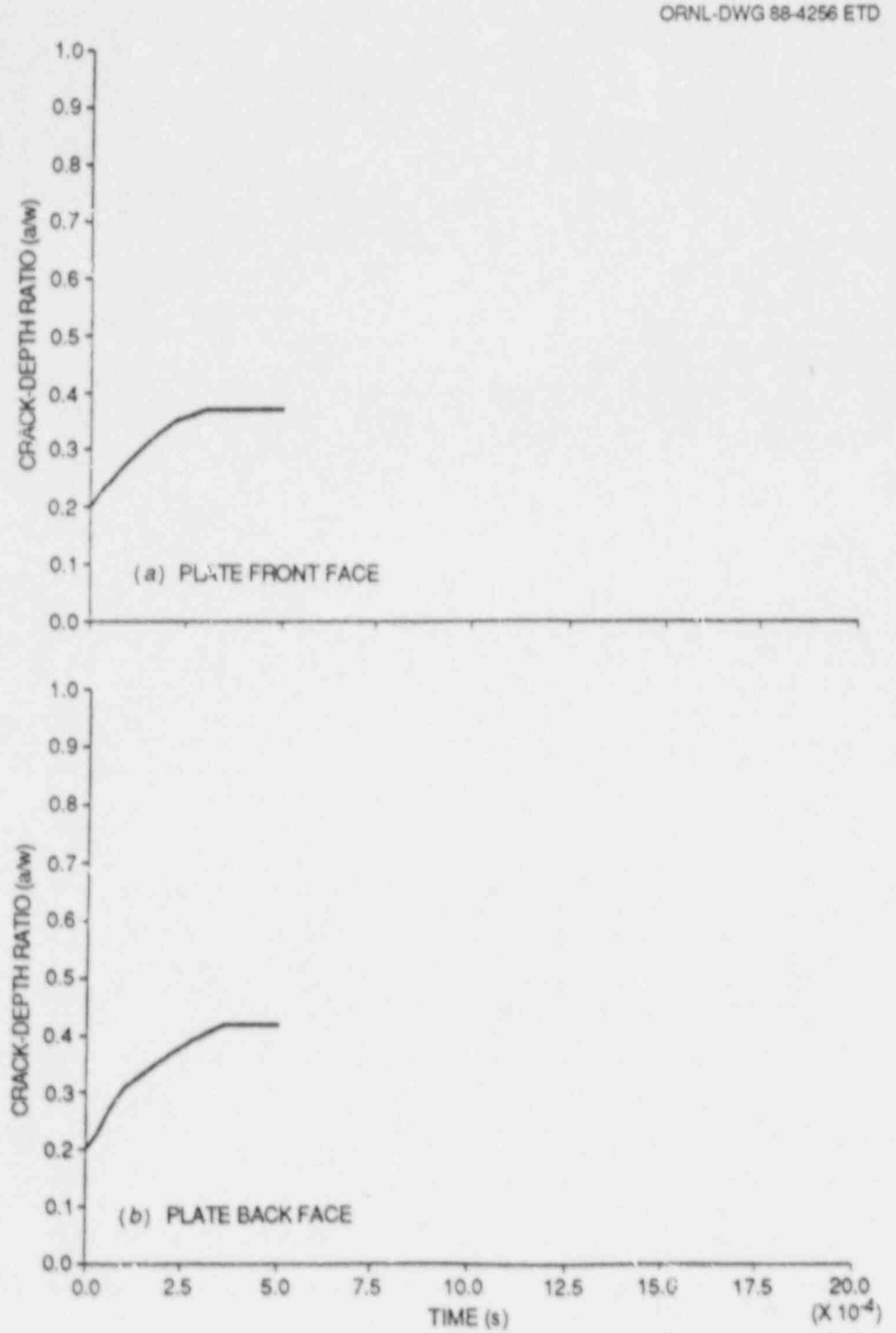

Fig. 5.68. Crack-front position history used as input for generation-mode dynamic analysis: Test WP-CE-1.

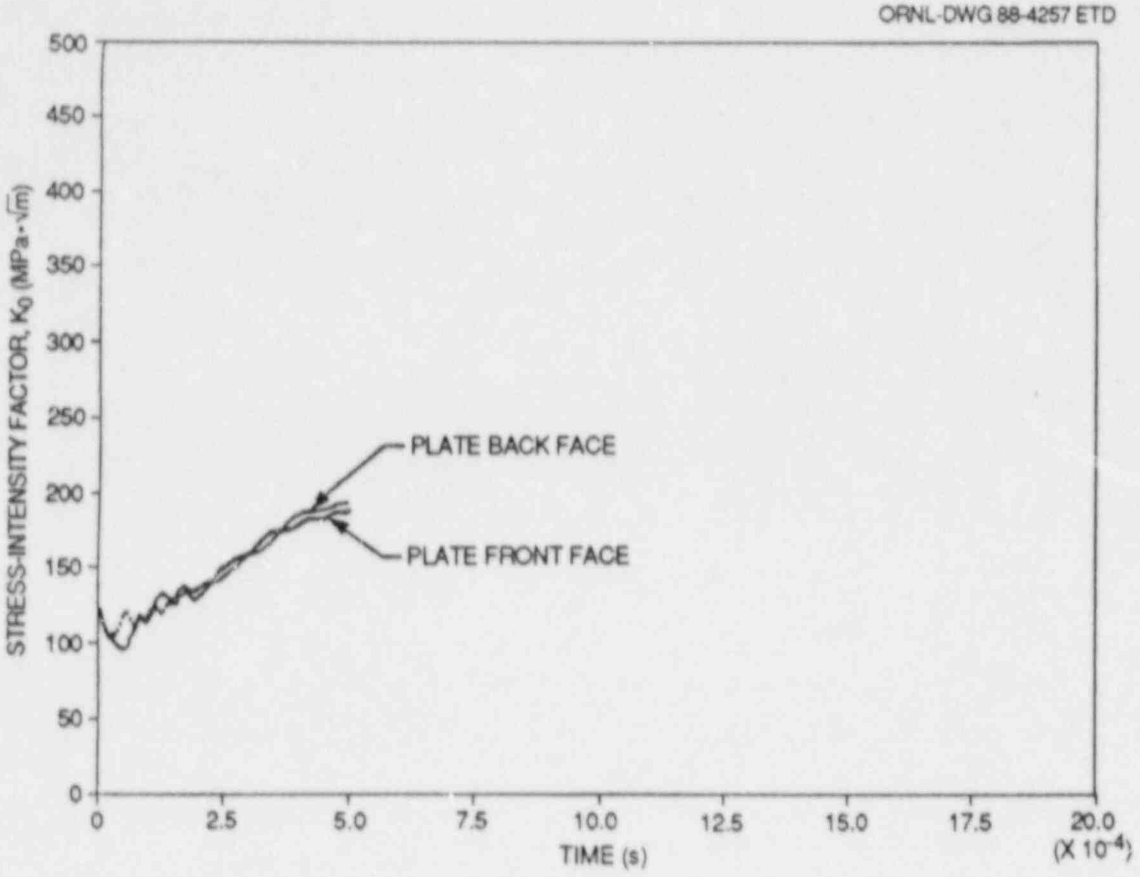

Fig. 5.69. Calculated stress-intensity factor vs time from the generation-mode dynamic analysis (fixed-load case): Test WP-CE-1.

Table 5.6. Summary of computed results for test WP-CE-1

Event	Time (ms)	a (m)	K^a (MPa·√m)
Initiation	0.0	0.200	130^b
Arrest			
Front face	0.308	0.370	159
Back face	0.364	0.420	170

[a] Generation-mode, fixed-load dynamic analysis.

[b] From ADINA static analysis.

ORNL-DWG 88-4258 ETD

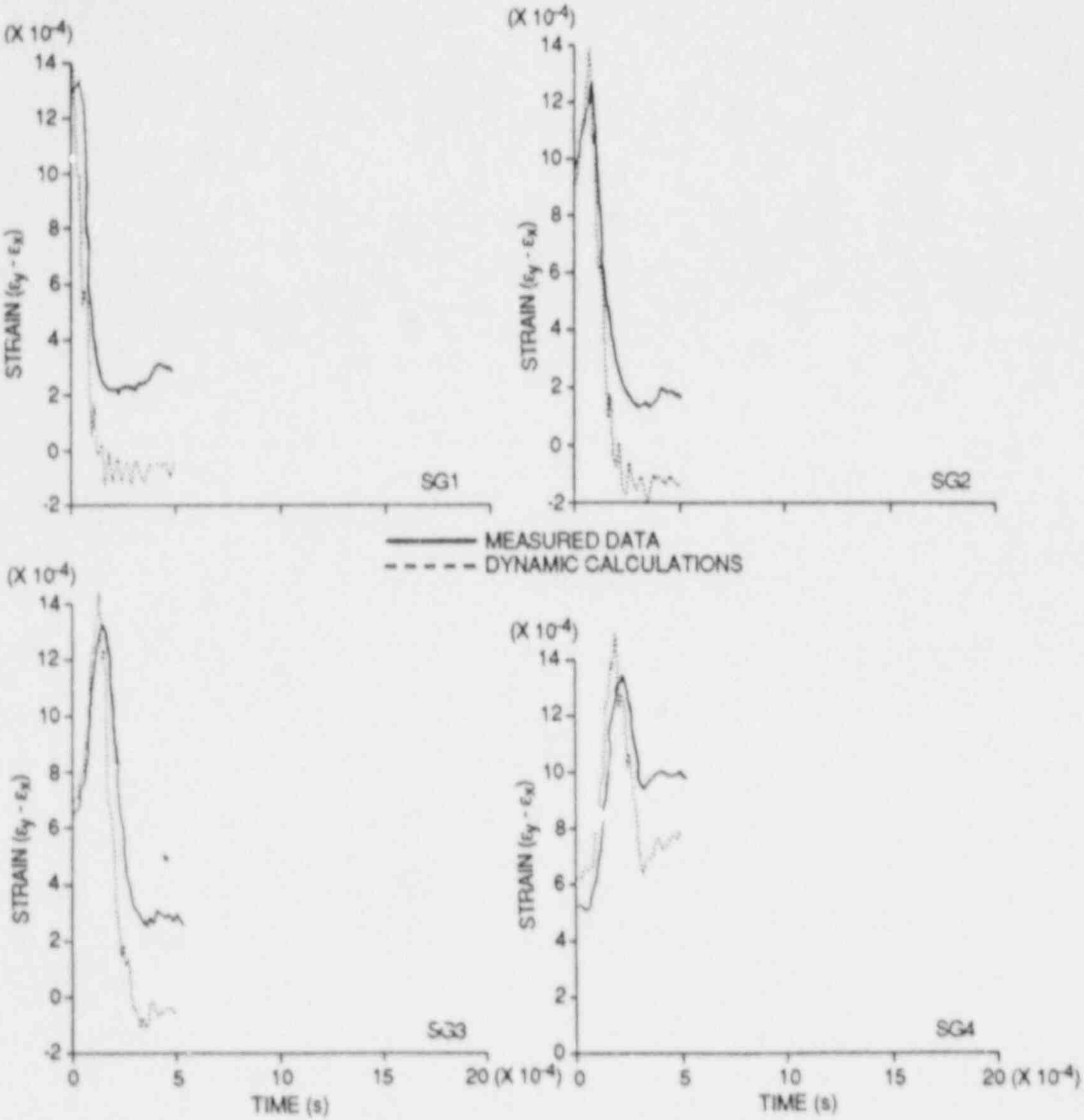

Fig. 5.70. Actual and computed strain histories for front-face crack-line gages: Test WP-CE-1.

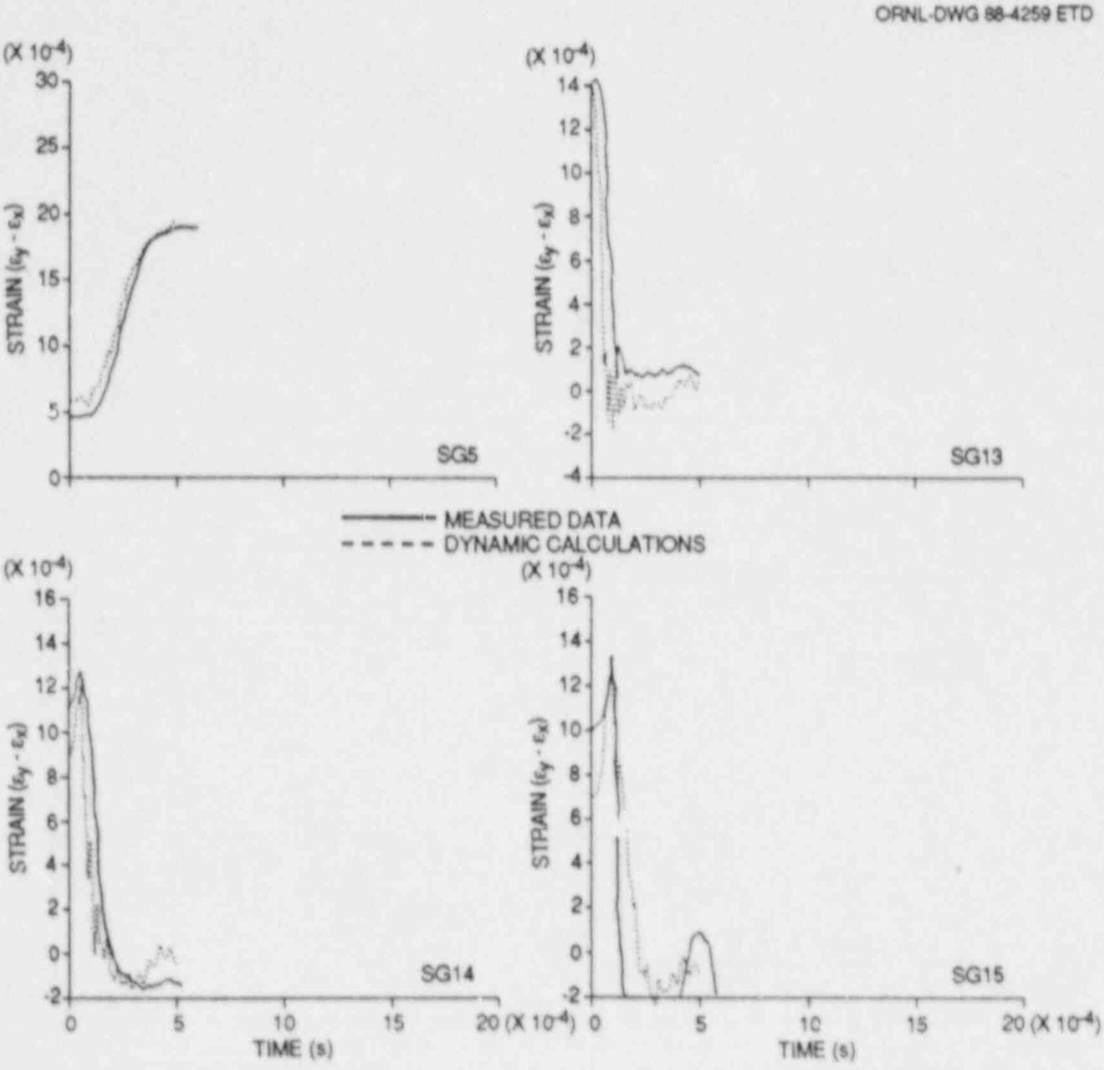

Fig. 5.71. Actual and computed strain histories for crack-line gages: Test WP-CE-1.

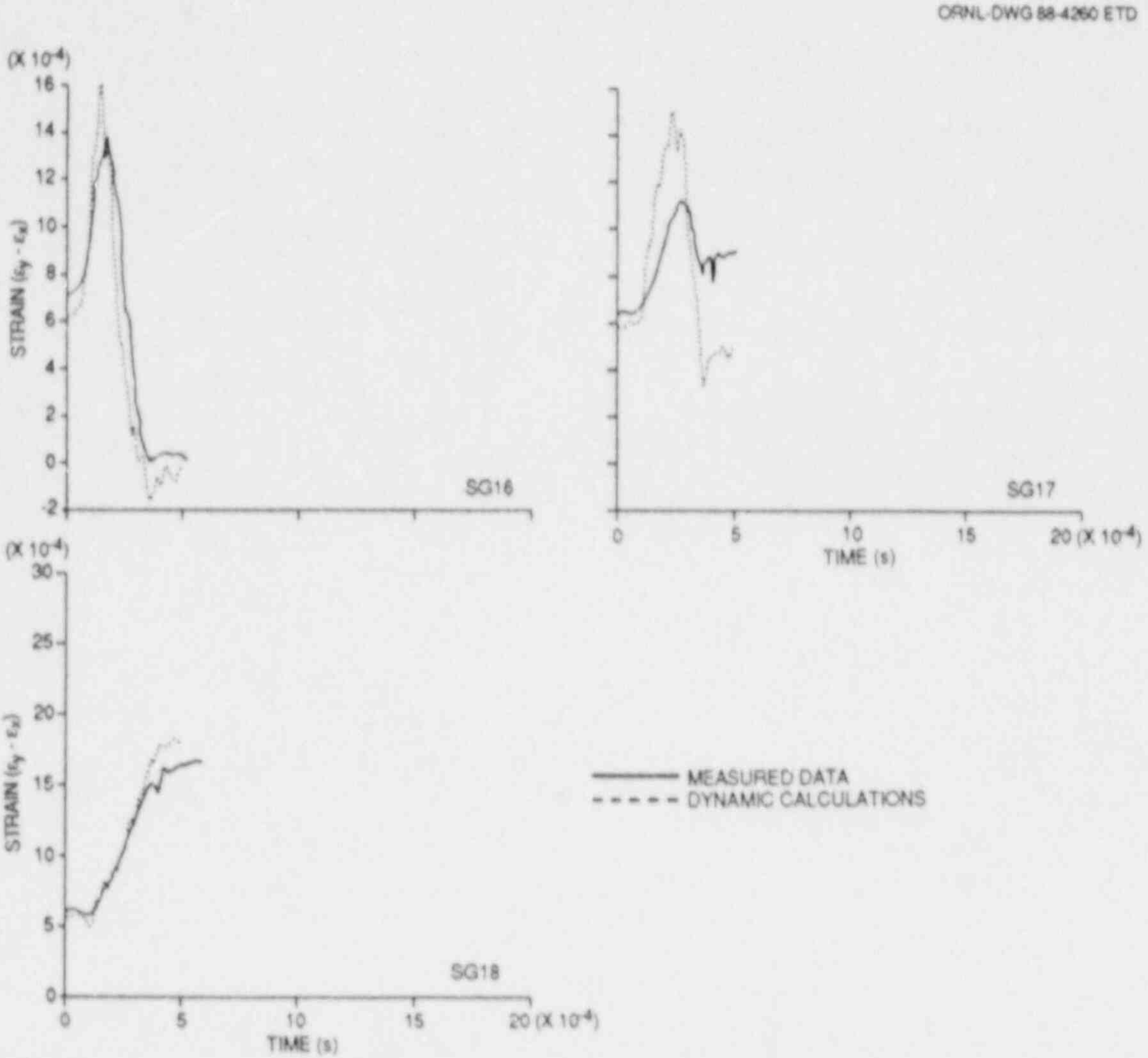

Fig. 5.72. Actual and computed strain histories for back-face crack-line gages: Test WP-CE-1.

5.4.3 Crack-arrest toughness determinations for wide-plate tests

Table 5.7 presents a summary of the general conditions for tests WP-1.7 and WP-CE-1. (Results for the previous tests in the WP-1 and WP-2 test series were presented in the two previous semiannual progress reports.[11,12]) Posttest analyses have been done for each of these tests by using both static- and dynamic-fracture analysis codes, as well as by applying handbook techniques. Some of these values[13] are presented in Table 5.8.

Table 5.7. Summary of HSST wide-plate crack-arrest test conditions for specimens WP-1.7 and WP-CE-1

Test No.	Crack location (cm)	Crack temperature (°C)	Initiation load (MN)	Arrest location (cm)	Arrest temperature (°C)	Arrest $T - RT_{NDT}$ (°C)
WP-1.7A	20.2[a]	−24	26.2	52.8	61	84
WP-1.7B	52.8	61	26.2	63.5	88	111
WP-CE-1	20.0[a]	−34	10.14	37.0[b]	22	57
				42.0[c]	36	70

[a] Crack front cut to truncated chevron configuration.

[b] Plate front-face arrest location.

[c] Plate back-face arrest location.

Table 5.8. Computed crack-arrest toughness values for HSST wide-plate crack-arrest specimens WP-1.7 and WP-CE-1

Test No.	Crack-arrest toughness values (MPa·√m)			
	Tada static SEN formulas		Fedderson alternate secant formula[c]	Dynamic FE[d]
	Displacement control[a]	Load control[b]		Generation mode
WP-1.7A	351	793	311	319
WP-1.7B	385	1312	381	555
WP-CE-1(F)[e]	169	241	135	159
WP-CE-1(B)[f]	180	293	148	170

[a] From Ref. 13 (pp. 2.10–2.11) while assuming $a = a_f$ and no further bending occurs caused by propagation of the crack.

[b] From Ref. 13 (pp. 2.10–2.11) while assuming $a = a_f$ and full bending according to SEN formula when the final crack depth is used.

[c] $K_I = \sigma \left[\pi a \sec\left(\frac{\pi a}{2w}\right)\right]^{1/2}$, with σ = far-field tensile stress, $a = a_f$ = final crack length, and w = full plate width.[14,15]

[d] Fixed-load condition.

[e] Plate front-face arrest location.

[f] Plate back-face arrest location.

5.4.4 Comparison of wide-plate crack-arrest toughness data with other large-scale test results

Fixed-load, generation-mode dynamic finite-element determinations of crack-arrest toughness values for the wide-plate specimens tested so far are shown in Fig. 5.73. This figure shows that the wide-plate K_{Ia} test data exhibit an increase in arrest-toughness values with increasing temperature. The trend for K_{Ia} values to extend consistently above the limit provided in ASME Sect. XI is further substantiated in Fig. 5.74, which presents data from several large-scale tests and from the wide-plate test results.[16-21]

5.5 Wide-Plate Analyses at UM

C. W. Schwartz

A generation-mode analysis using the program SAMCR (Ref. 22) was performed by UM for the wide-plate crack-arrest test WP-1.7. The UM analysis used the same crack position vs time data and thermal eccentricity as the ORNL analyses. Figures 5.75 and 5.76 compare UM and ORNL results for stress intensity vs time and axial displacement vs time, respectively. Both figures show the same general trends and magnitudes. The K values differ slightly for the first event (5–8% higher for UM), with the differences increasing for the second event. This is caused primarily by a slight phase shift between the two sets of computations. The results from the ORNL and UM elastodynamic analyses are summarized in Table 5.9.

Table 5.9. Comparison of UM and ORNL stress-intensity factor determination

Event	Stress intensity factor ($MPa \cdot \sqrt{m}$)	
	ORNL	UM
Initiation	223	236
Arrest A	319	334
Reinitiation	592	456
Arrest B	555	465
Reinitiation	961	1155

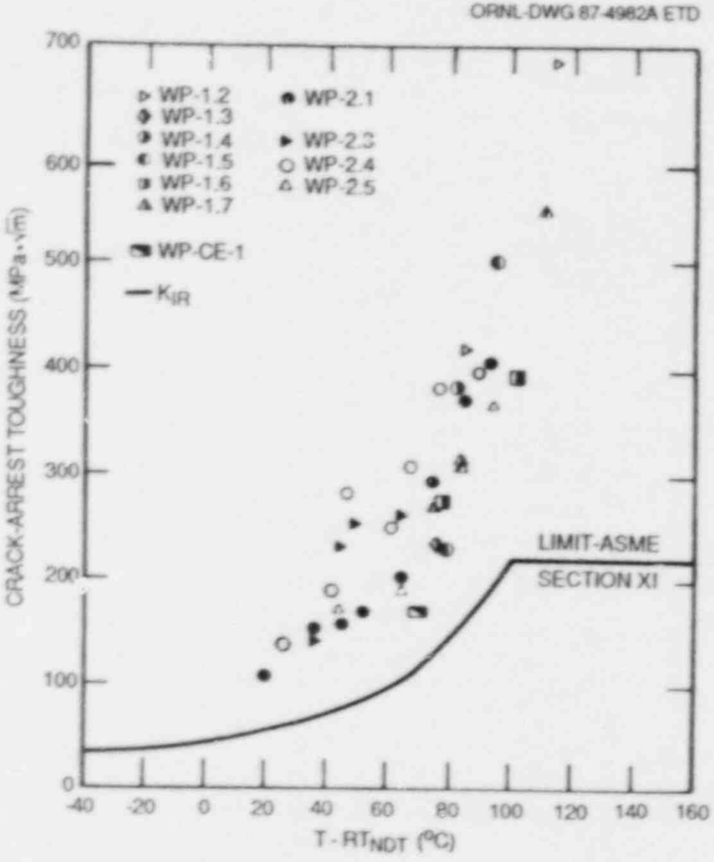

Fig. 5.73. Fixed-load, generation-mode, crack-arrest toughness results for wide-plate tests.

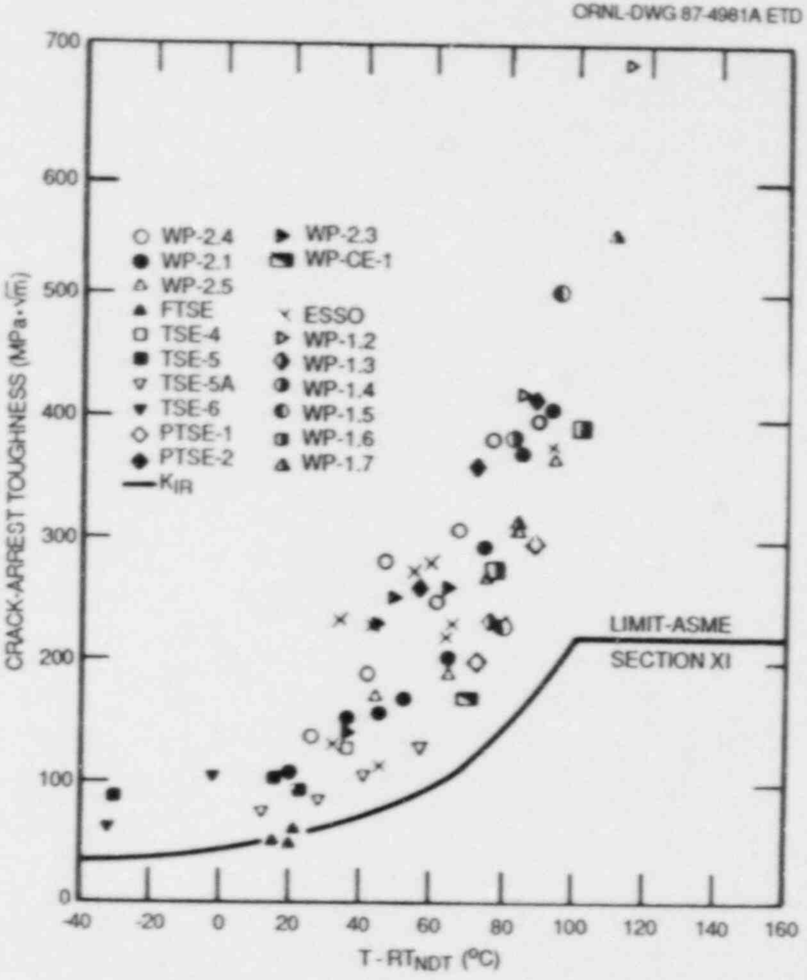

Fig. 5.74. Large-specimen data and fixed-load, generation-mode, crack-arrest toughness results exhibiting a consistent trend above the ASME limit.

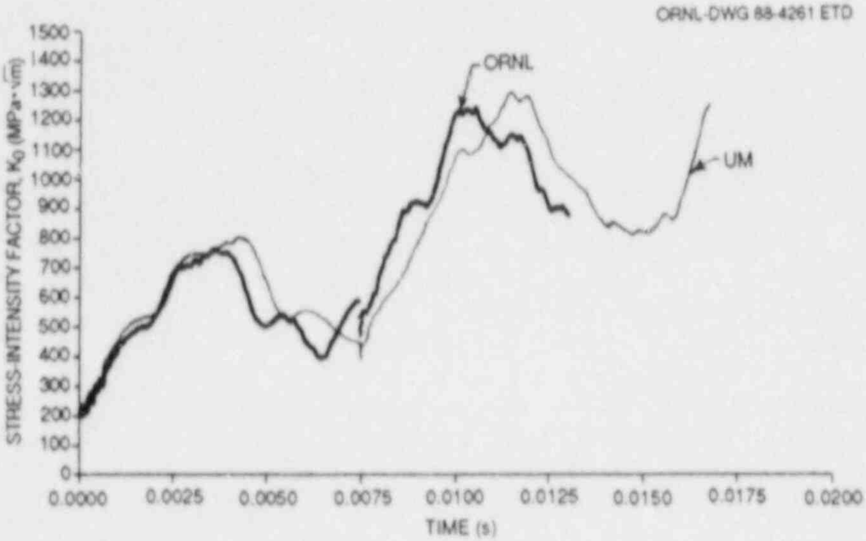

Fig. 5.75. Comparison of UM and ORNL generation-mode analysis results for stress-intensity factor vs time: Test WP-1.7.

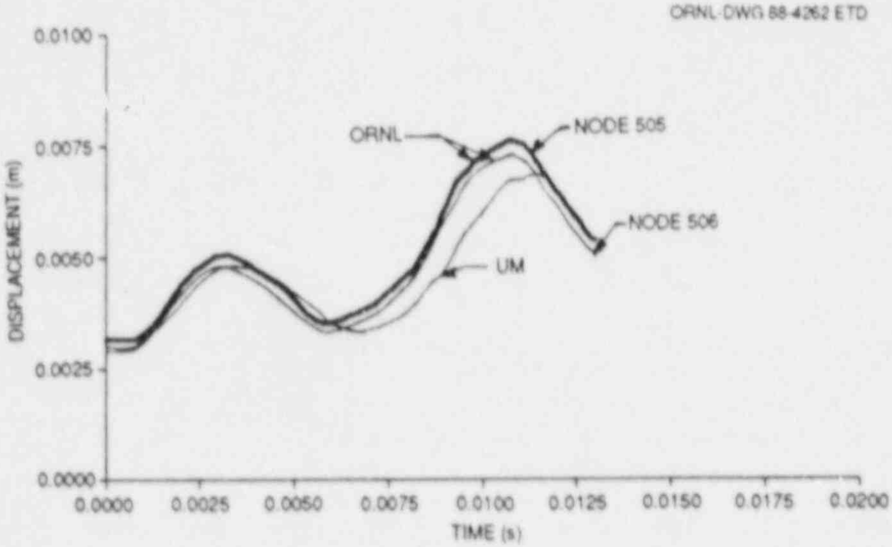

Fig. 5.76. Comparison of UM and ORNL generation-mode analysis results for axial displacement vs time: Test WP-1.7.

5.6 Stub-Panel Crack-Arrest Tests

A. Pini C. B. Oland
G. C. Robinson

Recent studies[23] have been conducted by the HSST Program to evaluate the usefulness of a relatively small panel specimen (45.7 × 76.2 × 2.54 cm) for crack-arrest experiments. The goal is for the panel to be designed for measurement of K_{Ia} values at temperatures approaching the upper shelf of the material. Additional conditions are that crack arrest should take place in a rising K_I field and that the resultant load should not exceed 2.5 MN (the capacity of the available testing machine). It is proposed that crack arrest in a rising K_I field be achieved by applying a temperature gradient across the specimen. Crack propagation must initiate at Charpy lower-shelf temperatures and run into a region of high temperature with high K_{Ia} levels. In Ref. 23, a panel specimen with a stub (Fig. 5.77) was proposed to meet those requirements. The stub is cooled to serve as a crack-starter region and is mechanically loaded to provide K_I levels that are high enough for initiation. An eccentric load is applied to the panel to produce a rising K_I field. Static analyses[23] were carried out for the specimen in Fig. 5.77 to determine the maximum attainable stress-intensity factor. For a resultant tensile load on the stub of $F_s = 66.7$ kN and panel load of $F_p = 2447$ kN, which were uniformly applied over $0 < Y_s < 10.2$ cm and $30.5 \text{ cm} < Y_p < 40.6$ cm, respectively (with Y measured from left edge), the K_I field has a value of 60.4 MPa$\cdot\sqrt{m}$ with the crack tip at Y = 20.3 cm, rising to a peak value of 220 MPa$\cdot\sqrt{m}$ at Y = 20.3 cm.

Having demonstrated the feasibility of using a stub-panel specimen to meet the goals stated previously, work was reinitiated in late 1987 to develop the required specimen geometry, instrumentation, heating-cooling, and loading systems.

5.6.1 Specimen geometry system

Final geometry of the specimen was based on meeting three general requirements: (1) measurement of crack-arrest toughness values >200 MPa$\cdot\sqrt{m}$; (2) following initiation, crack propagation and arrest within a rising K_I field; and (3) not exceeding the 2.5-MN load capacity of the testing machine. Figure 5.78 presents the geometry of a specimen that meets those requirements. The specimen dimensions are 45.1 × 99.1 × 3.39 cm. The specimen will be sidegrooved, with the depth of each groove being 12.5% of the specimen thickness. Loadings (F_p and F_s) will be applied to the specimen through the load-pin holes shown in Fig. 5.78. Load F_p is used to produce the rising K_I field and load F_s to initiate the crack run-arrest event(s).

5.6.2 Instrumentation systems

A series of steel specimens, Fig. 5.79, were tested to evaluate both strain-gage parameters and potential data acquisition systems. The specimens were loaded to failure in a hydraulic testing machine operated in a stroke-control mode. As the crack propagated, signals from strain gages positioned adjacent to the crack-propagation plane, as shown in Fig. 5.79, were recorded using digital oscilloscopes, an FM recorder, or a combination of digital oscilloscopes and an FM recorder.

Three types of strain gages were evaluated: stacked rosettes, "Tee" rosettes, and single element. The gages were placed at equal intervals adjacent to the plane of crack propagation. The spacing between gages and the spacing normal to the plane of crack propagation varied from test

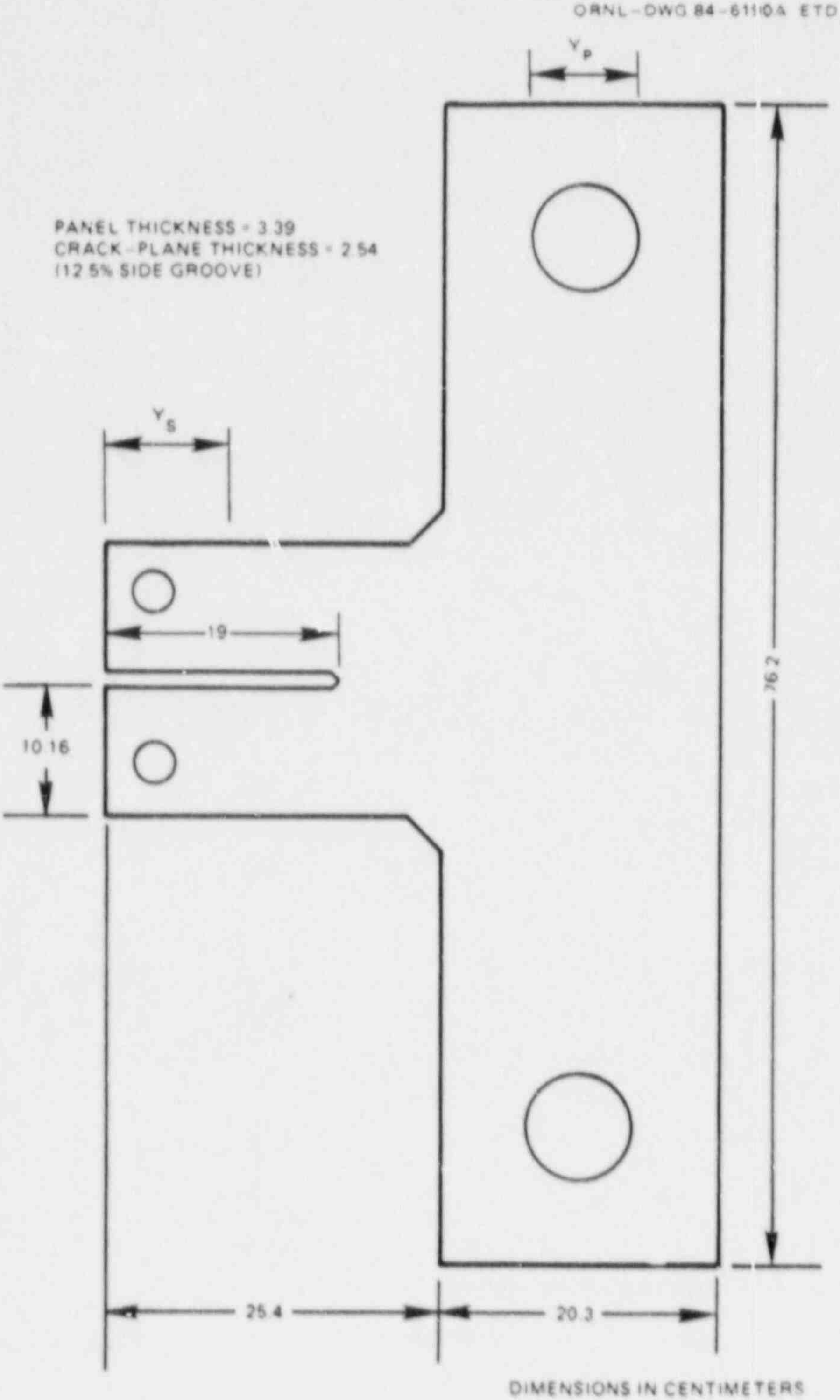

Fig. 5.77. Initial crack-arrest panel configuration.

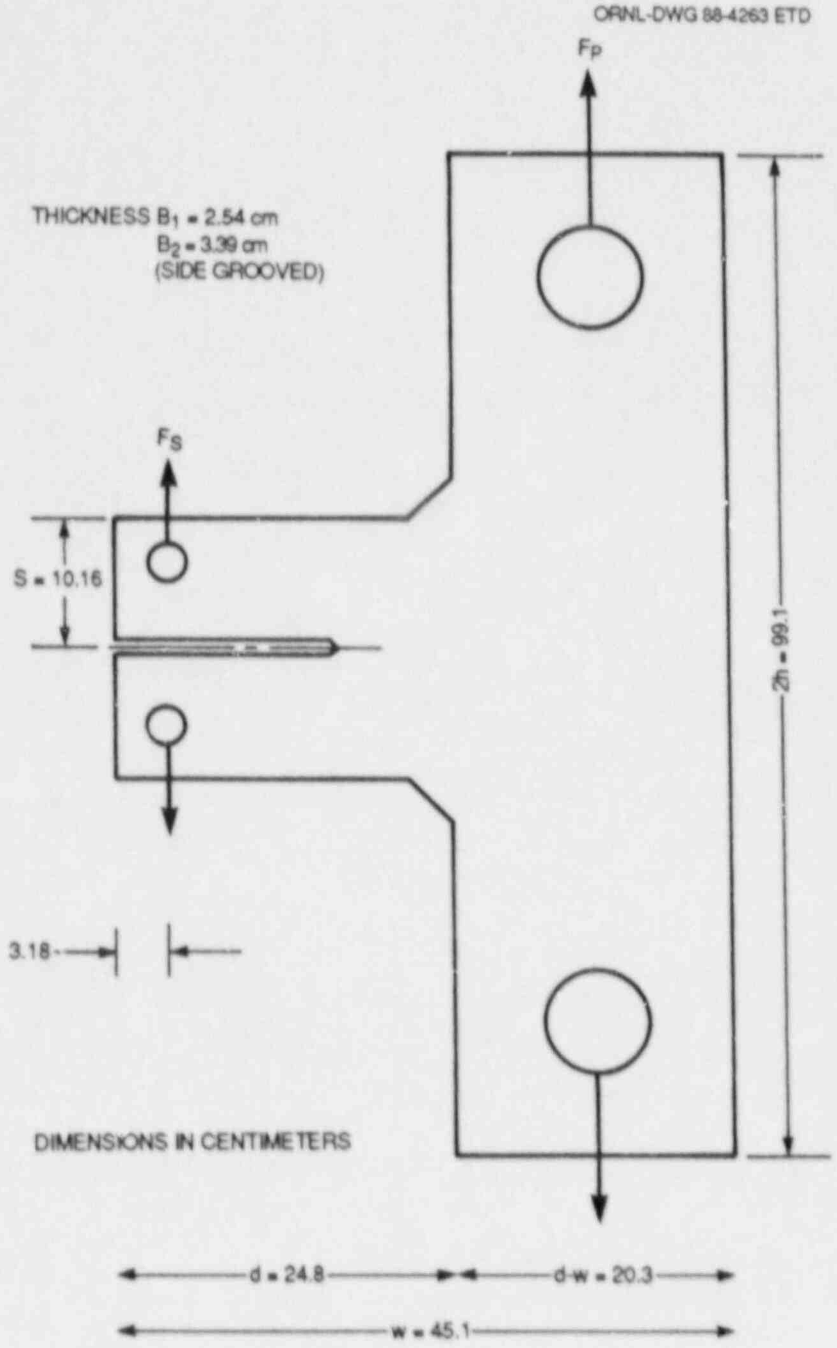

Fig. 5.78. Geometry and loading of stub-panel crack-arrest specimen.

ORNL-DWG 88-4264 ETD

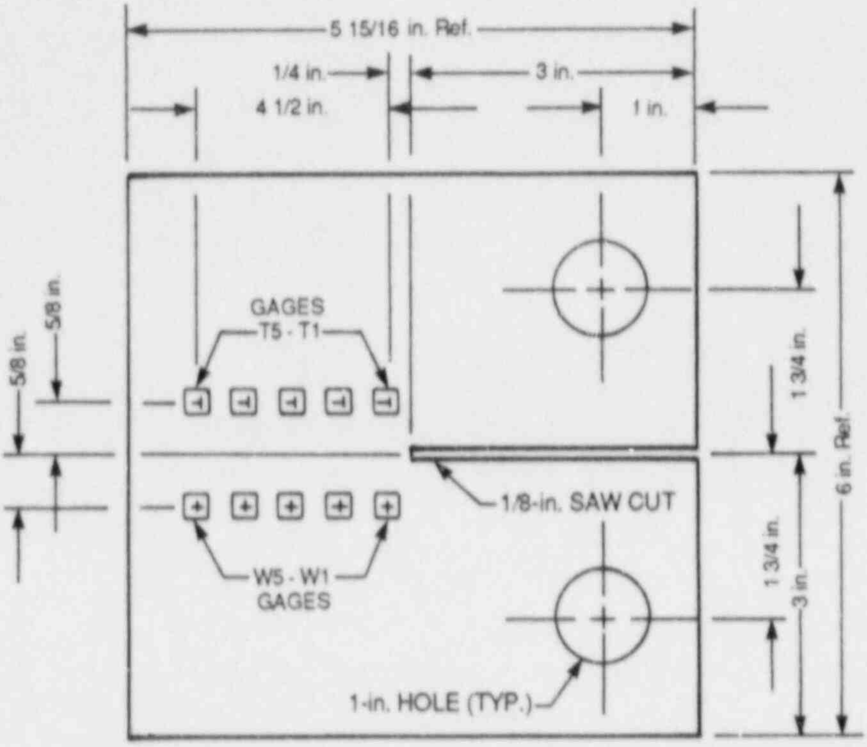

Fig. 5.79. Specimen geometry and typical strain-gage positioning used for strain gage and data acquisition system evaluations.

to test. Results from this series of tests are presently being analyzed to select the type of strain gage and gage positioning for the stub-panel crack-arrest tests.

Two types of dynamic data acquisition systems were investigated to evaluate their unique capabilities as well as their limitations: an FM recorder and digital waveform recorders. Because the digital systems are "memory" limited, the development of a triggering system was required. Also, since a test required the use of more than one digital waveform recorder, the triggering system that was developed was required to initiate data collection in each waveform recorder such that the point representing zero time was uniform for all recorders. So far, 12 specimens have been tested to failure in this series of tests. Data from these tests are now being reduced for analysis and evaluation so that a dynamic data acquisition system can be selected and a procurement specification developed.

5.6.3 Heating-cooling system

Initial design and fabrication of a heating-cooling system to apply the thermal gradient across the specimen has been completed. Specimen heating is now provided by two 500-W and one 300-W electrical resistance elements mounted on an aluminum bar that is attached to the back edge of the specimen. Cooling is provided by a liquid nitrogen reservoir chill block that is positioned around the specimen in the region of the crack tip. Check out of the system is in progress to demonstrate that it can provide the desired temperature gradients (T_{max} ≤ 180°C, T_{min} ≥ −40°C) across the specimen. Figure 5.80 presents a test specimen with the

ORNL PHOTO 8277–88

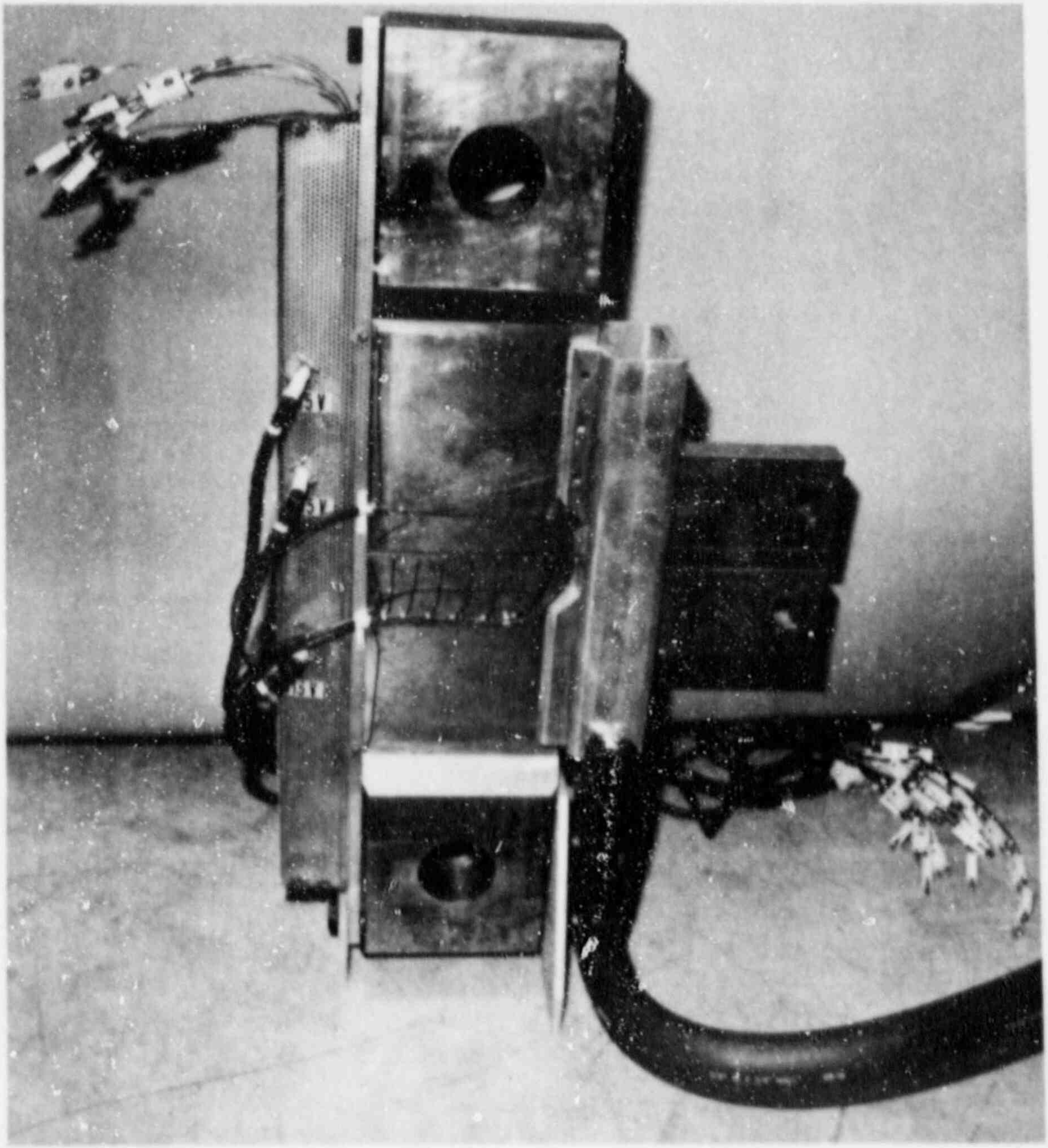

Fig. 5.80. Stub-panel crack-arrest specimen with heating-cooling system installed.

heating-cooling system installed. Temperature across the specimen is monitored by the ten thermocouples positioned adjacent to the anticipated plane of crack propagation. Software has been developed for providing a "real-time" display of actual vs desired temperature distribution across the specimen. The computer display will be used to assist in making decisions on adjusting the heating and cooling inputs while the thermal gradient is being established, as well as providing a rapid means for determining when the desired thermal gradient has been established.

5.6.4 Loading system

Mechanical loading devices have been developed for providing eccentric load F_p to produce a rising K_I field and also for producing a load (F_s) of sufficient magnitude for crack initiation. The load fixtures are now being fabricated.

References

1. C. E. Pugh, "Crack Arrest Technology," pp. 83–137 in *Heavy-Section Steel Technology Program Semiann. Prog. Rep. April–September 1984*, NUREG/CR-3744, Vol. 2 (ORNL/TM-9154/V2), Martin Marietta Energy Systems, Inc., Oak Ridge Natl. Lab.

2. D. J. Naus et al., "Summary of the Eleventh Heavy-Section Steel Technology (HSST) Wide-Plate Crack-Arrest Test (WP-1.7)," Attachment to letter, HSST Wide-Plate Crack-Arrest Test WP-1.7, from W. R. Corwin (Martin Marietta Energy Systems, Inc., Oak Ridge Natl. Lab.) to M. Mayfield (Nuclear Regulatory Commission), dated December 7, 1987.

3. D. J. Naus et al., "Summary of the Twelfth Heavy-Section Steel Technology (HSST) Wide-Plate Crack-Arrest Test (WP-CE-1)," Attachment to letter, HSST Wide-Plate Crack-Arrest Test WP-CE-1, from W. R. Corwin (Martin Marietta Energy Systems, Inc., Oak Ridge Natl. Lab.) to M. Mayfield (Nuclear Regulatory Commission), dated December 30, 1987.

4. M. F. Kanninen et al., "Preliminary Analysis of Japanese Wide-Plate Dynamic Crack Propagation Arrest Experiments," Subcontract report prepared by Battelle Columbus Laboratories for Martin Marietta Energy Systems, Inc., Oak Ridge Natl. Lab., December 1983.

5. D. J. Ayres et al., "Appendix G, Material Characterization in Tests and Analyses of Crack Arrest in Reactor Vessel Materials," EPRI NP5121-SP, prepared by Combustion Engineering, Inc., Windsor, Conn., for Electric Power Research Institute, Palo Alto, Calif., April 1987.

6. B. R. Bass and J. W. Bryson, *Applications of Energy Release Rate Technique to Part-Through Cracks in Plates and Cylinders, Volume 1, ORMGEN-3D: A Finite Element Mesh Generator for 3-Dimensional Crack Geometries*, NUREG/CR-2997, Vol. 1 (ORNL/TM-8527/V1), Union Carbide Corp. Nuclear Div., Oak Ridge Natl. Lab., December 1982.

7. B. R. Bass and J. W. Bryson, *Applications of Energy Release Rate Technique to Part-Through Cracks in Plates and Cylinders, Volume 2, ORVIRT: A Finite Element Program for Energy Release Rate Calculations for 2-D and 3-D Crack Models*, NUREG/CR-2997, Vol. 2 (ORNL/TM-8527/V2), Union Carbide Corp. Nuclear Div., Oak Ridge Natl. Lab, February 1983.

8. K. J. Bathe, *ADINA — A Finite Element Program for Automatic Dynamic Incremental Nonlinear Analyses*, Report A-1, Massachusetts Institute of Technology, Cambridge, Mass., 1984.

9. B. R. Bass, C. E. Pugh, and H. K. Stamm, "Dynamic Analyses of a Crack Run-Arrest Experiment in a Nonisothermal Plate," pp. 98–102, 175–84 in *Pressure Vessel Components Design and Analysis*, ASME Publication PVP, 1985.

10. B. R. Bass and J. Keeney-Walker, "Computer Program Development for Dynamic Fracture Analysis," pp. 5–12 in *Heavy-Section Steel Technology Program Semiann. Prog. Rep. April–September 1985*, NUREG/CR-4219, Vol. 2 (ORNL/TM-9593/V2), Martin Marietta Energy Systems, Inc., Oak Ridge Natl. Lab.

11. D. J. Naus, "Crack-Arrest Technology," pp. 129–210 in *Heavy-Section Steel Technology Program Semiann. Prog. Rep. April–September 1987*, NUREG/CR-4219, Vol. 4, No. 2 (ORNL/TM-9593/V4&N2), Martin Marietta Energy Systems, Inc., Oak Ridge Natl. Lab.

12. D. J. Naus and C. E. Pugh, "Crack-Arrest Technology" pp. 67–149 in *Heavy-Section Steel Technology Program Semiann. Prog. Rep. October 1986–March 1987*, NUREG/CR-4219, Vol. 4, No. 1 (ORNL/TM-9593/V4&N1), Martin Marietta Energy Systems, Inc., Oak Ridge Natl. Lab.

13. R. Tada, P. C. Paris, and G. R. Irwin, *The Stress Analysis of Cracks Handbook*, Del Research Corp., Hellertown, Pa., 1973.

14. C. F. Fedderson, *Current Status of Plane Strain Crack Toughness Testing of High-Strength Metallic Materials*, Crack Arrest Methodology and Applications, ASTM STP-410, American Society for Testing and Materials, Philadelphia, Pa., 1967.

15. G. R. Irwin, University of Maryland, "Notes on Testing Arrangements for Crack-Arrest Tests Using an SEN Specimen and a Temperature Gradient," private communication to C. E. Pugh, Union Carbide Corp. Nuclear Div., Oak Ridge Natl. Lab., October 1983.

16. R. D. Cheverton et al., "Fracture Mechanics Data Deduced from Thermal-Shock and Related Experiments with LWR Pressure Vessel Material," *J. Pressure Vessel Technol.* 105, 102–10 (May 1983).

17. R. H. Bryan et al., *Pressurized-Thermal-Shock Test of 6-in.-Thick Pressure Vessels. PTSE-1: Investigation of Warm Prestressing and Upper-Shelf Arrest*, NUREG/CR-4106 (ORNL-6135), Martin Marietta Energy Systems, Inc., Oak Ridge Natl. Lab., April 1985.

18. Japan Welding Council, *Structural Integrity of Very Thick Steel Plate for Nuclear Reactor Pressure Vessels*, JWES-AE-7806, Tokyo, 1977 (in Japanese).

19. A. Pellissier-Tanon, P. Sollogoub, and B. Houssin, "Crack Initiation and Arrest in an SA 508 Class-3 Cylinder Under Liquid Nitrogen Thermal-Shock Experiment," pp. 132–42 in *Transactions of the 7th International Conference on Structural Mechanics in Reactor Technology, Vols. G and H, Chicago, August 1983.*

20. R. H. Bryan et al., *Quick-Look Report on the Second HSST Pressurized-Thermal-Shock Test, PTSE-2*, ORNL/PTSE-2, Martin Marietta Energy Systems, Inc., Oak Ridge Natl. Lab., Feb. 19, 1987.

21. M. Satoh, "Crack Arrest Testing," Mitsubishi Heavy Industries, Ltd., Takasago, Japan, material presented to Heavy-Section Steel Technology Program personnel, November 11, 1987.

22. C. W. Schwartz et al., *SAMCR: A Two-Dimensional Dynamic Finite Element Code for the Stress Analysis of Moving Cracks*, NUREG/CR-3891 (ORNL/Sub/79-7778/3), Martin Marietta Energy Systems, Inc., Oak Ridge Natl. Lab., November 1984.

23. H. K. Stamm, "Analysis of a Panel Crack-Arrest Specimen," pp. 9–17 in *Heavy-Section Steel Technology Program Semiannual Prog. Rep. April–September 1984*, NUREG/CR-3744, Vol. 2 (ORNL/TM-9154/V2), Martin Marietta Energy Systems, Inc., Oak Ridge Natl. Lab., December 1984.

6. IRRADIATION EFFECTS STUDIES

R. K. Nanstad

The Heavy-Section Steel Technology (HSST) Irradiation Effects Task (Task H.6) consists of a number of projects concerned with the effects of neutron irradiation on the fracture toughness and mechanical properties of reactor pressure vessel (RPV) materials. The task currently involves seven designated series of experiments, the first four completed. The active series described here include (1) the Fifth and Sixth Series, which will characterize the shifts and shapes of the irradiated K_{Ic} and K_{Ia} curves, respectively, and (2) the Seventh Series, concerned with the irradiation resistance of stainless steel cladding.

6.1 Fifth Irradiation Series

R. K. Nanstad F. M. Haggag
R. L. Swain T. N. Jones

Fracture-toughness investigations continued with testing of irradiated 1TCS and 2TCS. All planned irradiated testing for the Fifth Series has now been completed. All tests were conducted with a computer-interactive test system, using the single-specimen compliance technique. No unloadings are performed before the PQ load defined in ASTM E399. Tests that do not satisfy the American Society of Testing and Materials (ASTM) criteria for a valid K_{Ic} are analyzed by computing the J-integral at the onset of cleavage J_c. An elastic-plastic fracture-toughness value K_{Jc} is calculated from the relationship

$$K_{Jc}^2 = EJ_c \ , \tag{1}$$

where E ≡ Young's modulus in megapascals.

Irradiated 1TCS and 2TCS were tested at Oak Ridge National Laboratory (ORNL), while irradiated 2TCS were tested by Materials Engineering Associates (MEA) at the University of Buffalo. For 72W, nine 1TCS were tested at 85°C, and five 1TCS were tested at 95°C. For 73W, ten 1TCS were tested at 85°C, and four 1TCS were tested at 105°C. Fatigue crack lengths and ductile crack extensions have been measured, and the final fracture-toughness analyses are under way. Additionally, photographs of all fracture surfaces have been completed.

Of particular importance to the analysis procedures is the treatment of specimens that exhibit small cleavage instabilities, pop-ins, before the final cleavage instability that leads to specimen fracture. Some of the irradiated 1TCS, 2TCS, and 4TCS experienced pop-ins of various amounts. The tentative method chosen for treating those events follows that of the ASTM Committee responsible for development of the test method for crack-tip-opening displacement (CTOD). That is, a line is drawn parallel to the initial slope of the load-displacement record and that passes through the crack initiation load point of the pop-in. A second line (secant line) that originates at the same point as the parallel line is then constructed but has a 5% reduced slope from that line. If the secant line intersects the load-displacement trace before the arrest point of the pop-in, the pop-in is defined as significant. In those cases, the J_c is calculated at the point of pop-in initiation and K_{Jc} is calculated using Eq. (1). Furthermore, a K_{Jc} value is also calculated corresponding to the point of cleavage instability, leading to specimen failure. Values of K_{Jc} based on small but significant (as defined above) pop-ins will be noted when the data are tabulated and plotted graphically.

Because of the relatively large data scatter, wide variations in specimen sizes, and the need to use elastic-plastic fracture mechanics, the use of statistical analyses is an important part of this program. The use of Weibull failure statistics is incorporated in the program as are standard statistics of variance procedures. Additionally, the use of empirical adjustment schemes and other statistical distributions are being investigated, all aimed toward the development of a rational scheme for constructing the irradiated K_{Ic} curves.

6.2 Sixth Irradiation Series: Crack Arrest

S. K. Iskander R. K. Nanstad
E. T. Manneschmidt R. L. Swain

6.2.1 Capsule disassembly

The first of two irradiation capsules containing compact crack-arrest specimens has been disassembled. The specimens have been retrieved and prepared for storage, and the dosimeters have been retrieved for analysis. The second capsule will be disassembled by the end of June.

6.2.2 Remote hot cell fixture for crack-arrest testing

The temperature-conditioning features of the remote hot cell fixture for crack-arrest testing have been exercised. Several thermocouples were attached to the top and bottom of various sizes of specimens and their readings compared with that registered by the fixture's thermocouple. The uniformity of all temperatures, at low and high temperatures well in excess of those envisioned for tests in the hot cell, was within ±1°C. The design of the thermocouple itself is similar to that being used in the temperature-conditioning chamber of three Charpy V-notch (CVN) testing machines, including that in the hot cell.

All three specimen sizes for which the fixture was designed were tested (see Sect. 3.1). Several enhancements need to be implemented to make its use in the hot cell as simple as possible. The Teflon strips used between the wedge and the split pins for unirradiated tests would be difficult to apply in the hot cell environment. Two kinds of lubricants were tested, but after a single loading/unloading cycle it was clear from the large force needed to extract the wedge that the lubricant had been wiped off the smooth ground finish. A fine sandblast finish to provide reservoirs of lubricant improved matters somewhat, but lubricant still had to be applied frequently. This matter is still under study.

6.3 Seventh HSST Irradiation Series

F. M. Haggag R. K. Nanstad
T. N. Jones E. T. Manneschmidt
R. L. Swain

6.3.1 Phase 1

Stainless steel cladding applied by the single-wire oscillating submerged-arc method was evaluated in the first phase of the Seventh Irradiation Series. Most of the work of this phase was completed and reported earlier.[1] It included results of Charpy impact and tensile specimens that were irradiated to 2×10^{19} neutrons/cm^2 (>1 MeV) at 288°C. However, eight irradiated 0.5TCS, each from types 308 and 309 stainless steel cladding, remain to be tested in the hot cell using the single-specimen unloading compliance technique. Furthermore, six irradiated precracked Charpy V-notch (PCVN) specimens, each from types 308 and 309 stainless steel cladding, will be tested dynamically. Unirradiated 0.5TCS from both types 308 and 309 stainless steel cladding were tested successfully. The results of these specimens will be reported later when testing of the irradiated specimens is completed.

6.3.2 Phase 2

In the second phase, currently in progress, a commercially produced three-wire series-arc cladding was evaluated under similar irradiation and testing conditions as in the first phase. The three-wire series-arc procedure, developed by Combustion Engineering, Inc., Chattanooga, Tennessee, produced a highly controlled weld chemistry, microstructure, and fracture properties in all three layers of the weld. The three layers of cladding were required to allow the fabrication of tensile, CVN, and 0.5TCS from the cladding. The tensile and CVN specimens were irradiated to 2 and 5×10^{19} neutrons/cm^2 (>1 MeV), while the eight 0.5TCS were irradiated only to 2×10^{19} neutrons/cm^2 (>1 MeV). Testing of the unirradiated (control) and irradiated tensile and CVN specimens is completed, and the results are presented below. Unirradiated (control) 0.5TCS were tested successfully using the single-specimen compliance technique, but the results will be presented later following testing of irradiated fracture-toughness specimens. Preparations have been made to complete testing of all remaining irradiated specimens from the Seventh Irradiation Series by the end of June 1988. Most of the Phase 2 results are described in Ref. 2.

6.3.3 Results and discussion

Photomicrographs of the three-wire stainless steel cladding (Fig. 6.1) show a distribution of delta-ferrite in an austenite matrix quite

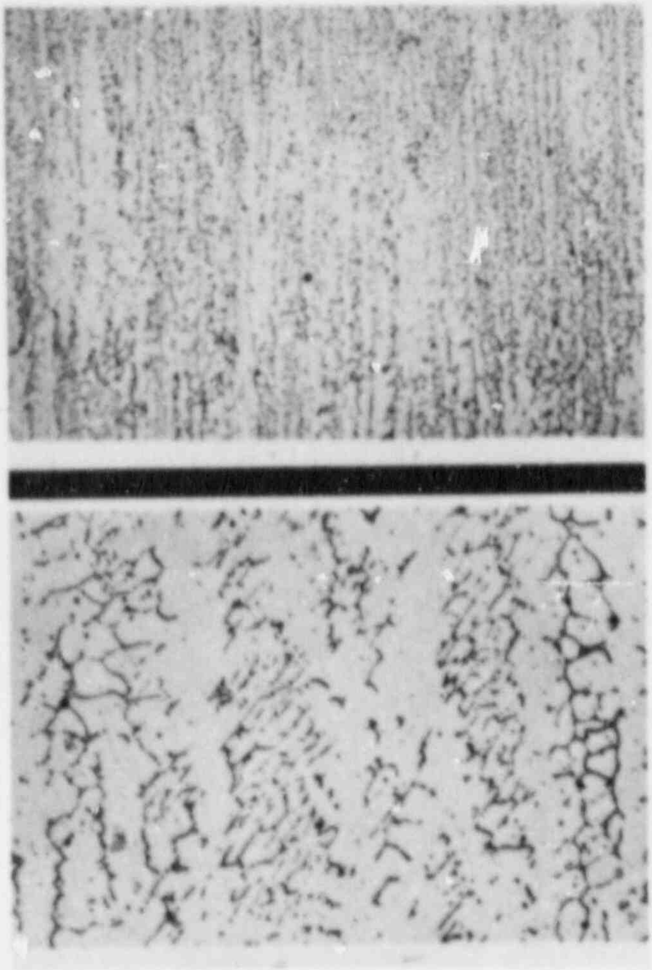

Fig. 6.1. Microstructure of three-wire stainless steel cladding weld overlay typical of RPV cladding with delta-ferrite in austenitic matrix, good-quality commercial cladding.

typical of microstructures seen in good practice, commercial-weld, overlay cladding in RPVs.

6.3.3.1 Irradiation history. The specimens were irradiated in two capsules by MEA in the core of the 2-MW pool reactor (UBR) at the Nuclear Science and Technology Facility in Buffalo, New York. Each capsule contained 20 CVN and 6 miniature tensile specimens and was instrumented with thermocouples and dosimeters. Each capsule was rotated 180° at least once during its irradiation exposure for side-to-side fluence balancing. Irradiation temperatures were maintained at 288 ± 11°C. The average fluence for the first capsule was 2.14×10^{19} neutrons/cm^2 (>1 MeV) ± 8%, following 631.5 h of irradiation. The second capsule reached an average fluence of 5.56×10^{19} neutrons/cm^2 (>1 MeV) ± 5% in 1607 h. These fluences are for a calculated spectrum based on Fe, Ni, and Co dosimeter wires.

6.3.3.2 Tensile properties. Tensile tests were conducted in the temperature range of −125 to 288°C. The effect of specimen orientation on tensile properties was insignificant (Fig. 6.2). Hence, only tensile specimens with their axes oriented in the longitudinal (rolling and

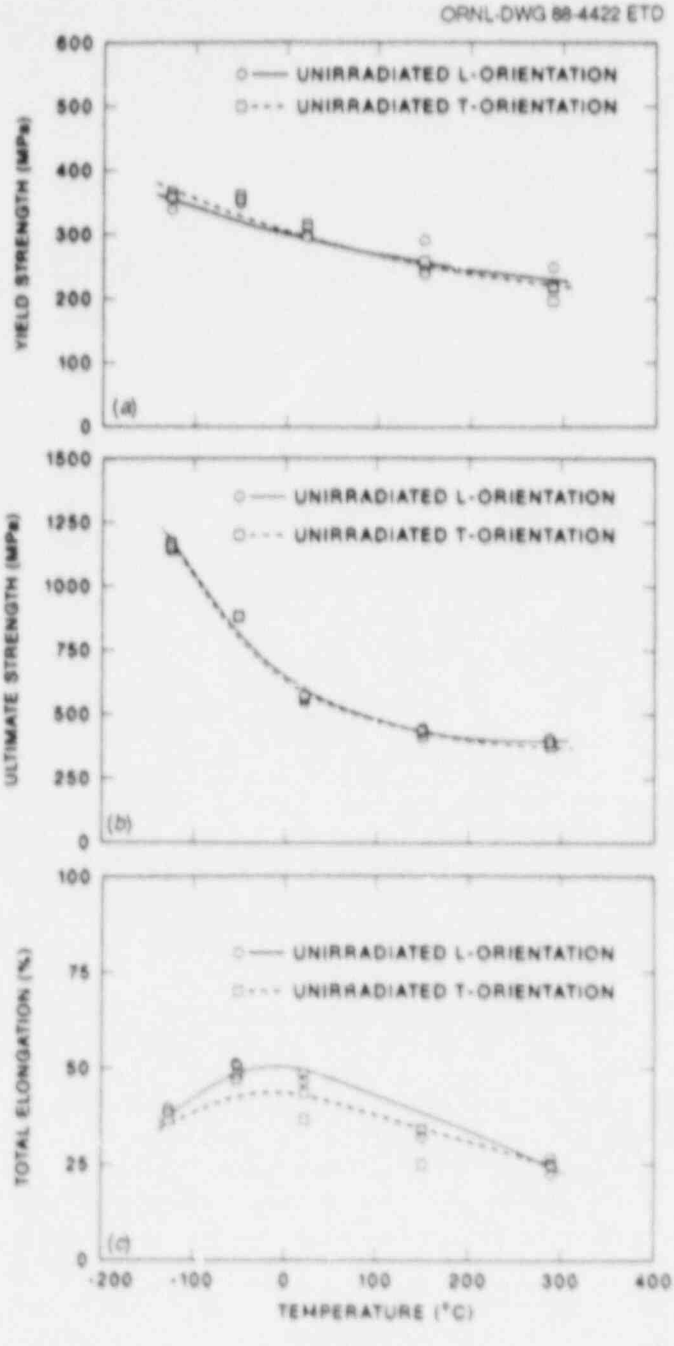

Fig. 6.2. Effect of specimen orientation on tensile properties of three-wire stainless steel cladding. (*a*) Yield strength vs temperature, (*b*) ultimate strength vs temperature, and (*c*) total elongation vs temperature.

welding) direction were irradiated at 288°C to the two fluence levels mentioned earlier. The cladding exhibits an extremely rapid rise in tensile strength below about 0°C, as shown in Fig. 6.2. This figure also shows that the ductility increases from high temperatures to about −50°C, then decreases at lower temperatures.

6.3.3.3 Impact testing properties. Charpy impact specimens were machined in the LT, LS, TL, and TS orientations. These four specimen orientations were chosen to simulate the possibilities of crack extension in the axial and circumferential orientations, both across and through the cladding of a pressure vessel. All three-wire stainless steel cladding specimens exhibited a behavior similar to the ductile-to-brittle transition behavior of ferritic steels (also similar to that of single-wire cladding[1]) during impact testing, because of the dominance of delta-ferrite failures at low temperatures. The test results also show relatively small variations of Charpy impact toughness in four orientations (Fig. 6.3). Thus, CVN irradiated specimens were machined only from the

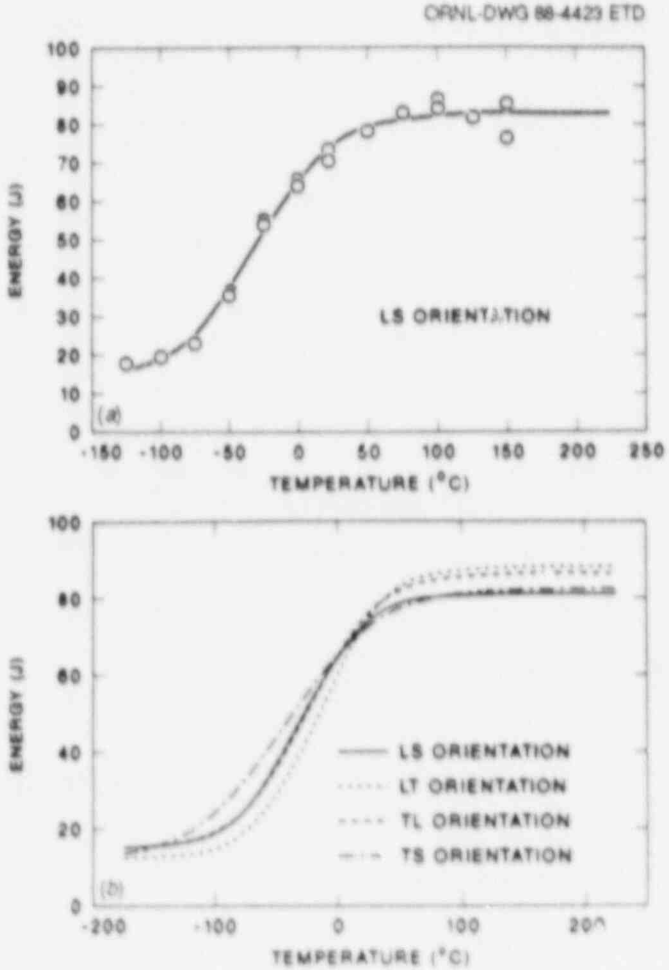

Fig. 6.3. Unirradiated three-wire stainless steel cladding shows Charpy impact transition behavior. (*a*) CVN energy vs temperature, LS orientation, and (*b*) effect of specimen orientation on CVN energy curves.

cladding in the LS orientation because this orientation exhibited a typical transition temperature as well as a slightly lower upper-shelf energy.

The fracture appearance macroscopically did not change significantly from the upper to lower shelf as shown in Fig. 6.4. These CVN specimens (unirradiated, LS orientation), shown in Fig. 6.4, were further examined in the scanning electron microscope. The specimen tested at 100°C absorbed 80 J and fractured in a fully ductile manner by microvoid coalescence. The spherical particles that initiated the dimples were readily visible on the fracture surface. In contrast, the specimen tested at −100°C absorbed only 20 J and fractured in a much more brittle mode. The fracture surface of this specimen contained areas of cleavage associated with the ferrite phase. Also present were smooth regions believed to be associated with the ferrite-austenite interfaces, indicating that fracture [illegible] by interphase separation. Some isolated patches of dimples and [illegible] initiating particles were also present. In conclusion, scanning electron microscope examination (Fig. 6.5) demonstrated that the fracture of stainless steel cladding is matrix controlled on the upper shelf and ferrite controlled at lower temperatures, as observed previously with the single-wire cladding.[1]

6.3.3.4 Effect of irradiation on tensile properties. The yield strength of three-wire stainless steel cladding was increased because of irradiation exposure. The effects were greater at room temperature and below (Fig. 6.6); for example, at the fluence of 2 × 10^{19} neutrons/cm^2, the yield strength increased by 9, 20, and 28% at test temperatures of 288°C, room temperature, and −125°C, respectively. At the higher fluence

M&C PHOTO YP4627

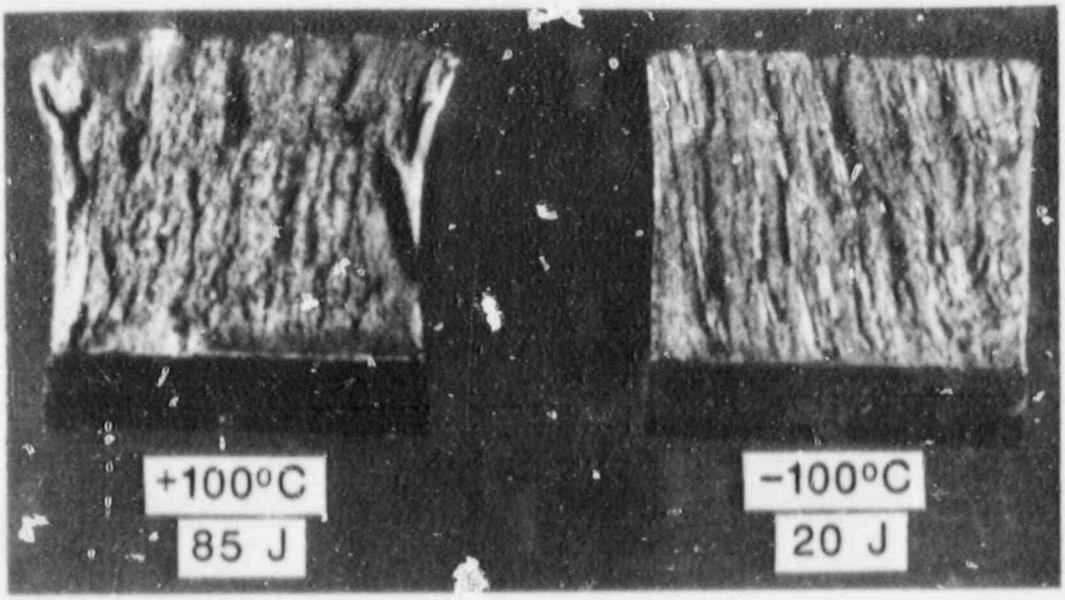

Fig. 6.4. Fracture surfaces of unirradiated CVN specimens tested at upper and lower shelves.

M&C PHOTO YP4624

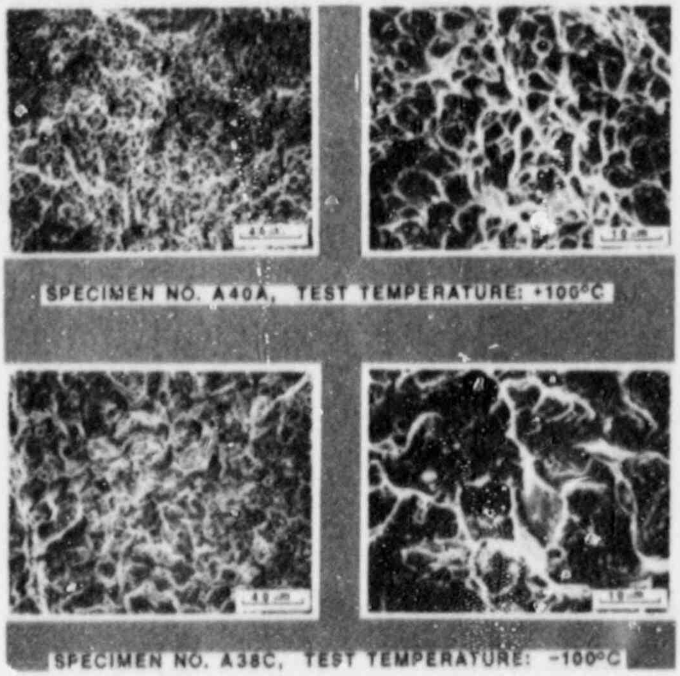

Fig. 6.5. Scanning electron microscopic examination demonstrates that fracture of stainless steel cladding is matrix controlled at upper shelf and ferrite controlled at lower temperatures.

ORNL-DWG 88-4424 ETD

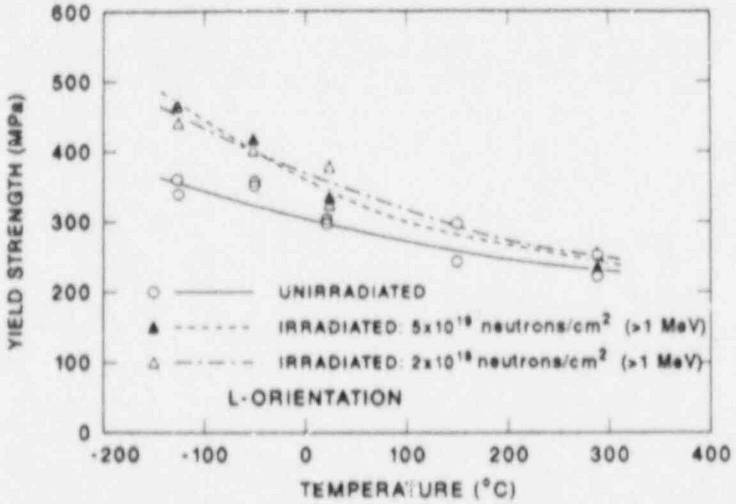

Fig. 6.6. Effect of neutron irradiation at 288°C on the yield strength of three-wire stainless steel cladding (yield strength vs test temperature).

level of 5 × 10^{19} neutrons/cm^2, the yield strength increased by 6, 16, and 34% at the test temperatures of 288°C, room temperature, and −125°C, respectively. Thus, most of the radiation damage occurred at the first fluence level; increasing the fluence by a factor of 2.5 did result in a relatively smaller radiation damage increase. The effects of irradiation on the ultimate strength and ductility were insignificant or very small (Fig. 6.7).

6.3.3.5 Effect of irradiation on Charpy impact properties. Irradiation of the three-wire series-arc stainless steel cladding specimens at 288°C to fluence levels of 2 and 5 × 10^{19} neutrons/cm^2 (>1 MeV) resulted in decreases of the CVN upper-shelf energy by 15 and 20% and increases of the 41-J transition temperature by 13 and 28°C, respectively (Fig. 6.8). Again, Fig. 6.9 shows that increasing irradiation from 2 to 5 × 10^{19} neutrons/cm^2 further degraded the three-wire stainless steel cladding. Irradiation also degraded the CVN lateral expansion significantly (Fig. 6.10). The upper-shelf lateral expansion was reduced by 43 and 41% at the low and high fluences, respectively. Furthermore, the

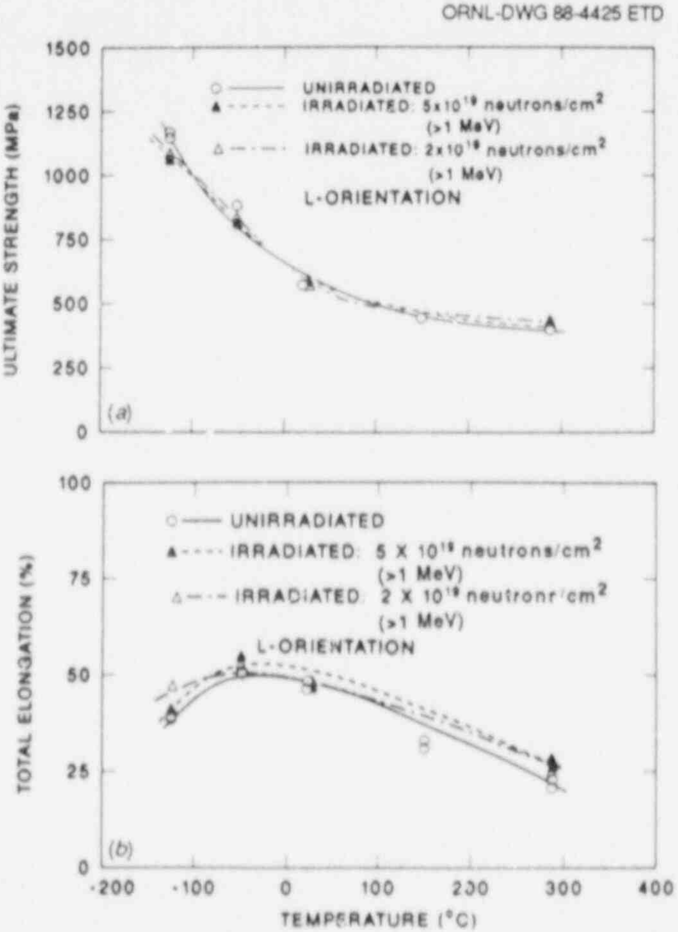

Fig. 6.7. Effect of irradiation on the ultimate strength and elongation of three-wire stainless steel cladding. (*a*) Ultimate strength vs temperature and (*b*) total elongation vs temperature.

ORNL-DWG 88-4426 ETD

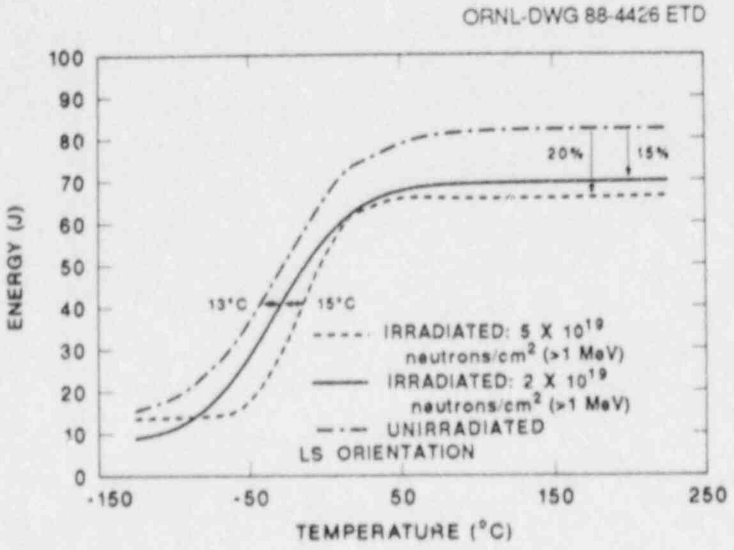

Fig. 6.8. Effect of irradiation on Charpy impact toughness of three-wire stainless steel cladding.

ORNL-DWG 88-4427 ETD

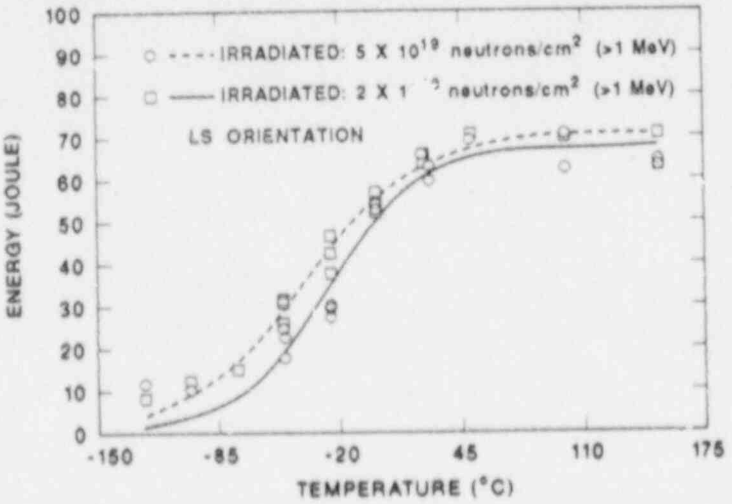

Fig. 6.9. Charpy impact energy vs test temperature for irradiated specimens in the LS orientation.

0.38-mm (0.015-in.) transition temperature shifts were 41 and 46°C for the low and high fluences, respectively. Table 6.1 also provides the CVN test results for the unirradiated and irradiated specimens. These results generally agree with those for the single-wire cladding produced with good welding practice.[1]

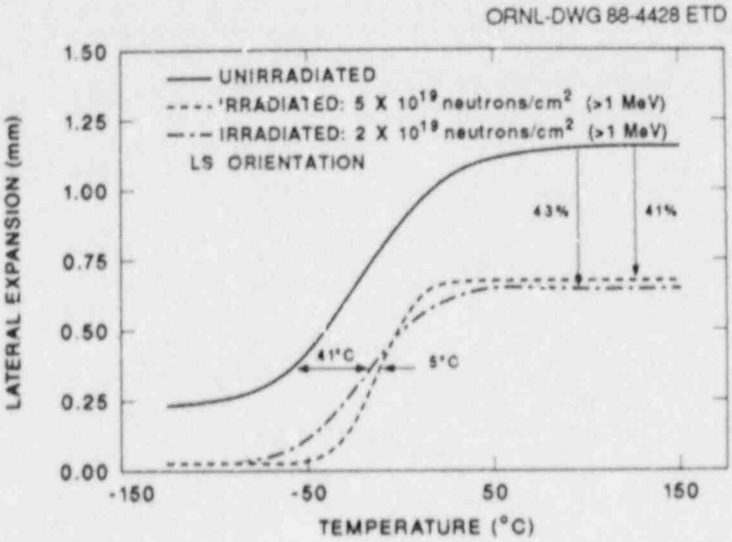

Fig. 6.10. Effect of irradiation on CVN lateral expansion of three-wire stainless steel cladding.

Table 6.1. Charpy impact test results for stainless steel three-wire series-arc cladding

Orientation[a]	Neutron fluence [neutrons/cm^2 (>1 MeV)]	Transition temperature criterion (°C)			Shelf energy (J)	
		41 J	68 J	0.38 mm	Upper	Lower
LS	0	−41	6	−57	82	13
LS	2 × 10^{19}	−28	56	−16	70	9
LS	5 × 10^{19}	−13		−11	68	12
LT	0	−28	11		88	14
TL	0	−40	4		86	16
TS	0	−55	7		83	12

[a] With respect to the base metal where L is the rolling as well as the welding direction.

References

1. W. R. Corwin et al., "Fracture Properties of a Neutron-Irradiated Stainless Steel Submerged-Arc Welding Cladding Overlay," pp. 26–47 in *Proceedings of the Twelfth Water Reactor Safety Research Information Meeting*, NUREG/CP-0058, Vol. 4, Oct. 22–26, 1984.

2. F. M. Haggag et al., "Effects of Irradiation on Strength and Toughness of Commercial LWR Vessel Cladding," pp. 177–93 in *Proceedings of the Fifteenth Water Reactor Safety Information Meeting*, NUREG/CP-0091, Vol. 2, Oct. 26–29, 1987.

7. CLADDING EVALUATIONS

7.1 Crack-Arrest Behavior in Clad Plates

S. K. Iskander
B. C. Oland
D. J. Alexander
K. V. Cook
G. C. Robinson
S. E. Bolt
E. T. Manneschmidt
R. L. Swain

7.1.1 Introduction

The objective of the clad-plate experiments is to determine the effect, if any, of stainless steel cladding upon the propagation of small surface cracks subjected to stress states similar to those produced by thermal shock conditions. Six plates have been already tested, and a detailed description of the experiments and results has been given previously.[1] One clad and one unclad plate were tested recently and are reported on in this section. The results of crack-arrest testing performed on the clad-plate base metal are given in Chap. 3.

In previous reports, the test specimen was described[2] and pretest material characterization given.[3] Posttest material characterizations presented in the preceding semiannual progress report[4] included Young's modulus and stress-strain curves for the base metal, heat-affected zone (HAZ), and cladding, as well as results of room-temperature tensile testing that had been performed on the HAZ from one of the broken halves of the first plate tested. The RT_{NDT} of the base metal, the variation of hardness across the thickness of the plate, results of metallographic examinations, fractography, and scanning electron microscopy (SEM) on the fracture surface of the first plate have also been reported in the previous semiannual report.[1,4]

The general test procedure was described previously, but for the sake of completeness, it will be repeated here to emphasize the similarities and differences between the tests on the previous six specimens and the present two. The test procedure will be followed by a description of the instrumentation and static and dynamic data acquisition systems (DASs) used. Then the tests and results will be presented, and some preliminary conclusions inferred from all eight tests are given.

7.1.2 General description of the test

In all eight tests performed, the general test procedure was essentially the same. The instrumented plate was mounted in a 1-MN Instron testing machine. For tests at other than room temperature, the plate was cooled to the specified temperature. The variation in temperature at various locations was kept within 3°C. All eight plates had an electron-beam (EB) weld in the base metal to serve as a flaw initiation site. The plate was loaded in four-point bending to induce a pure bending moment in the span including the EB weld region. For the previous six plates, the loads were chosen to induce a specified strain level on the surface of the base metal. The EB weld was then hydrogen-charged, while the load was maintained constant using stroke control, until a flaw initiates. This portion of the experiment on an initially unflawed plate is thus essentially an "arrest" experiment, the purpose of which is to study the effect of cladding on a running flaw.

With the two plates recently tested, the EB weld was hydrogen-charged until a flaw popped-in before installing in the testing machine. For brevity, this flaw will be referred to as the "EB flaw," and its shape is shown later. The plates were then mounted in the testing machine, and the load increased at a uniform rate under stroke control until this preexisting flaw either popped-in and arrested or the entire plate ruptured. Thus, the difference between the experiments on the two plates reported here and the previous six is the presence of a flaw when the plates were first mounted in the test machine.

In cases in which the flaw arrested, the plate is removed from the testing machine and heat-tinted to define the arrested flaw shape. Some nondestructive examination was performed to determine the extent of flaw propagation. After partial reinstrumentation, the plate is put back into the testing machine, and in some cases, cooled to a specified temperature. The load is increased at a uniform rate until the plate either ruptures or further pop-in occurs. In case of the latter event, the process is repeated. The purpose of reloading the arrested flaw shapes is to obtain data on the residual load-bearing capacity of flawed clad plates. This portion of the experiment is designated an "initiation" one in contrast with the "arrest" portion described above.

In all cases, the loading rate was chosen to be within the range prescribed by ASTM E399, 0.55 to 2.75 $\mathrm{MPa\cdot m\cdot s^{-1}}$.

7.1.3 Instrumentation and DAS

Figure 7.1 shows the layout of the instrumentation used for the tests on plates CP-16 and -22. Both plates were instrumented with four thermocouples, TE-1 through TE-4; one crack-opening-displacement (COD) gage ZE-1; and 12 strain gages, XE-1 to XE-12. Plate CP-16 carried extra instrumentation to capture the dynamic characteristics of crack propagation. The extra instrumentation consisted of strain gages XD-1 to XD-11 and two additional trigger strain gages. These were attached near the crack tip and in the path of possible crack propagation to trigger the DAS described below. Figure 7.2 shows a close-up of the flaw area and the strain gages in its vicinity. Load and stroke signals from the hydraulic testing machine were also recorded.

To provide additional test data, the load and COD were recorded on a strip-chart recorder. The load was plotted against the signal from strain gage XE-1 (on the cladding) on an X-Y plotter. The loads reported for initiation and arrest were taken from these plots.

Both static and, for plate CP-16 only, dynamic DAS were used. The static DAS recorded data every 6 min during the loading of the specimen, while the dynamic one recorded data from just before crack initiation to just after crack arrest. The static DAS recorded data from the four thermocouples; the COD gage; 12 strain gages, XE-1 to XE-12; the load cell; and the stroke transducer.

ORNL-DWG 88-4364 ETD

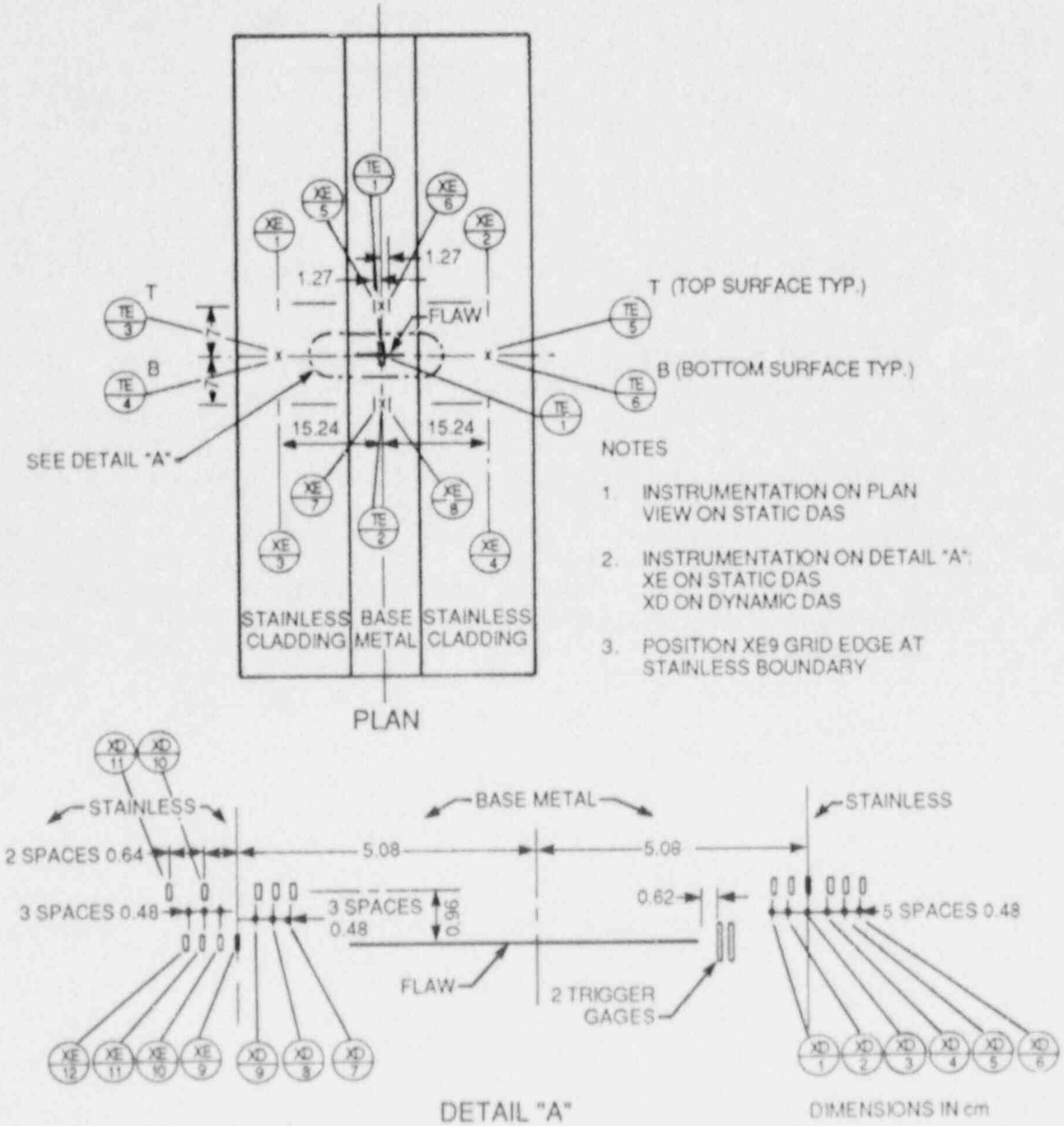

Fig. 7.1. Layout of instrumentation used for tests on plates CP-16 and -22.

The dynamic DAS recorded signals from 11 strain gages, XD-1 to XD-11; the trigger gages; and the load cell, using four LeCroy and three Nicolet digital oscilloscopes that were simultaneously triggered when the crack initiated. A separate trigger circuit was used to ensure that the oscilloscopes triggered simultaneously. This circuit, which consisted of two trigger strain gages, a strain gage conditioner, and a pulse generator, supplied a voltage spike of ~10 V when one of the trigger strain

M&C PHOTO YP5186

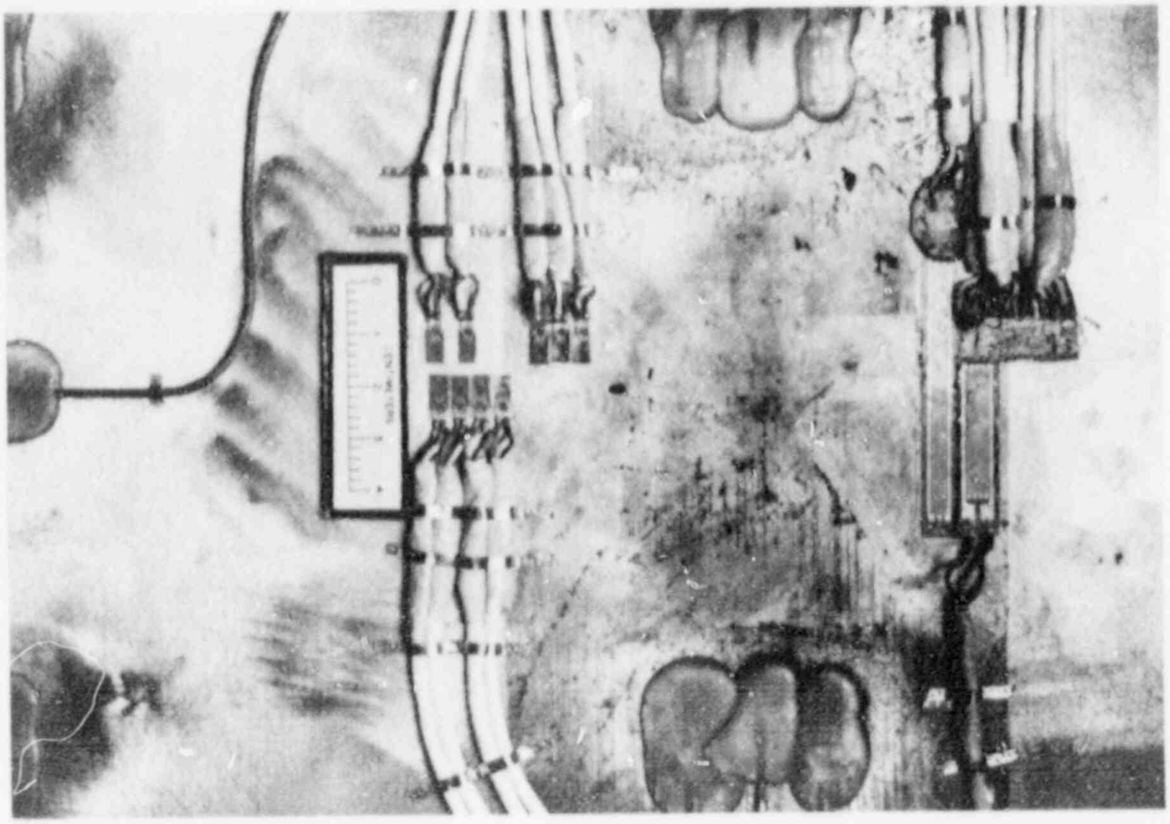

Fig. 7.2. Close-up of flaw area and strain gages in its vicinity.

gages was fractured by the propagating crack. Each oscilloscope was set to trigger on a voltage change of 5 V. The LeCroy and Nicolet oscilloscopes were set to record data at a rate of 20 and 500 ns/point, respectively.

7.1.4 Tests on clad plate CP-16 and unclad plate CP-22

As mentioned above, clad plate CP-16 and unclad plate CP-22 were tested. The flaws produced in both plates by the EB weld/hydrogen-charging technique were approximately elliptic in shape, 16 mm deep. The lengths of the flaws along the surface were 58 and 67 mm for the clad and unclad plate, respectively. The shape of the EB weld-induced flaw shape is apparent on the fracture surface shown later in this section.

Plate CP-16 was tested at room temperature (~21°C). Pop-in occurred at a load of 703 kN, and the drop in load to the arrest point was <1% (Fig. 7.3). It is believed that an earlier pop-in, also apparent in Fig. 7.3, occurring at 632 kN is associated with flaws lying in different planes on either side of the EB-weld HAZ joining together. On the basis of an ~1600-με increase, observed in strain gage XD-3 and indicating a sizeable crack-jump, the plate was unloaded.

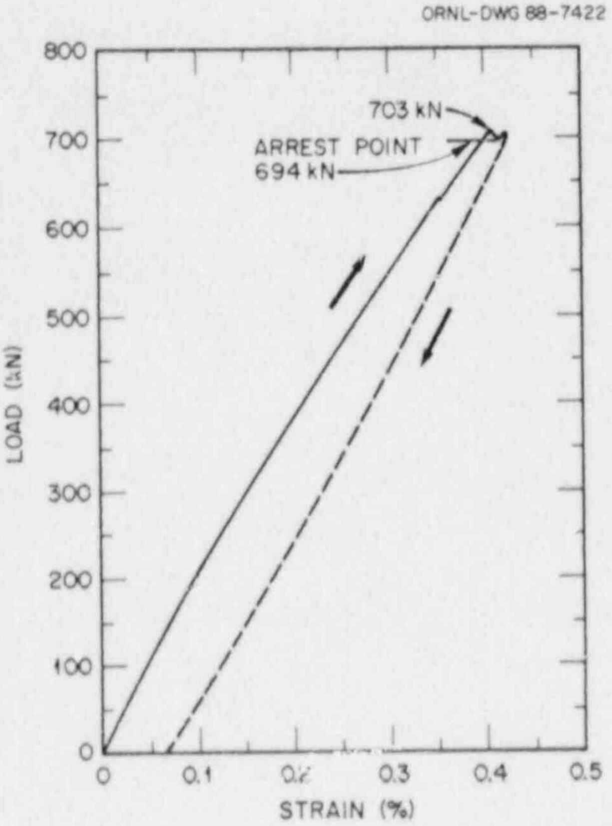

Fig. 7.3. Load vs strain gage XE-1 recorded on X-Y chart showing main pop-in at load of 703 kN and <1% drop in load to arrest point. Note earlier pop-in.

The flaw in the EB-weld HAZ was now more easily discernible, Fig. 7.4, but no evidence of propagation along the surface could be seen. However, dimpling that extended from the crack ends to the cladding (Fig. 7.4) indicated the presence of a subsurface flaw. The flaw area was examined with dye penetrant (Fig. 7.5), but no surface crack other than that in the EB-weld HAZ could be detected. In Fig. 7.5, the two parallel lines normal to the flaw were added to mark the start of the cladding.

After heat-tinting the plate, it was reinstalled in the test machine and reloaded again at the same constant stroke rate and at room temperature. A second pop-in event occurred at a load of 890 kN, with an arrest occurring after a 17% load drop (Fig. 7.6). From the dimple on the top surface of the cladding, it was apparent that the second event flaw had run beneath the entire width of the cladding to the edge of the plate. A second heat-tint was performed, and the plate was reloaded at −25°C until it broke in two halves at 689 kN.

The fracture surface of plate CP-16 is shown in Fig. 7.7. The HAZ has arrested the flaw in both first and second events. Figure 7.8 shows a close-up of the EB flaw and its arrested shape at the end of the first event, in which it tunneled slightly below the HAZ without penetrating

M&C PHOTO YP5202

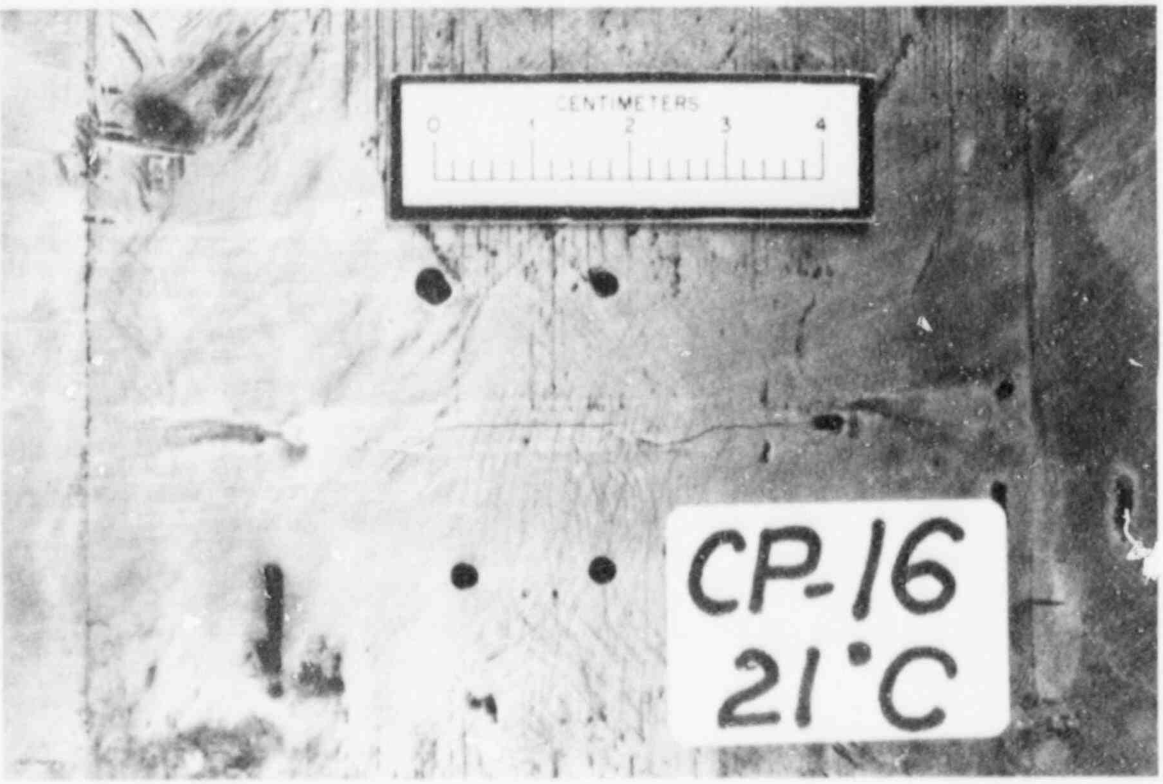

Fig. 7.4. Flaw in EB-weld HAZ after the first event. No evidence of propagation along the surface can be seen. Note dimpling that extends from crack ends to cladding.

the HAZ. A very thin layer on the plate surface covered the portion of the flaw that ran in the base metal, which explains why the dye penetrant examination mentioned previously did not reveal any significant extension beyond the preexisting flaw in the HAZ of the EB weld. During the second event, the flaw propagated across the full width of the plate within the central portion of the plate thickness (Fig. 7.7). However, substantial unbroken bands, ~10 and 16 mm thick, which remained across the top and bottom surfaces of the plate, respectively, kept the plate from failing catastrophically. Both bands ran across the full width of the plate except for the segment in base metal on its tensile side in between the side strips of cladding. This confirmed the previous observation that the dimple on the clad surface of the plate indicates tunnelling of the flaw beneath the cladding. Such indications of tunnelling have been observed several times before in the previous tests.[1]

Unclad plate CP-22, also tested at room temperature, ruptured at a load of 689 kN, within 1% of the load triggering pop-in of clad plate CP-16, except in this case no arrest occurred and the plate broke in two halves. A general view of the fracture surface is shown in Fig. 7.9, and a close-up of the EB flaw is presented in Fig. 7.10. The differing

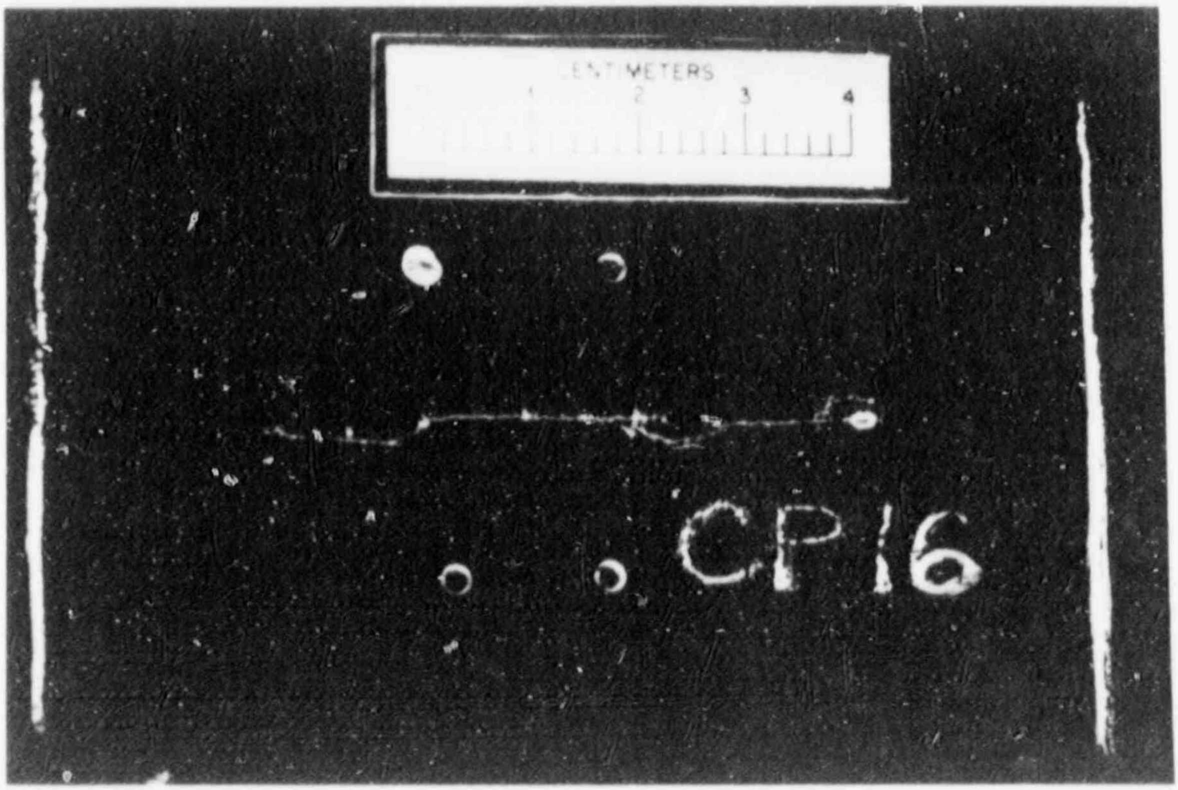

M&C PHOTO YP5201

Fig. 7.5. Dye penetrant indication of flaw in plate CP-16 after first event. This is the same area as shown in Fig 7.4, but no surface crack other than that in EB-weld HAZ could be detected. Two parallel lines normal to flaw were added to mark the start of cladding.

"textures" of the fracture surface seem to indicate that the crack front first propagates below the surface, leaving an unbroken ligament. This ligament then cleaves when the stresses become sufficiently high, thus reestablishing a through-crack configuration. The crack front propagates again below the surface, and the process repeats.

The profiles of the EB flaw as well as that of the flaw at the end of the first event in plate CP-16 are shown in Fig. 7.11. The initial EB flaw in plate CP-22 is presented in Fig. 7.12. These profiles will be used in the finite-element analysis of the tests.

7.1.5 Discussion of results

The loads at various events are shown in Table 7.1. There is little difference between the results from the two recent tests and the earlier six tests. For comparison, the test results on the previous six plates have been included in Table 7.2. Note that the pop-in load for plate CP-16 is within 5% of the target load (chosen on the basis of the yield

ORNL-DWG 88-7423

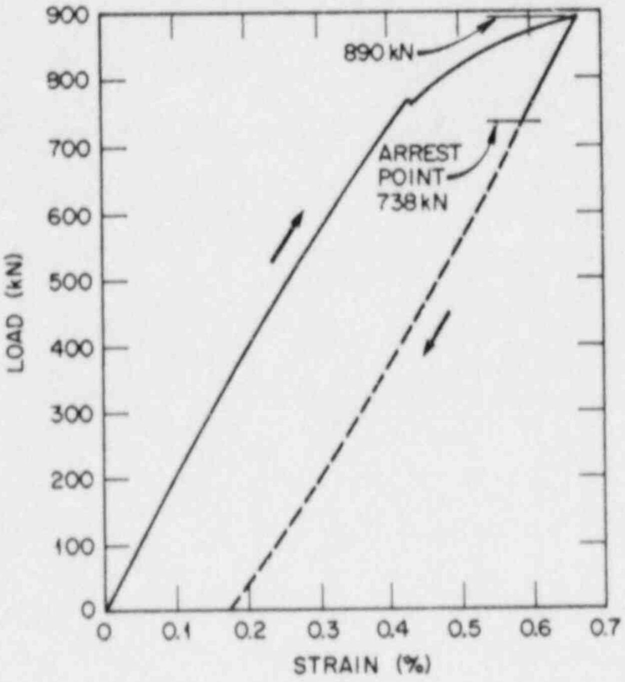

Fig. 7.6. X-Y chart of load vs strain gage XE-1 of second event showing pop-in at load of 890 kN, with an arrest occurring after a 17% load drop.

M&C PHOTO YP5228

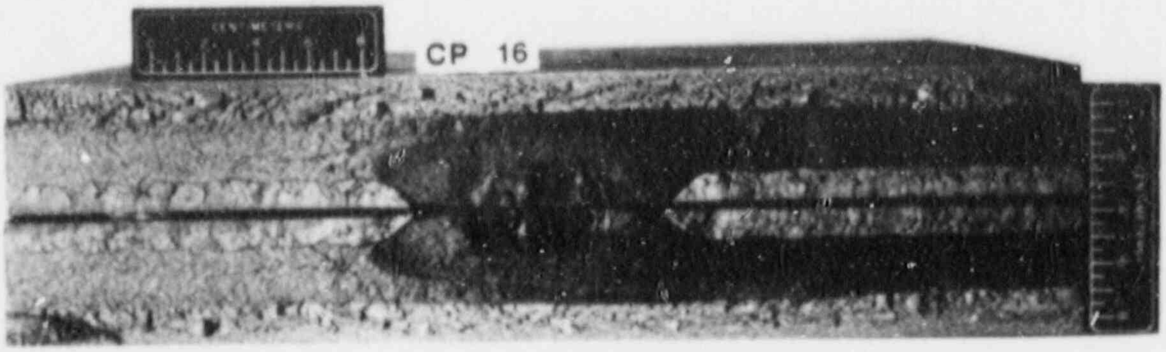

Fig. 7.7. Fracture surface of plate CP-16. During the second event, flaw propagated along central portion of the plate thickness, with intact ligaments ~10 and 16 mm thick along the top and bottom surfaces of the plate, respectively.

M&C PHOTO YP5227

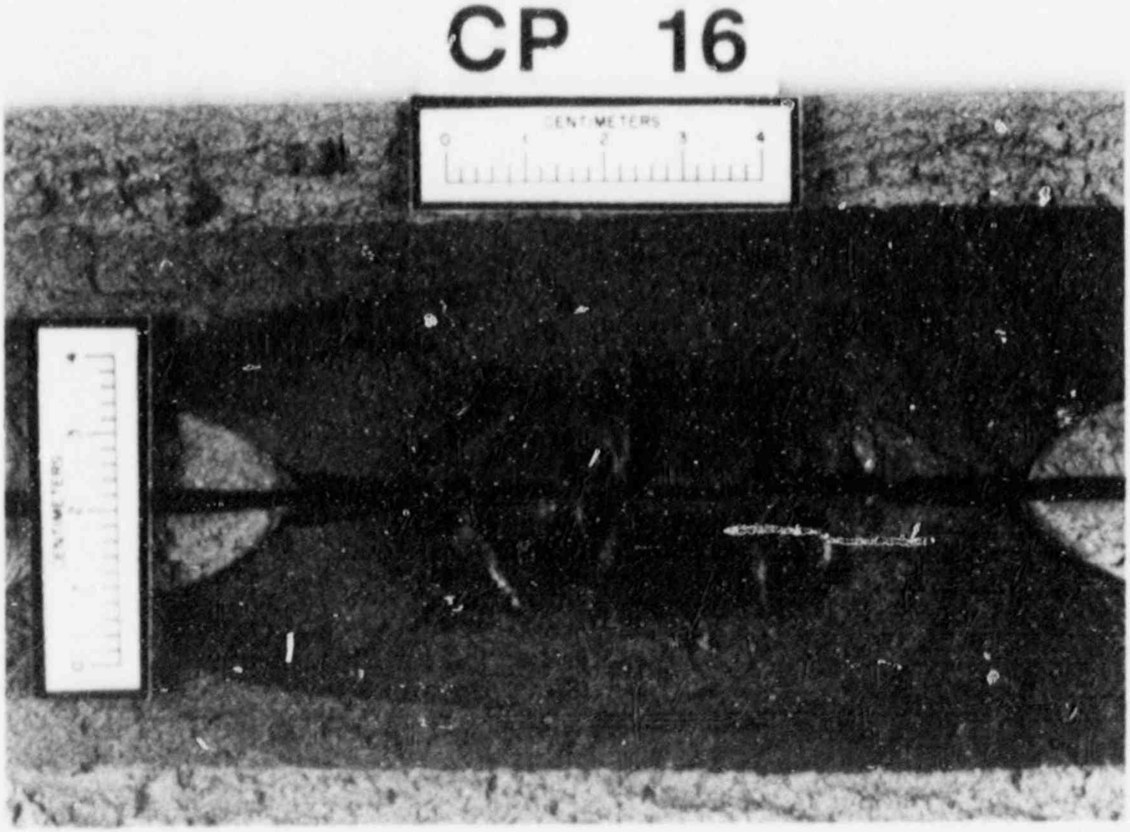

Fig. 7.8. Close-up of the EB flaw and its arrested shape in plate CP-16 at end of the first event.

M&C PHOTO YP5204

Fig. 7.9. General view of the fracture surface of plate CP-22.

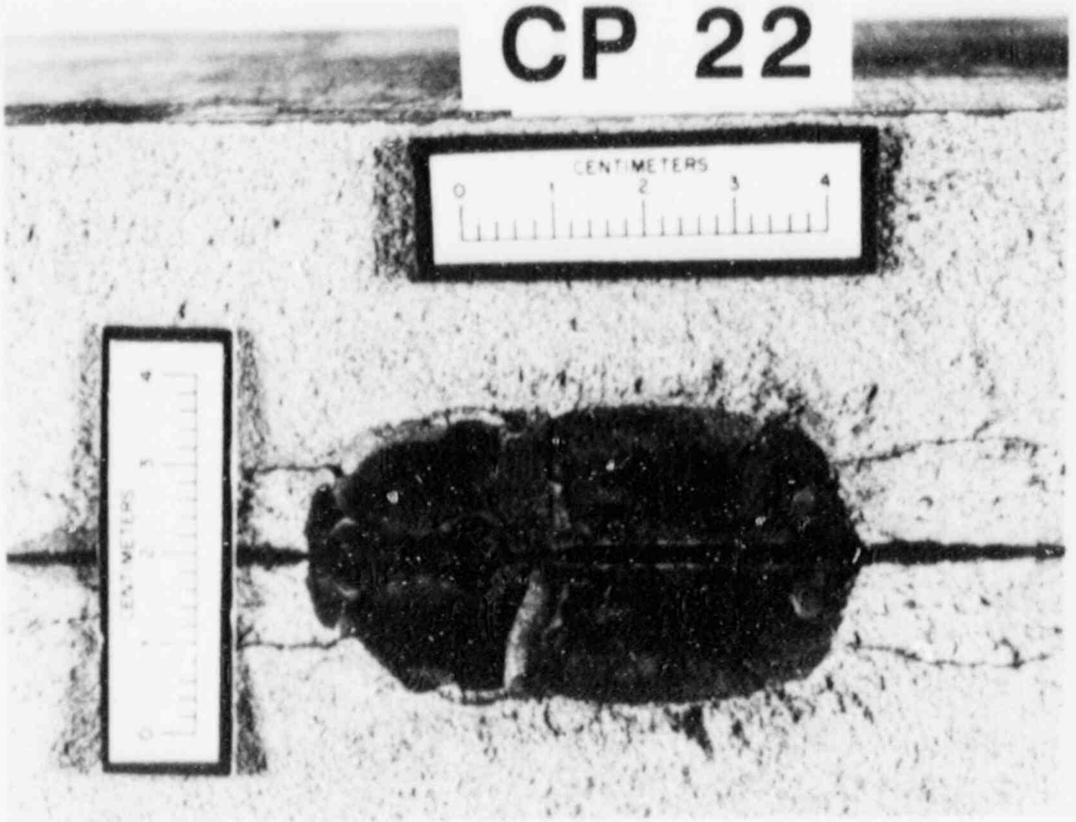
M&C PHOTO YP5203

Fig. 7.10. Close-up of EB flaw in plate CP-22.

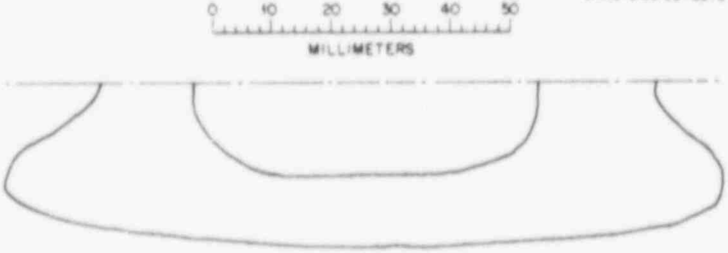
ORNL-DWG 88-8212

Fig. 7.11. Profiles of EB and arrested flaws at end of first event in plate CP-16.

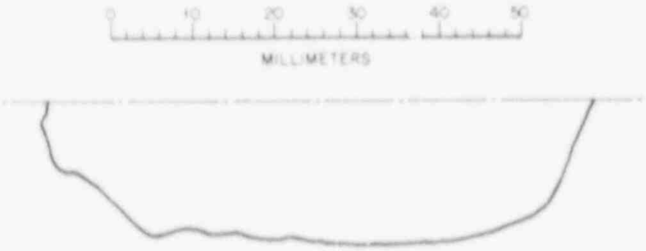
ORNL-DWG 88-8213

Fig. 7.12. Initial EB flaw in plate CP-22.

Table 7.1. Summary of initiation and arrest loads for plates CP-16 and -22

Plate	Condition	Test temperature (°C)	Load (kN)	
			Pop-in	Arrest
CP-16	Clad	21	703	694
		21	890	738
		−25	698	Rupture
CP-22	Unclad	21	689	Rupture

Table 7.2. Target surface strains and corresponding loads for the six plates tested

Plate	Condition	Test temperature[a] (°C)	Load (kN)		Target surface strain (%)
			Pop-in	Arrest[b]	
CP-15	Clad	RT	676	654	0.31
		−25	759	709	
		−100	600	R	
CP-17	Clad	RT	890	823	0.45
	Several pop-ins occurred before rupture	−25	756/725	R	
CP-19	Clad	RT	987	689	0.65
		−50	703	R	
CP-21	Unclad	RT	676	R	0.27
CP-18	Clad	−25	823	649	0.39
		−25	698	R	
CP-20	Clad	−25	868	R	0.41

[a] RT = room temperature, ~25°C.

[b] R = plate ruptured in two pieces.

on surface of base metal) for the "arrest" test on plate CP-15. The arrested crack shapes also are very similar.

Some of the data recorded by the static DAS during one scan just before crack initiation and the one just after are shown in Table 7.3. The strains in the base metal, gages XE-5 to XE-8, are slightly above the yield strain before crack initiation and drop to slightly below yield afterwards. Note that the large strain increase in gage XE-9, which is directly in the path and near the base/clad interface reflects the fact that the crack has propagated and arrested in its vicinity. The strain increase in gages XE-10, -11, and -12 are less than those in XE-9, reflecting their greater distance from the tip of the arrest flaw. The strains shown will be used with the finite-element calculations of the initiation and arrest events to analyze the test.

Table 7.3. Data recorded by the static DAS during one scan just before crack initiation and the one just after

Signal	Just before initiation	Just after arrest
Load	708 kN	703 kN
Stroke	9.2 mm	9.4 mm
COD gage	0.58 mm	0.81 mm
XE-1	4055 microstrain	4240 microstrain
XE-2	3554 microstrain	3746 microstrain
XE-3	4020 microstrain	4202 microstrain
XE-4	3805 microstrain	3970 microstrain
XE-5	2940 microstrain	2715 microstrain
XE-6	3059 microstrain	2759 microstrain
XE-7	2987 microstrain	2769 microstrain
XE-8	3094 microstrain	2802 microstrain
XE-9	4268 microstrain	5404 microstrain
XE-10	3710 microstrain	4391 microstrain
XE-11	3775 microstrain	4029 microstrain
XE-12	3634 microstrain	3809 microstrain

Figures 7.13 and 7.14 show data recorded by the dynamic DAS; the former are the strain gages on the right of the flaw, while the latter are on the left (see also Fig. 7.1). Time zero refers to the time the trigger gage broke because of the large strain caused by the underlying crack. Some of these figures were available immediately after the main pop-in and were invaluable in aiding the interpretation of the load drop as being a significant propagation event and not a pop-in of the EB weld. As mentioned previously, the 1600-με increase in gage XD-3 led to the decision of discontinuing the test and heat-tinting the flaw surface.

It may be observed from the response of gage XD-1 that the strain peaked while the crack passed in its vicinity and then dropped about

ORNL-DWG 88-4365 ETD

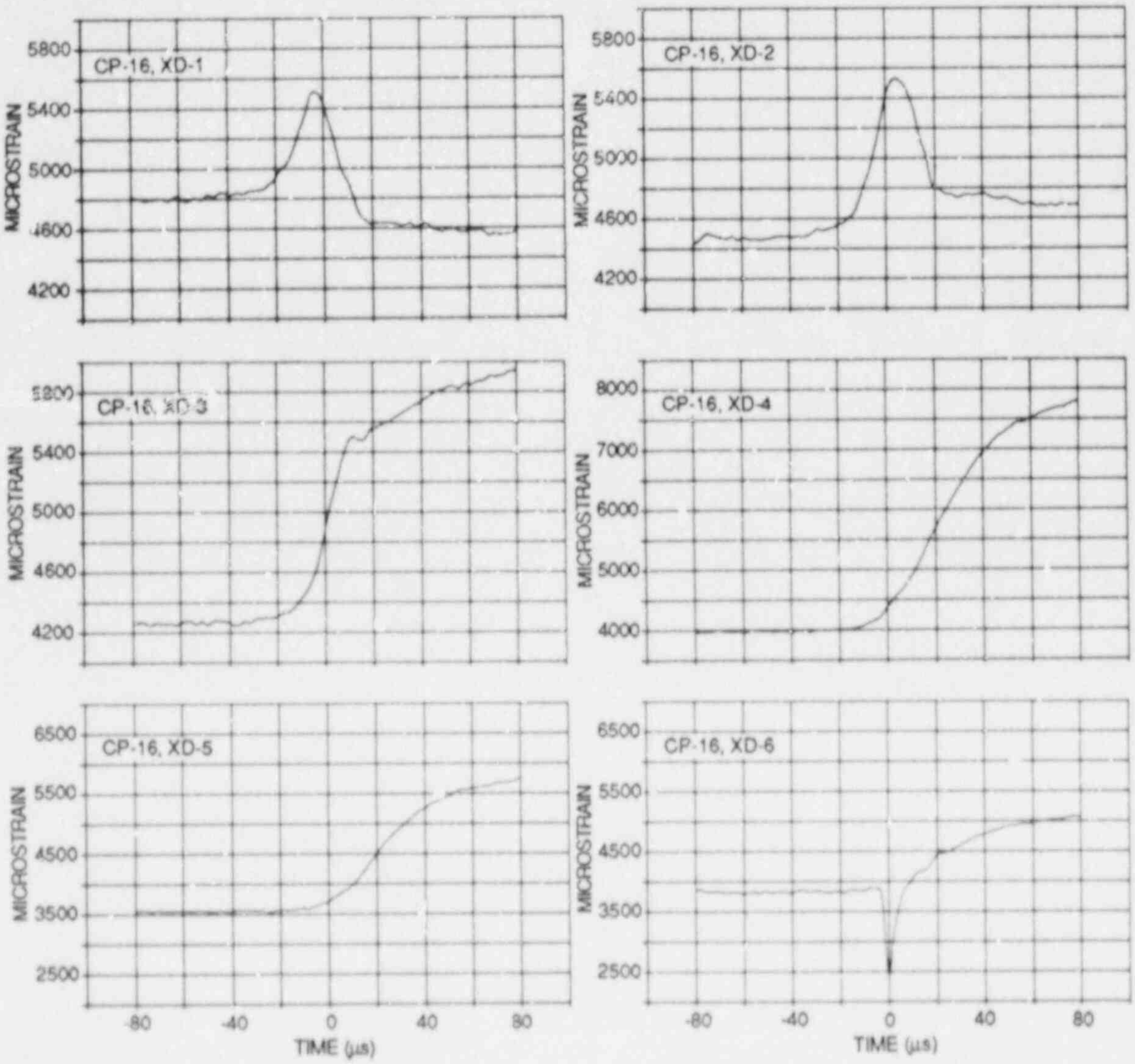

Fig. 7.13. Data recorded by dynamic DAS from gages on "right hand" of flaw during first event (plate CP-16).

ORNL-DWG 88-4366 ETD

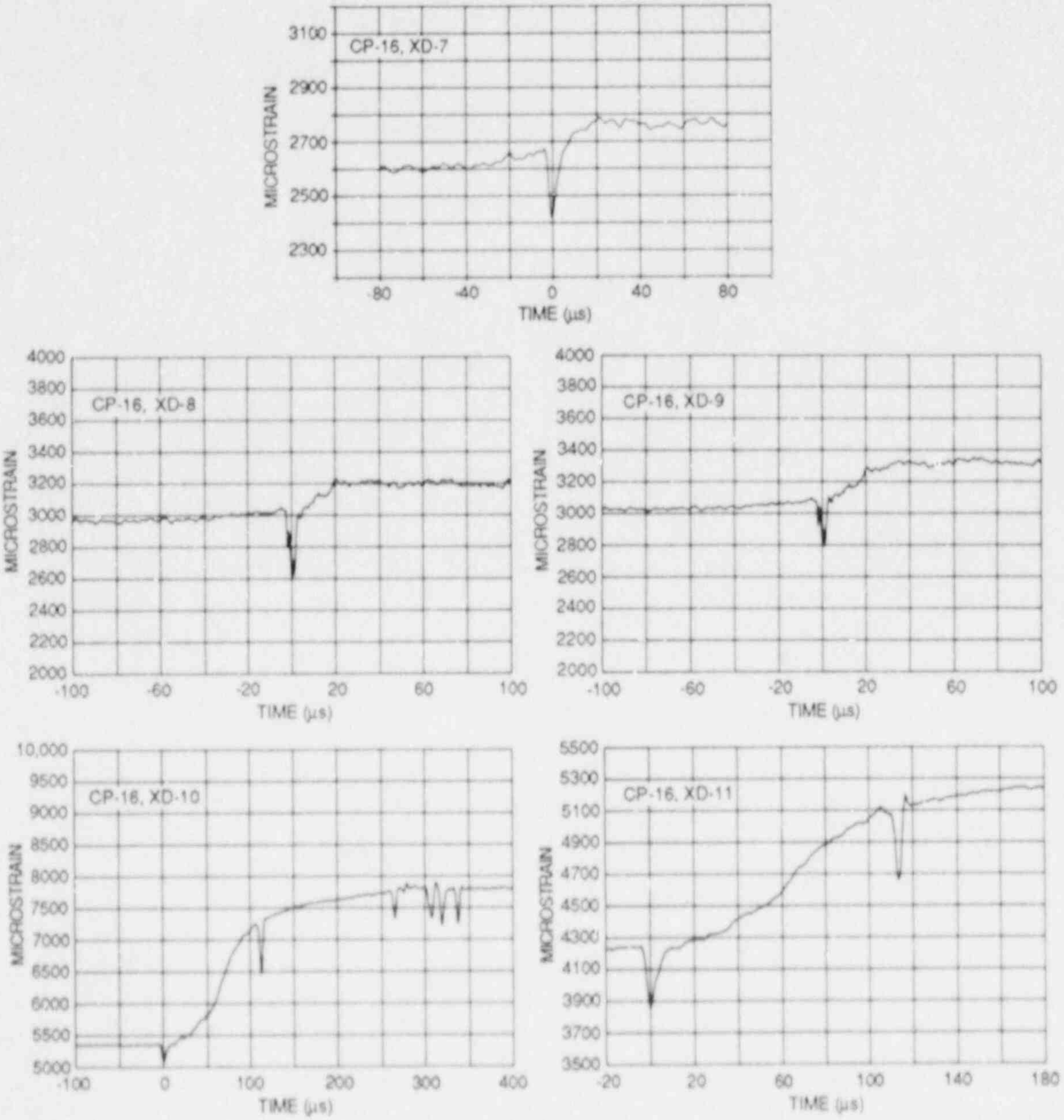

Fig. 7.14. Data recorded by dynamic DAS from gages on "left hand" of flaw during first event (plate CP-16).

200 $\mu\varepsilon$, indicating a relief of the surface strains. The behavior of gage XD-2 is similar, but the strains were slightly higher than their level before pop-in because the crack arrested in its vicinity. This elevation of strains after arrest is more apparent in gages XD-3 to XD-6. The strain gages on the other side of the flaw have all registered an increase in strain during the event. The cause of the dip in strain at time zero is not known but may be an electric transient precipitated by the triggering system.

The velocity of two events as registered by peaks of gages XD-1 and XD-2 was estimated to be about 3150 m/s. Such high crack-propagation velocities are improbable. It is more likely that these gages are registering the transverse wave precipitated by the first event. The transverse wave velocity v_t in isotropic materials is given by (values in parentheses are average values for steel):

$$v_t = \sqrt{G/d} ,$$

where G is shear modulus (79,200 MPa) and d is density (7850 kg/m^3). Thus, for steel v_t is about 3180 m/s.

Preliminary conclusions from tests on the two plates are still the same as those from the earlier six tests. The combined toughness of the cladding and HAZ seemed to have contributed significantly to the load-bearing capacity of the plates by arresting flaws at loads and temperatures that have ruptured unclad plates. This was observed in the present two tests as well as in plates CP-15 and -21 tested previously.[1]

Moreover, the residual load-bearing capacity of flawed plates, as measured by the critical loads in initiation experiments with fairly large flaws, was generally greater than that required to break the unclad plate.

The tests indicate a propensity of propagating flaws to tunnel, even without the aid of the tough surface layer composed of cladding/HAZ, as has occurred in the base metal portion of the clad plates and in the unclad plate. This potential for tunneling is related to the location of the maximum stress-intensity factor for short flaws, occurring somewhat below the surface, when the flaw is in a stress gradient.

The ductility of cladding appears to have been a necessary ingredient in increasing the load-bearing capacity of clad plates. However, it is not clear at this time whether cladding alone, without benefit of the tough HAZ that played a pronounced role in arresting propagating flaws, would have also elevated the load-bearing capacity. In case of radiation-embrittled reactor pressure vessels, the HAZ will most likely undergo toughness degradation similar to that of base metal and would therefore not play such a prominent role in arresting propagating flaws.

7.2 Flaw Characterization Studies of Clad LWR Vessel Material

K. V. Cook R. A. Cunningham, Jr.
R. W. McClung

7.2.1 Introduction

Nondestructive testing (NDT) tasks on segments of the Hope Creek Unit 2 boiling-water reactor (BWR) and the Pilgrim Unit 2 pressurized-water reactor (PWR) were completed. A revised topical report was published in February 1988.[5] The results indicate that the flaw density predictions being used for probabilistic risk analysis may be nonconservative for the small flaws. A paper[6] has been accepted for publication in *Nuclear Engineering and Design*.

An oral presentation was made at the Fifteenth Water Reactor Safety Information Meeting (October 27, 1987) entitled "Detection and Characterization of Flaws in Segments of Light-Water Reactor Pressure Vessels." A summary paper of the same title[7] was published in the transactions of this meeting. In addition, a full paper was submitted for the proceedings of this meeting (to be published in the spring of 1988).

The experimental studies and technical work performed during this period are summarized in the following subsections of this report. Further details are available in the referenced material.

7.2.2 Nondestructive examination of sections from Pilgrim Unit 2 pressure vessel

As reported previously,[8] block P-1 had calibration reflectors machined to provide for underclad calibration. Details about the calibration and the ultrasonic inspection were also provided in the last semiannual report. Block P-2 was the only one in which an indication of note was located. This indication was reported as being at a depth near the clad-to-vessel interface and at a position where the two 8.9-cm-wide (3.5-in.) strip clad sections join.

Confirmation studies on the underclad indication detected in block P-2. An approximate 15 × 15 × 23 cm (6 × 6 × 9 in.) section was flame cut from block P-2 that contained the one underclad indication of note detected in one of the three Pilgrim vessel segments. We confirmed the presence of this indication by manual ultrasonic examination after the cut section was delivered to the NDT laboratory. As was the case before removal of the indication-bearing section, the amplitude maximum from the discontinuity was about one-half that from the calibration reflector [which was ~11 mm (0.440 in.) below the surface]. Also, a stop-stare positioning of the search unit was required to obtain this maximum amplitude response. Further, a smoothing of the cladding (i.e., the raised surface contour where the strip clad sections join) reduced the maximum amplitude by about one-half again. Thus, if the surface contour had been ground flat before our inspection, we may not have detected this small reflector with the dual-angle 70° longitudinal search unit employed. This unit has an effective focal depth of about 9 mm (0.375 in.).

Subsequent sectioning at a midlength position (i.e., length along the clad strip joint as determined ultrasonically) of the underclad indication revealed the presence of a discontinuity (shown in Fig. 7.15). It is located ~4.1 mm (0.16 in.) below the clad surface and is about 1.1-mm (0.045-in.) maximum width. Also, note that the discontinuity was formed where the two strip clad sections join. Although not very evident from Fig. 7.15, an inclusionlike material is present at intervals along the length. An analysis was performed on this material with a technique that uses the SEM. Figure 7.16 shows the results of the SEM analysis with the inclusionlike material having relatively high values of silicon and calcium.

The overall length of this discontinuity in block P-2 was determined by grinding. The estimated length, established by the grinding was slightly less than 1.3 cm (0.5 in.). This was roughly three times longer than estimated with the dual-angle 70° search unit.

M&C PHOTO Y210099A

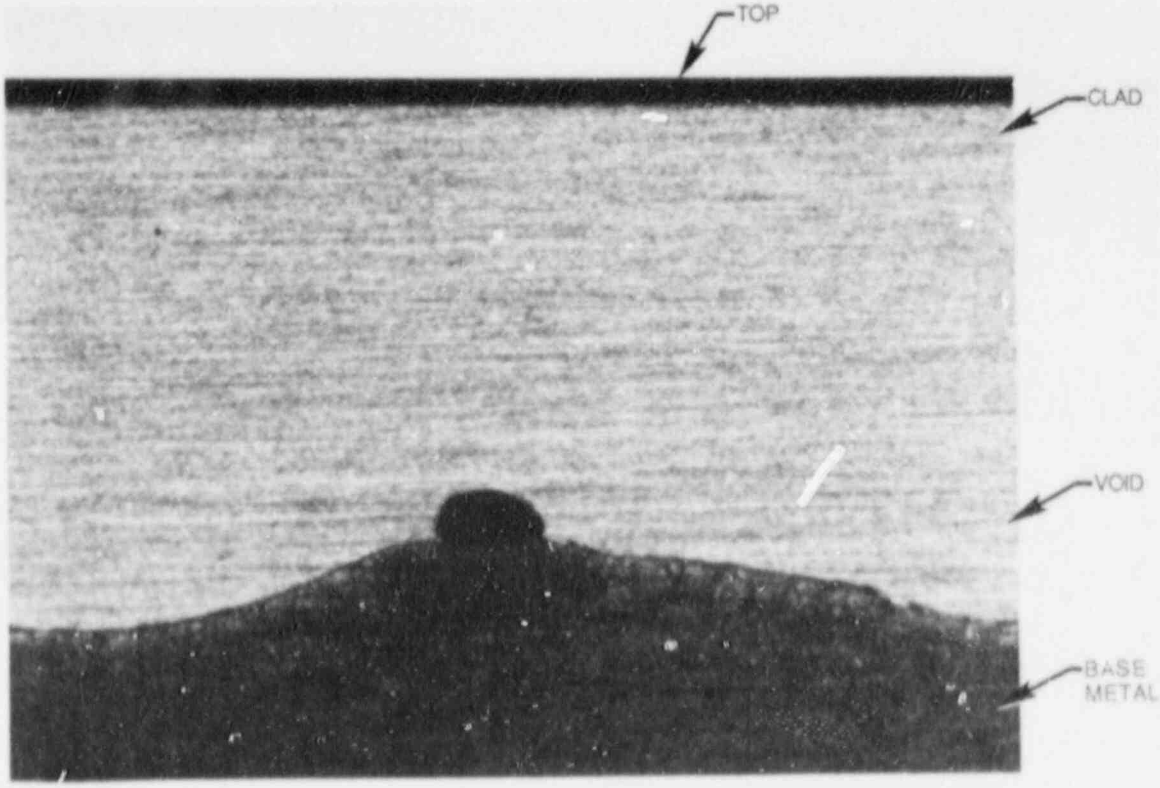

Fig. 7.15. Discontinuity, detected by ultrasonic inspection for underclad flaws, located in Pilgrim block P-2.

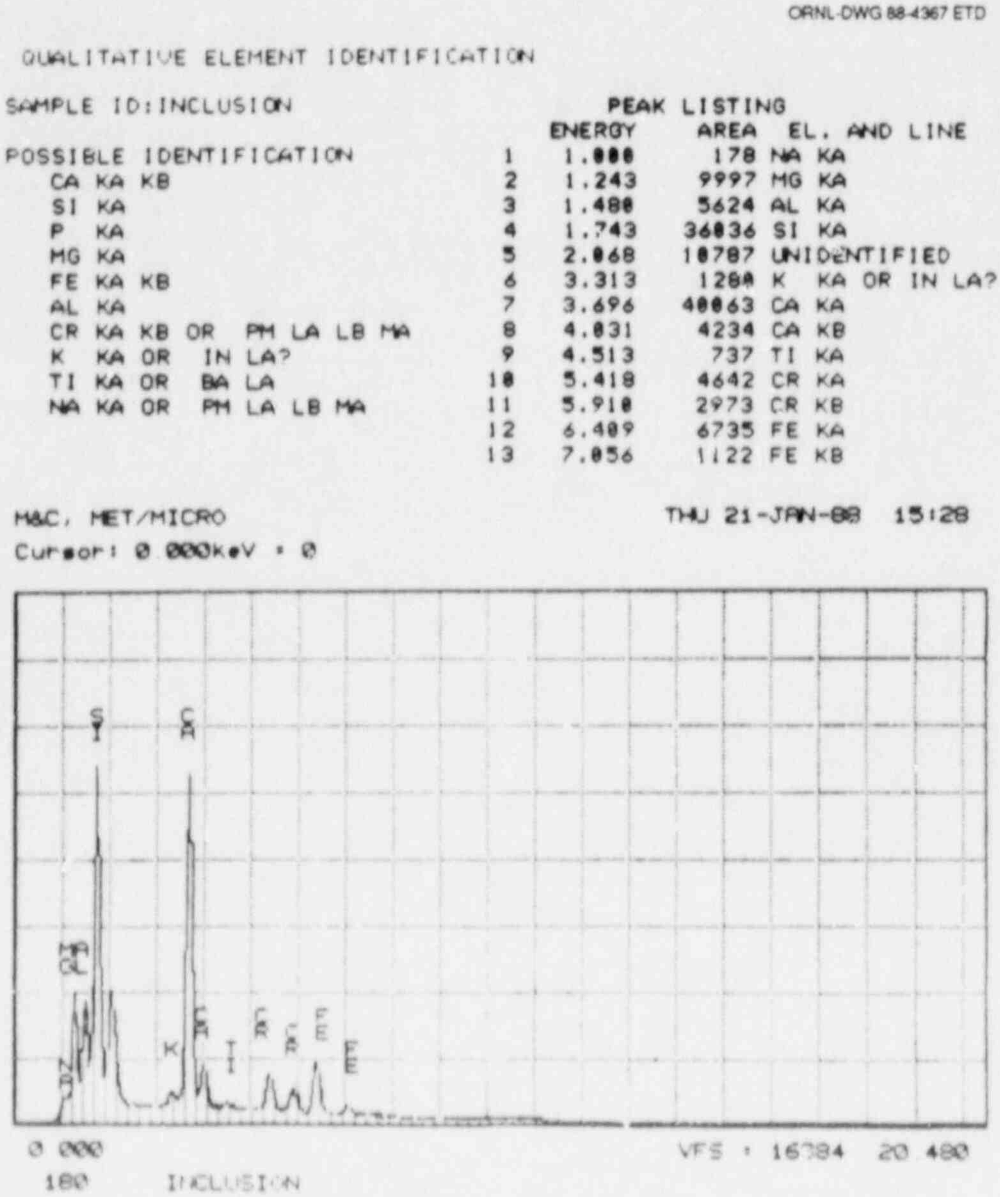

ORNL-DWG 88-4367 ETD

```
QUALITATIVE ELEMENT IDENTIFICATION

SAMPLE ID:INCLUSION                              PEAK LISTING
                                          ENERGY     AREA  EL. AND LINE
POSSIBLE IDENTIFICATION              1    1.000       178 NA KA
   CA KA KB                          2    1.243      9997 MG KA
   SI KA                             3    1.480      5624 AL KA
   P  KA                             4    1.743     36036 SI KA
   MG KA                             5    2.068     10787 UNIDENTIFIED
   FE KA KB                          6    3.313      1280 K  KA OR IN LA?
   AL KA                             7    3.696     40063 CA KA
   CR KA KB OR  PM LA LB MA          8    4.031      4234 CA KB
   K  KA OR  IN LA?                  9    4.513       737 TI KA
   TI KA OR  BA LA                  10    5.418      4642 CR KA
   NA KA OR  PM LA LB MA            11    5.910      2973 CR KB
                                    12    6.409      6735 FE KA
                                    13    7.056      1122 FE KB

M&C, MET/MICRO                               THU 21-JAN-88   15:28
Cursor: 0.000keV = 0
```

Fig. 7.16. SEM analysis of material inside discontinuity (underclad) located by ultrasonics in Pilgrim block P-2.

7.2.3 Results and conclusions

The destructive examination completed on the one indication of note detected in Pilgrim block P-2 confirmed the presence of a small discontinuity located under the clad at a clad-to-clad joint. This partially filled void contained relatively high values of silicon and calcium. It was located ~4.1 mm (0.16 in.) below the clad surface and had dimensions of 1.1-mm (0.045-in.) maximum width and length of about 1.3 cm (0.5 in.).

The detection of this discontinuity was dependent on the surface condition of the cladding. The misalignment of the dual-angle, dualelement search unit (caused by the raised surface contour where two clad strips join) increased the amplitude of the detected signal by 3 to 4 dB.

References

1. S. K. Iskander et al., "Crack Arrest Behavior in Clad Plates," pp. 222–42 in *Heavy-Section Steel Technology Program Semiann. Prog. Rep. April–September 1987*, NUREG/CR-4219, Vol. 4, No. 2 (ORNL/TM-9593/V4&N2), Martin Marietta Energy Systems, Inc., Oak Ridge Natl. Lab.

2. S. K. Iskander et al., "Crack Arrest Behavior in Clad Plates," pp. 169–73 in *Heavy-Section Steel Technology Program Semiann. Prog. Rep. October 1986–March 1987*, NUREG/CR-4219, Vol. 4, No. 1 (ORNL/TM-9593/V4&N1), Martin Marietta Energy Systems, Inc., Oak Ridge Natl. Lab.

3. W. R. Corwin, "Seventh HSST Irradiation Series: Stainless Steel Cladding," pp. 70–87 in *Heavy-Section Steel Technology Program Semiann. Prog. Rep. October 1985–March 1986*, NUREG/CR-4219, Vol. 3, No. 1 (ORNL/TM-9593/V3&N1), Martin Marietta Energy Systems, Inc., Oak Ridge Natl. Lab.

4. S. K. Iskander et al., "Posttest Material Characterization of Clad Plate Materials," pp. 115–26 in *Heavy-Section Steel Technology Program Semiann. Prog. Rep. April–September 1987*, NUREG/CR-4219, Vol. 4, No. 2 (ORNL/TM-9593/V4&N2), Martin Marietta Energy Systems, Inc., Oak Ridge Natl. Lab.

5. K. V. Cook and R. W. McClung, *Flaw Density Examinations of a Clad Boiling Water Reactor Pressure Vessel Segment*, NUREG/CR-4860, Rev. 1 (ORNL/TM-10364/R1), Martin Marietta Energy Systems, Inc., Oak Ridge Natl. Lab., February 1988.

6. K. V. Cook and R. W. McClung, "Flaw Density Examinations of a Clad Boiling Water Reactor Pressure Vessel Segment," submitted for publication in *Nuclear Engineering and Design*.

7. K. V. Cook and R. W. McClung, "Detection and Characterization of Flaws in Segments of Light-Water Reactor Pressure Vessels," pp. 11-13, -14 in *Transactions of the Fifteenth Water Reactor Safety Information Meeting*, NUREG/CP-0090, U.S. Nuclear Regulatory Commission, Washington, D.C., October 1987.

8. K. V. Cook and R. W. McClung, "Flaw Characterization Studies of Clad BWR Vessel Material," pp. 242–48 in *Heavy-Section Steel Technology Program Semiann. Prog. Rep. April–September 1987*, NUREG/CR-4219, Vol. 4, No. 2 (ORNL/TM-9593/V4&N2), Martin Marietta Energy Systems, Inc., Oak Ridge Natl. Lab.

8. INTERMEDIATE VESSEL TESTS AND ANALYSIS

No activity in the intermediate vessel tests and analysis task during this period.

9. THERMAL-SHOCK TECHNOLOGY

No activity in the thermal-shock technology task during this period.

10. PRESSURIZED-THERMAL-SHOCK TECHNOLOGY

10.1 Preliminary Investigations of Future Pressurized-Thermal-Shock Experiments

R. H. Bryan

During the current reporting period, a topical report on the second pressurized-thermal-shock experiment (PTSE-2) was published[1], and an investigation of the feasibility and utility of two additional experiments was initiated. Experiments with a flaw in stainless steel cladding were considered during the inception of the pressurized-thermal-shock experimental task in 1981. Such an experiment, tentatively designated PTSE-3, would demonstrate the influence of cladding on the evolution of the flaw geometry during crack propagation. The other type of pressurized-thermal-shock experiment under consideration, PTSE-4, would demonstrate fracture processes of special importance in low-upper-shelf seam welds.

The cladding problem has recently been the object of two HSST program studies: isothermal clad-plate tests initiated in 1981 (Refs. 2–4) and an experimental determination of the properties of irradiated cladding.[5] These two studies and the PTSE-3 investigation have a common objective: to identify potential beneficial or harmful effects of cladding on the evolution of short, through-the-cladding flaws. The clad-plate tests were simple experiments designed to determine whether cladding could inhibit the lengthwise propagation of short cracks. These tests showed that, in some instances, fast-running cracks were arrested without the rupture of cladding or the cracks tunneled beneath the cladding.[3,4]

The current PTSE-3 investigation deals with whether cladding effects would be significant under relevant overcooling accident conditions, particularly conditions attainable in HSST pressurized-thermal-shock experiments. Two computer programs are being prepared to evaluate potential cladding effects. The OCA/USA program, used extensively in the planning and interpretation of PTSE-1 and PTSE-2, is being modified to facilitate the analysis of flaws with changing lengths. The SHAPE program is being developed to model the mechanistic changes in flaw shape in a clad vessel under combined pressure and thermal loads. The SHAPE program also models clad plates under bending loads and will be used to evaluate the results of the clad-plate tests. PTSE-3 analyses will take into account the properties of irradiated cladding. The results of the Seventh HSST Irradiation Series,[5] which are becoming available, will be an important source of information on irradiated cladding.

The other pressurized-thermal-shock experiment being evaluated, PTSE-4, would require the fabrication of a new insert for the vessel used in PTSE-2 (Ref. 1). The focus of PTSE-4 is to confirm the fracture behavior of a weld deposit with properties representative of irradiated high-copper welds that exhibit low tearing resistance (i.e., low upper shelf). Three HSST irradiation series (2, 3, and 8) deal with this type of material. In PTSE-2, the flaw was in a low-upper-shelf insert, but the material was not representative because it was not a weld and its tensile strength was very low. There is no evidence that the fracture behavior of a weld would have differed from the behavior of the insert in

PTSE-2 if the tensile strengths had been the same. However, since the fracture phenomena observed in PTSE-2 were complex, it would be preferable to use a weld deposit to represent welds in reactor pressure vessels. Accordingly, preliminary work has been initiated to develop specifications for the procurement of a low-upper-shelf weld insert for PTSE-4, as discussed in Sect. 10.2 of this chapter.

In PTSE-2, the final fracture event (cleavage followed by immediate unstable tearing) caused the vessel wall to rupture. This rupture was not unexpected because the final tearing instability had been deliberately planned. However, it is not known whether the instability was solely a consequence of low tearing resistance or principally a consequence of low strength. Furthermore, the stable tearing observed in PTSE-1 (Ref. 6) and PTSE-2 (Ref. 1) is inconsistent with analysis based on J-resistance curve data. An experiment with low-tearing-resistance material having normal strength, as proposed for PTSE-4, is crucial for resolving these issues.

10.2 PTSE-4 Fabrication Feasibility

G. C. Robinson

An informal inquiry was sent to several prospective vendors to establish the technical feasibility of obtaining a high-transition-temperature, low-upper-shelf Charpy submerged-arc weldment test material (1) for incorporation into the ITV-8 intermediate test vessel (recently used as the test vessel in the PTSE-2 experiment) and (2) for use in wide-plate specimens and associated characterization weldments. A preliminary draft procurement specification was the basis for technical evaluation by the various vendors. Table 10.1, taken from the specification, gives the strength and toughness properties now considered necessary to perform a viable PTSE-4 experiment.

One of the prospective vendors believed that the objectives could be achieved by using the standard weld wire ordinarily used in A 533 grade B class 1 weldments and by using Linde 80 flux (or perhaps Linde 60) with increased oxygen potential to achieve the required low-upper-shelf properties. The high-transition-temperature requirements would be achieved by increasing the silicon content to ~1%.

Two other vendors preferred 2 1/4 Cr-1 Mo weld wire, American Welding Society classification EB-3. Tentative flux choices included Linde 60 and Linde 80, and possibly Linde 100. In addition, if possible, a "dirty" wire chemistry, consisting of high phosphorus, sulfur, and high silicon, would be chosen. However, the speculation was that improvements in manufacturing practice would probably preclude such choices because of material availability.

The preliminary procurement specification depends on a two-phase operati[illegible] vendo[illegible] the first phase, the vendor would explore a matrix [illegible] (e[illegible] [illegible]e of flux, postweld heat treatment temperature, a[illegible] [illegible]ment cooling rate) to establish parameters that wo[illegible] [illegible]d objectives. With the first phase successfully comp[illegible] [illegible] phase would consist of confirmatory tests and the incor[illegible] [illegible]referred weld into the vessel, the six wide-plate specimens, [illegible] characterization weldments. The specification

Table 10.1. Impact and tensile property requirements

Property	Desired value	Acceptable values	
		Minimum	Maximum
Yield strength,[a] MPa (psi)	600 (87,000)	520 (75,000)	760 (110,000)
Charpy-V upper-shelf energy,[b] J (ft·lb)	61 (45)	54 (40)	68 (50)
Temperature at which Charpy-V energy is at the midpoint of the transition[c] (TT), °C (°F)	100 (212)	90 (194)	140 (284)
Lowest temperature at which 100% shear first occurs, °C (°F)	TT+30 (TT+54)		TT+75 (TT+135)

[a] To be measured at room temperature.

[b] The upper shelf energy shall be determined by averaging the impact energy of the specimens exhibiting 100% shear.

[c] Midpoint energy shall be determined by adding 6.8 J (5 ft·lb) to the average of the values obtained with 100% shear and dividing the result by 2.

also depends on the finished thickness dimension of the wide-plate specimens being 15.24 cm (6 in.). The latter requirement may result in a severely prolonged schedule because of the unavailability of heavy plate. Only one of the potential vendors could identify a source of plate (exclusive to that vendor) immediately available for the proposed work. Estimates of 28 weeks or longer were presumed by vendors to represent a typical delivery period of a contract for plate placed with Lukens Steel Company, the only U.S. supplier. According to unconfirmed reports, plate may also be available from Korean sources.

During the course of these inquiries, a source of old, relatively dirty, 2 1/4 Cr-1 Mo weld wire was located in sufficient quantity to do the proposed work. A purchase order has been prepared for the procurement of this material to permit an "in-house" feasibility evaluation of the parameters required to achieve the properties given in Table 10.1.

10.3 Stress-Intensity Factor Influence Coefficients for Surface Flaws in Pressure Vessels

J. Keeney-Walker D. A. Steinart
J. S. Parrott

In the fracture-mechanics analysis of reactor pressure vessels, stress-intensity-factor influence coefficients are used with superposition techniques to reduce the cost of calculating stress-intensity factors. Using the ORMGEN/ADINA/ORVIRT analysis system, influence coefficients were generated for several axially oriented, semielliptical, outer-surface flaws in a cylinder for use in the OCA/USA computer program to analyze PTSE-3 and -4. The ratio of surface length (2b) to wall thickness (w) of the flaws ranged from 0.4 to 6.776, and the ratio of depth (a) to wall thickness ratio ranged from 0.1 to 0.9. The ratios are summarized below.

2b/w	0.4	0.6	1.0	1.4	1.8	3.0	4.0	5.0	6.0	6.776
a/w	0.1	0.2	0.3	0.5	0.7	0.9				

ORMGEN automatically generates a complete 3-D finite-element model of the cracked structure with typically 5299 nodes and 1134 elements. Figures 10.1 and 10.2 illustrate a typical mesh design for a semielliptical surface flaw, with $a/w = 0.3$ and $b/w = 0.3$. The influence coefficients generated for this flaw are shown in Fig. 10.3. The stress-intensity factors obtained by superposition for a thermal transient loading condition (see Fig. 10.4) were compared with values calculated by a direct finite-element method and closely agreed, as shown in Fig. 10.5. Figure 10.6 indicates that this similarity continues with the addition of pressure loading.

The OCAUSA and OCAPLOT computer programs have been modified in preparation for PTSE-3 and -4. The modifications allow the codes to calculate and plot stress-intensity factors for multiple crack lengths and crack depths (the previous versions only allowed for a fixed crack length). The OCAUSA code creates a data set that is read by a computer program designed to calculate crack shapes. Several key subroutines in the OCAUSA program were rewritten using Fortran 77 conventions. Other modifications to the codes included restructuring the output tables, reformulating the 3-D K_{Inom} calculations, and separating 2-D and 3-D calculations. Both the OCAUSA and OCAPLOT codes are compiled and executed on the STC Vax 8600's at ORNL to allow for greater user interaction with the codes during execution.

10.4 Mesh Convergence Study for PTSE-3 and -4 Pretest

J. S. Parrott J. Keeney-Walker
D. A. Steinart

In the PTSE-3 and -4 pretest analysis, a mesh convergence study was conducted. This study consisted of determining the effect that mesh refinement had on the K_I distribution along the crack front for a crack 1/10 the cylinder thickness in depth and 1.4 times the cylinder thickness in length. The mesh generator used for the analysis was ORMGEN.

The mesh parameters are as follows. NZ is the number of elements along the circumference of the cylinder in addition to the two elements that the program automatically assigns. GRADZ is the mesh expansion factor in the circumferential direction (i.e., considering only the set of elements along the circumference the user defines, an element has an arc length that differs from the arc length of the neighboring element closest to the crack by a factor of GRADZ). NCRS is the number of elements along the crack front.

ORNL-DWG 88-4285 ETD

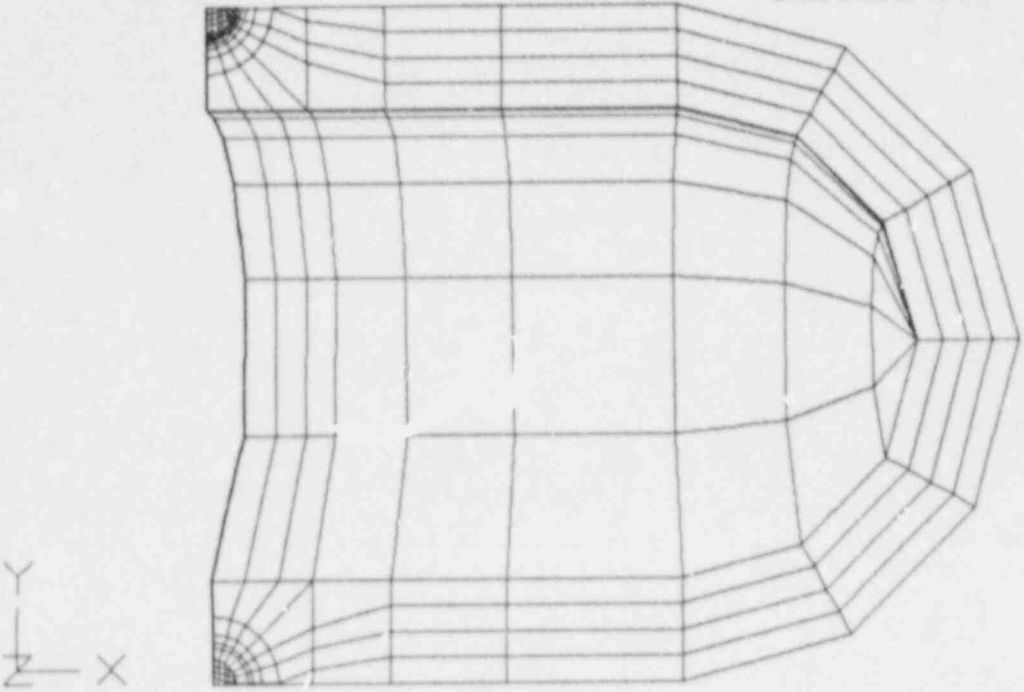

Fig. 10.1. Sample mesh of semielliptical surface flaw: a/w = 0.3, b/2 = 0.3, w = 147.6 mm.

ORNL-DWG 88-4286 ETD

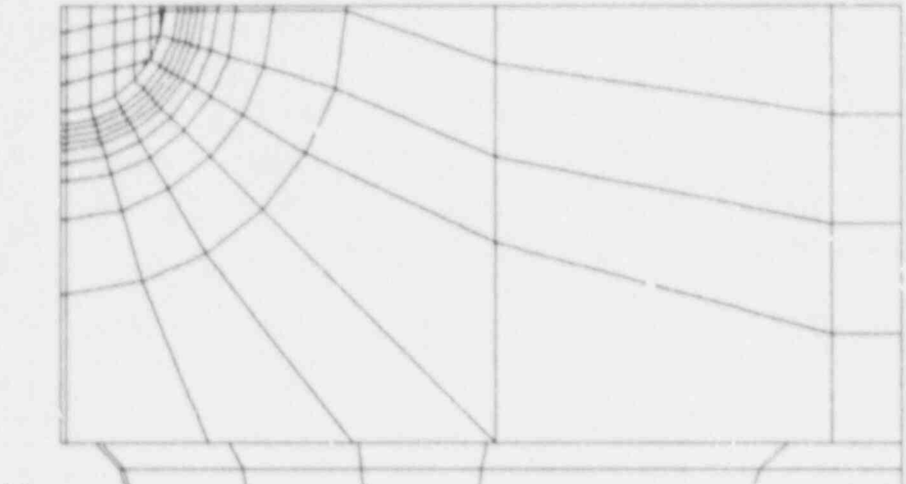

Fig. 10.2. Crack-plane closeup view of sample mesh.

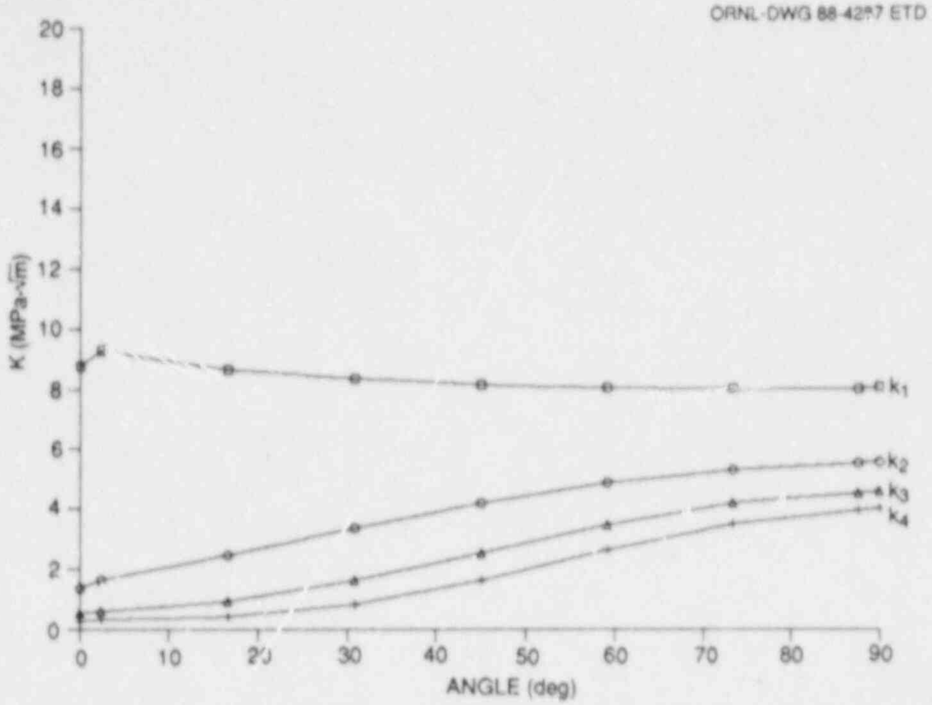

Fig. 10.3. Influence coefficients for semielliptical surface flaw: a/w = 0.3, b/w = 0.3, w = 147.6 mm.

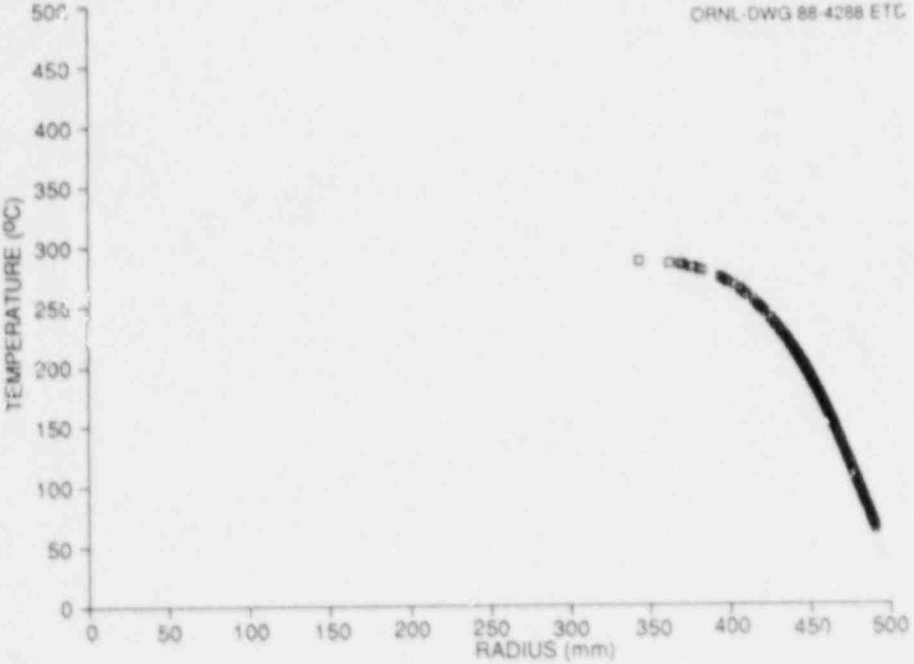

Fig. 10.4. Temperature profile used in direct finite-element analysis of model in Fig. 10.1.

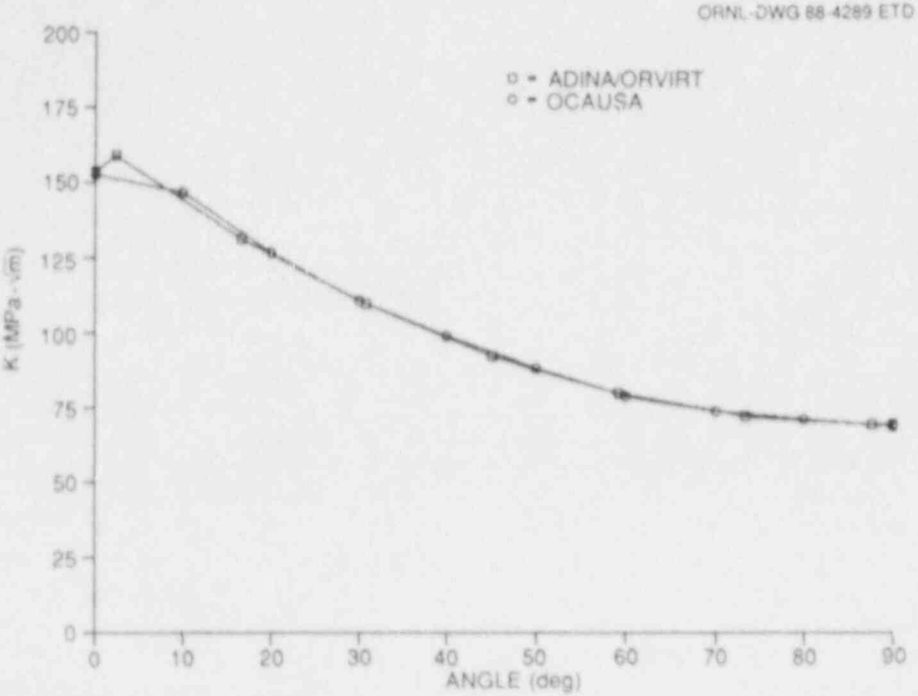

Fig. 10.5. Comparison of K_I values calculated by superposition and direct finite-element techniques for thermal loading.

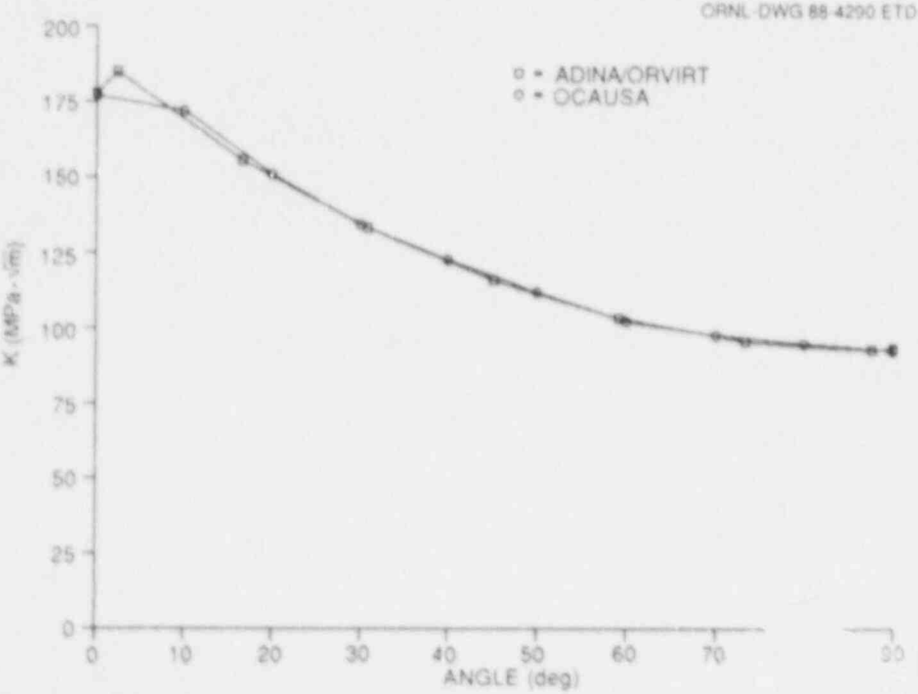

Fig. 10.6. Comparison of K_I values calculated by superposition and direct finite-element techniques for thermal and pressure loading.

The finite-element model used as the base for this study had the following mesh parameter values: NZ = 6, GRADZ = 1.5, and NCRS = 8. A complete view of the crack plane of this model is shown in Fig. 10.7. In Figs. 10.8 and 10.9, closeups of the crack are presented. A circumferential view of the model is shown in Fig. 10.10.

For the second model, all of the mesh parameter values were kept the same as those used for the base model except the value of NZ, which was increased from 6 to 8. This change is shown in Fig. 10.11, which is the circumferential view of the second model.

For the third model, NA and GRADZ were the only mesh parameters wich values that were changed from those used for the base model. The value of NZ was increased from 6 to 8, and the value of GRADZ was decreased from 1.5 to 1.1. These changes are shown in Fig. 10.12, which is the circumferential view of the third model.

For the fourth model, the only mesh parameter with a value that was changed from the one used in the base model was NCRS. The value of this parameter was increased from 8 to 10. In Figs. 10.13 and 10.14, closeups of the crack in the fourth model are presented to show this change.

After the development of the four models, the ADINA finite-element program was executed to calculate stress throughout the model. Note that the same crack-face loading was used for each execution. The ORVIRT finite-element program was then used to determine the K_I distribution influence coefficients along the crack front. Each model's K_I distributions, one for each load step, were superposed in Fig. 10.15. For the scale used in this plot, each mesh refinement gave results that were only negligibly different from the results given by the base mesh.

ORNL-DWG 88-4291 ETD

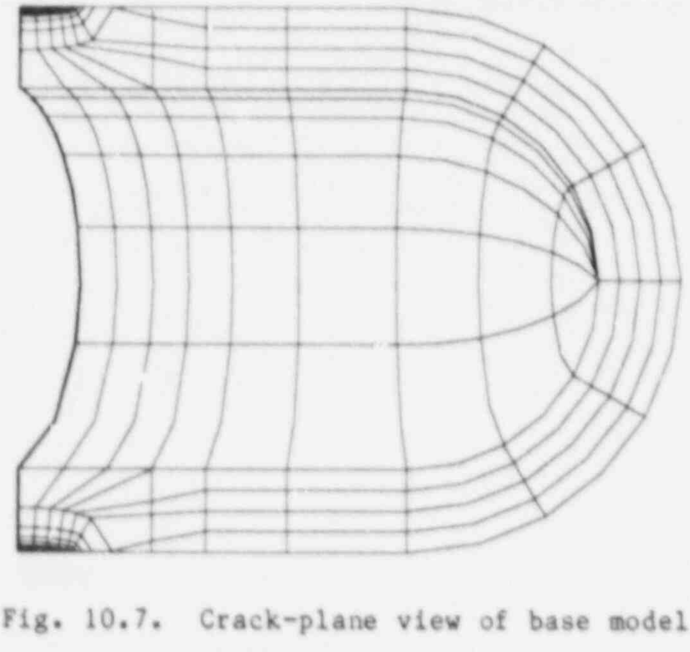

Fig. 10.7. Crack-plane view of base model.

ORNL-DWG 88-4292 ETD

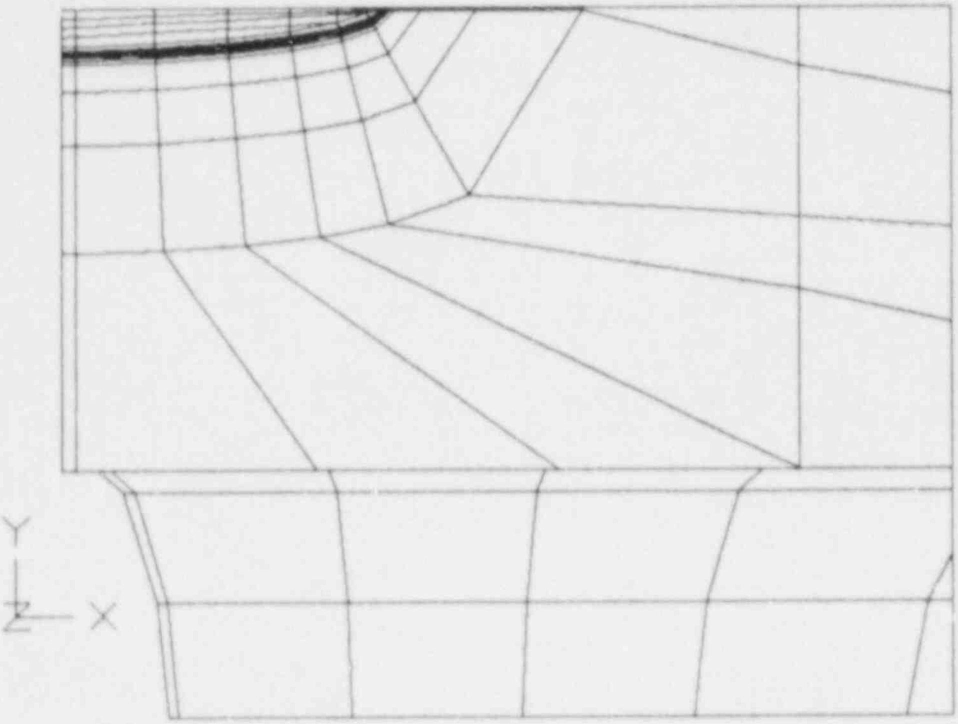

Fig. 10.8. Crack-plane closeup view of base model.

ORNL-DWG 88-4293 ETD

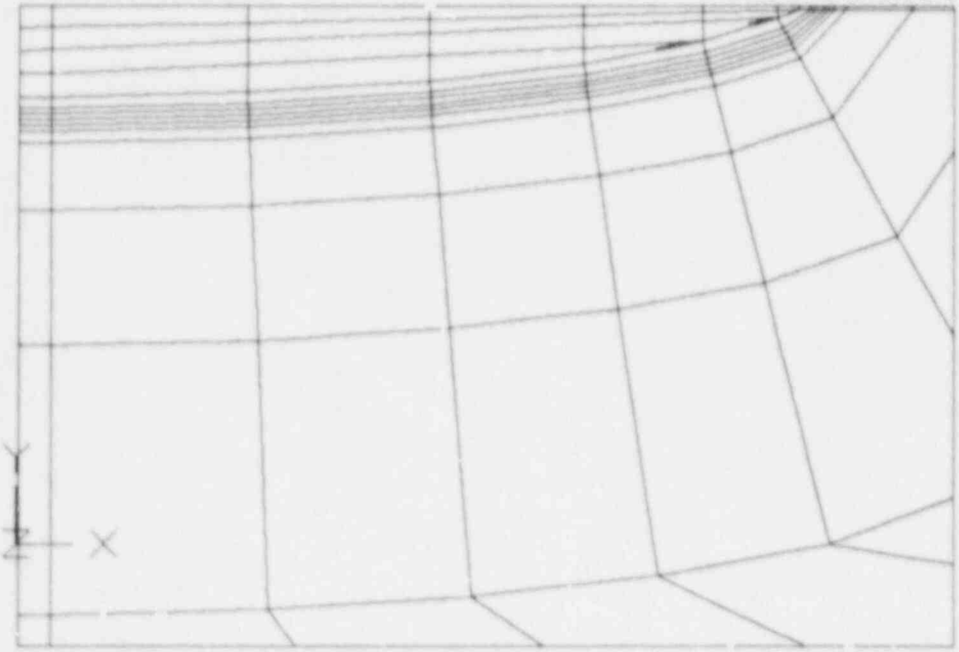

Fig. 10.9. Crack-plane closeup view of base model.

ORNL-DWG 88-4294 ETD

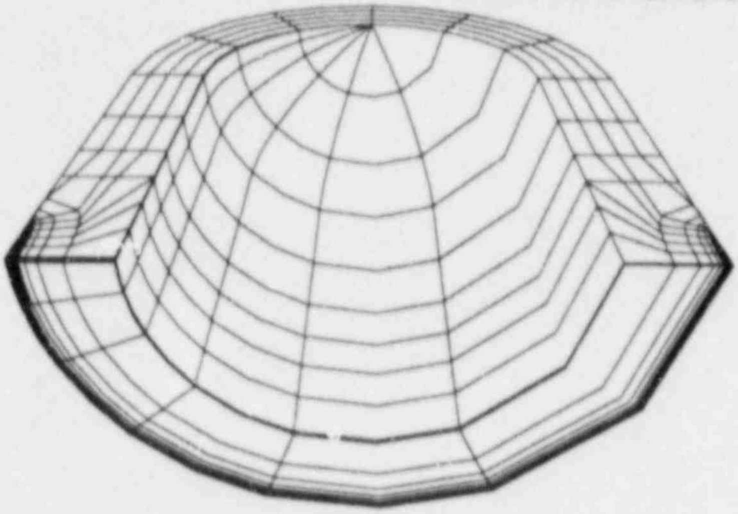

Fig. 10.10. Circumferential view of base model.

ORNL-DWG 88-4295 ETD

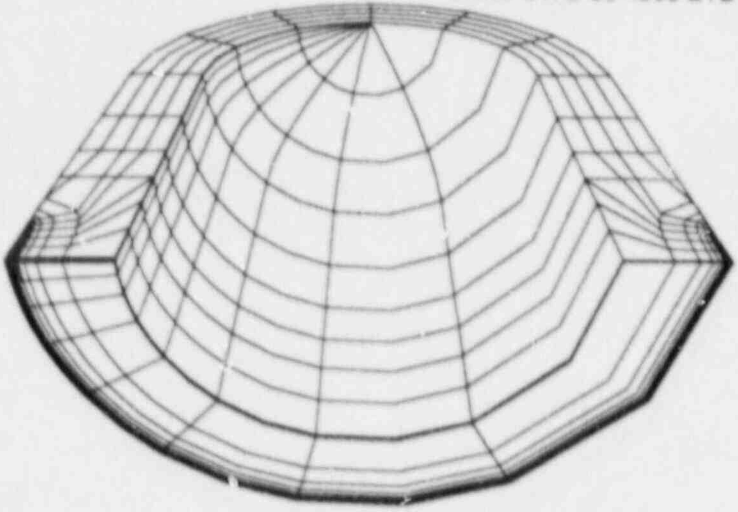

Fig. 10.11. Circumferential view of second model.

ORNL-DWG 88-4296 ETD

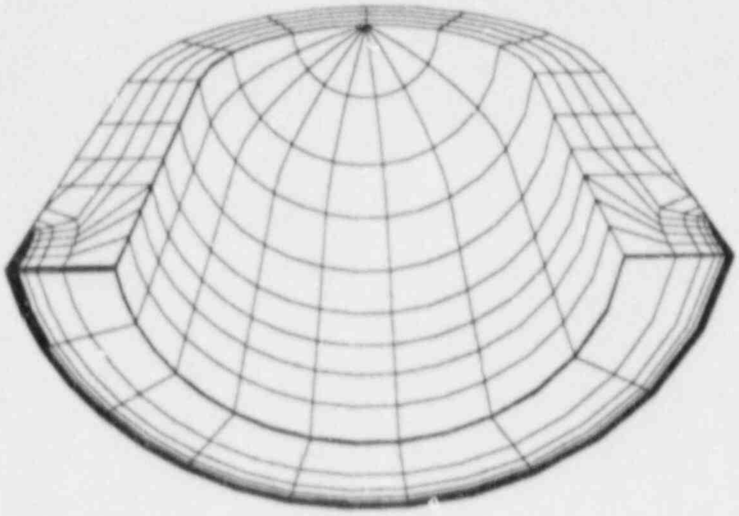

Fig. 10.12. Circumferential view of third model.

ORNL-DWG 88-4297 ETD

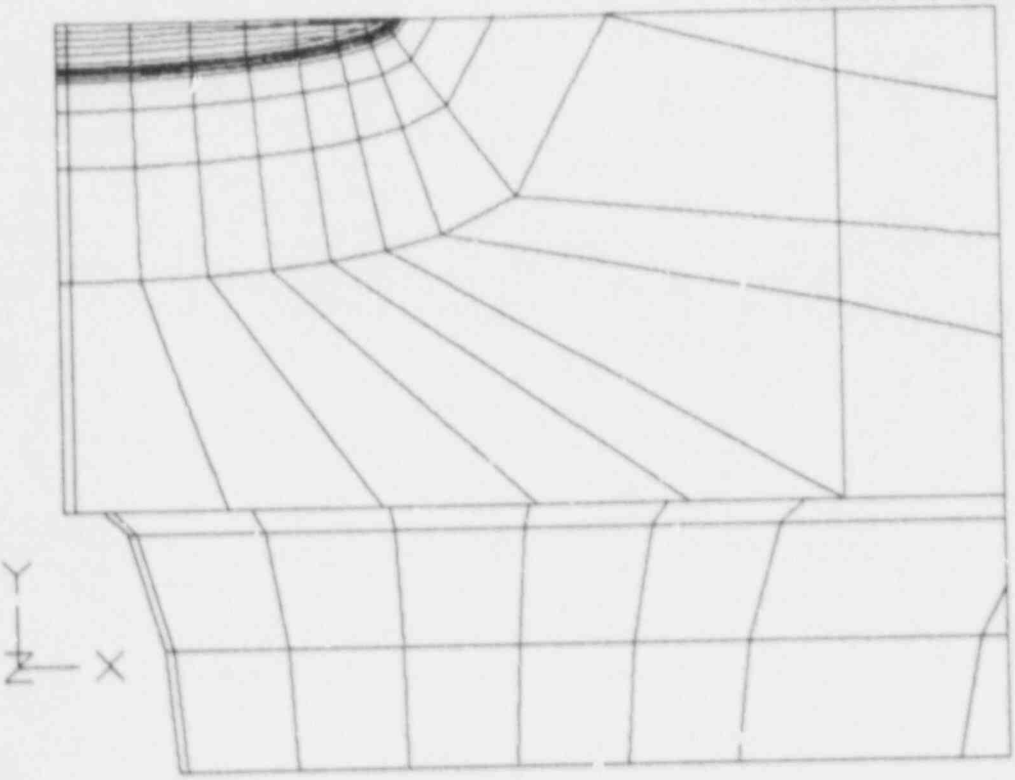

Fig. 10.13. Crack-plane closeup view of fourth model.

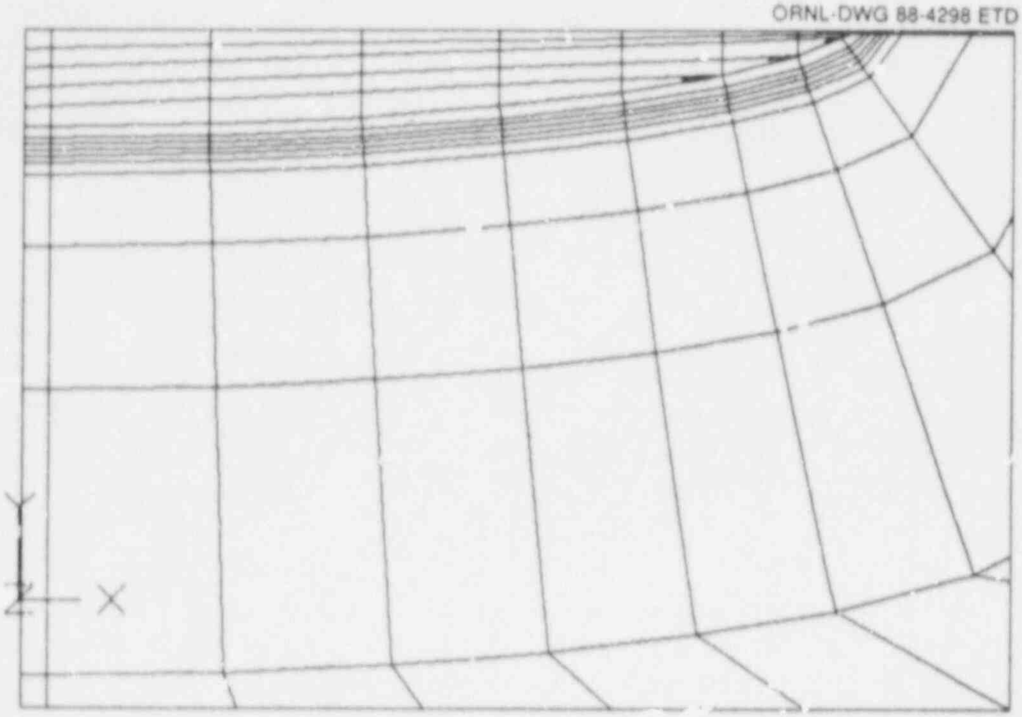

Fig. 10.14. Crack-plane closeup view of fourth model.

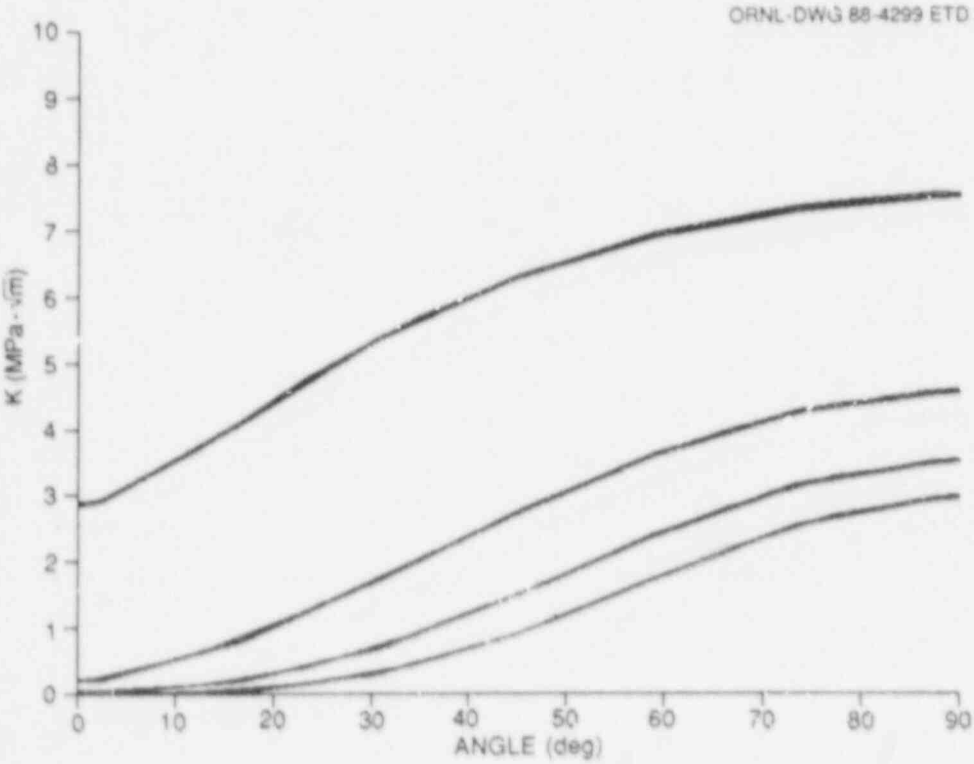

Fig. 10.15. K_I vs angle plot (superposition of four models).

References

1. R. H. Bryan et al., *Pressurized-Thermal-Shock Test of 6-in.-Thick Pressure Vessels. PTSE-2: Investigation of Low Tearing Resistance and Warm Prestressing*, NUREG/CR-4888 (ORNL-6377), Martin Marietta Energy Systems, Inc., Oak Ridge Natl. Lab., December 1987.

2. G. C. Robinson and J. G. Merkle, "Scoping Studies," pp. 118–23 in *Heavy-Section Steel Technology Program Quart. Prog. Rep. October–December 1981*, NUREG/CR-2141, Vol. 4 (ORNL/TM-8252), Union Carbide Corp. Nuclear Div., Oak Ridge Natl. Lab.

3. W. R. Corwin et al., *Effect of Stainless Steel Weld Overlay Cladding on the Structural Integrity of Flawed Steel Plates in Bending*, NUREG/CR-4015 (ORNL/TM-9390), Martin Marietta Energy Systems, Inc., Oak Ridge Natl. Lab., April 1985.

4. S. K. Iskander et al., "Crack-Arrest Behavior in Clad Plates," pp. 222–42 in *Heavy-Section Steel Technology Program Semiann. Prog. Rep. April–September 1987*, NUREG/CR-4219, Vol. 4, No. 2 (ORNL/TM-9593/V4&N2), Martin Marietta Energy Systems, Inc., Oak Ridge Natl. Lab.

5. F. M. Haggag et al., "Seventh HSST Irradiation Series," pp. 214–21 in *Heavy-Section Steel Technology Program Semiann. Prog. Rep. April–September 1987*, NUREG/CR-4219, Vol. 4, No. 2 (ORNL/TM-9593/V4&N2), Martin Marietta Energy Systems, Inc., Oak Ridge Natl. Lab.

6. R. H. Bryan et al., *Pressurized-Thermal-Shock Test of 6-in.-Thick Pressure Vessels. PTSE-1: Investigation of Warm Prestressing and Upper-Shelf Arrest*, NUREG/CR-4106 (ORNL-6135), Martin Marietta Energy Systems, Inc., Oak Ridge Natl. Lab., April 1985.

11. FLAW DENSITY STUDIES FOR PRESSURE-VESSEL-RESEARCH USERS' FACILITY

R. W. McClung R. A. Cunningham, Jr.
K. V. Cook

11.1 Nondestructive Testing Plans

A preliminary plan for the nondestructive evaluation of the Pressure-Vessel-Research User's Facility (PVRUF) vessel for flaw density was drafted near the beginning of this reporting period. The PVRUF vessel is located near the south end of Building K-702 at the Oak Ridge K-25 Plant. It has an outside diameter (beltline) of 4.5 m (15 ft), weighs over 3.5 MN (400 tons), and is lying on its side (horizontal orientation on supporting stands). The preliminary plan addressed complications for the nondestructive examination because of the satellite (field) inspection requirement and the vessel orientation. To meet the satellite inspection requirement, support services and facilities have been added to the site. Since the vessel will not be housed in an appropriate facility until funding is arranged, we concluded that manual ultrasonic scanning procedures must be used or special scanning systems must be purchased and used while the PVRUF is in the temporary location. Once the vessel is inside and in a normal vertical position, it will be possible to apply commercial or advanced automated in-service inspection (ISI) equipment. These inspection systems normally use a long vertical boom to center and locate tooling from the inner diameter of the vessel. The cantilever action of this boom for operation in the horizontal orientation would require costly revision to a very expensive system. Also, immersion testing is normally done with these systems, whereas the horizontal position of the PVRUF would dictate contact or squirter hardware, another expensive modification.

Our preliminary plan was discussed by personnel from the Nuclear Regulatory Commission (NRC), the Oak Ridge National Laboratory (ORNL), and Pacific Northwest Laboratory (PNL) at a meeting in Gaithersburg, Maryland, in October 1987. A consensus draft plan was submitted for consideration in March 1988. Background information for the Phase 1 studies, which has been taken from the introductory material of the current draft, follows.

> The acquisition of a full-scale commercial nuclear reactor pressure vessel by the Oak Ridge National Laboratory provides a unique facility for many studies of value to nuclear reactors. Application and development of nondestructive examination (NDE) methods is one of the technical disciplines of interest.
>
> The initial planned studies (Phase 1) are a continuation of earlier studies to carefully determine the presence of flaws in pressure vessel materials. The earlier work was carried out on large sections of pressure vessels from canceled BWR and PWR plants. The purpose of the earlier work and Phase 1 of this plan is to provide experimental flaw

characterization data from nuclear vessels for use in probabilistic risk assessments. This is accomplished by quantitatively establishing the density, location, orientation, and size of surface and volumetric flaws in segments of as many vessels of the greatest volume possible. The near-term flaw examinations on PVRUF are guided by recognition of the greater priority for flaws in cladding and subcladding regions but with recognition that volumetric flaws are also important. Of course, verified evaluation of detected discontinuities is necessary. Initial studies will be in the cylindrical portion of the vessel with manual techniques. It is felt that use of this technique will provide a valid examination without delays and costs for acquisition of scanners.

11.2 Temporary Facilities for PVRUF NDE Activities

As previously reported,[1] the PVRUF vessel was transported to Oak Ridge near the end of September 1987 and unloaded by a subcontractor using a modified J-skid support to position the vessel horizontally on timbers. Figure 11.1 is a view looking approximately northward showing the PVRUF vessel as positioned by the subcontractor in the foreground and the K-700 building complex in the background.

In order to implement the manual inspection activities described in Sect. 11.1, several modifications were made to render the interior of the vessel accessible and habitable. These modifications include access stairs, platform and double entry doors, movable interior scaffolding, exterior and interior lighting, air conditioning, electrical heating, water spray exterior cooling feature, and an array of 110- and 220-V electrical general service receptacles. Also provided is a nearby trailer to provide convenient office space.

Figure 11.2 shows some of the modifications that have been made to the PVRUF vessel, including access stairway, exterior platform, and double entry doors through the flange plywood cover originally installed by Combustion Engineering (CE) for long-term storage. Also shown are exterior lights, air conditioner housings, modified cover support brackets, and the modified seal arrangement of the cover/flange edge to prevent delamination of the plywood. Figure 11.3 is a view of the interior of the PVRUF vessel showing entry platforms, nozzle covers, and movable scaffolding. Figure 11.4 shows the position of the office trailer in relation to the PVRUF vessel.

11.3 Complementary Procurement Activities

11.3.1 Ultrasonic calibration blocks for PVRUF

As described in Sect. 11.1, the first activity planned for PVRUF is examining the vessel ultrasonically. In the originating utility/vendor purchase order for the vessel, seven calibration blocks for in-service ultrasonic testing were included. However, their use in PVRUF testing

K/PH 87-3497

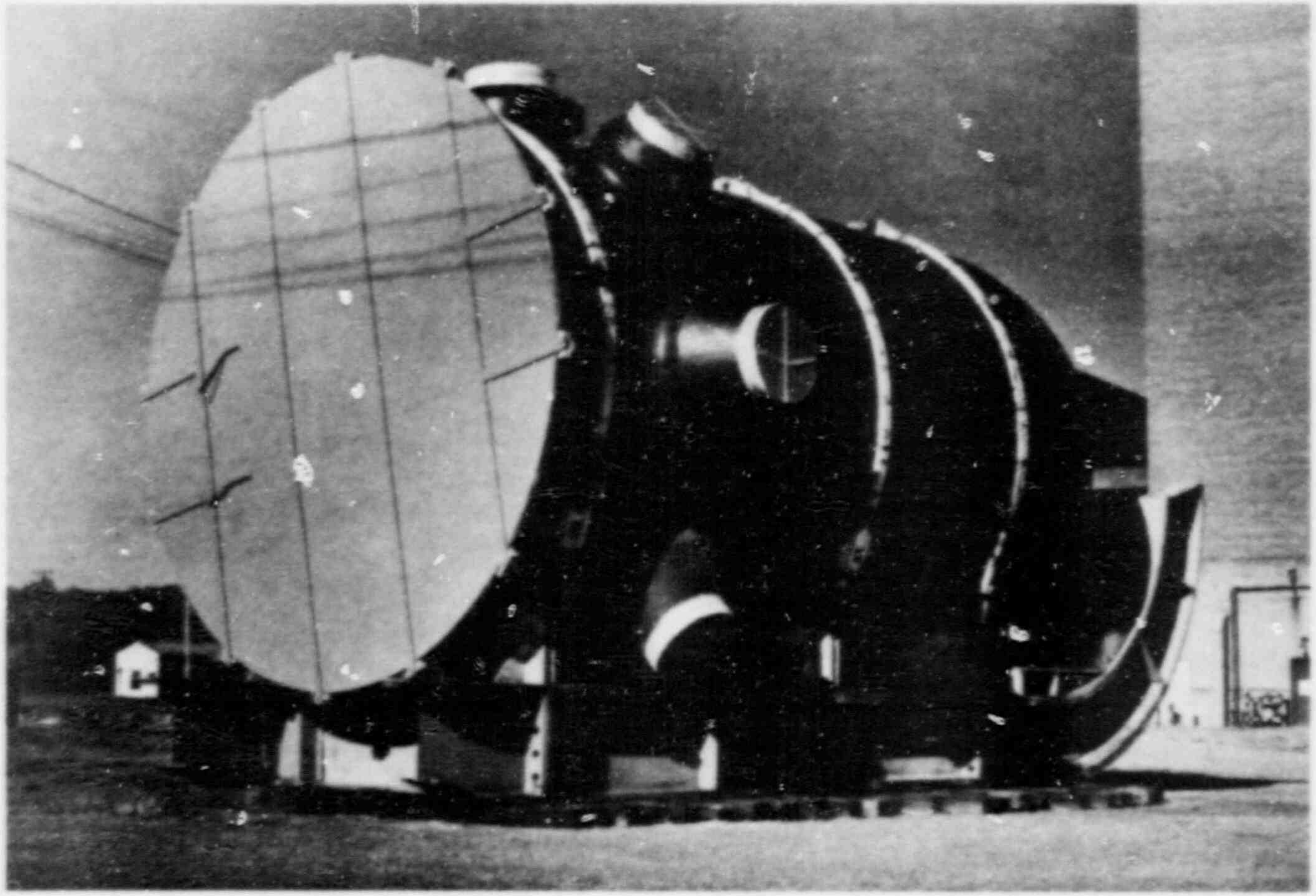

Fig. 11.1. View of PVRUF vessel as positioned by subcontractor in the vicinity of the K-700 building complex.

ORNL PHOTO 8307-88

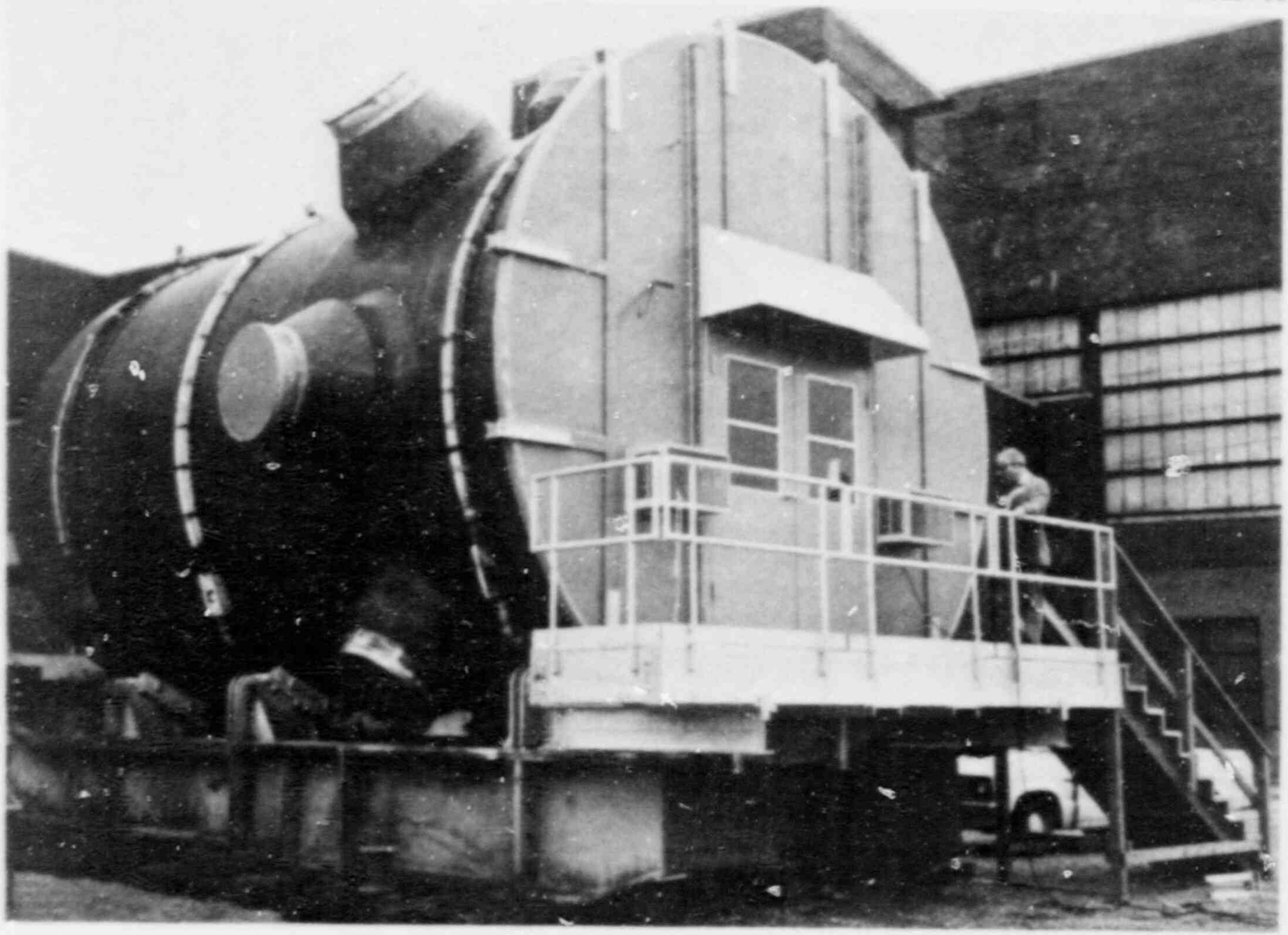

Fig. 11.2. View of the PVRUF vessel following modifications to permit personnel access and occupancy.

ORNL PHOTO 8309-88

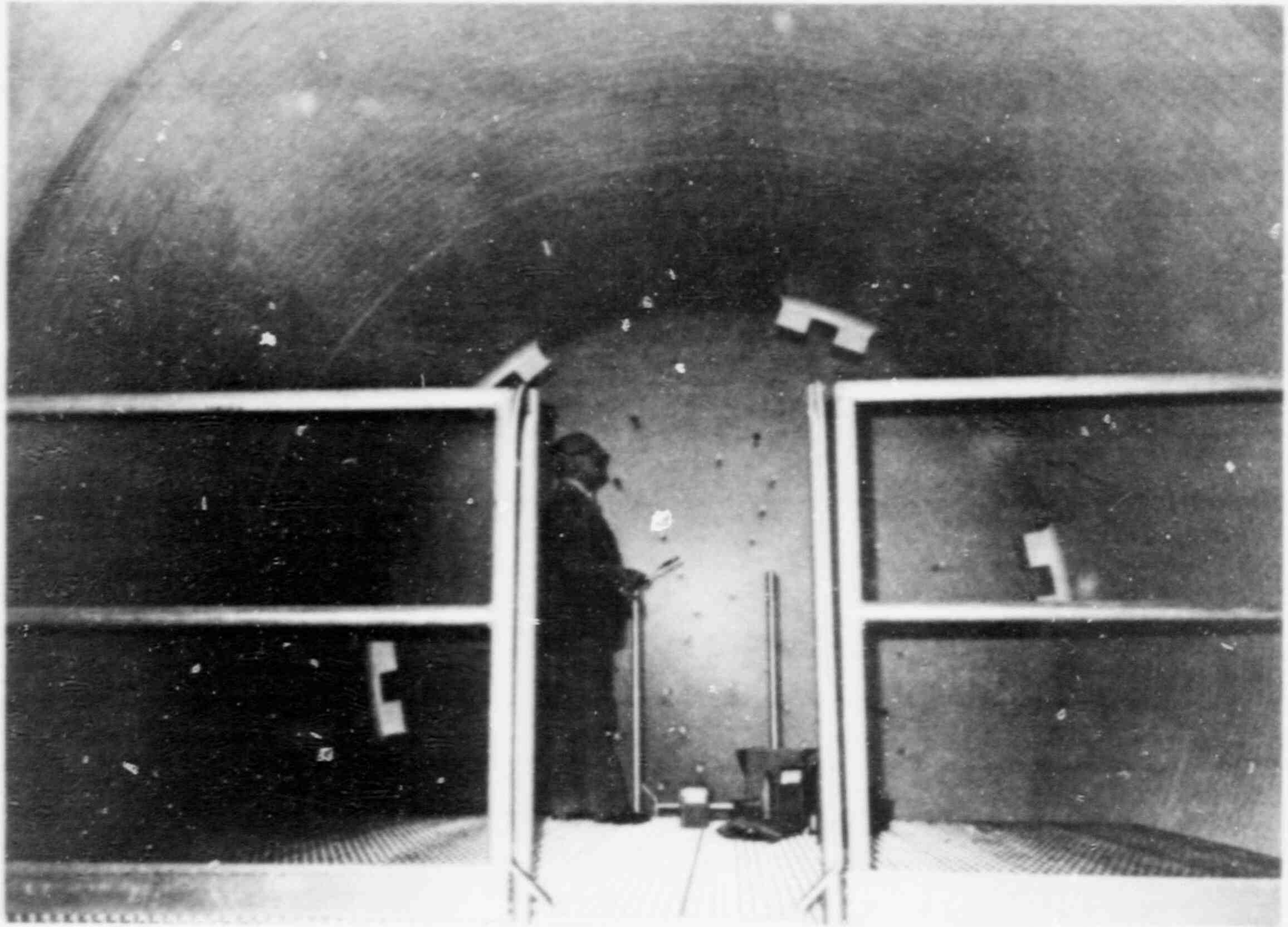

Fig. 11.3. View of interior of PVRUF vessel showing the floor surface of the movable scaffolding and the vessel cladding.

ORNL PHOTO 8308-83

Fig. 11.4. View of the office trailer, access road, and PVRUF vessel established for interim activities.

activities has been delayed because CE has not yet received permission from the owner of these calibration blocks to sell them to Martin Marietta Energy Systems, Inc. A request for such permission is being processed. The seven calibration blocks include one each for 12.7-cm (5-in.), 17.8-cm (9-in.), and 27.9-cm (11-in.) wall thicknesses, and also one each for the vessel flange, nozzle safe ends, and control-rod-drive mechanism nozzles.

11.3.2 Complementary weld seams

When the PVRUF vessel was procured from CE, ORNL learned that CE was flame-cut dismantling a companion vessel to the PVRUF vessel for selling as scrap. Two weldments located in the companion vessel, shown in Fig. 11.5, have been procured from CE for future NDE studies to improve the data base on flaw density in light-water reactor vessels.

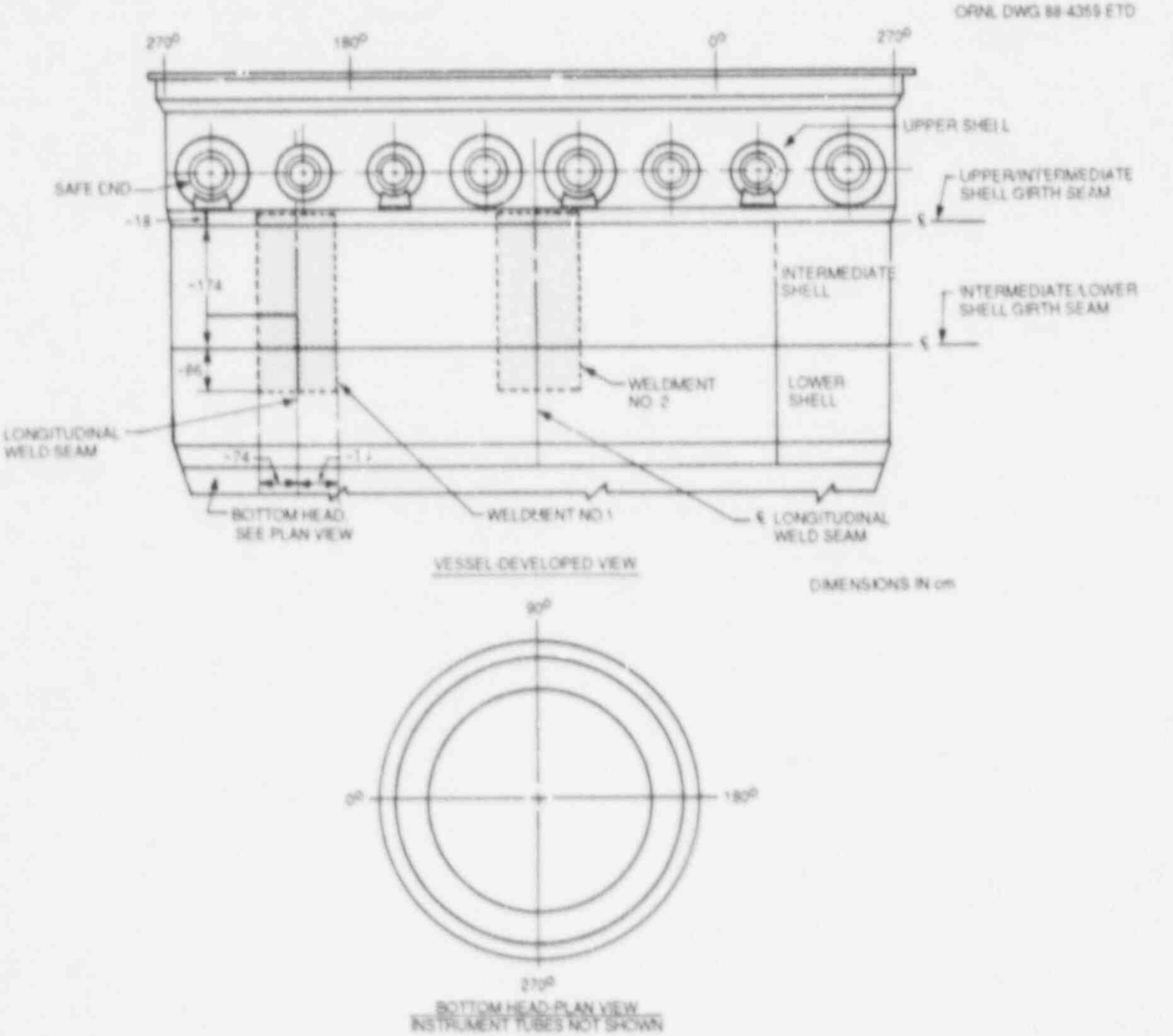

Fig. 11.5. Location of weldments in companion vessel to the PVRUF vessel.

Reference

1. C. E. Pugh and G. C. Robinson, "Pressure-Vessel-Research Users' Facility," pp. 284–95 in *Heavy-Section Steel Technology Program Semiann. Prog. Rep. April–September 1987*, NUREG/CR-4219, Vol. 4, No. 2 (ORNL/TM-9593/V4&N2), Martin Marietta Energy Systems, Inc., Oak Ridge Natl. Lab.

CONVERSION FACTORS[a]

SI unit	English unit	Factor
mm	in.	0.0393701
cm	in.	0.393701
m	ft	3.28084
m/s	ft/s	3.28084
kN	lb_f	224.809
kPa	psi	0.145038
MPa	ksi	0.145038
$MPa\cdot\sqrt{m}$	$ksi\cdot\sqrt{in.}$	0.910048
J	ft•lb	0.737562
K	°F or °R	1.8
kJ/m^2	$in.\text{-}lb/in.^2$	5.71015
$W\cdot m^{-2}\cdot K^{-1}$	$Btu/h\cdot ft^2\cdot °F$	0.176110
kg	lb	2.20462
kg/m^3	$lb/in.^3$	3.61273×10^{-5}
mm/N	$in./lb_f$	0.175127
T(°F) = 1.8 T(°C) + 32		

[a] Multiply SI quantity by given factor to obtain English quantity.

NUREG/CR-4219
Vol. 5, No. 1
ORNL/TM-9593/V5&N1
Dist. Category RF

Internal Distribution

1. D. J. Alexander
2. B. R. Bass
3. S. E. Bolt
4. R. H. Bryan
5. J. W. Bryson
6. R. D. Cheverton
7. J. M. Corum

8-12. W. R. Corwin

13. J. A. Getsi
14. R. C. Gwaltney
15. F. M. Haggag
16. S. K. Iskander
17. F. B. Kam
18. A. P. Malinauskas
19. J. G. Merkle

20-21. R. K. Nanstad

22. D. J. Naus
23. J. S. Parrott
24. W. E. Pennell
25. N. Perrone
26. C. B. Oland
27. C. E. Pugh
28. G. C. Robinson
29. G. M. Slaughter
30. J. E. Smith
31. R. W. Swindeman
32. K. R. Thoms
33. H. E. Trammell
34. J. Keeney-Walker
35. ORNL Patent Office
36. Central Research Library
37. Document Reference Section

38-39. Laboratory Records Department

40. Laboratory Records (RC)

External Distribution

41. C. Z. Serpan, Division of Engineering, Nuclear Regulatory Commission, Washington, DC 20555
42. Michael E. Mayfield, Division of Engineering, Nuclear Regulatory Commission, Washington, DC 20555
43. J. R. Strosnider, Region I, Nuclear Regulatory Commission, 631 Park Avenue, King of Prussia, PA 19406
44. A. Gilat, Department of Mechanical Engineering, Ohio State University, 115 W. Woodruff Ave., Columbus, OH 43210
45. R. J. Fields, Fracture and Deformation Division, National Bureau of Standards, Gaithersburg, MD 20899
46. W. L. Fourney, Department of Mechanical Engineering, University of Maryland, College Park, MD 20742
47. M. F. Kanninen, Engineering and Material Science Division, Southwest Research Institute, San Antonio, TX 78284
48. J. W. Hutchinson, Division of Applied Science, Pierce Hall, Harvard University, Cambridge, MA 02138
49. E. T. Wessel, P.O. Box 0788, Andover, OH 44003-0788
50. Office of Assistant Manager for Energy Research and Development, DOE, ORO, Oak Ridge, TN 37831

51-52. Office of Scientific and Technical Information, P.O. Box 62, Oak Ridge, TN 37831

53-302. Given distribution as shown in category RF (NTIS — 10)

©U.S. GOVERNMENT PRINTING OFFICE 1988-548-118/80076

NRC FORM 335
(2-84)
NRCM 1102,
3201, 3202

U.S. NUCLEAR REGULATORY COMMISSION

BIBLIOGRAPHIC DATA SHEET

SEE INSTRUCTIONS ON THE REVERSE

1. REPORT NUMBER (Assigned by TIDC, add Vol. No., if any)
NUREG/CR-4219, Vol. 5, No.1
ORNL/TM-9593/V5&N1

2. TITLE AND SUBTITLE
Heavy-Section Steel Technology Program Semiannual
Progress Report for October 1987 - March 1988

3. LEAVE BLANK

4. DATE REPORT COMPLETED

MONTH	YEAR
July	1988

5. AUTHOR(S)
W. R. Corwin

6. DATE REPORT ISSUED

MONTH	YEAR
August	1988

7. PERFORMING ORGANIZATION NAME AND MAILING ADDRESS (Include Zip Code)
Oak Ridge National Laboratory
P. O. Box 2008
Oak Ridge, TN 37831

8. PROJECT/TASK/WORK UNIT NUMBER

9. FIN OR GRANT NUMBER
B0119

10. SPONSORING ORGANIZATION NAME AND MAILING ADDRESS (Include Zip Code)
Division of Engineering
Office of Nuclear Regulatory Research
U. S. Nuclear Regulatory Commission
Washington, DC 20555

11a. TYPE OF REPORT
Semiannual

b. PERIOD COVERED (Inclusive dates)
October 1987 - March 1988

12. SUPPLEMENTARY NOTES

13. ABSTRACT (200 words or less)

The Heavy-Section Steel Technology (HSST) Program is an engineering research activity conducted by the Oak Ridge National Laboratory for the Nuclear Regulatory Commission. The Program comprises studies related to all areas of the technology of materials fabricated into thick-section primary-coolant containment systems of light-water-cooled nuclear power reactors. The investigation focuses on the behavior and structural integrity of steel pressure vessels containing cracklike flaws. Current work is organized into twelve tasks: (1) program management, (2) fracture methodology and analysis, (3) material characterization and properties, (4) special technical assistance, (5) crack-arrest technology, (6) irradiation effects studies, (7) cladding evaluations, (8) intermediate vessel tests and analysis, (9) thermal-shock technology, (10) pressurized thermal-shock technology, (11) Pressure Vessel Research Users' Facility, and (12) shipping-cask material evaluations.

14. DOCUMENT ANALYSIS - a. KEYWORDS/DESCRIPTORS

Pressure vessels
Ferritic steels
Weldments
Irradiation
Cladding
Flaws
Thermal shock
Fracture mechanics
Crack arrest
Crack growth

b. IDENTIFIERS/OPEN-ENDED TERMS

15. AVAILABILITY STATEMENT
Unlimited

16. SECURITY CLASSIFICATION
(This page)
Unclassified
(This report)
Unclassified

17. NUMBER OF PAGES

18. PRICE

120555139217 1 1AN1RF
US NRC-OARM-ADM
DIV FOIA & PUBLICATIONS SVCS
RRES-PDR NUREG
P-210
WASHINGTON DC 20555